**UNIVERSITÀ DEGLI STUDI DI NAPOLI FEDERICO II**

DIPARTIMENTO DI MATEMATICA E APPLICAZIONI

'RENATO CACCIOPPOLI'

DOTTORATO DI RICERCA IN MATEMATICA E APPLICAZIONI

XXXIV CICLO

PH.D. THESIS

# FREE BOUNDARY APPROACH TO MODEL GRANULAR BIOFILMS: APPLICATION TO WASTEWATER TREATMENT

FABIANA RUSSO

This PhD research was conducted as part of the Campania Region Operational Program, European Social Fund, 2014-2020 ASSE III - Specific objective 14 Action 10.5.2 - Public notice "Innovative Doctorates with Industrial Characterization".

*PhD Promoter*

**Prof. L. Frunzo**,

Associate Professor
Department of Mathematics and Applications "Renato Caccioppoli"
University of Naples "Federico II", Naples, Italy

*Industrial Partner*

**COGEI Srl**, Naples, Italy

# Thesis Committee

*Thesis Supervisors*

**Prof. L. Frunzo**,

Associate Professor
Department of Mathematics and Applications "Renato Caccioppoli"
University of Naples "Federico II", Naples, Italy

**Dr. M.R. Mattei**,

Research fellow
Department of Mathematics and Applications "Renato Caccioppoli"
University of Naples "Federico II", Naples, Italy

*Thesis Co-Supervisor*

**Dr. V. Luongo**,

Research fellow
Department of Mathematics and Applications "Renato Caccioppoli"
University of Naples "Federico II", Naples, Italy

# Acknowledgments

I would like to express my sincere gratitude to all the people I met during the last three years. First of all, I would like to thank Prof. Berardino D'Acunto for being an inspiring and motivating guide throughout my research activities. I wish to acknowledge Prof. Florinda Capone, for the great availability and thoughtfulness she had towards me. I specially thank my supervisors Prof. Luigi Frunzo and Dr. Maria Rosaria Mattei for all their help and support along these three years and for believing in my abilities. Their comments and suggestions have made me grow personally as well as scientifically. They have always encouraged me to do more and better and taught me how to overcome problems and difficulties. I would also like to thank Dr. Vincenzo Luongo, who has always behaved like a friend. He has helped me during my research activities and supported me in the preparation of all my scientific presentations. Thank you to all the colleagues and friends with whom I shared this wonderful period of my life. Thanks to Grazia for supporting me and for always being there in good and bad moments. Thanks to Alberto for being my main collaborator during these years: our long discussions and conversations have been fundamental for my research activities. Thanks to Daniele for supporting me in the realization of my first work. Thanks also to Giuliana, Jacopo, and Peppe, for sharing with me joy and anxiety moments. All of you guys made these years unforgettable! I am particularly grateful to my family and my old friends, who have been a constant source of support and encouragement. Thank you for believing in me! Finally, I would like to thank my boyfriend, who always supported and encouraged me. Your love and passion in the work made me who I am today!

# Abstract

## English

The present dissertation relates to the mathematical modelling of innovative biotechnologies for wastewater treatment. Novel mathematical models are derived and presented, with the aim of investigating new treatment processes and examining crucial aspects of such biological processes never or not exhaustively explored by mathematical models present in literature.

In the first study, the mathematical model simulates the metals leaching from electronic waste induced by dark fermentation effluents. It consists of a system of non-linear ordinary differential equations (ODEs), accounting for the main biological, chemical, and physical processes occurring during the fermentation of soluble biodegradable substrates and the dissolution process of metals in an anaerobic environment. The second part of the thesis deals with biofilm modelling and focuses on the genesis and formation of granular biofilms, with a special interest in anaerobic granules, anammox granules and oxygenic photogranules. The models presented here are formulated as spherical free boundary problems under the assumption of radial symmetry, which describe the evolution of granular biofilms. Such biofilm models are conceived in the framework of continuum mathematical modelling of biofilm growth, and consists of systems of partial differential equations (PDEs): non-linear hyperbolic PDEs model

the advective transport and growth of sessile biomasses which constitute the biofilm solid matrix; quasi-linear parabolic PDEs govern the diffusive transport and conversion of soluble substrates; and quasi-linear parabolic PDEs describe the invasion phenomena and conversion of planktonic cells suspended in the surrounding environment. The free boundary evolution is governed by an ODE, which accounts for the growth of sessile biomass as well as exchange fluxes with the bulk liquid. In addition, a system of ODEs derived from mass balance considerations is accounted to describe the dynamics of dissolved substrates and suspended biomasses within the bulk liquid. In the second study, a multiscale model on the genesis and growth of granular biofilms within a completely mixed continuous reactor is presented. The mathematical model is derived for a generic granular-based bioreactor and applied to the anaerobic granulation process to test the model behaviour and study the formation, evolution and ecology of anaerobic granules. In the third study, the qualitative analysis of the initial formation of a multispecies granular biofilm, through the modelling of the initial attachment by pioneer microbial cells, is addressed. A theorem of existence and uniqueness of the solutions, based on the fixed-point theorem, is presented. In the fourth study, the mathematical model derived in the second study is applied to the partial nitritation/anammox process occurring in a granular-based system. It mainly addresses the invasion phenomena influence on the *de novo* granulation process of anammox granules and on the microbial stratification. The multiscale approach of the model allows to simulate both the evolution of anammox granules and dynamics of the bioreactor where granules develop. Finally, the fifth model is aimed at describing for the first time the metals biosorption process on oxygenic photogranules, recognized as a promising alternative technology for the contextual removal of organic and inorganic compounds from wastewater. Such model describes the genesis and growth processes of oxygenic photogranules within a sequencing batch reactor (SBR) and metals adsorption on their solid matrix. The main factors influencing both granulation and adsorption processes, the symbiotic and competitive microbial mechanisms driving the treatment process, and the key role that

phototrophs and $EPS$ play on metals adsorption are included in the model.

All models are integrated numerically through the development of original code in MatLab platform. The main numerical methods used are the method of characteristics and method of lines. Furthermore, numerical simulations are carried out to analyze aspects and factors influencing the biological processes investigated in the present dissertation.

# Italian

Il presente lavoro di tesi riguarda la modellizzazione matematica di biotecnologie innovativi per il trattamento delle acque reflue. Cinque nuovi modelli matematici sono stati derivati e presentati, con l'obiettivo di indagare nuovi processi di trattamento ed esaminare aspetti cruciali di tali processi biologici mai o non esplorati in modo esaustivo dai modelli matematici presenti in letteratura.

Nel primo studio, il modello matematico simula la lisciviazione dei metalli contenuti all'interno di rifiuti elettronici indotta da effluenti provenienti dalla dark fermentation e consiste in un sistema di equazioni differenziali ordinarie (ODE) non lineari, che tengono conto dei principali processi biologici, chimici e fisici che avvengono durante la fermentazione di substrati biodegradabili solubili e il processo di dissoluzione dei metalli in ambiente anaerobico. La seconda parte della tesi si occupa della modellazione matematica di biofilm e si focalizza sulla genesi e sulla formazione di biofilm granulari, con particolare interesse verso i granuli anaerobici, i granuli anammox e i fotogranuli ossigenici. I modelli qui presentati sono formulati come problemi a frontiera libera sferica sotto l'ipotesi di simmetria radiale, che descrivono l'evoluzione di biofilm granulari. Tali modelli di biofilm sono concepiti nell'ambito della modellazione matematica della crescita di biofilm con approccio continuo e sono costituiti da sistemi di equazioni differenziali alle derivate parziali (PDE): PDE iperboliche non lineari modellano il trasporto advettivo e la crescita di biomasse sessili che costituiscono la

matrice solida del biofilm; PDE paraboliche quasi-lineari governano il trasporto diffusivo e la conversione dei substrati solubili; e PDE paraboliche quasi-lineari descrivono i fenomeni di invasione e la conversione delle cellule planctoniche sospese nell'ambiente circostante. L'evoluzione della frontiera libera è governata da un'ODE che tiene conto della crescita della biomassa sessile e dei flussi di scambio con il bulk liquido. Inoltre, si considera un sistema di ODE derivate da considerazioni di bilancio di massa per descrivere la dinamica dei substrati disciolti e delle biomasse sospese nel bulk liquido. Nel secondo studio viene presentato un modello multiscala sulla genesi e crescita di biofilm granulari all'interno di un reattore continuo completamente miscelato. Il modello matematico viene derivato per un bioreattore generico a base granulare e applicato al processo di granulazione anaerobica per testare il comportamento del modello e studiare la formazione, l'evoluzione e l'ecologia dei granuli anaerobici. Nel terzo studio viene affrontata l'analisi qualitativa della formazione iniziale di un biofilm granulare multispecie, attraverso la modellizzazione dell'attachment iniziale da parte di cellule microbiche pioniere. Viene presentato un teorema di esistenza e unicità della soluzione, basato sul teorema del punto fisso. Nel quarto studio il modello matematico derivato nel secondo studio è applicato al processo di nitrificazione parziale/anammox che si verifica in un sistema granulare e affronta l'influenza dei fenomeni di invasione sul processo di granulazione *de novo* dei granuli anammox e sulla stratificazione microbica. L'approccio multiscala del modello consente di simulare sia l'evoluzione dei biofilm granulari che le dinamiche del bioreattore in cui i granuli si sviluppano. Infine, il quinto modello ha lo scopo di descrivere per la prima volta il processo di adsorbimento di metalli su fotogranuli ossigenici, riconosciuto come una promettente tecnologia alternativa per la contestuale rimozione di composti organici e inorganici dalle acque reflue. Tale modello descrive i processi di genesi e di crescita dei fotogranuli ossigenici all'interno di un sistema SBR e l'adsorbimento dei metalli sulla loro matrice solida. I principali fattori che influenzano i processi di granulazione e di adsorbimento, i meccanismi microbici simbiotici e competitivi che guidano il processo di trattamento e il ruolo chiave

che i fototrofi e l'$EPS$ svolgono nel processo di adsorbimento dei metalli sono inclusi nel modello.

Tutti i modelli sono integrati numericamente attraverso lo sviluppo di codici originali in piattaforma MatLab. I principali metodi numerici utilizzati sono il metodo delle caratteristiche e il metodo delle linee. Inoltre, vengono effettuate simulazioni numeriche per analizzare aspetti e fattori che influenzano i processi biologici indagati nel presente lavoro di tesi.

# Contents

**Acknowledgments** **ii**

**Abstract** **iii**

**1 Introduction** **1**

1.1 Research context . . . . . 1

1.1.1 Multispecies biofilms . . . . . 2

1.1.2 Granular biofilms and applications . . . . . 4

1.1.3 Biofilm modelling . . . . . 6

1.2 Scope of the thesis . . . . . 7

**2 Modelling metal recovery from E-waste using a Dark-Fermentation-Leaching process** **11**

2.1 Introduction . . . . . 11

2.2 Biochemical framework: dark fermentation and leaching processes . . . 16

2.3 Mathematical model . . . . . 18

2.3.1 Model definition . . . . . 18

2.3.2 Model application . . . . . 22

2.4 Model calibration . . . . . 30

2.5 Numerical studies and results . . . . . 38

2.5.1 NS1 - Effects of metal inhibition . . . . . 40

2.5.2 NS2 and NS3 - Effects of F/M ratio on DF process . . . . . 42

2.5.3 NS4 - Effects of metal concentration on leaching process . . . . 46
2.6 Conclusions . . . . . 47
2.7 Appendix A . . . . . 48

**3 Multiscale modelling of *de novo* anaerobic granulation 51**
3.1 Introduction . . . . . 51
3.2 Mathematical Model . . . . . 56
3.2.1 Modelling granule scale . . . . . 57
3.2.2 Modelling reactor scale . . . . . 63
3.2.3 Initial and boundary conditions . . . . . 65
3.3 Modelling *de novo* anaerobic granulation . . . . . 69
3.4 Numerical simulations and results . . . . . 77
3.4.1 NS1 - Anaerobic granulation process . . . . . 79
3.4.2 NS2 - Effects of influent wastewater composition . . . . . 83
3.4.3 NS3 - Effects of granulation properties . . . . . 88
3.4.4 NS4 - Effects of biomass density . . . . . 93
3.4.5 NS5 - Effects of erosive detachment . . . . . 97
3.4.6 NS6 - Effects of number of granules . . . . . 100
3.5 Discussion . . . . . 104
3.5.1 Model assumptions . . . . . 104
3.5.2 Size, microbial distribution, and ecology of biofilm granules, and the evolution of bulk liquid characteristics . . . . . 106
3.6 Conclusions . . . . . 110

**4 Spherical free boundary problem for the initial phase of multispecies granular biofilm growth 114**
4.1 Introduction . . . . . 114
4.2 Modelling the initial phase of multispecies granular biofilm growth . . 118
4.2.1 Remark 1 . . . . . 123

4.2.2 Characteristic coordinates . . . . . 124
4.3 Spherical free boundary value problem in characteristic coordinates . . 131
4.4 Uniqueness and existence theorem . . . . . 135
4.5 Conclusions . . . . . 138

**5 Multiscale modelling of the start-up process of anammox-based granular reactors 140**

5.1 Introduction . . . . . 140
5.2 Mathematical Model . . . . . 146
5.3 Modelling *de novo* anammox granulation . . . . . 153
5.4 Numerical studies and results . . . . . 162
5.4.1 Influent characteristics, reactor configuration and simulation parameters. . . . . 162
5.4.2 S1 - Partial nitritation/anammox process in granular-based reactors . . . . . 164
5.4.3 S2 - Effects of the anammox addition time on the process . . . . 170
5.4.4 S3 - Effects of the anammox inoculum size on the process . . . 175
5.4.5 S4 - Combined effects of anammox addition time and anammox inoculum size . . . . . 179
5.5 Conclusions . . . . . 182

**6 Multiscale modelling of heavy metals adsorption on algal-bacterial photogranules 184**

6.1 Introduction . . . . . 184
6.2 Mathematical model . . . . . 189
6.2.1 Granule mesoscale model . . . . . 190
6.2.2 Bioreactor macroscale model . . . . . 195
6.2.3 Initial and boundary conditions . . . . . 200
6.3 Biochemical framework: OPGs granulation and adsorption processes . . 202

6.3.1 Metabolic kinetics of OPGs . . . . . 202
6.3.2 Adsorption process . . . . . 204
6.3.3 Modelling of heavy metals adsorption on OPGs . . . . . 205
6.4 Numerical studies and results . . . . . 215
6.4.1 SET1 - Evaluation of metal removal from industrial wastewater in OPGs-based system . . . . . 217
6.4.2 SET2 - Effects of metal concentration on OPGs formation and adsorption processes . . . . . 226
6.4.3 SET3 - Effects of metal adsorption capabilities on OPGs formation and adsorption processes . . . . . 233
6.5 Discussion and conclusions . . . . . 239

**7 Conclusion and future perspectives** **242**

# List of Figures

2.1 Scheme of dark fermentation and leaching processes. . . . . 13

2.2 Conversion scheme of the dark fermentation and the leaching process (adapted and modified from Batstone et al. (2002) [1]). Solid arrows: biological reactions; dashed arrows: acid-base equilibrium; dash-dot arrows: liquid-gas transfer; dotted arrows: leaching process. Biochemical and leaching reactions are modelled as irreversible processes, while physico-chemical reactions (acid-base and liquid-gas equilibria) are implemented as reversible processes. Glucose: $S_{su}$; butyric acid: $S_{bu}$; butyrate: $S_{bu}^{-}$; acetic acid: $S_{ac}$; acetate: $S_{ac}^{-}$; hydrogen: $S_{H_2}$; hydrogen gas: $S_{gas,H_2}$; oxygen dioxide: $S_{CO_2}$; bicarbonate: $S_{HCO_3}^{-}$; oxygen dioxide gas: $S_{gas,CO_2}$; metal in solid form: $M$; metal in liquid form: $M_{liq}$. 19

2.3 $IC1$ - Evolution over time of measured and simulated values of pH (a), glucose $S_{su}$ (a), butyric acid $S_{bu}$ (b), acetic acid $S_{ac}$ (c) concentrations, cumulative hydrogen production $V_{H_2}$ (d), and concentration of metal in solution $M_{liq}$ (e). . . . . 35

2.4 $IC2$ - Evolution over time of measured and simulated values of pH (a), glucose $S_{su}$ (a), butyric acid $S_{bu}$ (b), acetic acid $S_{ac}$ (c) concentrations, cumulative hydrogen production $V_{H_2}$ (d), and concentration of metal in solution $M_{liq}$ (e). . . . . 37

2.5 $NS1$ - Evolution over time of simulated values of glucose $S_{su}$ (a), butyric acid $S_{bu}$ (b), acetic acid $S_{ac}$ (c) concentrations, cumulative hydrogen production $V_{H_2}$ (d), and concentration of metal in solution $M_{liq}$ (e) for different initial concentration of metal $M^0$. $R1$: $M^0 = 6.5\ g\ L^{-1}$; $R2$: $M^0 = 3\ g\ L^{-1}$; $R3$: $M^0 = 1.5\ g\ L^{-1}$; $R4$: $M^0 = 0.5\ g\ L^{-1}$. Initial concentration of sugar and sugar fermenters: $S^0_{su} = 10\ gCOD\ L^{-1}$ and $X^0_{su} = 5\ gCOD\ L^{-1}$. Red rhombus represents the maximum removal efficiency. . . . . 41

2.6 $NS2$ - Evolution over time of simulated values of glucose $S_{su}$ (a), butyric acid $S_{bu}$ (b), acetic acid $S_{ac}$ (c) concentrations, cumulative hydrogen production $V_{H_2}$ (d), and concentration of metal in solution $M_{liq}$ (e) for different initial concentration of sugar $S^0_{su}$. $R5$: $S^0_{su} = 5\ gCOD\ L^{-1}$; $R6$: $S^0_{su} = 10\ gCOD\ L^{-1}$; $R7$: $S^0_{su} = 15\ gCOD\ L^{-1}$; $R8$: $S^0_{su} = 20\ gCOD\ L^{-1}$; $R9$: $S^0_{su} = 25\ gCOD\ L^{-1}$; $R10$: $S^0_{su} = 30\ gCOD\ L^{-1}$; $R11$: $S^0_{su} = 35\ gCOD\ L^{-1}$; $R12$: $S^0_{su} = 40\ gCOD\ L^{-1}$; $R13$: $S^0_{su} = 45\ gCOD\ L^{-1}$; $R14$: $S^0_{su} = 50\ gCOD\ L^{-1}$. Initial concentration of sugar fermenters and metal concentration: $X^0_{su} = 5\ gCOD\ L^{-1}$ and $M = 6.5\ g\ L^{-1}$. Red rhombus represents the removal efficiency after 24 hours. . . . . 43

2.7 $NS3$ - Evolution over time of simulated values of glucose $S_{su}$ (a), butyric acid $S_{bu}$ (b), acetic acid $S_{ac}$ (c) concentrations, cumulative hydrogen production $V_{H_2}$ (d), and concentration of metal in solution $M_{liq}$ (e) for different initial concentration of sugar $S^0_{su}$. $R15$: $S^0_{su} = 5\, gCOD\, L^{-1}$; $R16$: $S^0_{su} = 10\ gCOD\ L^{-1}$; $R17$: $S^0_{su} = 15\ gCOD\ L^{-1}$; $R18$: $S^0_{su} = 20\ gCOD\ L^{-1}$; $R19$: $S^0_{su} = 25\ gCOD\ L^{-1}$; $R20$: $S^0_{su} = 30\, gCOD\, L^{-1}$; $R21$: $S^0_{su} = 35\, gCOD\, L^{-1}$; $R22$: $S^0_{su} = 40\, gCOD\, L^{-1}$; $R23$: $S^0_{su} = 45\ gCOD\ L^{-1}$; $R24$: $S^0_{su} = 50\ gCOD\ L^{-1}$. Initial concentration of sugar fermenters and metal concentration: $X^0_{su} = 10\ gCOD\ L^{-1}$ and $M = 6.5\ g\ L^{-1}$. Red rhombus represents the removal efficiency after $24$ hours. . . . . 45

2.8 $NS4$ - Evolution over time of simulated values of glucose $S_{su}$ (a), butyric acid $S_{bu}$ (b), acetic acid $S_{ac}$ (c) concentrations, cumulative hydrogen production $V_{H_2}$ (d), and concentration of metal in solution $M_{liq}$ (e) for different concentration of metal $M(t_W)$. $R25$: $M = 10\ g\ L^{-1}$; $R26$: $M = 6.5\ g\ L^{-1}$; $R27$: $M = 3\ g\ L^{-1}$; $R28$: $M = 1\ g\ L^{-1}$; $R29$: $M = 0.5\ g\ L^{-1}$; $R30$: $M = 0.1\ g\ L^{-1}$. Initial concentration of sugar and sugar fermenters: $S^0_{su} = 40\, gCOD\, L^{-1}$ and $X^0_{su} = 10\, gCOD\, L^{-1}$. Red rhombus represents the removal efficiency after $24$ hours. . . . . 46

2.9 Experimental campaigns bioreactors. . . . . 49

3.1 Multiscale representation of the model. The bioreactor is modelled as a perfectly mixed continuous system (on the left), having volume $V$, where $N_G$ biofilm granules are immersed. A focus on a single granule is presented on the right, with all processes considered in the model. The granule has a zero initial radius $R(0)$, which varies over time due to the effect of various biological processes. Metabolic processes within the granule are carried out by the sessile biomass $X_i(r,t)$, which grows by converting the substrates dissolved in the biofilm liquid $S_j(r,t)$, while metabolic processes within the bulk liquid are carried out by the planktonic biomasses $\psi_i^*(t)$, which grows by converting the substrates dissolved in the bulk liquid $S_j^*(t)$. The superficial exchange processes of attachment and detachment are considered at the interface granule-bulk liquid. Moreover, invasion processes are modelled: the planktonic biomass $\psi_i(r,t)$ invades the solid matrix of the granule and switches its phenotype from planktonic to sessile. Finally, process of diffusion of substrates across the granule is included in the model. Solid arrows: processes within the granule. Dash-dot arrows: processes within the bulk liquid. Dash arrows: exchange processes between granule and bulk liquid. . . . . 57

3.2 NS1 - Biofilm radius evolution over time. Influent wastewater composition: $S_{Su}^{in} = 3500\ g\ m^{-3}$ (Sugar), $S_{Bu}^{in} = 0$ (Butyrate), $S_{Pro}^{in} = 0$ (Propionate), $S_{Ac}^{in} = 0$ (Acetate), $S_{CH_4}^{in} = 0$ (Methane). . . . . 79

3.3 NS1 - Microbial species distribution in the diametrical section and across the radius of the granule, at $T = 5\ d$, $T = 15\ d$, $T = 40\ d$ and $T = 70\ d$. Influent wastewater composition: $S_{Su}^{in} = 3500\ g\ m^{-3}$ (Sugar), $S_{Bu}^{in} = 0$ (Butyrate), $S_{Pro}^{in} = 0$ (Propionate), $S_{Ac}^{in} = 0$ (Acetate), $S_{CH_4}^{in} = 0$ (Methane). . . . . 80

3.4 NS1 - Distribution of soluble substrates along the granule radius at $T = 300\ d$. $S_{Su}$: Sugar, $S_{Bu}$: Butyrate, $S_{Pro}$: Propionate, $S_{Ac}$: Acetate, $S_{CH_4}$: Methane. Influent wastewater composition: $S_{Su}^{in} = 3500\ g\ m^{-3}$ (Sugar), $S_{Bu}^{in} = 0$ (Butyrate), $S_{Pro}^{in} = 0$ (Propionate), $S_{Ac}^{in} = 0$ (Acetate), $S_{CH_4}^{in} = 0$ (Methane). . . . . 81

3.5 NS1 - Evolution of mass of sessile species within the reactor. $m_{Su}$: mass of sugar fermenters, $m_{Bu}$: mass of butyrate consumers, $m_{Pro}$: mass of propionate consumers, $m_{Ac}$: mass of acetoclastic methanogens, $m_{tot}$: total sessile mass. Influent wastewater composition: $S_{Su}^{in} = 3500\ g\ m^{-3}$ (Sugar), $S_{Bu}^{in} = 0$ (Butyrate), $S_{Pro}^{in} = 0$ (Propionate), $S_{Ac}^{in} = 0$ (Acetate), $S_{CH_4}^{in} = 0$ (Methane). . . . . 82

3.6 NS1 - Evolution of soluble substrates (top) and planktonic biomass (bottom) concentrations within the bulk liquid. $S_{Su}^{*}$: Sugar, $S_{Bu}^{*}$: Butyrate, $S_{Pro}^{*}$: Propionate, $S_{Ac}^{*}$: Acetate, $S_{CH_4}^{*}$: Methane, $\psi_{Su}^{*}$: Sugar fermenters, $\psi_{Bu}^{*}$: Butyrate consumers, $\psi_{Pro}^{*}$: Propionate consumers, $\psi_{Ac}^{*}$: Acetoclastic methanogens. Influent wastewater composition: $S_{Su}^{in} = 3500\ g\ m^{-3}$ (Sugar), $S_{Bu}^{in} = 0$ (Butyrate), $S_{Pro}^{in} = 0$ (Propionate), $S_{Ac}^{in} = 0$ (Acetate), $S_{CH_4}^{in} = 0$ (Methane). . . . . 83

3.7 NS2 - Biofilm radius evolution over time for different influent wastewater compositions. $S_{Su}^{in}$: Sugar, $S_{Bu}^{in}$: Butyrate, $S_{Pro}^{in}$: Propionate, $S_{Ac}^{in}$: Acetate, $S_{CH_4}^{in}$: Methane. . . . . 84

3.8 NS2 - Microbial species distribution in the diametrical section and across the radius of the granule at $T = 70\ d$, for different influent wastewater compositions. RUN1: $S_{Su}^{in} = 3500\ g\ m^{-3}$, $S_{Bu}^{in} = S_{Pro}^{in} = S_{Ac}^{in} = S_{CH_4}^{in} = 0$; RUN2: $S_{Su}^{in} = 2000\ g\ m^{-3}$, $S_{Bu}^{in} = S_{Pro}^{in} = S_{Ac}^{in} = 500\ g\ m^{-3}$, $S_{CH_4}^{in} = 0$; RUN3: $S_{Su}^{in} = S_{Bu}^{in} = S_{Pro}^{in} = S_{Ac}^{in} = 880\ g\ m^{-3}$, $S_{CH_4}^{in} = 0$; RUN4: $S_{Su}^{in} = 0$, $S_{Bu}^{in} = S_{Pro}^{in} = S_{Ac}^{in} = 1170\ g\ m^{-3}$, $S_{CH_4}^{in} = 0$. $S_{Su}^{in}$: Sugar, $S_{Bu}^{in}$: Butyrate, $S_{Pro}^{in}$: Propionate, $S_{Ac}^{in}$: Acetate, $S_{CH_4}^{in}$: Methane. . . . . 85

3.9 NS2 - Relative abundances of microbial species within the granule at several times under different influent wastewater compositions. $S_{Su}^{in}$: Sugar, $S_{Bu}^{in}$: Butyrate, $S_{Pro}^{in}$: Propionate, $S_{Ac}^{in}$: Acetate, $S_{CH_4}^{in}$: Methane. . 86

3.10 NS2 - Evolution of soluble substrates concentrations within the bulk liquid for different influent wastewater compositions. $S_{Su}^{*}$: Sugar, $S_{Bu}^{*}$: Butyrate, $S_{Pro}^{*}$: Propionate, $S_{Ac}^{*}$: Acetate, $S_{CH_4}^{*}$: Methane. . . . . 87

3.11 NS2 - Evolution of planktonic biomass concentrations within the bulk liquid for different influent wastewater compositions. $\psi_{Su}^{*}$: Sugar fermenters, $\psi_{Bu}^{*}$: Butyrate consumers, $\psi_{Pro}^{*}$: Propionate consumers, $\psi_{Ac}^{*}$: Acetoclastic methanogens. . . . . 88

3.12 NS3 - Biofilm radius evolution over time for different attachment velocities $v_{a,i}$ (left), with a focus on the first 10 days (right). $\tilde{v}_{a,i}$: value of attachment velocity of the $i^{th}$ planktonic species set in RUN1. Influent wastewater composition: $S_{Su}^{in} = 3500\ g\ m^{-3}$ (Sugar), $S_{Bu}^{in} = 0$ (Butyrate), $S_{Pro}^{in} = 0$ (Propionate), $S_{Ac}^{in} = 0$ (Acetate), $S_{CH_4}^{in} = 0$ (Methane). 89

3.13 NS3 - Mass of microbial species within the granule at $T = 10\ d$, $T = 20\ d$, $T = 30\ d$, $T = 50\ d$, $T = 100\ d$ and $T = 300\ d$ under different attachment velocities $v_{a,i}$. RUN5: $v_{a,i} = 0.05\ \tilde{v}_{a,i}$, RUN6: $v_{a,i} = 0.1\ \tilde{v}_{a,i}$, RUN7: $v_{a,i} = 0.25\ \tilde{v}_{a,i}$, RUN8: $v_{a,i} = 0.5\ \tilde{v}_{a,i}$, RUN9: $v_{a,i} = \tilde{v}_{a,i}$, RUN10: $v_{a,i} = 2\ \tilde{v}_{a,i}$, RUN11: $v_{a,i} = 3\ \tilde{v}_{a,i}$, RUN12: $v_{a,i} = 4\ \tilde{v}_{a,i}$, RUN13: $v_{a,i} = 5\ \tilde{v}_{a,i}$. $\tilde{v}_{a,i}$: value of attachment velocity of the $i^{th}$ planktonic species set in RUN1. Influent wastewater composition: $S_{Su}^{in} = 3500\ g\ m^{-3}$ (Sugar), $S_{Bu}^{in} = 0$ (Butyrate), $S_{Pro}^{in} = 0$ (Propionate), $S_{Ac}^{in} = 0$ (Acetate), $S_{CH_4}^{in} = 0$ (Methane). . . . . 90

3.14 NS3 - Relative abundances of microbial species within the granule at $T = 10\ d$, $T = 20\ d$, $T = 30\ d$, $T = 50\ d$, $T = 100\ d$ and $T = 300\ d$ under different attachment velocities $v_{a,i}$. RUN5: $v_{a,i} = 0.05\ \tilde{v}_{a,i}$, RUN6: $v_{a,i} = 0.1\ \tilde{v}_{a,i}$, RUN7: $v_{a,i} = 0.25\ \tilde{v}_{a,i}$, RUN8: $v_{a,i} = 0.5\ \tilde{v}_{a,i}$, RUN9: $v_{a,i} = \tilde{v}_{a,i}$, RUN10: $v_{a,i} = 2\ \tilde{v}_{a,i}$, RUN11: $v_{a,i} = 3\ \tilde{v}_{a,i}$, RUN12: $v_{a,i} = 4\ \tilde{v}_{a,i}$, RUN13: $v_{a,i} = 5\ \tilde{v}_{a,i}$. $\tilde{v}_{a,i}$: value of attachment velocity of the $i^{th}$ planktonic species set in RUN1. Influent wastewater composition: $S_{Su}^{in} = 3500\ g\ m^{-3}$ (Sugar), $S_{Bu}^{in} = 0$ (Butyrate), $S_{Pro}^{in} = 0$ (Propionate), $S_{Ac}^{in} = 0$ (Acetate), $S_{CH_4}^{in} = 0$ (Methane). . . . . 91

3.15 NS3 - Evolution of planktonic biomass concentrations within the bulk liquid for different attachment velocities $v_{a,i}$. $\psi_{Su}^{*}$: Sugar fermenters, $\psi_{Bu}^{*}$: Butyrate consumers, $\psi_{Pro}^{*}$: Propionate consumers, $\psi_{Ac}^{*}$: Acetoclastic methanogens. $\tilde{v}_{a,i}$: value of attachment velocity of the $i^{th}$ planktonic species set in RUN1. Influent wastewater composition: $S_{Su}^{in} = 3500\ g\ m^{-3}$ (Sugar), $S_{Bu}^{in} = 0$ (Butyrate), $S_{Pro}^{in} = 0$ (Propionate), $S_{Ac}^{in} = 0$ (Acetate), $S_{CH_4}^{in} = 0$ (Methane). . . . . 92

3.16 NS3 - Evolution of soluble substrates concentrations within the bulk liquid for different attachment velocities $v_{a,i}$. $S^*_{Su}$: Sugar, $S^*_{Bu}$: Butyrate, $S^*_{Pro}$: Propionate, $S^*_{Ac}$: Acetate, $S^*_{CH_4}$: Methane. $\tilde{v}_{a,i}$: value of attachment velocity of the $i^{th}$ planktonic species set in RUN1. Influent wastewater composition: $S^{in}_{Su} = 3500\ g\ m^{-3}$ (Sugar), $S^{in}_{Bu} = 0$ (Butyrate), $S^{in}_{Pro} = 0$ (Propionate), $S^{in}_{Ac} = 0$ (Acetate), $S^{in}_{CH_4} = 0$ (Methane). 93

3.17 NS4 - Biofilm radius evolution over time for different biomass densities $\rho$. Influent wastewater composition: $S^{in}_{Su} = 3500\ g\ m^{-3}$ (Sugar), $S^{in}_{Bu} = 0$ (Butyrate), $S^{in}_{Pro} = 0$ (Propionate), $S^{in}_{Ac} = 0$ (Acetate), $S^{in}_{CH_4} = 0$ (Methane). . . . . 94

3.18 NS4 - Microbial species distribution in the diametrical section and across the radius of the granule at $T = 70\ d$, for different biomass densities. RUN14: $\rho = 20000\ g\ m^{-3}$, RUN15: $\rho = 70000\ g\ m^{-3}$, RUN16: $\rho = 120000\ g\ m^{-3}$, RUN17: $\rho = 170000\ g\ m^{-3}$. Influent wastewater composition: $S^{in}_{Su} = 3500\ g\ m^{-3}$ (Sugar), $S^{in}_{Bu} = 0$ (Butyrate), $S^{in}_{Pro} = 0$ (Propionate), $S^{in}_{Ac} = 0$ (Acetate), $S^{in}_{CH_4} = 0$ (Methane). . . . . 95

3.19 NS4 - Mass (left) and relative abundances (right) of microbial species within the granule at $T = 300\ d$ for different biomass densities $\rho$. Influent wastewater composition: $S^{in}_{Su} = 3500\ g\ m^{-3}$ (Sugar), $S^{in}_{Bu} = 0$ (Butyrate), $S^{in}_{Pro} = 0$ (Propionate), $S^{in}_{Ac} = 0$ (Acetate), $S^{in}_{CH_4} = 0$ (Methane). 96

3.20 NS5 - Biofilm radius evolution over time for different detachment coefficients $\lambda$. Influent wastewater composition: $S^{in}_{Su} = 3500\ g\ m^{-3}$ (Sugar), $S^{in}_{Bu} = 0$ (Butyrate), $S^{in}_{Pro} = 0$ (Propionate), $S^{in}_{Ac} = 0$ (Acetate), $S^{in}_{CH_4} = 0$ (Methane). . . . . 97

3.21 NS5 - Microbial species distribution in the diametrical section and across the radius of the granule at $T = 70\ d$, for different detachment coefficients. RUN18: $\lambda = 4\ m^{-1}\ d^{-1}$, RUN19: $\lambda = 8\ m^{-1}\ d^{-1}$, RUN21: $\lambda = 16\ m^{-1}\ d^{-1}$, RUN25: $\lambda = 32\ m^{-1}\ d^{-1}$. Influent wastewater composition: $S_{Su}^{in} = 3500\ g\ m^{-3}$ (Sugar), $S_{Bu}^{in} = 0$ (Butyrate), $S_{Pro}^{in} = 0$ (Propionate), $S_{Ac}^{in} = 0$ (Acetate), $S_{CH_4}^{in} = 0$ (Methane). . . . . 98

3.22 NS5 - Mass (top) and relative abundances (bottom) of microbial species within the granule at $T = 300\ d$ for different detachment coefficients $\lambda$. Influent wastewater composition: $S_{Su}^{in} = 3500\ g\ m^{-3}$ (Sugar), $S_{Bu}^{in} = 0$ (Butyrate), $S_{Pro}^{in} = 0$ (Propionate), $S_{Ac}^{in} = 0$ (Acetate), $S_{CH_4}^{in} = 0$ (Methane). . . . . 100

3.23 NS6 - Biofilm radius evolution over time for different numbers of granules $N_G$. Influent wastewater composition: $S_{Su}^{in} = 3500\ g\ m^{-3}$ (Sugar), $S_{Bu}^{in} = 0$ (Butyrate), $S_{Pro}^{in} = 0$ (Propionate), $S_{Ac}^{in} = 0$ (Acetate), $S_{CH_4}^{in} = 0$ (Methane). . . . . 101

3.24 NS6 - Evolution of mass of sessile species within the reactor. $m_{Su}$: mass of sugar fermenters, $m_{Bu}$: mass of butyrate consumers, $m_{Pro}$: mass of propionate consumers, $m_{Ac}$: mass of acetoclastic methanogens. Influent wastewater composition: $S_{Su}^{in} = 3500\ g\ m^{-3}$ (Sugar), $S_{Bu}^{in} = 0$ (Butyrate), $S_{Pro}^{in} = 0$ (Propionate), $S_{Ac}^{in} = 0$ (Acetate), $S_{CH_4}^{in} = 0$ (Methane). . . . . 101

3.25 NS6 - Microbial species distribution in the diametrical section and across the radius of the granule at $T = 70\ d$, for different numbers of granules $N_G$. RUN26: $N_G = 2.4e9$, RUN27: $N_G = 7.4e9$, RUN28: $N_G = 2.4e10$, RUN29: $N_G = 7.4e10$, RUN30: $N_G = 2.4e11$. Influent wastewater composition: $S_{Su}^{in} = 3500\ g\ m^{-3}$ (Sugar), $S_{Bu}^{in} = 0$ (Butyrate), $S_{Pro}^{in} = 0$ (Propionate), $S_{Ac}^{in} = 0$ (Acetate), $S_{CH_4}^{in} = 0$ (Methane). 102

3.26 NS6 - Evolution of soluble substrates concentrations within the bulk liquid for different numbers of granules $N_G$. $S^*_{Su}$: Sugar, $S^*_{Bu}$: Butyrate, $S^*_{Pro}$: Propionate, $S^*_{Ac}$: Acetate, $S^*_{CH_4}$: Methane. Influent wastewater composition: $S^{in}_{Su} = 3500\ g\ m^{-3}$ (Sugar), $S^{in}_{Bu} = 0$ (Butyrate), $S^{in}_{Pro} = 0$ (Propionate), $S^{in}_{Ac} = 0$ (Acetate), $S^{in}_{CH_4} = 0$ (Methane). . . . . 103

3.27 NS6 - Evolution of planktonic biomass concentrations within the bulk liquid for different numbers of granules $N_G$. $\psi^*_{Su}$: Sugar fermenters, $\psi^*_{Bu}$: Butyrate consumers, $\psi^*_{Pro}$: Propionate consumers, $\psi^*_{Ac}$: Acetoclastic methanogens. Influent wastewater composition: $S^{in}_{Su} = 3500\ g\ m^{-3}$ (Sugar), $S^{in}_{Bu} = 0$ (Butyrate), $S^{in}_{Pro} = 0$ (Propionate), $S^{in}_{Ac} = 0$ (Acetate), $S^{in}_{CH_4} = 0$ (Methane). . . . . 103

4.1 Biofilm lifecycle. (I) *De novo* granulation: biofilm formation by self-immobilization of planktonic species. (II) Granular biofilm growth: switch of mode of growth from planktonic to sessile; EPS production; attachment phenomena by planktonic species. (III) Granular biofilm maturation: invasion phenomena by planktonic species; detachment and dispersal phenomena. . . . . 115

5.1 S1 - Evolution of soluble substrates (top) and planktonic biomasses (bottom) concentrations within the bulk liquid in the first 3 days. $S^*_{NH_4}$: Ammonium, $S^*_{NO_2}$: Nitrite, $S^*_{NO_3}$: Nitrate, $S^*_{OC}$: Organic carbon, $\psi^*_{AOB}$: Aerobic ammonia-oxidizing bacteria, $\psi^*_{AMX}$: Anaerobic ammonia-oxidizing bacteria, $\psi^*_{NOB}$: Aerobic nitrite-oxidizing bacteria, $\psi^*_{HB}$: Heterotrophic bacteria. Wastewater influent composition: $S^{in}_{NH_4} = 300\ gN\ m^{-3}$ (Ammonium), $S^{in}_{NO_2} = 0.0001\ gN\ m^{-3}$ (Nitrite), $S^{in}_{NO_3} = 0.0001\ gN\ m^{-3}$ (Nitrate), $S^{in}_{OC} = 50\ gCOD\ m^{-3}$ (Organic carbon). Fixed oxygen concentration within the reactor: $\overline{S}_{O_2} = 0.75\ gO_2\ m^{-3}$. Concentration of $AMX$ bacteria added in the reactor: $\psi^*_{AMX,t_{AMX}} = 500\ gCOD\ m^{-3}$. Addition time of $AMX$ sludge: $t_{AMX} = 10\ d$. . . . . 165

5.2 S1 - Evolution and steady-state of soluble substrates and $AMX$ planktonic biomass concentrations within the bulk liquid (top) and of mass of active sessile species within the granule (bottom). $S^*_{NH_4}$: Ammonium, $S^*_{NO_2}$: Nitrite, $S^*_{NO_3}$: Nitrate, $S^*_{OC}$: Organic carbon, $\psi^*_{AMX}$: Anaerobic ammonia-oxidizing bacteria, $m_{Su}$: mass of aerobic ammonia-oxidizing bacteria, $m_{Bu}$: mass of anaerobic ammonia-oxidizing bacteria, $m_{Pro}$: mass of aerobic nitrite-oxidizing bacteria, $m_{Ac}$: mass of heterotrophic bacteria. Wastewater influent composition: $S^{in}_{NH_4} = 300\ gN\ m^{-3}$ (Ammonium), $S^{in}_{NO_2} = 0.0001\ gN\ m^{-3}$ (Nitrite), $S^{in}_{NO_3} = 0.0001\ gN\ m^{-3}$ (Nitrate), $S^{in}_{OC} = 50\ gCOD\ m^{-3}$ (Organic carbon). Fixed oxygen concentration within the reactor: $\overline{S}_{O_2} = 0.75\ gO_2\ m^{-3}$. Concentration of $AMX$ bacteria added in the reactor: $\psi^*_{AMX,t_{AMX}} = 500\ gCOD\ m^{-3}$. Addition time of $AMX$ sludge: $t_{AMX} = 10\ d$. . . . . 166

5.3 S1 - Active microbial species distribution in the diametrical section, at $T = 15\ d$, $T = 50\ d$, $T = 120\ d$, $T = 150\ d$, $T = 300\ d$. Wastewater influent composition: $S^{in}_{NH_4} = 300\ gN\ m^{-3}$ (Ammonium), $S^{in}_{NO_2} = 0.0001\ gN\ m^{-3}$ (Nitrite), $S^{in}_{NO_3} = 0.0001\ gN\ m^{-3}$ (Nitrate), $S^{in}_{OC} = 50\ gCOD\ m^{-3}$ (Organic carbon). Fixed oxygen concentration within the reactor: $\overline{S}_{O_2} = 0.75\ gO_2\ m^{-3}$. Concentration of $AMX$ bacteria added in the reactor: $\psi^*_{AMX,t_{AMX}} = 500\ gCOD\ m^{-3}$. Addition time of $AMX$ sludge: $t_{AMX} = 10\ d$. . . . . 168

5.4 S1 - Biofilm radius evolution over time. Wastewater influent composition: $S^{in}_{NH_4} = 300\ gN\ m^{-3}$ (Ammonium), $S^{in}_{NO_2} = 0.0001\ gN\ m^{-3}$ (Nitrite), $S^{in}_{NO_3} = 0.0001\ gN\ m^{-3}$ (Nitrate), $S^{in}_{OC} = 50\ gCOD\ m^{-3}$ (Organic carbon). Fixed oxygen concentration within the reactor: $\overline{S}_{O_2} = 0.75\ gO_2\ m^{-3}$. Concentration of $AMX$ bacteria added in the reactor: $\psi^*_{AMX,t_{AMX}} = 500\ gCOD\ m^{-3}$. Addition time of $AMX$ sludge: $t_{AMX} = 10\ d$. . . . . 170

5.5 S2 - Oxygen concentration within the granule (diametrical section) at the addition time of $AMX$ sludge $t_{AMX}$. Wastewater influent composition: $S^{in}_{NH_4} = 300\ gN\ m^{-3}$ (Ammonium), $S^{in}_{NO_2} = 0.0001\ gN\ m^{-3}$ (Nitrite), $S^{in}_{NO_3} = 0.0001\ gN\ m^{-3}$ (Nitrate), $S^{in}_{OC} = 50\ gCOD\ m^{-3}$ (Organic carbon). $RUN3$: $t_{AMX} = 3\ d$; $RUN4$: $t_{AMX} = 5\ d$; $RUN5$: $t_{AMX} = 10\ d$; $RUN6$: $t_{AMX} = 20\ d$; $RUN7$: $t_{AMX} = 40\ d$. Fixed oxygen concentration within the reactor: $\overline{S}_{O_2} = 0.75\ gO_2\ m^{-3}$. Concentration of $AMX$ bacteria added in the reactor: $\psi^*_{AMX,t_{AMX}} = 500\ gCOD\ m^{-3}$. . . . . 171

5.6 S2 - $AMX$ distribution within the granule (diametrical section) at $T = 90\ d$, $T = 120\ d$, $T = 150\ d$, $T = 180\ d$, $T = 260\ d$ for different addition times of $AMX$ sludge $t_{AMX}$. Wastewater influent composition: $S^{in}_{NH_4} = 300\ gN\ m^{-3}$ (Ammonium), $S^{in}_{NO_2} = 0.0001\ gN\ m^{-3}$ (Nitrite), $S^{in}_{NO_3} = 0.0001\ gN\ m^{-3}$ (Nitrate), $S^{in}_{OC} = 50\ gCOD\ m^{-3}$ (Organic carbon). $RUN2$: $t_{AMX} = 0$; $RUN4$: $t_{AMX} = 5\ d$; $RUN5$: $t_{AMX} = 10\ d$; $RUN7$: $t_{AMX} = 40\ d$. Fixed oxygen concentration within the reactor: $\overline{S}_{O_2} = 0.75\ gO_2\ m^{-3}$. Concentration of $AMX$ bacteria added in the reactor: $\psi^*_{AMX,t_{AMX}} = 500\ gCOD\ m^{-3}$. . . . . 172

5.7 S2 - Evolution of soluble substrates and planktonic $AMX$ concentrations within the bulk liquid for different addition times of $AMX$ sludge $t_{AMX}$. $S^*_{NH_4}$: Ammonium, $S^*_{NO_2}$: Nitrite, $S^*_{NO_3}$: Nitrate, $S^*_{OC}$: Organic carbon, $\psi^*_{AMX}$: Anaerobic ammonia-oxidizing bacteria. Wastewater influent composition: $S^{in}_{NH_4} = 300\ gN\ m^{-3}$ (Ammonium), $S^{in}_{NO_2} = 0.0001\ gN\ m^{-3}$ (Nitrite), $S^{in}_{NO_3} = 0.0001\ gN\ m^{-3}$ (Nitrate), $S^{in}_{OC} = 50\ gCOD\ m^{-3}$ (Organic carbon). $RUN2$: $t_{AMX} = 0$; $RUN3$: $t_{AMX} = 3\ d$; $RUN4$: $t_{AMX} = 5\ d$; $RUN5$: $t_{AMX} = 10\ d$; $RUN6$: $t_{AMX} = 20\ d$; $RUN7$: $t_{AMX} = 40\ d$. Fixed oxygen concentration within the reactor: $\overline{S}_{O_2} = 0.75\ gO_2\ m^{-3}$. Concentration of $AMX$ bacteria added in the reactor: $\psi^*_{AMX,t_{AMX}} = 500\ gCOD\ m^{-3}$. . . . . 173

5.8 S2 - Relative abundances of active microbial species within the granule at $T = 100\ d$, $T = 120\ d$, $T = 140\ d$, $T = 160\ d$, $T = 180\ d$, $T = 260\ d$ for different addition times of $AMX$ sludge $t_{AMX}$. Wastewater influent composition: $S^{in}_{NH_4} = 300\ gN\ m^{-3}$ (Ammonium), $S^{in}_{NO_2} = 0.0001\ gN\ m^{-3}$ (Nitrite), $S^{in}_{NO_3} = 0.0001\ gN\ m^{-3}$ (Nitrate), $S^{in}_{OC} = 50\ gCOD\ m^{-3}$ (Organic carbon). $RUN2$: $t_{AMX} = 0$; $RUN3$: $t_{AMX} = 3\ d$; $RUN4$: $t_{AMX} = 5\ d$; $RUN5$: $t_{AMX} = 10\ d$; $RUN6$: $t_{AMX} = 20\ d$; $RUN7$: $t_{AMX} = 40\ d$. Fixed oxygen concentration within the reactor: $\overline{S}_{O_2} = 0.75\ gO_2\ m^{-3}$. Concentration of $AMX$ bacteria added in the reactor: $\psi^*_{AMX,t_{AMX}} = 500\ gCOD\ m^{-3}$. . . . . 174

5.9 S2 - Biofilm radius evolution for different addition times of $AMX$ sludge $t_{AMX}$ (left), with a focus to the last 210 days (right). Wastewater influent composition: $S^{in}_{NH_4} = 300\ gN\ m^{-3}$ (Ammonium), $S^{in}_{NO_2} = 0.0001\ gN\ m^{-3}$ (Nitrite), $S^{in}_{NO_3} = 0.0001\ gN\ m^{-3}$ (Nitrate), $S^{in}_{OC} = 50\ gCOD\ m^{-3}$ (Organic carbon). Fixed oxygen concentration within the reactor: $\overline{S}_{O_2} = 0.75\ gO_2\ m^{-3}$. Concentration of $AMX$ bacteria added in the reactor: $\psi^*_{AMX,t_{AMX}} = 500\ gCOD\ m^{-3}$. . . . . 175

5.10 S3 - $AMX$ distribution within the granule (diametrical section) at $T = 90\ d$, $T = 120\ d$, $T = 150\ d$, $T = 180\ d$, $T = 260\ d$ for different concentrations of $AMX$ bacteria added in the reactor $\psi^*_{AMX,t_{AMX}}$. Wastewater influent composition: $S^{in}_{NH_4} = 300\ gN\ m^{-3}$ (Ammonium), $S^{in}_{NO_2} = 0.0001\ gN\ m^{-3}$ (Nitrite), $S^{in}_{NO_3} = 0.0001\ gN\ m^{-3}$ (Nitrate), $S^{in}_{OC} = 50\ gCOD\ m^{-3}$ (Organic carbon). $RUN8$: $\psi^*_{AMX,t_{AMX}} = 100\ gCOD\ m^{-3}$; $RUN10$: $\psi^*_{AMX,t_{AMX}} = 500\ gCOD\ m^{-3}$; $RUN11$: $\psi^*_{AMX,t_{AMX}} = 700\ gCOD\ m^{-3}$; $RUN12$: $\psi^*_{AMX,t_{AMX}} = 1000\ gCOD\ m^{-3}$. Fixed oxygen concentration within the reactor: $\overline{S}_{O_2} = 0.75\ gO_2\ m^{-3}$. Addition time of $AMX$ sludge: $t_{AMX} = 10\ d$. . . . . 176

5.11 S3 - Evolution of soluble substrates and planktonic $AMX$ concentrations within the bulk liquid for different concentrations of $AMX$ bacteria added in the reactor $\psi^*_{AMX,t_{AMX}}$. $S^*_{NH_4}$: Ammonium, $S^*_{NO_2}$: Nitrite, $S^*_{NO_3}$: Nitrate, $S^*_{OC}$: Organic carbon, $\psi^*_{AMX}$: Anaerobic ammonia-oxidizing bacteria. Wastewater influent composition: $S^{in}_{NH_4} = 300\, gN\, m^{-3}$ (Ammonium), $S^{in}_{NO_2} = 0.0001\, gN\, m^{-3}$ (Nitrite), $S^{in}_{NO_3} = 0.0001\, gN\, m^{-3}$ (Nitrate), $S^{in}_{OC} = 50\, gCOD\, m^{-3}$ (Organic carbon). $RUN8$: $\psi^*_{AMX,t_{AMX}} = 100\ gCOD\ m^{-3}$; $RUN9$: $\psi^*_{AMX,t_{AMX}} = 300\ gCOD\ m^{-3}$; $RUN10$: $\psi^*_{AMX,t_{AMX}} = 500\, gCOD\, m^{-3}$; $RUN11$: $\psi^*_{AMX,t_{AMX}} = 700\, gCOD\, m^{-3}$; $RUN12$: $\psi^*_{AMX,t_{AMX}} = 1000\ gCOD\ m^{-3}$; $RUN13$: $\psi^*_{AMX,t_{AMX}} = 1500\, gCOD\, m^{-3}$. Fixed oxygen concentration within the reactor: $\overline{S}_{O_2} = 0.75\ gO_2\ m^{-3}$. Addition time of $AMX$ sludge: $t_{AMX} = 10\, d$. . . . . 177

5.12 S3 - Relative abundances of active microbial species within the granule at $T = 100\ d$, $T = 120\ d$, $T = 140\ d$, $T = 160\ d$, $T = 180\ d$, $T = 260\ d$ for different concentrations of $AMX$ bacteria added in the reactor $\psi^*_{AMX,t_{AMX}}$. Wastewater influent composition: $S^{in}_{NH_4} = 300\, gN\, m^{-3}$ (Ammonium), $S^{in}_{NO_2} = 0.0001\, gN\, m^{-3}$ (Nitrite), $S^{in}_{NO_3} = 0.0001\ gN\ m^{-3}$ (Nitrate), $S^{in}_{OC} = 50\ gCOD\ m^{-3}$ (Organic carbon). $RUN8$: $\psi^*_{AMX,t_{AMX}} = 100\ gCOD\ m^{-3}$; $RUN9$: $\psi^*_{AMX,t_{AMX}} = 300\ gCOD\ m^{-3}$; $RUN10$: $\psi^*_{AMX,t_{AMX}} = 500\ gCOD\ m^{-3}$; $RUN11$: $\psi^*_{AMX,t_{AMX}} = 700\, gCOD\, m^{-3}$; $RUN12$: $\psi^*_{AMX,t_{AMX}} = 1000\, gCOD\, m^{-3}$; $RUN13$: $\psi^*_{AMX,t_{AMX}} = 1500\ gCOD\ m^{-3}$. Fixed oxygen concentration within the reactor: $\overline{S}_{O_2} = 0.75\ gO_2\ m^{-3}$. Addition time of $AMX$ sludge: $t_{AMX} = 10\, d$. . . . . 178

5.13 S3 - Biofilm radius evolution for different concentrations of $AMX$ bacteria added in the reactor $\psi^*_{AMX,t_{AMX}}$ (left), with a focus to the last 210 days (right). Wastewater influent composition: $S^{in}_{NH_4} = 300\ gN\ m^{-3}$ (Ammonium), $S^{in}_{NO_2} = 0.0001\ gN\ m^{-3}$ (Nitrite), $S^{in}_{NO_3} = 0.0001\ gN\ m^{-3}$ (Nitrate), $S^{in}_{OC} = 50\ gCOD\ m^{-3}$ (Organic carbon). Fixed oxygen concentration within the reactor: $\overline{S}_{O_2} = 0.75\ gO_2\ m^{-3}$. Addition time of $AMX$ sludge: $t_{AMX} = 10\ d$. . . . . 179

5.14 S4 - Amount of $AMX$ sessile biomass $m_{AMX}$ at $T = 170\ d$ for different addition times of $AMX$ sludge $t_{AMX}$ [3 - 40 $d$] and different concentrations of $AMX$ bacteria added in the reactor $\psi^*_{AMX,t_{AMX}}$ [100 - 1500 $gCOD\ m^{-3}$]. Wastewater influent composition: $S^{in}_{NH_4} = 300\ gN\ m^{-3}$ (Ammonium), $S^{in}_{NO_2} = 0.0001\ gN\ m^{-3}$ (Nitrite), $S^{in}_{NO_3} = 0.0001\ gN\ m^{-3}$ (Nitrate), $S^{in}_{OC} = 50\ gCOD\ m^{-3}$ (Organic carbon). Fixed oxygen concentration within the reactor: $\overline{S}_{O_2} = 0.75\ gO_2\ m^{-3}$. . 180

5.15 S4 - Time necessary to achieve the steady-state ammonium concentration $T^*$ for different addition times of $AMX$ sludge $t_{AMX}$ [3 - 40 $d$] and different concentrations of $AMX$ bacteria added in the reactor $\psi^*_{AMX,t_{AMX}}$ [100 - 1500 $gCOD\ m^{-3}$]. Wastewater influent composition: $S^{in}_{NH_4} = 300\ gN\ m^{-3}$ (Ammonium), $S^{in}_{NO_2} = 0.0001\ gN\ m^{-3}$ (Nitrite), $S^{in}_{NO_3} = 0.0001\ gN\ m^{-3}$ (Nitrate), $S^{in}_{OC} = 50\ gCOD\ m^{-3}$ (Organic carbon). Fixed oxygen concentration within the reactor: $\overline{S}_{O_2} = 0.75\ gO_2\ m^{-3}$. . . . . 181

6.1 $SET1$ - Evolution of biofilm radius and mass of sessile species over time. Wastewater influent composition: $S_{IC}^{in} = 180\ g\ m^{-3}$ (inorganic carbon), $S_{DOC}^{in} = 500\ g\ m^{-3}$ (organic carbon), $S_{NH_3}^{in} = 50\ g\ m^{-3}$ (ammonia), $S_{NO_3}^{in} = 0$ (nitrate), $S_{O_2}^{in} = 0$ (oxygen), $M^{in} = 100\ g\ m^{-3}$ (metal). Incident light intensity: $I_0 = 0.008\ kmol\ m^{-2}\ d^{-1}$. Duration of the cycle: $\tau = 6\ h$. Time of light exposure: $t_{light} = 50\%\ \tau$. . . . . 218

6.2 $SET1$- Active microbial species distribution and concentration of free metal within the diametrical section of the granule, at $T = 20\ d$, $T = 30\ d$, $T = 40\ d$, $T = 50\ d$, $T = 80\ d$. Wastewater influent composition: $S_{IC}^{in} = 180\ g\ m^{-3}$ (inorganic carbon), $S_{DOC}^{in} = 500\ g\ m^{-3}$ (organic carbon), $S_{NH_3}^{in} = 50\ g\ m^{-3}$ (ammonia), $S_{NO_3}^{in} = 0$ (nitrate), $S_{O_2}^{in} = 0$ (oxygen), $M^{in} = 100\ g\ m^{-3}$ (metal). Incident light intensity: $I_0 = 0.008\ kmol\ m^{-2}\ d^{-1}$. Duration of the cycle: $\tau = 6\ h$. Time of light exposure: $t_{light} = 50\%\ \tau$. . . . . 219

6.3 $SET1$ - Distribution of microbial species and free binding sites across the radius of the granule, at $T = 20\ d$, $T = 40\ d$, $T = 60\ d$, $T = 80\ d$. Wastewater influent composition: $S_{IC}^{in} = 180\ g\ m^{-3}$ (inorganic carbon), $S_{DOC}^{in} = 500\ g\ m^{-3}$ (organic carbon), $S_{NH_3}^{in} = 50\ g\ m^{-3}$ (ammonia), $S_{NO_3}^{in} = 0$ (nitrate), $S_{O_2}^{in} = 0$ (oxygen), $M^{in} = 100\ g\ m^{-3}$ (metal). Incident light intensity: $I_0 = 0.008\ kmol\ m^{-2}\ d^{-1}$. Duration of the cycle: $\tau = 6\ h$. Time of light exposure: $t_{light} = 50\%\ \tau$. . . . . 221

6.4 $SET1$ - Evolution of soluble substrates and metal concentrations within the reactor. Wastewater influent composition: $S_{IC}^{in} = 180\ g\ m^{-3}$ (inorganic carbon), $S_{DOC}^{in} = 500\ g\ m^{-3}$ (organic carbon), $S_{NH_3}^{in} = 50\ g\ m^{-3}$ (ammonia), $S_{NO_3}^{in} = 0$ (nitrate), $S_{O_2}^{in} = 0$ (oxygen), $M^{in} = 100\ g\ m^{-3}$ (metal). Incident light intensity: $I_0 = 0.008\ kmol\ m^{-2}\ d^{-1}$. Duration of the cycle: $\tau = 6\ h$. Time of light exposure: $t_{light} = 50\%\ \tau$. . . . . 222

6.5 $SET1$ - Evolution of soluble substrates and metal concentrations within the reactor, from 199 $d$ to 200 $d$ (four consecutive six-hours treatment cycles). Wastewater influent composition: $S_{IC}^{in} = 180\ g\ m^{-3}$ (inorganic carbon), $S_{DOC}^{in} = 500\ g\ m^{-3}$ (organic carbon), $S_{NH_3}^{in} = 50\ g\ m^{-3}$ (ammonia), $S_{NO_3}^{in} = 0$ (nitrate), $S_{O_2}^{in} = 0$ (oxygen), $M^{in} = 100\ g\ m^{-3}$ (metal). Incident light intensity: $I_0 = 0.008\ kmol\ m^{-2}\ d^{-1}$. Duration of the cycle: $\tau = 6\ h$. Time of light exposure: $t_{light} = 50\%\ \tau$ (grey portions indicate the dark phases, white portions indicate the light phases). 223

6.6 $SET1$ - Evolution of planktonic and detached biomasses concentrations within the reactor over time. Wastewater influent composition: $S_{IC}^{in} = 180\ g\ m^{-3}$ (inorganic carbon), $S_{DOC}^{in} = 500\ g\ m^{-3}$ (organic carbon), $S_{NH_3}^{in} = 50\ g\ m^{-3}$ (ammonia), $S_{NO_3}^{in} = 0$ (nitrate), $S_{O_2}^{in} = 0$ (oxygen), $M^{in} = 100\ g\ m^{-3}$ (metal). Incident light intensity: $I_0 = 0.008\ kmol\ m^{-2}\ d^{-1}$. Duration of the cycle: $\tau = 6\ h$. Time of light exposure: $t_{light} = 50\%\ \tau$. . . . . 225

6.7 $SET2$ - Phototrophs distribution within the granule (diametrical section) at $T = 20\ d$, $T = 40\ d$, $T = 60\ d$, $T = 180\ d$, $T = 200\ d$ for different metal concentrations in the influent $M^{in}$. Wastewater influent composition: $S_{IC}^{in} = 180\ g\ m^{-3}$ (inorganic carbon), $S_{DOC}^{in} = 500\ g\ m^{-3}$ (organic carbon), $S_{NH_3}^{in} = 50\ g\ m^{-3}$ (ammonia), $S_{NO_3}^{in} = 0$ (nitrate), $S_{O_2}^{in} = 0$ (oxygen). $S4 : M^{in} = 40\ g\ m^{-3}$, $S6 : M^{in} = 80\ g\ m^{-3}$, $S7 : M^{in} = 100\ g\ m^{-3}$, $S8 : M^{in} = 120\ g\ m^{-3}$, $S10 : M^{in} = 160\ g\ m^{-3}$. Incident light intensity: $I_0 = 0.008\ kmol\ m^{-2}\ d^{-1}$. Duration of the cycle: $\tau = 6\ h$. Time of light exposure: $t_{light} = 50\%\ \tau$. . . . . 227

6.8 $SET2$ - Mass of microbial species within the granule at $T = 20\ d$, $T = 30\ d$, $T = 40\ d$, $T = 50\ d$, $T = 60\ d$, $T = 200\ d$ for different metal concentrations in the influent $M^{in}$. Wastewater influent composition: $S_{IC}^{in} = 180\ g\ m^{-3}$ (inorganic carbon), $S_{DOC}^{in} = 500\ g\ m^{-3}$ (organic carbon), $S_{NH_3}^{in} = 50\ g\ m^{-3}$ (ammonia), $S_{NO_3}^{in} = 0$ (nitrate), $S_{O_2}^{in} = 0$ (oxygen). $S2 : M^{in} = 0$, $S3 : M^{in} = 20\ g\ m^{-3}$, $S4 : M^{in} = 40\ g\ m^{-3}$, $S5 : M^{in} = 60\ g\ m^{-3}$, $S6 : M^{in} = 80\ g\ m^{-3}$, $S7 : M^{in} = 100\ g\ m^{-3}$, $S8 : M^{in} = 120\ g\ m^{-3}$, $S9 : M^{in} = 140\ g\ m^{-3}$, $S10 : M^{in} = 160\ g\ m^{-3}$, $S11 : M^{in} = 180\ g\ m^{-3}$, $S12 : M^{in} = 200\ g\ m^{-3}$. Incident light intensity: $I_0 = 0.008\ kmol\ m^{-2}\ d^{-1}$. Duration of the cycle: $\tau = 6\ h$. Time of light exposure: $t_{light} = 50\%\ \tau$. . . . . 228

6.9 $SET2$ - Biofilm radius evolution over time for different metal concentrations in the influent $M^{in}$. Wastewater influent composition: $S_{IC}^{in} = 180\ g\ m^{-3}$ (inorganic carbon), $S_{DOC}^{in} = 500\ g\ m^{-3}$ (organic carbon), $S_{NH_3}^{in} = 50\ g\ m^{-3}$ (ammonia), $S_{NO_3}^{in} = 0$ (nitrate), $S_{O_2}^{in} = 0$ (oxygen). $S2 : M^{in} = 0$, $S3 : M^{in} = 20\ g\ m^{-3}$, $S4 : M^{in} = 40\ g\ m^{-3}$, $S5 : M^{in} = 60\ g\ m^{-3}$, $S6 : M^{in} = 80\ g\ m^{-3}$, $S7 : M^{in} = 100\ g\ m^{-3}$, $S8 : M^{in} = 120\ g\ m^{-3}$, $S9 : M^{in} = 140\ g\ m^{-3}$, $S10 : M^{in} = 160\ g\ m^{-3}$, $S11 : M^{in} = 180\ g\ m^{-3}$, $S12 : M^{in} = 200\ g\ m^{-3}$. Incident light intensity: $I_0 = 0.008\ kmol\ m^{-2}\ d^{-1}$. Duration of the cycle: $\tau = 6\ h$. Time of light exposure: $t_{light} = 50\%\ \tau$. . . . . 229

6.10 $SET2$ - Metal concentration evolution within the reactor for different metal concentrations in the influent $M^{in}$. Wastewater influent composition: $S_{IC}^{in} = 180\ g\ m^{-3}$ (inorganic carbon), $S_{DOC}^{in} = 500\ g\ m^{-3}$ (organic carbon), $S_{NH_3}^{in} = 50\ g\ m^{-3}$ (ammonia), $S_{NO_3}^{in} = 0$ (nitrate), $S_{O_2}^{in} = 0$ (oxygen). $S2 : M^{in} = 0$, $S3 : M^{in} = 20\ g\ m^{-3}$, $S4 : M^{in} = 40\ g\ m^{-3}$, $S5 : M^{in} = 60\ g\ m^{-3}$, $S6 : M^{in} = 80\ g\ m^{-3}$, $S7 : M^{in} = 100\ g\ m^{-3}$, $S8 : M^{in} = 120\ g\ m^{-3}$, $S9 : M^{in} = 140\ g\ m^{-3}$, $S10 : M^{in} = 160\ g\ m^{-3}$, $S11 : M^{in} = 180\ g\ m^{-3}$, $S12 : M^{in} = 200\ g\ m^{-3}$. Incident light intensity: $I_0 = 0.008\ kmol\ m^{-2}\ d^{-1}$. Duration of the cycle: $\tau = 6\ h$. Time of light exposure: $t_{light} = 50\%\ \tau$. . . . . 230

6.11 $SET2$ - Evolution of soluble substrates concentration within the reactor for different metal concentrations in the influent $M^{in}$. Wastewater influent composition: $S_{IC}^{in} = 180\ g\ m^{-3}$ (inorganic carbon), $S_{DOC}^{in} = 500\ g\ m^{-3}$ (organic carbon), $S_{NH_3}^{in} = 50\ g\ m^{-3}$ (ammonia), $S_{NO_3}^{in} = 0$ (nitrate), $S_{O_2}^{in} = 0\ g\ m^{-3}$ (oxygen). $S2 : M^{in} = 0$, $S3 : M^{in} = 20\ g\ m^{-3}$, $S4 : M^{in} = 40\ g\ m^{-3}$, $S5 : M^{in} = 60\ g\ m^{-3}$, $S6 : M^{in} = 80\ g\ m^{-3}$, $S7 : M^{in} = 100\ g\ m^{-3}$, $S8 : M^{in} = 120\ g\ m^{-3}$, $S9 : M^{in} = 140\ g\ m^{-3}$, $S10 : M^{in} = 160\ g\ m^{-3}$, $S11 : M^{in} = 180\ g\ m^{-3}$, $S12 : M^{in} = 200\ g\ m^{-3}$. Incident light intensity: $I_0 = 0.008\ kmol\ m^{-2}\ d^{-1}$. Duration of the cycle: $\tau = 6\ h$. Time of light exposure: $t_{light} = 50\%\ \tau$. 232

6.12 $SET2$ - Distribution of the residual free binding site across the radius of the granule for different metal concentrations in the influent $M^{in}$ at $T = 200\ d$. Wastewater influent composition: $S^{in}_{IC} = 180\ g\ m^{-3}$ (inorganic carbon), $S^{in}_{DOC} = 500\ g\ m^{-3}$ (organic carbon), $S^{in}_{NH_3} = 50\ g\ m^{-3}$ (ammonia), $S^{in}_{NO_3} = 0$ (nitrate), $S^{in}_{O_2} = 0$ (oxygen). $S2 : M^{in} = 0$, $S3 : M^{in} = 20\ g\ m^{-3}$, $S4 : M^{in} = 40\ g\ m^{-3}$, $S5 : M^{in} = 60\ g\ m^{-3}$, $S6 : M^{in} = 80\ g\ m^{-3}$, $S7 : M^{in} = 100\ g\ m^{-3}$, $S8 : M^{in} = 120\ g\ m^{-3}$, $S9 : M^{in} = 140\ g\ m^{-3}$, $S10 : M^{in} = 160\ g\ m^{-3}$, $S11 : M^{in} = 180\ g\ m^{-3}$, $S12 : M^{in} = 200\ g\ m^{-3}$. Incident light intensity: $I_0 = 0.008\ kmol\ m^{-2}\ d^{-1}$. Duration of the cycle: $\tau = 6\ h$. Time of light exposure: $t_{light} = 50\%\ \tau$. . . . . 233

6.13 $SET3$ - Biofilm radius evolution over time for different densities of binding sites $\rho_\theta$. Wastewater influent composition: $S^{in}_{IC} = 180\ g\ m^{-3}$ (inorganic carbon), $S^{in}_{DOC} = 500\ g\ m^{-3}$ (organic carbon), $S^{in}_{NH_3} = 50\ g\ m^{-3}$ (ammonia), $S^{in}_{NO_3} = 0$ (nitrate), $S^{in}_{O_2} = 0$ (oxygen). $S13 : \rho_\theta = 10\ N^{\circ}_{sites}\ m^{-3}$, $S14 : \rho_\theta = 20\ N^{\circ}_{sites}\ m^{-3}$, $S15 : \rho_\theta = 30\ N^{\circ}_{sites}\ m^{-3}$, $S16 : \rho_\theta = 40\ N^{\circ}_{sites}\ m^{-3}$, $S17 : \rho_\theta = 50\ N^{\circ}_{sites}\ m^{-3}$. Incident light intensity: $I_0 = 0.008\ kmol\ m^{-2}\ d^{-1}$. Duration of the cycle: $\tau = 6\ h$. Time of light exposure: $t_{light} = 50\%\ \tau$. . . . . 234

6.14 $SET3$ - Mass of microbial species within the granule at $T = 20\ d$, $T = 30\ d$, $T = 40\ d$, $T = 50\ d$, $T = 60\ d$, $T = 200\ d$ for different densities of binding sites $\rho_\theta$. Wastewater influent composition: $S^{in}_{IC} = 180\ g\ m^{-3}$ (inorganic carbon), $S^{in}_{DOC} = 500\ g\ m^{-3}$ (organic carbon), $S^{in}_{NH_3} = 50\ g\ m^{-3}$ (ammonia), $S^{in}_{NO_3} = 0$ (nitrate), $S^{in}_{O_2} = 0$ (oxygen). $S13 : \rho_\theta = 10\ N^{\circ}_{sites}\ m^{-3}$, $S14 : \rho_\theta = 20\ N^{\circ}_{sites}\ m^{-3}$, $S15 : \rho_\theta = 30\ N^{\circ}_{sites}\ m^{-3}$, $S16 : \rho_\theta = 40\ N^{\circ}_{sites}\ m^{-3}$, $S17 : \rho_\theta = 50\ N^{\circ}_{sites}\ m^{-3}$. Incident light intensity: $I_0 = 0.008\ kmol\ m^{-2}\ d^{-1}$. Duration of the cycle: $\tau = 6\ h$. Time of light exposure: $t_{light} = 50\%\ \tau$. . . . . 235

6.15 $SET3$ - Phototrophs distribution within the granule (diametrical section) at $T = 20\ d$, $T = 30\ d$, $T = 40\ d$, $T = 50\ d$, $T = 200\ d$ for different densities of binding sites $\rho_\theta$. Wastewater influent composition: $S_{IC}^{in} = 180\ g\ m^{-3}$ (inorganic carbon), $S_{DOC}^{in} = 500\ g\ m^{-3}$ (organic carbon), $S_{NH_3}^{in} = 50\ g\ m^{-3}$ (ammonia), $S_{NO_3}^{in} = 0$ (nitrate), $S_{O_2}^{in} = 0$ (oxygen). $S13 : \rho_\theta = 10\ N_{sites}^{\circ}\ m^{-3}$, $S14 : \rho_\theta = 20\ N_{sites}^{\circ}\ m^{-3}$, $S15 : \rho_\theta = 30\ N_{sites}^{\circ}\ m^{-3}$, $S16 : \rho_\theta = 40\ N_{sites}^{\circ}\ m^{-3}$, $S17 : \rho_\theta = 50\ N_{sites}^{\circ}\ m^{-3}$. Incident light intensity: $I_0 = 0.008\ kmol\ m^{-2}\ d^{-1}$. Duration of the cycle: $\tau = 6\ h$. Time of light exposure: $t_{light} = 50\%\ \tau$. 236

6.16 $SET3$ - Distribution of the residual free binding site across the radius of the granule for different densities of binding sites $\rho_\theta$ at $T = 200\ d$. Wastewater influent composition: $S_{IC}^{in} = 180\ g\ m^{-3}$ (inorganic carbon), $S_{DOC}^{in} = 500\ g\ m^{-3}$ (organic carbon), $S_{NH_3}^{in} = 50\ g\ m^{-3}$ (ammonia), $S_{NO_3}^{in} = 0$ (nitrate), $S_{O_2}^{in} = 0$ (oxygen). $S13 : \rho_\theta = 10\ N_{sites}^{\circ}\ m^{-3}$, $S14 : \rho_\theta = 20\ N_{sites}^{\circ}\ m^{-3}$, $S15 : \rho_\theta = 30\ N_{sites}^{\circ}\ m^{-3}$, $S16 : \rho_\theta = 40\ N_{sites}^{\circ}\ m^{-3}$, $S17 : \rho_\theta = 50\ N_{sites}^{\circ}\ m^{-3}$. Incident light intensity: $I_0 = 0.008\ kmol\ m^{-2}\ d^{-1}$. Duration of the cycle: $\tau = 6\ h$. Time of light exposure: $t_{light} = 50\%\ \tau$. . . . . 237

6.17 $SET3$ - Soluble substrates concentration evolution within the reactor for different densities of binding sites $\rho_\theta$. Wastewater influent composition: $S_{IC}^{in} = 180\ g\ m^{-3}$ (inorganic carbon), $S_{DOC}^{in} = 500\ g\ m^{-3}$ (organic carbon), $S_{NH_3}^{in} = 50\ g\ m^{-3}$ (ammonia), $S_{NO_3}^{in} = 0$ (nitrate), $S_{O_2}^{in} = 0$ (oxygen). $S13 : \rho_\theta = 10\ N_{sites}^{\circ}\ m^{-3}$, $S14 : \rho_\theta = 20\ N_{sites}^{\circ}\ m^{-3}$, $S15 : \rho_\theta = 30\ N_{sites}^{\circ}\ m^{-3}$, $S16 : \rho_\theta = 40\ N_{sites}^{\circ}\ m^{-3}$, $S17 : \rho_\theta = 50\ N_{sites}^{\circ}\ m^{-3}$. Incident light intensity: $I_0 = 0.008\ kmol\ m^{-2}\ d^{-1}$. Duration of the cycle: $\tau = 6\ h$. Time of light exposure: $t_{light} = 50\%\ \tau$. 238

6.18 $SET3$ - Evolution of metal concentration within the reactor for different densities of binding sites $\rho_\theta$. Wastewater influent composition: $S_{IC}^{in} = 180\ g\ m^{-3}$ (inorganic carbon), $S_{DOC}^{in} = 500\ g\ m^{-3}$ (organic carbon), $S_{NH_3}^{in} = 50\ g\ m^{-3}$ (ammonia), $S_{NO_3}^{in} = 0$ (nitrate), $S_{O_2}^{in} = 0$ (oxygen). $S13 : \rho_\theta = 10\ N_{sites}^{\circ}\ m^{-3}$, $S14 : \rho_\theta = 20\ N_{sites}^{\circ}\ m^{-3}$, $S15 : \rho_\theta = 30\ N_{sites}^{\circ}\ m^{-3}$, $S16 : \rho_\theta = 40\ N_{sites}^{\circ}\ m^{-3}$, $S17 : \rho_\theta = 50\ N_{sites}^{\circ}\ m^{-3}$. Incident light intensity: $I_0 = 0.008\ kmol\ m^{-2}\ d^{-1}$. Duration of the cycle: $\tau = 6\ h$. Time of light exposure: $t_{light} = 50\%\ \tau$. 239

# List of Tables


2.1 Initial conditions and operating parameters used for model calibration. . 32

2.2 Kinetic, stoichiometric and and operating parameters. . . . . 33

2.3 Performance indicators. . . . . 34

3.1 Model equations and initial and boundary conditions. . . . . 68

3.2 Kinetic, stoichiometric and operating parameters used for numerical simulations. . . . . 75

3.3 Initial and boundary conditions and operating parameters adopted in numerical studies. . . . . 76

5.1 Kinetic, stoichiometric and operating parameters used for numerical simulations. . . . . 161

5.2 Wastewater influent and inoculum composition. . . . . 163

5.3 Values of the parameters investigated in the numerical study S4. . . . . 180

6.1 Biochemical rate coefficients ($\alpha_{i,k}$) of the biological processes within the biofilm. . . . . 210

6.2 Biochemical rate coefficients ($\beta_{j,k}$) of the biological processes within the biofilm. . . . . 210

6.3 Kinetic rate expressions ($\nu_k$) of the biological processes within the biofilm. 211

6.4 Biochemical rate coefficients ($\alpha^*_{i,k}$ and $\bar{\alpha}^*_{i,k}$) of the biological processes within the bulk liquid. . . . . 212

6.5 Biochemical rate coefficients ($\beta^*_{i,k}$) of the biological processes within the bulk liquid. . . . . 212

6.6 Kinetic rate expressions ($\nu^*_k$) of the biological processes within the bulk liquid. . . . . 213

6.7 Kinetic, stoichiometric and operating parameters used for numerical simulations. . . . . 214

# Chapter 1

# Introduction

## 1.1 Research context

Microbial biofilms are complex and well-organized communities of microorganisms widespread in nature. Their formation represents a strategy implemented by microorganisms to survive in hostile environments [2]. Within a biofilm, a variety of microbial groups can contribute to the conversion of different organic and inorganic substrates. For these reasons, the application of biofilms as an alternative technology for the treatment of wastewater under various operational conditions has stimulated great scientific interest. In this context, understanding the fundamental mechanisms regulating biofilm growth and performance is crucial to effectively utilize and control biofilms in industrial and medical settings.

Due to the complexity of the processes and phenomena involved, modelling biofilm formation represents a scientific challenge and requires the cooperation of several research fields: biology and microbiology, chemistry, ecology and engineering. Indeed, biofilms occur in many different branches of science and technology, from wastewater treatment to medicine. The wide applicability of biofilm models in the treatment

field of industrial and municipal wastewater has driven the development of numerous biofilm models able to capture all the main physical, chemical, and biological factors occurring in a biofilm-based system. Because of the flexibility offered by modelling, biofilm models allow gaining a better understanding of biofilm formation, structure and population dynamics, and are becoming increasingly useful and reliable tools in biofilm research [3].

The description of biofilms and continuum modelling of biofilms are briefly presented in the following sections.

### 1.1.1 Multispecies biofilms

Multispecies biofilms are sessile microbial consortia growing as a three-dimensional structure and are commonly defined as aggregates of microorganisms in which cells are frequently embedded in a self-produced matrix of extracellular polymeric substances ($EPS$) [4]. The matrix consists of a conglomeration of different types of biopolymers, which are responsible for self-aggregation or adhesion to surfaces, and for cohesion within the biofilm [5]. The biofilm lifestyle is clearly distinct from that of free-living bacterial cells, as $EPS$ matrix protects organisms against desiccation, oxidizing, antibiotic, chlorine, detergents, and metallic compounds [5]. For these reasons, biofilm constitutes the preferred form of microbial life [2, 4, 3]. Moreover, $EPS$ mediates the formation of the biofilm architecture, through a continuous and dynamic process consisting of several steps: adhesion to support, attachment, cell proliferation, development of mature biofilm, and detachment. The formation of bacterial biofilms starts when pioneering planktonic cells adhere to a living or inert suitable surface. Once attached to the surface, microorganisms switch their phenotype from planktonic to sessile, proliferate, secrete $EPS$ and form microcolonies [6]. The growth of the biofilm depends on nutrients availability within the voids and channels of the porous matrix, the synthesis and secretion of extracellular materials, shear stress, and competition between microor-

ganisms [4]. At the final stage of its maturation, the biofilm external layers are eroded releasing biofilm clusters into the surrounding medium [7]. Nevertheless, detachment can be initiated also internally leading to the dispersion of individual cells [8]. Lastly, specific planktonic cells have the ability to penetrate the porous matrix of the biofilm from the surrounding liquid medium, colonizing it and influencing the biofilm evolution [9].

Biofilms are found in extremely varied environments when there are ideal conditions for their microbial metabolic activity, and can be divided in two main categories: harmful and beneficial biofilms. Unwanted biofilms are a problem in biological fouling of heat exchanges and membrane systems, dental hygiene, infectious diseases, infections related to medical implants, drinking water distribution system, and biologically induced corrosion [3]. Nevertheless, in the last decades there is a growing interest in the utilization of biofilms in environmental engineering and biotechnology fields, ranging from: wastewater treatment plants (fixed bed biofilm reactors, rotating biological contactors, granular biofilm-based systems), groundwater protection, and soils bioremediation [3]. Overall, biofilms play an important role in many natural and engineering systems, and understanding the mechanisms of biofilm formation, growth, and removal is a key factor for promoting good biofilms and reducing bad biofilms.

Since the end of the $19^{th}$ century, biofilms have been widely used for the treatment of wastewater to remove unwanted substances, such as organic matter, nutrients and inorganic compounds [3]. Although attached and suspended growth systems are based on the same biological metabolic processes, biofilms are usually preferred over biomass growing in suspension as they can provide important competitive advantages. Compared to suspended biomass systems, biofilm-based reactors allow having higher concentrations of biomass in the reactor and avoiding settling systems. Moreover, bacteria in suspension can be washed out from the bioreactor, while the ability of bacteria to attach to surfaces and to form biofilms allows to protect them from washout and grow in locations where the nutrients necessary for their metabolic activities remains

abundant.

### 1.1.2 Granular biofilms and applications

Although natural biofilms typically grow as planar layers attached to solid supports, under specific environmental conditions the biofilms formation occurs without the involvement of a surface. Thanks to their self-immobilization capabilities, some planktonic species can attach with each other leading to the formation of approximately spherical-shaped granular biofilms [10]. In this case, the formation process is known as granulation process. In the recent years, granular bioreactors have become increasingly popular in the field of sustainable and high-rate wastewater treatment, as they offer numerous advantages. Granular-based systems are biofilm systems where biomass grows arranged in dense and compact aggregates [11]. Compared to suspended biomass, granular biofilms have a denser, stronger and more regular structure, which allows improving settling properties of the biomasses and liquid-solid separation [12, 13], allowing higher biomass concentrations in the system and reducing bioreactor footprints [14]. Additionally, granular biofilm systems based on constant moving of spherical microbial aggregates allow mitigating boundary layer resistances and enhancing the mass transfer of substrates across the biofilm granule [14].

In the last decades, great attention has been paid to specific processes of engineering and biological interest, such as: anammox and algal-bacterial granulation process. The combination of partial nitritation and anammox processes (PN/A) has been increasingly studied for the treatment of industrial wastewater rich in nitrogen compounds. Early anammox applications have been carried out in two separate reactors arranged in series, since these two processes require aerobic and anoxic conditions, respectively [11]. However, innovative anammox granular-based systems allow the application of a single granular-based reactor where nitritation and anammox processes are contextually carried out [11]. Such granular systems have revolutionized the treatment process of ni-

trogenous wastewater, as thanks to the invasion process anammox bacteria can penetrate within the granules core where anoxic conditions are guaranteed. Indeed, supplying a constant and low oxygen level in the reactor, the formation of two distinct zones inside the granules is induced: an external zone where there is the oxygen necessary for the partial nitritation, and an internal zone where oxygen is not present and anammox processes occur. Compared to the traditional nitritation/denitrification process, PN/A granular process results in lower aeration costs, $CO_2$ emissions, and no external carbon supplementation [11].

Furthermore, the latest advancement in the field of granular biofilms-based technologies has brought attention to another granules type, that are the oxygenic photogranules (OPGs), which form in presence of an illumination source. These oxygenic photogranules are different from conventional aerobic granules due to the presence of phototrophic communities, including microalgae and cyanobacteria, along with heterotrophic and nitrifying bacteria [15]. Hence, OPGs can remove organic matter and nutrients by using oxygen produced through photosynthesis rather than relying on external oxygen supplementation with energy intensive aeration mechanisms [15, 16]. Therefore, OPGs systems are expected to have great potentials for reducing energy consumption and operation costs. In addition, algal-bacterial photogranules can be used as biosorbents to remove hazardous toxic metals present in industrial and municipal wastewater [17, 18]. Indeed, OPGs have remarkably high metal adsorption capacity and granular stability during the biosorption process [19], and in metal-stressed conditions microorganisms are induced to produce large amount of $EPS$, increasing the adsorption potential of the biofilm granules [20, 21]. Compared to the other biosorbents and, more in general, to conventional physical/chemical processes for metal removal, systems based on algal-bacterial photogranules are regarded as an efficient and environmentally sustainable technology for the removal of organic and inorganic compounds.

### 1.1.3 Biofilm modelling

Biofilm modelling is considered an active research field, marked by a scientific development which is continuously evolving and relies on interdisciplinary cooperation. Biofilm models have been recognized as sufficiently accurate tools to predict and evaluate biofilm reactor performances. Specifically, they are able to provide the following outputs: biofilm thickness evolution over time, biofilm composition in terms of relative abundances due to microbial competition; microbial distribution along the biofilm; concentration of the particulate components in the bulk liquid; spatial profiles of dissolved compounds in the biofilm; soluble substrates dynamics within the bulk liquid and effluent composition. The most used mathematical model on biofilms has been introduced by Wanner and Gujer (1986) [22]. Such model considers a continuum approach and is formulated as a free boundary problem applied to a $1D$ domain. Model equations are derived from mass conservation principles, considering biofilm growth and transport as an advective mechanism and substrate transport as a diffusive mechanism. The advective transport and growth of sessile biomass are modelled through non-linear hyperbolic partial differential equations (PDEs), while the diffusive transport and conversion of soluble compounds are described through quasi-linear parabolic PDEs. In addition, the free boundary expansion is governed by microbial growth and decay processes and detachment phenomena. The biochemical processes regulating the metabolic activities of the microbial species are modelled through non-linear growth kinetics. This basic version of the model has been extended in order to include or detail additional phenomena such as microbial invasion [23], attachment [24] and dispersal [8] phenomena.

Over the years, the one-dimensional biofilm model introduced by Wanner and Gujer has been used to describe the ecology and evolution of granular biofilms. Several modelling works have been proposed to mainly describe aerobic [25], anaerobic [26, 27, 28] and anammox [29, 30, 31] processes occurring in granular-based systems.

Nevertheless, no work present in the literature reports a complete overview of the granular biofilm model, describing assumptions, equations, initial and boundary conditions. The initial granulation process has never been addressed by modelling works. Indeed, all the granular biofilm models consider granules already formed and arbitrarily fix the initial microbial composition of the biofilms. Moreover, such models focus on important aspects of the treatment process but only from an engineering point of view, and the numerical studies proposed in literature do not investigate aspects and factors affecting the biofilms genesis and the start-up process of granular systems from a biological point of view. Finally, algal-bacterial granular biofilms for the contextual removal of organic and inorganic compounds have attracted a growing interest in engineering and biological fields for their numerous competitive advantages. However, none of the existing models have addressed the dynamics of algal-bacterial biofilms for the treatment of industrial wastewater rich in toxic inorganic compounds, as their utilization is very recent.

## 1.2 Scope of the thesis

The main objective of the thesis is to qualitatively and numerically investigate models describing multispecies granular biofilms devoted to organic and inorganic compounds removal. In particular, the main goals of this study include: qualitative analysis of the spherical free boundary value problem governing the initial phase of a granular biofilm growth; development of numerical simulations to describe the genesis and growth of granular biofilms, by modelling all the main physical, biological and chemical processes occurring in granular biofilms systems; investigation of inorganic compounds effect on the microbial metabolism with a particular interest in toxic metals; modelling of innovative biofilm based systems devoted to removal of organic matter, nitrogen compounds and toxic metals from industrial wastewater combining the degradation and absorption capabilities of biofilms. For these purposes, a mathematical model is pro-

posed in Chapter 2 as first attempt to study metals removal and their toxic effect on a biological process in a suspended biomass system. In Chapter 3, a multiscale model on the genesis and growth of granular biofilms within a completely mixed continuous reactor is derived. In Chapter 4, a mathematical model describing the attachment process during the initial phase of the growth of a granular biofilm is presented and qualitatively analyzed. Chapter 5 deals with the granular biofilms modelling to predict the wastewater treatment process occurring in an anammox-based granular reactor. Starting from this, in Chapter 6 a mathematical model able to simulate the treatment process of industrial wastewater rich in organic substances, nitrogen compounds and metals, obtained from the integration of the degradation process with the metals biosorption on granular biofilms matrix, is proposed.

In Chapter 2, a mathematical model able to describe the evolution of an integrated dark fermentation-leaching process is presented. The model is based on mass balances and consists of a system of non-linear ordinary differential equations (ODEs) where the state variables only depend on time. The model is able to account for biological, chemical, and physical processes taking place during the dark fermentation, and the metals physico-chemical dynamics related to leaching mechanisms. Chapter 3 presents a multiscale mathematical model on the formation and growth of *de novo* granular biofilms, by modelling the initial attachment process by planktonic microbial cells present in the surrounding liquid medium. Biofilm granules are modelled as spherical free boundary domains under the assumption of radial symmetry. Moreover, the dynamics of soluble substrates and planktonic biomasses within the bulk liquid are accounted. A complete overview of the model is performed, by deriving equations and by describing all assumptions, variables, initial and boundary conditions involved. Furthermore, this model is used to simulate the *de novo* granulation and evolution of anaerobic granules. In Chapter 4, a mathematical model based on a continuum approach, and able to describe the initial phase of granular biofilm growth, is presented. A theorem of existence and uniqueness of the solutions, based on the fixed-point theorem, is proved for this model.

In Chapter 5, the multiscale model derived in Chapter 3 is applied to investigate the genesis and growth of *de novo* anammox granules within a completely mixed continuous reactor, focusing on both the biofilm mesoscale and the granular bioreactor macroscale. In Chapter 6, the mathematical formulation introduced in Chapter 3 is adapted to model the formation and ecology of oxygenic phototrophic granules and to investigate the removal process of organic and inorganic compounds. This multiscale model allows to accurately describe the growth of algal-bacterial granules within a granular-based sequencing batch reactor by considering the following items: attachment phenomena which lead to the genesis of the granules; metabolic activities of phototrophic microalgae and their microbial interactions with heterotrophic and nitrifying bacteria; detachment process which leads to the release of biofilm clusters in the surrounding medium; metals adsorption on granules matrix and key factors driving the adsorption process; reactor dynamics including mass exchange processes with the granules, soluble substrates consumption/production, planktonic and detached biomasses metabolic activities, and metals removal.

All biofilm models have been integrated numerically by developing original codes in MatLab platform. The ODEs system constituting the suspended biomass model has been integrated by using the MatLab routine ode15s, based on a Runge–Kutta method. This mathematical model has been calibrated based on experimental data achieved with ad-hoc lab-scale tests. More sophisticated numerical methods have been used for the numerical integration of the granular biofilm model equations, due to their greater complexity. Hyperbolic PDEs have been integrated by using the method of characteristics, applied for the first time in the planar biofilm context by D'Acunto and Frunzo (2011) [32], while the method of lines has been adopted to integrate the diffusion-reaction PDEs. In Chapters 2, 3, 5 and 6, original numerical studies of scientific interest have been performed, and specific aspects and phenomena partially or never addressed by models available in the literature have been investigated. Numerical simulations demonstrate the applicability of these models to investigate significant engineering, bi-

ological and ecological aspects of the processes studied: toxic metal effects on the biological process taken into account, metals removal efficiency, ecology of anaerobic granules, anammox granules and oxygenic photogranules, interactions between the microbial species involved in the biological process studied, treatment performances of granular-based systems. The model outputs include: evolution of granules over time, relative abundances of microbial species and their distribution within granular biofilms, spatial profiles of substrates and planktonic biomasses within the granular biofilms, concentration trends of soluble substrates, metals, and planktonic and detached biomasses within the reactor.

In Chapter 7, conclusions and recommendation for future research are presented.

# Chapter 2

# Modelling metal recovery from E-waste using a Dark-Fermentation-Leaching process

## 2.1 Introduction

Over the last decades, the growing production and usage of electronic and electrical equipment both for commercial and domestic purposes resulted in a fast replacement of any type of electronic device [33, 34, 35]. Consequently, a huge amount of waste was generated at an alarming rate, when obsolete technologies are disposed and substituted [33, 34]. This class of waste is known as electric waste (E-waste). In recent years, different management strategies for E-waste are increasingly attracting the interest of the scientific community. This is due to the wide variety of materials contained in E-waste, which are potentially dangerous for the human health and environment. Indeed,

This Chapter has been accepted on Scientific Reports as: Russo, F., Luongo, V., Mattei, M.R., Frunzo, L. Mathematical Modeling of metal recovery from E-waste using a Dark-Fermentation-Leaching process.

E-waste is characterized by the presence of huge amounts of toxic metals, such as copper (Cu), cobalt (Co), nickel (Ni), and lithium (Li) [36, 37]. At the same time, they can contain valuable metals, such as gold (Au), and silver (Ag) [33]. Then, the definition of an adequate management strategy which allows to avoid pollutants release into the environment, and to recover and reuse valuable metals from E-waste is a crucial topic in both academic and industrial research. Nowadays, the most used methods for E-waste treatment and metals recovery are pyrometallurgical or hydrometallurgical processes. In pyrometallurgical processes, waste is usually burnt off, causing high energy consumption and emission of hazardous gases [38]. On the other hand, hydrometallurgical processes just use aqueous solutions during the E-waste treatment. For this reason, the latter are generally preferred at a large scale [39, 40]. Indeed, hydrometallurgical processes have some attractive advantages, such as high recovery rates of metals, low consumption of energy, and minimal gas emission [35, 39, 41]. Among hydrometallurgical treatments, the most common strategy is the leaching process, which consists in the metals dissolution into the liquid phase. In this process both inorganic and organic acids can be used as leaching agents. Nevertheless, the leaching process catalyzed by inorganic acids has several environmental disadvantages, such as considerable emission of toxic gases, and water and soil contamination [35, 38, 41, 42]. Indeed, residual compounds of the leaching process, including the liquid fraction, should be pretreated before their disposal [35, 42, 43]. Compared with inorganic acids, organic acids can be easily degraded and recycled, and their utilization as leaching agents does not cause secondary pollutants production [44]. For this reason, the liquid fraction is not considered potentially dangerous for the environment [35, 38, 39, 45] when organic acids are used for the leaching process.

Recently, the effective application of leaching processes using inorganic [46, 47, 48] and organic [41, 44, 49] has been proven in lab-scale. The latter evidence suggests that metals dissolution can be achieved using organic acids (OAs) produced by the dark fermentation (DF) process, resulting from the degradation of biodegradable sub-

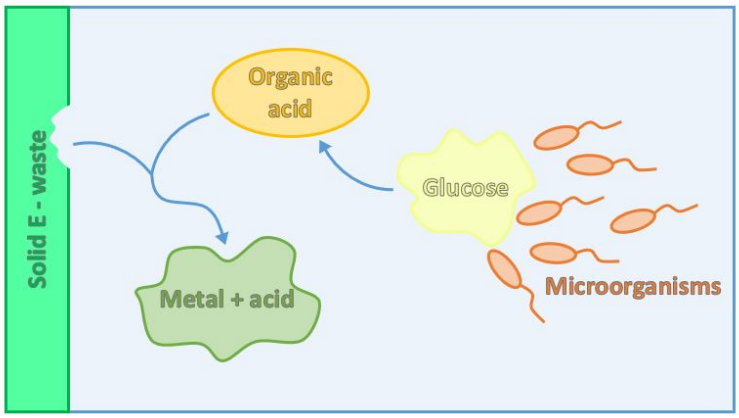


Figure 2.1: Scheme of dark fermentation and leaching processes.

stances with a contextual hydrogen production. Indeed, DF is a biological anaerobic process, which allows to the conversion of carbohydrates rich substrates into hydrogen ($H_2$), and other organic compounds, such as volatile fatty acids (VFAs). It represents a promising technology for waste valorization, as organic waste can be used as feeding substrate with consequent production of a renewable energy source. Usually, DF complexity depends on the specific microbial species involved in the bioprocess and on the biodegradability and composition characteristics of the substrate. On the other hand, it is a common practice referring to simple biodegradable compounds to compare hydrogen yields and effluent composition with experiments on raw waste biomasses. During the fermentation process, glucose is mainly converted into butyric and acetic acids. Such OAs are able to react with metals contained in the solid E-waste, and produce metallic compounds dissolved in the liquid effluent (Fig. 2.1). The utilization of a VFAs-rich effluent as a leaching solution represents a suitable strategy to recover metals from both economical and environmental points of view. The residual VFAs can be processed with subsequent biological treatments for DF effluents. For instance, photofermentation (PF) allows to obtain an additional source of biohydrogen due to VFAs degradation by specific light dependent Purple Bacteria [50, 51, 52], while anaerobic digestion (AD) leads to the conversion of organic acids in a methane-rich biogas [50]. Therefore, the integration of the leaching with the DF process represents a promis-

ing strategy for metal recovery as: (i) organic acids produced in the fermentative process avoid the utilization of chemicals; (ii) no external energy supply is required for metals recovery; (iii) PF or AD can be adopted for the leachate downstream treatment with the production of a renewable energy source (hydrogen or methane); (iv) the use of organic waste to feed the DF stage leads to biomass valorization in the biorefinery context; (v) any additional gaseous compounds can be trapped avoiding toxic emissions.

The integration of the DF with the leaching process still requires high research efforts, mainly due to the uncertainty and the limited knowledge on inhibition/stimulation dynamics generated by metals in DF reactors. In this framework, mathematical modelling represents a useful tool for investigating innovative and still poorly known processes; it allows for testing a wide range of environmental conditions avoiding experimental tests, and for designing the correct management of any-scale applications. Moreover, it can be used to combine the DF and the leaching processes with the aim of optimizing metal recovery efficiency and hydrogen production, and minimizing energy consumption. Despite the great interest in this field, there is a lack of mathematical models taking into account contextually organic substrates degradation and metals dissolution during the DF-leaching process. Several models were employed for metals recovery by leaching process from waste and mineral materials. Such models are known as geochemical models, and are usually based on computer software interfaces, such as PHREEQC [53, 54, 55], Visual Minteq [56] and ORCHESTRA [57, 58, 59]. These tools are able to calculate the equilibrium composition of a diluted aqueous system, and they are generally applied to determine metal concentrations in lab-scale experiments or natural ecosystems.

In this Chapter, a mathematical model able to describe the evolution of an integrated DF-leaching is proposed. The model is based on mass balance equations for soluble substrates, particulate and gaseous components, and metals in solid and liquid form. It consists of a system of non-linear ordinary differential equations (ODEs) where the state variables only depend on time. The model is able to account for biological, chemical,

and physical processes taking place during the DF, and the related physico-chemical dynamics of metals due to leaching mechanisms in anaerobic reactors. Biomass growth and decay, substrates degradation, acid-base equilibrium, liquid-gas transfer, metals dissolution/precipitation, inhibition/limitation due to the process conditions were originally included in the present work. The mathematical model was calibrated based on experimental data achieved with ad-hoc lab-scale tests. Cumulative hydrogen production, glucose degradation, OAs accumulation, and metals concentration trends were monitored, and used to calibrate the model. The bioreators were carried out in batch conditions by using a synthetic solution of glucose, an anaerobic digestate, and spent button batteries, to provide a feeding organic substrate, a microbial inoculum, and a suitable metals source, respectively. Numerical simulations demonstrated the applicability of the model for an accurate prediction of the DF-leaching process. The calibrated model can be applied as an optimizing tool supporting lab-scale or higher scale applications. Four numerical studies were also presented aimed at optimizing the recovery of toxic and valuable metals from wastes or minerals, and to demonstrate the applicability of the model in the leaching process management. In particular, the numerical studies investigate three fundamental aspects: how metals inhibition affects the DF process; how $F/M$ ratio affects the DF process and leaching efficiency; and how metal concentration affects the efficiency of the leaching process.

The Chapter is organized as follows. In Section 2.2 the integrated DF-leaching process is detailed. The mathematical model, including assumptions, equations, variables, and initial conditions, and experimental tests and model application are described in Section 2.3. Model calibration and numerical studies are reported in Section 2.4 and Section 2.5, respectively. Finally, conclusions and future goals are outlined in Section 2.6 .

## 2.2 Biochemical framework: dark fermentation and leaching processes

DF is a promising technology for biohydrogen production, due to its high production rate and hydrolytic effect on organic waste. In DF process, carbohydrates rich substrates are anaerobically converted by hydrogen-producing microorganisms to hydrogen and organic acids. DF is a complex biotechnology as many factors, such as bioreactor configuration, operating conditions, substrate to inoculum ratio and composition, inoculum pretreatment method, temperature, and pH, are able to influence metabolic pathways affecting the production rate and the effluent composition [50, 60]. Organic substrate characteristics, e.g. carbohydrates content, bioavailability, and biodegradation rate, play an important role in the biohydrogen generation [50]. Glucose and sucrose are the most common substrates used for lab-scale DF experiments [50, 52, 60, 61, 62]. To provide a suitable mixed culture DF inoculum, cow dung, anaerobic sludge, municipal solid waste, and compost, are usually adopted as a source of microorganisms [50, 52, 60]. To enhance biohydrogen production and to inhibit hydrogen consumers activity (*methanogens*), an adequate pretreatment strategy, such as thermal/chemical inoculum treatment, is required [60, 62, 63]. Temperature and pH are crucial parameters for fermentative processes [60]. Increasing temperature usually leads to microorganism selection and enhancement of hydrogen production rates, while a neutral pH is usually recommended for DF processes devoted to $H_2$ generation. Indeed, an acidic environment may inhibit the metabolic activity of hydrogen-producers microorganisms both in mesophilic ($35$°C) or thermofilic ($55$°C) conditions [50]. However, the most common temperature used in DF applications is $35$°C, as this condition positively affects the hydrogen production and limits the management costs due to energy supplementation to bioreactors [50].

In DF processes, glucose $C_6H_{12}O_6$ is mainly converted to acetic acid $CH_3COOH$, butyric acid $CH_3CH_2CH_2COOH$, hydrogen $H_2$, and carbon dioxide $CO_2$ [50, 61,

64] during *acidogenesis* [1]. It can be assumed that *acidogenesis* and $H_2$ generation are contextually performed by sugar fermenters, whose metabolism is described by biochemical reactions:

$$C_6H_{12}O_6 + 2H_2O \rightarrow 2CH_3COOH + 2CO_2 + 4H_2, \tag{2.1}$$

$$C_6H_{12}O_6 \rightarrow CH_3CH_2CH_2COOH + 2CO_2 + 2H_2. \tag{2.2}$$

In glucose fermentation, enzymatic conversion processes involving composite particulate materials, such as *disintegration* and *hydrolysis*, can be neglected, as the organic substrate is already fed in soluble form. In addition, the *acetogenesis* and *methanogenesis* processes, usually occurring during the anaerobic digestion, are inhibited by inoculum pretreatment [50, 60, 63]. An additional contribution to *methanogenesis* inhibition is provided by the substrate, or food (F), to inoculum, or microorganisms (M), ratio. An high $F/M$ favours organic acids production and accumulation in DF reactors, with consequent pH level reduction and inhibition of methane generation.

On the other hand, the leaching process is a hydrometallurgical treatment consisting of dissolution reactions. Solid metals contained in various wastes are converted to the liquid form due to the interaction with a leaching agent [38]. To this aim, inorganic acids, such as $H_2SO_4$, $HCl$, and $HNO_3$ [38, 39, 65], are commonly used, as they contextually allow for the E-waste treatment and metal recovery. Despite the high efficiency rate of inorganic acids in leaching processes, further treatments are required for the resulting acidic effluent. Moreover, hazardous gases are typically produced during the dissolution phase and a notable amount of inorganic acids, with significant market value, is required. To overcome these disadvantages, the use of organic acids as leaching agents for metal recovery was recently introduced. These biodegradable compounds can be obtained by organic waste fermentation, and are characterized by adequate acidity for the metal dissolution. Citric acid, oxalic acid, and acetic acid are

the most common organic acids tested for the leaching process [35, 43]. As reported in Golmohammadzadeh et al. (2018) [35], acetic acid allows for the dissolution of a generic metal with the leaching reaction:

$$n[C_2H_3O_3^-]_{(liq)} + M_{(s)}^{n+} \rightarrow M[C_2H_3O_2]_{n_{(liq)}} \tag{2.3}$$

where $n$ represents the oxidation states of the metal. Once the dissolution is complete, the metals can be recovered from the leachate by different chemical methods, such as precipitation, solvent extraction, and electrolytic deposition [38, 41, 66]. However, precipitation represents the most common method adopted for the final metal recovery [38, 39].

## 2.3 Mathematical model

### 2.3.1 Model definition

In this Chapter, the complete mathematical model describing the integrated DF-leaching process for metals recovery is presented. The dissolution process is described by chemical reactions involving the organic acids produced in the DF process and the metals supplemented to the system. The reactor is modelled as a continuous stirred tank reactor (CSTR) with a constant total volume $V$. As shown in Fig. 2.2, the reactor is constituted by the liquid and the gaseous phases. The mathematical model is able to account for all liquid-gas interactions occurring during the anaerobic fermentation, i.e. *acidogenesis*, $H_2$ production, biomass growth and decay, acid-base reactions, physical interactions, and leaching reactions. The proposed model is described by a system of nonlinear differential equations for soluble, particulate and gaseous components. These components, expressed in terms of concentration, are divided in: $n_1$ soluble substrates $S_i(t)$ involved in the biochemical processes; $n_2 - n_1$ particulate materials $X_i(t)$, representing the microbial groups operating the biochemical conversion; $n_1$ gas components

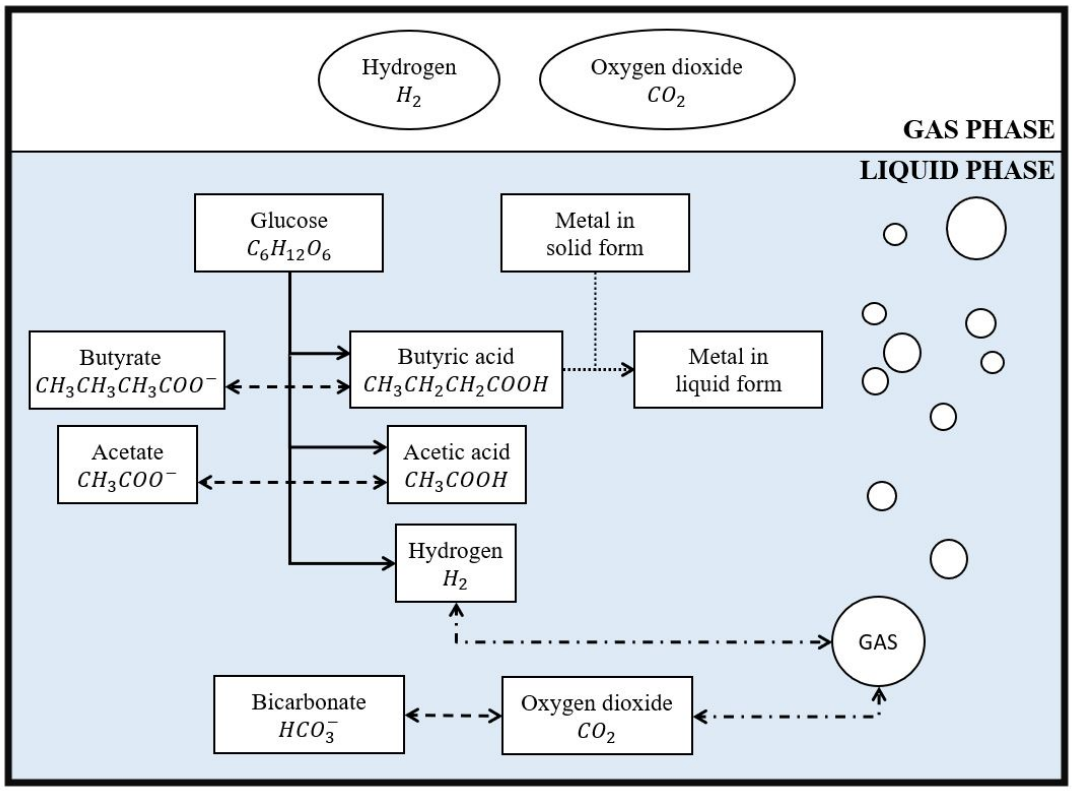


Figure 2.2: Conversion scheme of the dark fermentation and the leaching process (adapted and modified from Batstone et al. (2002) [1]). Solid arrows: biological reactions; dashed arrows: acid-base equilibrium; dash-dot arrows: liquid-gas transfer; dotted arrows: leaching process. Biochemical and leaching reactions are modelled as irreversible processes, while physico-chemical reactions (acid-base and liquid-gas equilibria) are implemented as reversible processes. Glucose: $S_{su}$; butyric acid: $S_{bu}$; butyrate: $S_{bu}^-$; acetic acid: $S_{ac}$; acetate: $S_{ac}^-$; hydrogen: $S_{H_2}$; hydrogen gas: $S_{gas,H_2}$; oxygen dioxide: $S_{CO_2}$; bicarbonate: $S_{HCO_3}^-$; oxygen dioxide gas: $S_{gas,CO_2}$; metal in solid form: $M$; metal in liquid form: $M_{liq}$.

$S_{gas,i}(t)$ involved in the liquid-gas equilibrium; $n_3$ metals in solid $M_i(t)$ and liquid $M_{liq,i}(t)$ dominated by the leaching process. Such concentrations vary over time due to biological and chemical processes and operating parameters of the reactor. The differential equations governing soluble, particulate, gaseous components, and metals are described by Eqs. (2.4)-(2.8):

$$\frac{dS_i}{dt} = \frac{Q^{in}S_i^{in}(t)}{V_{liq}} - \frac{Q^{out}S_i(t)}{V_{liq}} + \sum_{j=1}^{m_1}\alpha_{i,j}\rho_j(t,\mathbf{S},\mathbf{X},\mathbf{M}) + \sum_{j=1}^{m_2}\beta_{i,j}\rho_{A,j}(t,\mathbf{S})+$$

$$+\sum_{j=1}^{m_3}\gamma_{i,j}\rho_{M,j}(t,\mathbf{S},\mathbf{M})-\rho_{T,i}(t,\mathbf{S},\mathbf{S_{gas}}),\ i=1,...,n_1,\ t>0, \tag{2.4}$$

$$\frac{dX_i}{dt}=\frac{Q^{in}X_i^{in}(t)}{V_{liq}}-\frac{Q^{out}X_i(t)}{V_{liq}}+\sum_{j=1}^{m_1}\alpha_{i,j}\rho_j(t,\mathbf{S},\mathbf{X},\mathbf{M}),\ i=n_1+1,...,n_2,\ t>0, \tag{2.5}$$

$$\frac{dS_{gas,i}}{dt}=-\frac{Q_{gas}S_{gas,i}}{V_{gas}}+\frac{V_{liq}}{V_{gas}}+\rho_{T,i}(t,\mathbf{S},\mathbf{S_{gas}}),\ i=1,...,n_1,\ t>0, \tag{2.6}$$

$$\frac{dM_i}{dt}=\frac{Q^{in}M_i^{in}(t)}{V_{liq}}-\frac{Q^{out}M_i(t)}{V_{liq}}+\sum_{j=1}^{m_3}\delta_{i,j}\rho_{M,j}(t,\mathbf{S},\mathbf{M}),\ i=1,...,n_3,\ t>0, \tag{2.7}$$

$$\frac{dM_{liq,i}}{dt}=\frac{Q^{in}M_{liq,i}^{in}(t)}{V_{liq}}-\frac{Q^{out}M_{liq,i}(t)}{V_{liq}}+\sum_{j=1}^{m_3}\bar{\delta}_{i,j}\rho_{M,j}(t,\mathbf{S},\mathbf{M}),\ i=1,...,n_3,\ t>0, \tag{2.8}$$

where $m_1$, $m_2$, and $m_3$ denote the number of biochemical, acid-base and physico-chemical processes accounted in the mathematical model; $\rho_j(t,\mathbf{S},\mathbf{X},\mathbf{M})$ represents the kinetic rate equation for the $j^{th}$ biochemical process, respectively; $\rho_{A,j}(t,\mathbf{S})$ represents the kinetic rate equation for the $j^{th}$ acid-base reaction; $\rho_{M,j}(t,\mathbf{S},\mathbf{M})$ represents the reaction rate equation for the $j^{th}$ physico-chemical process; $\rho_{T,i}(t,\mathbf{S},\mathbf{S_{gas}})$ represents the rate equation for the liquid-gas transfer process of the $i^{th}$ component; $\alpha_{i,j}$ is the rate coefficient of the $i^{th}$ component referred to the $j^{th}$ biochemical process; $\beta_{i,j}$ is the rate coefficient of the $i^{th}$ component referred to the $j^{th}$ acid-base process; $\gamma_{i,j}$, $\delta_{i,j}$ and $\bar{\delta}_{i,j}$ are the rate coefficients of the $i^{th}$ component referred to the $j^{th}$ physico-chemical process; $\mathbf{S}=(S_1,...,S_{n_1})$, $\mathbf{X}=(X_{n_1+1},...,X_{n_2})$, $\mathbf{S_{gas}}=(S_{gas,1},...,S_{gas,n_1})$,

$\mathbf{M} = (M_1, ..., M_{n_3})$, and $\mathbf{M_{liq}} = (M_{liq,1}, ..., M_{liq,n_3})$. Regarding the operating parameters, $Q^{in}$ and $Q^{out}$ are the inlet and outlet wastewater flow of the biological reactor; $Q_{gas}$ is the total gas flow; $S_i^{in}$, $X_i^{in}$, $M_i^{in}$ and $M_{liq,i}^{in}$ represent the influent concentrations of the $i^{th}$ solute, particulate component and metal in solid and liquid form, respectively; $V_{liq}$ and $V_{gas}$ are the liquid volume and the gas volume of the biological reactor and their sum gives the constant total volume $V$. Such mass balance equations represent a system of nonlinear ordinary differential equations, where the state variables depend on time, and the non-linearity is due to the reaction terms. The initial condition required to solve the system is reported in Eqs. (2.9)-(2.13):

$$S_i(0) = S_i^0, \;\; i = 1, ..., n_1, \tag{2.9}$$

$$X_i(0) = X_i^0, \;\; i = n_1 + 1, ..., n_2, \tag{2.10}$$

$$S_{gas,i}(0) = S_{gas,i}^0, \;\; i = 1, ..., n_1, \tag{2.11}$$

$$M_i(0) = M_i^0, \;\; i = 1, ..., n_3, \tag{2.12}$$

$$M_{liq,i}(0) = M_{liq,i}^0, \;\; i = 1, ..., n_3, \tag{2.13}$$

where $S_i^0$, $X_i^0$, $S_{gas,i}^0$, $M_i^0$ and $M_{liq,i}^0$ are, the initial concentrations of the $i^{th}$ soluble substrate, particulate component, gas component, and metal in solid and liquid form, respectively.

### 2.3.2 Model application

The mathematical model was applied to simulate metal recovery from spent lithium-ion batteries (LIBs) during glucose fermentation. Ad-hoc experimental activities were set-up in batch conditions to achieve the required data for model calibration. Biochemical and physico-chemical processes occurring in DF experiments (metabolic pathways, acid-base reactions, liquid-gas equilibrium) as well as dissolution reaction kinetics of the leaching process were monitored during the tests. Based on experimental observations (Appendix A), different variables, in terms of concentrations, were accounted in the model: 10 soluble substrates (glucose $S_{su}$, butyric acid $S_{bu}$, acetic acid $S_{ac}$, hydrogen $S_{H_2}$, inorganic carbon $S_{IC}$, inorganic nitrogen $S_{IN}$, butyrate $S_{bu^-}$, acetate $S_{ac^-}$, bicarbonate $S_{HCO_3^-}$, ammonia $S_{NH_3}$); 1 particulate component (sugar fermenters $X_{su}$); 2 gas components (hydrogen gas $S_{gas,H_2}$, carbon dioxide $S_{gas,CO_2}$); manganese in solid form ($M$); manganese in liquid form ($M_{liq}$). Due to the batch condition adopted for lab-scale tests, the inlet and outlet wastewater flow were assumed to be equal to 0 ($Q^{in} = Q^{out} = 0$), and Eqs. (2.4)-(2.8) were specified as:

$$\frac{dS_{su}}{dt} = -\rho_1, \tag{2.14}$$

$$\frac{dS_{bu}}{dt} = (1 - Y_{su}) f_{bu,su} \rho_1 - n\rho_{M,1}, \tag{2.15}$$

$$\frac{dS_{ac}}{dt} = (1 - Y_{su}) f_{ac,su} \rho_1, \tag{2.16}$$

$$\frac{dS_{H_2}}{dt} = (1 - Y_{su}) f_{H_2,su} \rho_1 - \rho_{T,H_2}, \tag{2.17}$$

$$\frac{dS_{IC}}{dt} = C_{su}\rho_1 - (1 - Y_{su})(f_{bu,su}C_{bu} + f_{pro,su}C_{pro} + f_{ac,su}C_{ac})\rho_1 +$$

$$-Y_{su}C_{biom}\rho_1 + C_{biom}\rho_2 - \rho_{T,IC}, \tag{2.18}$$

$$\frac{dS_{IN}}{dt} = -Y_{su}N_{biom}\rho_1 + N_{biom}\rho_2, \tag{2.19}$$

$$\frac{dS_{bu^-}}{dt} = -\rho_{A,bu^-}, \tag{2.20}$$

$$\frac{dS_{ac^-}}{dt} = -\rho_{A,ac^-}, \tag{2.21}$$

$$\frac{dS_{HCO_3^-}}{dt} = -\rho_{A,HCO_3^-}, \tag{2.22}$$

$$\frac{dS_{NH_3}}{dt} = -\rho_{A,NH_3}, \tag{2.23}$$

$$\frac{dX_{su}}{dt} = Y_{su}\rho_1 - \rho_2, \tag{2.24}$$

$$\frac{dS_{gas,H_2}}{dt} = -\frac{Q_{gas}S_{gas,H_2}}{V_{gas}} + \frac{V_{liq}}{V_{gas}}\rho_{T,H_2}, \tag{2.25}$$

$$\frac{dS_{gas,CO_2}}{dt} = -\frac{Q_{gas}S_{gas,CO_2}}{V_{gas}} + \frac{V_{liq}}{V_{gas}}\rho_{T,IC}, \tag{2.26}$$

$$\frac{dM}{dt} = -\rho_{M,1}, \tag{2.27}$$

$$\frac{dM_{liq}}{dt} = \rho_{M,1} - \rho_{M,2}, \tag{2.28}$$

where $Y_{su}$ is the yield of sugar fermenters; $f_{bu,su}$, $f_{ac,su}$, and $f_{H_2,su}$ represent the fractions of butyrate, acetate, and hydrogen generated from sugar fermentation, respectively; $C_{su}$, $C_{bu}$, and $C_{ac}$ are the carbon content of sugar, butyrate, and acetate, respectively; $C_{biom}$, and $N_{biom}$ are the carbon and nitrogen content of the biomass; and $n$ represents the oxidation states of the metal (Eq. (2.3)). The characterization of the spent button LIBs was carried out following the procedure proposed by Russo et al. (2022) [67] (Appendix A). The internal part of batteries was mainly composed by: Manganese ($45.0\%$), Lithium ($9.45\%$), Silicon ($0.18\%$), Iron ($0.11\%$), Sodium ($0.13\%$), Calcium ($0.05\%$), Magnesium ($0.04\%$), Potassium ($0.03\%$), Nickel ($0.01\%$), Aluminium ($0.01\%$) and Chromium ($0.01\%$). Some of these metals are potentially dangerous for human health and environment [68]. Specifically, among all the metals contained in LIBs, the experimental campaign focused on manganese leaching as it was one of the most abundant metal in the specific E-waste. For this reason, only the dissolution process of manganese was considered in the mathematical model, assuming that other metals contained in the waste did not take part in the dissolution process, and the butyric acid $S_{bu}$ consumption was related to the leaching process exclusively of manganese $M$. In particular, the most common oxidation state of manganese is $+2$ ($n = 2$). Furthermore, according to the experimental data the concentration of the metal in the liquid form increased at the beginning of the leaching process, while a subsequent reduction was observed in the last experimental days. Based on this evidence, both the manganese dissolution ($\rho_{M,1}$) and subsequent reduction phase ($\rho_{M,2}$) were modeled.

**Biochemical reaction rates**

The DF process is performed by a single microbial group defined as sugar fermenters $X_{su}$. The growth process leads to the consumption and/or production of one or more soluble substrates, and a negative term was considered to account for microorganisms decay during the process. In particular, $X_{su}$ operate the glucose $S_{su}$ degradation and the contextual production of VFAs, such as butyric $S_{bu}$ and acetic acid $S_{ac}$, and hydrogen

$S_{H_2}$. The kinetic rate equation related to the *acidogenesis* process $\rho_1$ in Eqs. (2.14)-(2.19) and Eq.(2.24) was considered as a Monod-type kinetic:

$$\rho_1 = k_{m,su}\frac{S_{su}}{K_{su}+S_{su}}X_{su}I, \tag{2.29}$$

while, the decay rate $\rho_2$ in Eq. (2.18), Eq.(2.19), and Eq.(2.24) was modelled as a first order kinetic:

$$\rho_2 = k_{dec,X_{su}}X_{su}, \tag{2.30}$$

where $k_{m,su}$ is the Monod maximum specific uptake rate, which is achieved by dividing $\mu_{max,su}$ by $Y_{su}$, $\mu_{max,su}$ is the Monod maximum specific growth rate of sugar fermenters, $K_{su}$ is the affinity constant, $k_{dec,X_{su}}$ is the first order decay rate of sugar fermenters, and $I$ represents an inhibition function depending on pH value, inorganic nitrogen limitation, and metal concentration within the bioreactor. The inhibition function is detailed in the following.

**Leaching reaction rates**

In both experimental sets, manganese $M$ dissolution, induced by organic acids generation, was followed by a reduction of the liquid metal concentration due to precipitation/complexation phenomena. The reaction rate equation related to the dissolution process $\rho_{M,1}$ (Eq. (2.15), Eq. (2.27), and Eq. (2.28)) and the subsequent reduction of the metal concentration in soluble form $\rho_{M,2}$ (Eq. (2.28)) were modelled by equations:

$$\rho_{M,1} = k_d M^a S_{bu}^b. \tag{2.31}$$

$$\rho_{M,2} = k_r M_{liq}^c, \tag{2.32}$$

where $a$, $b$, and $c$ are the reaction order parameters, and $k_d$, and $k_r$ represent the dissolution and reduction constants of the leaching process, respectively.

The dissolution process (Eq. (2.31)) was modelled as a first order kinetic referred to the manganese concentration in solid form $M$ ($a$ equal to 1), and a second order kinetic referred to the butyric acid $S_{bu}$ ($b$ equal to 2). This assumption was supported by experimental evidence [44, 48] demonstrating that the metals leaching is strongly affected by the acid concentration in the case of both inorganic and organic acids. According to a previous study [66], the subsequent decrease of soluble metal in the anaerobic environment was ascribed to adsorption or precipitation phenomena (Eq. (2.32)). Due to the complexity of the reaction environment of experiments, from the available data it was not possible to distinguish the adsorption or the precipitation contributions during the dark fermentation-leaching process. For this reason, the reduction of metal in solution was simply modelled as a first order kinetic referred to the manganese concentration in solution (assuming the reaction order parameter $c$ equal to 1). Indeed, other models considered the same approximation to reproduce metals precipitation and metals adsorption phenomena [69, 70, 71].

**Acid-base process rates**

As mentioned above, pH and temperature play an important role in the evolution of the biochemical pathways involved in the DF process. To achieve high substrate degradation efficiency and $H_2$ yield, experimental findings showed that the pH level may vary from 4.5 to 7, and mesophilic temperatures (about 35$^{\circ}$C) are adequate for mixed culture fermentation [50]. During DF, high concentration of VFAs are produced, leading to the pH decrease in the reaction environment. Such acidification may lead to a partial or complete inhibition of microbial consortia, and may directly affect the $H_2$ generation rate. The acid-base equilibrium equations play an important role for pH calculation. In aqueous solution, any organic or inorganic compound leads to the production of acid-base pairs (e.g. proton $H^+$ and conjugate base) depending on the specific pH level.

In order to simulate pH variation over time, a charge balance equation, accounting for all the dissolved ionic species, was considered in the mathematical model and was expressed as:

$$\sum_i \mathbf{S_i^+} - \sum_i \mathbf{S_i^-} = 0, \tag{2.33}$$

where $\mathbf{S_i^+}$ and $\mathbf{S_i^-}$ represent the cationic and anionic equivalent concentration of the $i^{th}$ component. The $H^+$ concentration $S_{H^+}$ was obtained solving Eq. (2.33), which takes the form:

$$S_{H^+} + S_{NH_4^+} - S_{HCO_3^-} - \frac{S_{bu^-}}{160} - \frac{S_{ac^-}}{64} - S_{OH^-} = 0 \tag{2.34}$$

where $S_{NH_4^+}$ is the $NH_4^+$ concentration given by the difference of the inorganic nitrogen $S_{IN}$ and the ammonia $S_{NH_3}$ concentrations in the system; $S_{IN}$, $S_{bu^-}$, $S_{ac^-}$, $S_{HCO_3^-}$, and $S_{NH_3}$ were obtained solving Eqs. (2.19)-(2.23). The kinetic rates defined for each acid-base equilibrium in Eqs. (2.20)-(2.23) are listed below:

$$\rho_{A,bu^-} = K_{A/B,bu}(S_{bu^-}(S_{H^+}K_{a,bu}) - K_{a,bu}S_{bu}), \tag{2.35}$$

$$\rho_{A,ac^-} = K_{A/B,ac}(S_{ac^-}(S_{H^+}K_{a,ac}) - K_{a,ac}S_{ac}), \tag{2.36}$$

$$\rho_{A,HCO_3^-} = K_{A/B,CO_2}(S_{HCO_3^-}(S_{H^+}K_{a,CO_2}) - K_{a,CO_2}S_{IC}), \tag{2.37}$$

$$\rho_{A,NH_3} = K_{A/B,IN}(S_{NH_3}(S_{H^+}K_{a,IN}) - K_{a,IN}S_{IN}). \tag{2.38}$$

where $K_{A/B,i}$ and $K_{a,i}$ are the acid-base kinetic parameter and the acid-base equilibrium coefficient for the $i^{th}$ component.

**Physico-chemical processes**

Liquid-gas transfer equations were used to describe hydrogen $S_{H_2}$ and inorganic carbon $S_{IC}$ evolution in the liquid and the gas phase of bioreactors. When the liquid phase is relatively dilute, Henry's law can be used to describe the liquid-gas equilibrium. The liquid-gas transfer kinetic rates in Eq. (2.17), Eq. (2.18), Eq. (2.25), and Eq. (2.26) were expressed as:

$$\rho_{T,H_2} = kLa(S_{H_2} - 16K_{H,H_2}p_{gas,H_2}), \tag{2.39}$$

$$\rho_{T,IC} = kLa(S_{CO_2} - K_{H,CO_2}p_{gas,CO_2}), \tag{2.40}$$

where $kLa$ is the gas-liquid transfer coefficient, $K_{H,i}$ is the Henry's law coefficient of the $i^{th}$ component, $p_{gas,i}$ is the steady-state gas phase partial pressure of the $i^{th}$ component, and $S_{CO_2}$ is the $CO_2$ concentration given by the difference of $S_{IC}$ and $S_{HCO_3^-}$. The computation of $p_{gas,i}$ is required to compute the mass transfer kinetic rates, and it is given by:

$$p_{gas} = p_{gas,H_2} + p_{gas,CO_2} + p_{gas,H_2O}, \tag{2.41}$$

where:

$$p_{gas,H_2} = S_{gas,H_2}\frac{RT}{16}, \tag{2.42}$$

$$p_{gas,CO_2} = S_{gas,CO_2}RT, \tag{2.43}$$

$$p_{gas,H_2O} = 0.0313\ exp\Big(5290\Big(\frac{1}{298} - \frac{1}{T}\Big)\Big), \tag{2.44}$$

while, the gas flow $Q_{gas}$ necessary to solve Eq. (2.25) and Eq. (2.26) was set equal to the total gas transfer:

$$Q_{gas} = \frac{RT}{p_{gas} - p_{gas,H_2O}} V_{liq} \Big( \frac{\rho_{T,H_2}}{16} + \rho_{T,CO_2} \Big), \tag{2.45}$$

where $R$ and $T$ are the gas law constant and temperature, respectively.

### Inhibition functions

Several inhibition mechanisms were considered in the mathematical model to account for the influence of: i) the pH level on the process evolution; ii) the inorganic nitrogen concentration; iii) the presence of toxic metals. Then, the inhibition function $I$ in Eq. (2.29) was expressed as follows:

$$I = I_{pH} I_{IN,lim} I_L. \tag{2.46}$$

The inhibition term $I_{pH}$ describes that the pH level of the reaction environment directly affects metabolic activities of anaerobic bacteria. In accordance with previous studies [1], the optimal range of pH values are between $5.5$ and $7$. To account of upper and lower inhibition pH level, the pH inhibition term $I_{pH}$ was implemented with the following empirical equation [1, 72]:

$$I_{pH} = \frac{1 + 2 \cdot 10^{0.5(pH_{LL} - pH_{UL})}}{1 + 10^{(pH - pH_{UL})} + 10^{(pH_{LL} - pH)}}, \tag{2.47}$$

where $pH_{UL}$ and $pH_{LL}$ are upper and lower limits. These represent the pH values which lead to a maximum growth rate reduction of $50\%$.

The inorganic nitrogen limitation term $I_{IN,lim}$ was included to describe the decrease of the maximum growth rate due to a reduced nitrogen $S_{IN}$ availability in bioreactors

[1]. The limiting term $I_{IN,lim}$ was described as:

$$I_{IN,lim} = \frac{1}{1 + \frac{K_{IN}}{S_{IN}}}, \tag{2.48}$$

where $K_{S,IN}$ represents the $S_{IN}$ affinity constant for $X_{su}$.

Finally, the metals inhibition term $I_L$ was included to describe the condition in which high concentration of toxic metals negatively affects the metabolic activity [73, 74]. Toxic metals, such as cadmium (Cd), chromium (Cr), zinc (Zn), copper (Cu), nickel (Ni), and manganese (Mn), may be present in E-waste and inhibit or upset the fermentative process due to the increase of the toxicity level of the environment. The presence of high concentrations of metals is able to reduce the hydrogen production rate by $50\%$ [50]. The metals inhibition term $I_L$ was modelled with a non-competitive inhibition function [1]:

$$I_L = \frac{1}{1 + \frac{M}{K_L}}, \tag{2.49}$$

where $K_L$ is the inhibition constant related to the leaching process. The inhibition term $I_L$ assumes a value lower than $1$ since the metal concentration $M$ is greater than $0$. In particular, the higher is the metal concentration, the stronger is the inhibition effect. On the contrary, if $M$ is equal to $0$, the inhibition term $I_L$ assumes a constant value equal to $1$.

## 2.4 Model calibration

Due to the scarcity of literature data related to the leaching process conducted with DF produced OAs, ad-hoc experimental activities were carried out for model calibration purposes. To investigate different interactions occurring between the biological and the chemical process investigated, it was necessary to set up $2$ different initial conditions (IC) for bioreactors as reported in Appendix A. The E-waste was added at the beginning of the DF experiments ($IC1$) and when it was possible to consider that the DF process

was completely developed ($IC2$). The aim of this strategy was to build-up a complete data set to calibrate all the different parameters related to metals inhibition, biological process evolution and leaching process. Indeed, in the $IC1$ the inhibition effects related to the presence of metals delayed the DF evolution, increasing the initial toxicity level in the bioreactors. On the contrary, in the $IC2$ no inhibition phenomena occurred at the beginning of the biological process. However, the metal dissolution was observed in both cases, but with different evolution trends. In addition, to allow the model for reproducing an impulsive addition of the E-waste at a specific time, Eq. (2.27) was replaced by the following impulsive ordinary differential equation (IDE):

$$\frac{dM}{dt} = -\rho_{M,1}(t, \mathbf{S}, \mathbf{M}),\ t \neq t_W,\ t > 0, \tag{2.50}$$

$$\Delta M(t_W) = M(t_W) = M(t_W^+) - M(t_W^-), \tag{2.51}$$

where $t_W$ is the addition time, and $M(t_W)$ is the concentration of the metal added at $t_W$. $M(t_W^+)$ and $M(t_W^-)$ are the right and left limits of $M$ at $t_W$, corresponding to the concentrations of the metal later and before the addition of the waste. In particular, when $t_W$ is equal to 0, $M(t_W)$ represents the initial condition of metal in solid form ($M^0$).

The experimental data were compared with model predictions, adjusting and varying specific kinetic, stoichiometric, and physico-chemical parameters until model results adequately fitted the experimental data. The calibration phase was based on experimental data of glucose degradation, butyric and acetic acid production, cumulative hydrogen generation and manganese trend in the tests. The required initial condition for model calibration was set according to lab-scale experiments and are reported in Table 2.1.

According to the literature [72, 75, 76], the common parameters with the ADM1 were selected as base-values due to the similarity of anaerobic digestion and DF pro-

| Parameter | Definition | Unit | IC1 | IC2 |
|---|---|---|---|---|
| $S^0_{su}$ | Initial concentration of glucose | $kgCOD\ m^{-3}$ | 10 | 10 |
| $S^0_{bu}$ | Initial concentration of butyric acid | $kgCOD\ m^{-3}$ | 0 | 0 |
| $S^0_{ac}$ | Initial concentration of acetic acid | $kgCOD\ m^{-3}$ | 0 | 0 |
| $S^0_{H_2}$ | Initial concentration of hydrogen | $kgCOD\ m^{-3}$ | 0 | 0 |
| $S^0_{IC}$ | Initial concentration of inorganic carbon | $kmole\ m^{-3}$ | 0.1 | 0.1 |
| $S^0_{IN}$ | Initial concentration of inorganic nitrogen | $kmole\ m^{-3}$ | 0.06 | 0.06 |
| $S^0_{bu^-}$ | Initial concentration of butyrate | $kgCOD\ m^{-3}$ | 0 | 0 |
| $S^0_{ac^-}$ | Initial concentration of acetate | $kgCOD\ m^{-3}$ | 0 | 0 |
| $S^0_{HCO_3^-}$ | Initial concentration of bicarbonate | $kmole\ m^{-3}$ | 0 | 0 |
| $S^0_{NH_3}$ | Initial concentration of ammonia | $kmole\ m^{-3}$ | 0 | 0 |
| $X^0_{su}$ | Initial concentration of sugar fermenters | $kgCOD\ m^{-3}$ | 5 | 5 |
| $S^0_{gas,H_2}$ | Initial concentration of hydrogen gas | $kgCOD\ m^{-3}$ | 0 | 0 |
| $S^0_{gas,CO_2}$ | Initial concentration of carbon dioxide gas | $kmole\ m^{-3}$ | 0 | 0 |
| $M^0_{liq}$ | Initial concentration of metal in liquid form | $kg\ m^{-3}$ | 0 | 0 |
| $M(t_W)$ | Metal concentration added to the bioreactor at $t_W$ | $kg\ m^{-3}$ | 6.5 | 6.5 |
| $t_W$ | Addition time of E-waste | $d$ | 0 | 8 |

Table 2.1: Initial conditions and operating parameters used for model calibration.

cesses. Indeed, DF can be seen as an anaerobic digestion process in which the last step of *methanogenesis* is suppressed to produce hydrogen instead of methane. The numerical results were achieved with an original code implemented in MatLab platform. The model was rerun several times by increasing/reducing each parameter, one by one, until the model well reproduced the experimental data. All the values of stoichiometric, kinetic and operating parameters resulting from the calibration phase are reported in Table 2.2.

In particular, the parameters related to the leaching process play a fundamental role. Indeed, the leaching inhibition constant $K_L$ regulates the metals inhibition function $I_L$ (Eq. (2.49)). When the waste is added at the beginning of the process ($IC1$), $I_L$ is less than $1$ and the DF process is inhibited. The higher is the amount of waste added to the bioreactor, the lower is $I_L$. When the waste is added later ($IC2$), the DF evolves without inhibition and $I_L$ is equal to $1$. The dissolution and reduction constants ($k_d$ and $k_r$) regulate the processes in which the metals are involved. The constant $k_d$ is related to the conversion of the metal from the solid to the liquid form, while the subsequent reduction of metals directly depends on $k_r$. According to experimental data, manganese was initially dissolved consuming butyric acid. Subsequently, a reduction of the dissolved

| Parameter | Definition | Unit | Value | Ref |
|---|---|---|---|---|
| $V$ | Reactor volume | $mL$ | 120 | (a) |
| $V_{liq}$ | Reactor volume | $mL$ | 70 | (a) |
| $V_{gas}$ | Reactor volume | $mL$ | 50 | (a) |
| $Y_{su}$ | $X_{su}$ yield on $S_{su}$ | $kgCOD\ kgCOD^{-1}$ | 0.5 | (b) |
| $f_{bu,su}$ | fraction of $S_{bu}$ from $S_{su}$ | $kgCOD\ kgCOD^{-1}$ | 0.79 | (b) |
| $f_{ac,su}$ | fraction of $S_{ac}$ from $S_{su}$ | $kgCOD\ kgCOD^{-1}$ | 0.10 | (b) |
| $f_{H_2,su}$ | fraction of $S_{H_2}$ from $S_{su}$ | $kgCOD\ kgCOD^{-1}$ | 0.11 | (b) |
| $C_{su}$ | Carbon content of $S_{su}$ | $kmoleC\ kgCOD^{-1}$ | 0.0313 | [1] |
| $C_{bu}$ | Carbon content of $S_{bu}$ | $kmoleC\ kgCOD^{-1}$ | 0.025 | [1] |
| $C_{ac}$ | Carbon content of $S_{ac}$ | $kmoleC\ kgCOD^{-1}$ | 0.0313 | [1] |
| $C_{biom}$ | Carbon content of biomass | $kmoleC\ kgCOD^{-1}$ | 0.0313 | [1] |
| $N_{biom}$ | Nitrogen content of biomass | $kmoleN\ kgCOD^{-1}$ | 0.00625 | [1] |
| $\mu_{max,su}$ | Monod maximum specific uptake rate of $X_{su}$ | $d^{-1}$ | 2 | (b) |
| $K_{su}$ | $S_{su}$ affinity constant for $X_{su}$ | $kgCOD\ m^{-3}$ | 1.5 | (b) |
| $k_{dex,X_{su}}$ | Decay-inactivation rate for $X_{su}$ | $d^{-1}$ | 0.02 | [1] |
| $k_d$ | Dissolution constant | $kgCOD^2\ m^{-6}\ d^{-1}$ | 0.005 | (b) |
| $k_r$ | Reduction constant | $d^{-1}$ | 17 | (b) |
| $K_{A/B,bu}$ | $S_{bu}$ acid-base kinetic parameter | $m^3\ kmole^{-1}\ d^{-1}$ | $10^{10}$ | [1] |
| $K_{A/B,ac}$ | $S_{ac}$ acid-base kinetic parameter | $m^3\ kmole^{-1}\ d^{-1}$ | $10^{10}$ | [1] |
| $K_{A/B,CO_2}$ | $S_{CO_2}$ acid-base kinetic parameter | $m^3\ kmole^{-1}\ d^{-1}$ | $10^{10}$ | [1] |
| $K_{A/B,IN}$ | $S_{IN}$ acid-base kinetic parameter | $m^3\ kmole^{-1}\ d^{-1}$ | $10^{10}$ | [1] |
| $K_{a,bu}$ | $S_{bu}$ acid-base equilibrium parameter | $kmole\ m{-}3$ | $1.51\ 10^{-5}$ | [1] |
| $K_{a,ac}$ | $S_{ac}$ acid-base equilibrium parameter | $kmole\ m{-}3$ | $1.51 \cdot 10^{-5}$ | [1] |
| $K_{a,CO_2}$ | $S_{CO_2}$ acid-base equilibrium parameter | $kmole\ m{-}3$ | $4.94 \cdot 10^{-7}$ | [1] |
| $K_{a,IN}$ | $S_{IN}$ acid-base equilibrium parameter | $kmole\ m{-}3$ | $1.11 \cdot 10^{-9}$ | [1] |
| $K_{H,H_2}$ | Henry's law coeffiecient of $S_{H_2}$ | $kmole\ m^{-3}\ bar^{-1}$ | $2.72 \cdot 10^{-2}$ | [1] |
| $K_{H,CO_2}$ | Henry's law coeffiecient of $S_{CO_2}$ | $kmole\ m^{-3}\ bar^{-1}$ | $7.3847 \cdot 10^{-4}$ | [1] |
| $kLa$ | gas-liquid transfer coefficient | $d^{-1}$ | 200 | [1] |
| $R$ | Gas law constant | $bar\ m^3\ kmole^{-1}\ K^{-1}$ | 0.083145 | [1] |
| $T$ | Temperature within the reactor | K | 308 | (a) |
| $pH_{UL}$ | pH upper limit | $--$ | 5.5 | [1] |
| $pH_{LL}$ | pH lower limit | $--$ | 4 | [1] |
| $K_{IN}$ | $S_{IN}$ affinity constant for $X_{su}$ | $kgCOD\ m^{-3}$ | $1 \cdot 10^{-4}$ | [1] |
| $K_L$ | Leaching inhibition constant | $kg\ m^{-3}$ | 5.6 | (b) |
| $Time$ | Simulation time | $d$ | 16 | (a) |

(a) Experimental

(b) Calibrated

Table 2.2: Kinetic, stoichiometric and and operating parameters.

metal concentration was observed. Noteworthy, the only manganese leaching process was considered in the mathematical model, and butyric acid was exclusively used for the dissolution process. This can represent a limiting assumption for the model, but the main scope of this Chapter was to study the feasibility of the combined DF-leaching process and to develop a mathematical model that can catch the main phenomena.

The biological parameters, $f_{bu,su}$, $f_{pro,su}$, $f_{ac,su}$, $f_{H_2,su}$, $Y_{su}$, $K_{su}$, and $\mu_{max,su}$ were calibrated without considering the inhibition of metals. Indeed, the fraction of hydro-

gen, butyric, propionic, and acetic acid from sugar ($f_{H_2,su}$, $f_{bu,su}$, $f_{pro,su}$, and $f_{ac,su}$) describe the amount of these products deriving from the glucose conversion. Differently from ADM1, propionic acid was not considered in the model as it was not produced in the bioreactors. Moreover, propionic acid production pathway is usually neglected in DF modelling. Butyrate was the major end-product, followed by acetate. This result is in accordance with the work of Gadhamshetty et al. (2010) [72], which obtained a quasi null value of $f_{pro,su}$, a $f_{bu,su}$ value grater than $f_{ac,su}$, and a $f_{H_2,su}$ value lower than $20\%$. The other calibrated values of Monod maximum specific uptake rate ($\mu_{max,su}$), yield of biomass ($Y_{su}$), and affinity constant ($K_{su}$) are within the range of values reported in literature [72, 76].

**IC1**

| **Variable** | **NMAE** | **ME** | **IoA** | **FB** |
|---|---|---|---|---|
| $S_{su}$ | 0.0927 | 0.9772 | 0.9946 | 0.0862 |
| $S_{bu}$ | 0.1445 | 0.9279 | 0.9802 | 0.0178 |
| $S_{ac}$ | 0.0691 | 0.9842 | 0.9959 | -0.0088 |
| $V_{H_2}$ | 16.479 | -338.107 | 0.1277 | 1.7835 |
| $M_{liq}$ | 0.4213 | 0.2426 | 0.8734 | 0.3092 |

**IC2**

| **Variable** | **NMAE** | **ME** | **IoA** | **FB** |
|---|---|---|---|---|
| $S_{su}$ | 0.0593 | 0.9958 | 0.9990 | 0.0301 |
| $S_{bu}$ | 0.1146 | 0.9397 | 0.9846 | -0.0654 |
| $S_{ac}$ | 0.0726 | 0.9376 | 0.9851 | 0.0665 |
| $V_{H_2}$ | 0.0507 | 0.9850 | 0.9963 | 0.0448 |
| $M_{liq}$ | 0.1161 | 0.9932 | 0.9958 | 0.0837 |

Table 2.3: Performance indicators.

The quality of the calibration was evaluated through the determination of performance indexes [77]: the mean absolute error (MAE), including its normalized form (NMAE), the modelling efficiency (ME), the index of agreement (IoA), and the fractional mean bias (FB). Such indexes were frequently used for calibration purposes [78], and are usually reported as:

$$MAE = \frac{\sum_{i=1}^{N} |P_i - O_i|}{N} \tag{2.52}$$

$$NMAE = \frac{MAE}{\bar{O}} \tag{2.53}$$

$$ME = 1 - \frac{\sum_{i=1}^{N} (P_i - O_i)^2}{\sum_{i=1}^{N} \left(O_i - \bar{O}\right)^2} \tag{2.54}$$

$$IoA = 1 - \frac{\sum_{i=1}^{N} (P_i - O_i)^2}{\sum_{i=1}^{N} \left(\left|P_i - \bar{O}\right| + \left|O_i - \bar{O}\right|\right)^2} \tag{2.55}$$

$$FB = \frac{\bar{P} - \bar{O}}{\frac{1}{2}(\bar{P} + \bar{O})} \tag{2.56}$$

where $N$ is the number of available values; $P_i$ and $O_i$ denote the $i^{th}$ predicted value and the $i^{th}$ observed value, respectively; $\bar{P}$ and $\bar{O}$ denote their mean values. The performance indicators are provided in Table 2.3. The results related to the $IC1$ showed that the $NMAE$ and $FB$ error indexes were lower than about $14\%$, and the $ME$ and $IoA$ error indexes were greater than about $93\%$, except for $V_{H_2}$ and $M_{liq}$ (Fig. 2.3). In the case of $IC2$, the $NMAE$ and $FB$ error indexes were lower than about $11\%$, while the $ME$ and $IoA$ error indexes were greater than about $94\%$ for all model variables.

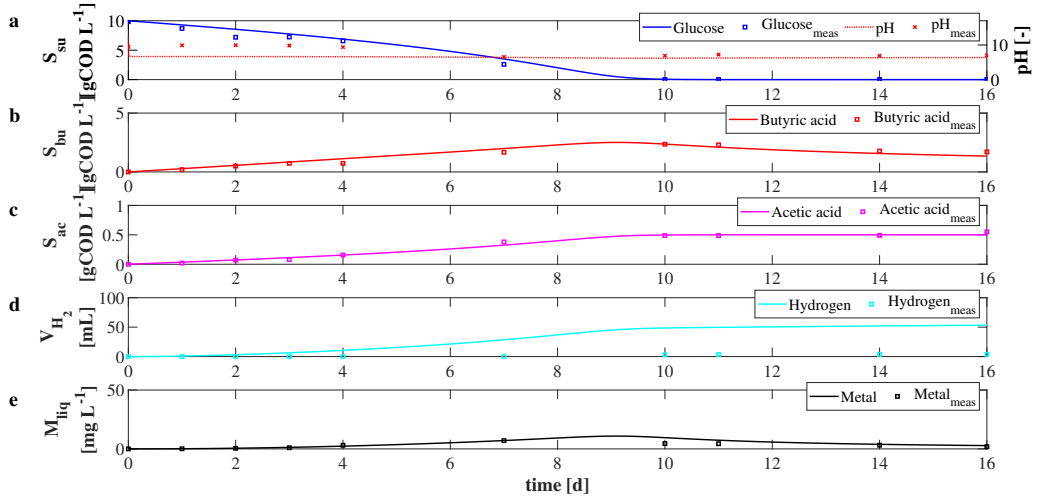


Figure 2.3: $IC1$ - Evolution over time of measured and simulated values of pH (a), glucose $S_{su}$ (a), butyric acid $S_{bu}$ (b), acetic acid $S_{ac}$ (c) concentrations, cumulative hydrogen production $V_{H_2}$ (d), and concentration of metal in solution $M_{liq}$ (e).

Experimental and model results related to the $IC1$ are reported in Fig. 2.3. The initial condition of model simulation was characterized by: $10\ gCOD\ L^{-1}$ of glucose ($S^0_{su}$), $5\ gCOD\ L^{-1}$ of mixed culture ($X^0_{su}$), and $1\ g$ of E-waste added at $t_W = 0\ d$. Figure 2.3 shows that the model was able to fit experimental data related to the biological process. The addition of E-waste negatively affected the DF process in terms of hydrogen and VFAs yields. Indeed, the complete conversion of glucose (Fig. 2.3a) was achieved in about $10$ days, due to a partial inhibition of the E-waste on sugar fermenters $X_{su}$. Consequently, the production of VFAs and hydrogen was observed. The butyric acid (Fig. 2.3b) initially had an increasing trend, and it reached the maximum predicted value of $2.5\ gCOD\ L^{-1}$ at $t = 9\ d$. Due to the dissolution process, butyric acid consumption occurred in the second part of the experiments. At $t = 16\ d$ the measured residual concentration of butyric acid was equal to $1.7\ gCOD\ L^{-1}$. This result is confirmed by Wang et al. (2019), who reported that butyric acid is the most effective leaching reagent [45]. Similar carboxylic acids, such as acetic and propionic acids, are characterized by a lower efficiency than butyric acid, and their presence has limited effect on the leaching process [79]. The acetic acid (Fig. 2.3c) showed an increasing trend in all the observation period. The predicted values of both butyric acid and acetic acid at $t = 16\ d$ were approximately equal to the measured residual concentrations. The model accurately reproduced experimental data except for the cumulative hydrogen production (Fig. 2.3d). Its overestimation is probably due to the presence of other chemical compounds contained in the E-waste, as it is well known that hydrogen is a high reactive compound for secondary reactions. Nevertheless, these chemical reactions were not considered in the mathematical model. For this reason, at $t = 16\ d$ the predicted value of hydrogen was $53.6\ mL$, while the measured value was equal to $3.7\ mL$. As shown in Fig. 2.3a, it is possible to observe an reasonable fit in the case of pH values. High pH was observed at the beginning of the process due to the waste addition, while the value decreased over time due to acids accumulation. Figure 2.3e shows the results related to the metal leaching and precipitation processes. The leach-

ing process begun at day 1 and the concentration of the leached manganese reached the maximum predicted value of 10.8 $mg\ L^{-1}$ at $t = 9\ d$. Subsequently, a slow decrease was observed and the predicted and the measured concentrations of 2.7 $mg\ L^{-1}$ and 1.9 $mg\ L^{-1}$ were observed at $t = 16\ d$, respectively. Such reduction can be ascribed to precipitation and/or adsorption phenomena observed in previous studies [66]. Nevertheless, the model prediction of $M_{liq}$ was less accurate than other variables due to the uncertainty about all the possible chemical reactions occurring in the bioreactors.

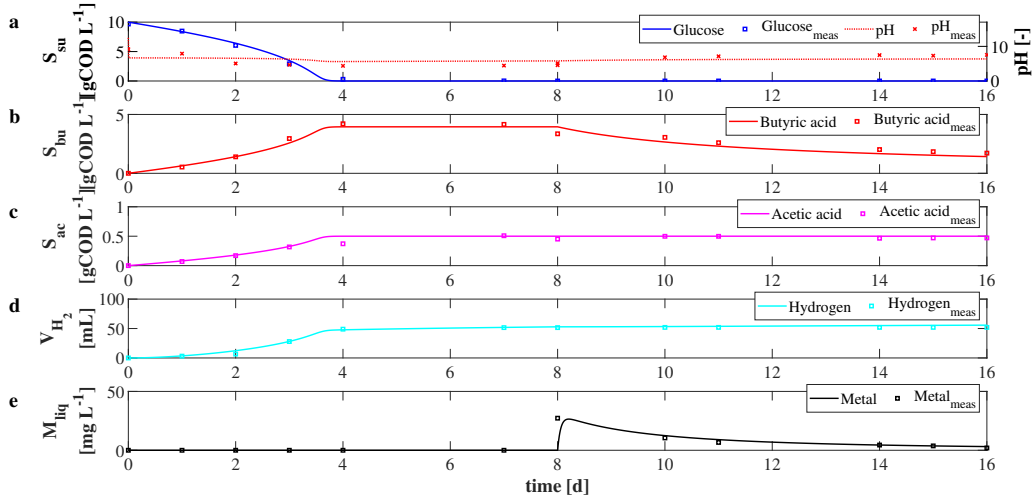


Figure 2.4: $IC2$ - Evolution over time of measured and simulated values of pH (a), glucose $S_{su}$ (a), butyric acid $S_{bu}$ (b), acetic acid $S_{ac}$ (c) concentrations, cumulative hydrogen production $V_{H_2}$ (d), and concentration of metal in solution $M_{liq}$ (e).

Experimental and model results related to the $IC2$ are reported in Fig. 2.4. In this case, the initial conditions were set to: 10 $gCOD\ L^{-1}$ of glucose ($S^0_{su}$), 5 $gCOD\ L^{-1}$ of mixed culture ($X^0_{su}$), and 1 $g$ of E-waste added once the produced hydrogen by the DF process achieved a constant value ($t_W = 8\ d$). In this case, a good agreement between predicted and experimental data was observed. Obviously, the biological process was not negatively affected by metal concentration and the complete consumption of glucose (Fig. 2.4a) was obtained after about 4 days. Consequently, the production of butyric acid (Fig. 2.4b), acetic acid (Fig. 2.4c), and hydrogen (Fig. 2.4d) was observed. The predicted maximum values of butyric and acetic acids were 3.9 $gCOD\ L^{-1}$ and

$0.5\ gCOD\ L^{-1}$, respectively. Once the waste was added to the bioreactors, $S_{bu}$ decreased over time due to the leaching process. The production and consumption phases are clearly separated and take place consecutively. It means that butyric acid initially produced during the fermentation, and it was consumed when the leaching process begun. However, a residual butyric acid concentration was observed. The predicted and measured residual concentration at $t = 16\ d$ were equal to $1.5\ gCOD\ L^{-1}$ and $1.7\ gCOD\ L^{-1}$. The cumulative predicted and measured hydrogen production after $16$ days were equal to $55\ mL$ and $52\ mL$, respectively. As shown in Fig. 2.4a, pH decreased during the fermentation due to acids production. In Fig. 2.4e the results related to the metal leaching process are reported. Once the E-waste was added to bioreactors, the butyric acid and the solid manganese were rapidly involved in the leaching process. The maximum value of manganese in the solution was observed after a few hours of simulation, and it was equal to $26.5\ mg\ L^{-1}$. Subsequently, the dissolved manganese concentration decreased due to the precipitation/adsorption process, and it reached a residual value according to the experimental evidence (predicted and measured concentration of $3\ mg\ L^{-1}$ and $2\ mg\ L^{-1}$, respectively).

## 2.5 Numerical studies and results

Further numerical simulations were performed to study the removal efficiency of toxic metals from E-waste by adopting the DF process. To optimize the integrated DF-leaching process, three fundamental aspects were investigated: (i) the effect of metal inhibition on the biological process; (ii) the effect of $F/M$ ratio on the bioconversion of sugars; and (iii) the effect of butyric acid and metal concentration on the leaching efficiency. To this aim, four numerical studies were implemented:

- $NS1$ examines the effect of the initial metal concentration, $M^0$, on the microbial activity;

- $NS2$ and $NS3$ investigate the effect of the $F/M$ ratio variation, $S^0_{su}/X^0_{su}$, on the DF process and on the leaching efficiency;
- $NS4$ explores the effect of E-waste concentration, $M(t_W)$, on the metal removal efficiency.

To mitigate the negative effect of metals on the biological process, the strategy adopted in the numerical study $NS1$ was to change the initial metal concentration in the bioreactor. In this case, the results are presented in the timescale from day $0$ to day $16$. As shown in the experimental results, the concentration of the dissolved metal decreased in the last part of the experiments. This reduction was due to the precipitation of the metal in the bioreactor or to the adsorption of the metal on solid components involved in the process [49, 66]. Since the recovery of metals can be easier achieved from the leachate solution [41], such reduction makes the leaching process inefficient [45]. This naturally leads to consider a sequential batch reactor or two separate reactors, to avoid inhibition effects of metals during DF and to maximize metal recovery using the clarified DF effluent as leaching agent. For this reason, the strategy adopted in the numerical studies $NS2$, $NS3$, and $NS4$ consisted in separating the biological process and the leaching reaction in two different consecutive reactors. The first bioreactor contains the microbial inoculum, and, it is fed with sugar and inoculum, allowing for the biological process evolution. Once the DF is completely developed, the effluent, rich in VFAs, is used for the leaching process in the second reactor. To avoid precipitation and/or adsorption phenomena and to maximize the metal recovery, the treatment time of the waste in the second reactor was fixed to $24$ hours [66]. Indeed, the dissolution reaction can be considered significantly faster than the precipitation/adsorption process. In this condition, it can be assumed that a negligible precipitation/adsorption of the metal occurs. With these assumptions, the precipitation process was neglected ($\rho_{M,2} = 0$) in numerical studies $NS2$, $NS3$, and $NS4$. The results related to the biological process are presented in the timescale from day $0$ to day $8$, and the results related to the

leaching process are presented in the same Figure in the timescale from day $8$ to day $9$. Successively, ad-hoc and controlled processes can be further used for the final recovery of metals from the DF effluent-leachate solution, such as electrochemical, precipitation, or solvent extraction techniques [38, 39, 41, 66].

The initial conditions $S_{su}^0$, $X_{su}^0$, $M^0$, and $M(t_W)$, were varied in numerical studies. Their values have been highlighted below for each numerical study. The values of kinetic, stoichiometric and leaching parameters were derived from the calibration phase. All the values of stoichiometric, kinetic and operating parameters are summarized in Table 2.2.

### 2.5.1 NS1 - Effects of metal inhibition

As aforementioned, metals are able to inhibit the fermentative process evolution due to their toxic effect. The experimental data clearly showed this inhibition phenomenon when the waste was added at the beginning of the experiments. In this context, a numerical study $NS1$ was performed to study the metal inhibition effect on the biological process. Four numerical simulations were carried out with different initial concentrations of metal $M^0$ ($6.5$, $3$, $1.5$, and $0.5$ $g\ L^{-1}$). The same initial concentration of glucose and sugar fermenters were used: $S_{su}^0 = 10\ gCOD\ L^{-1}$ and $X_{su}^0 = 5\ gCOD\ L^{-1}$. Consequently, the value of $F/M$ ratio used in the numerical simulations was $2\ gCOD_{substrate}\ gVS_{inoculum}^{-1}$. The remaining initial conditions set for this numerical study were the same used in the calibration phase.

The model results of $NS1$ are shown in Fig. 2.5. The time required for the complete glucose degradation decreased from $10$ to $4$ days (Fig. 2.5a) when the initial concentration of metal decreased from $6.5$ to $0.5$ $g\ L^{-1}$. Clearly, this behaviour can be attributed to the metal inhibition function, which is inversely proportional to the concentration of the metal in solid form. Consequently, the productions rates of VFAs (Figs. 2.5b and 2.5c) and hydrogen (Fig. 2.5d) were faster for low values of $M^0$. All DF end-products

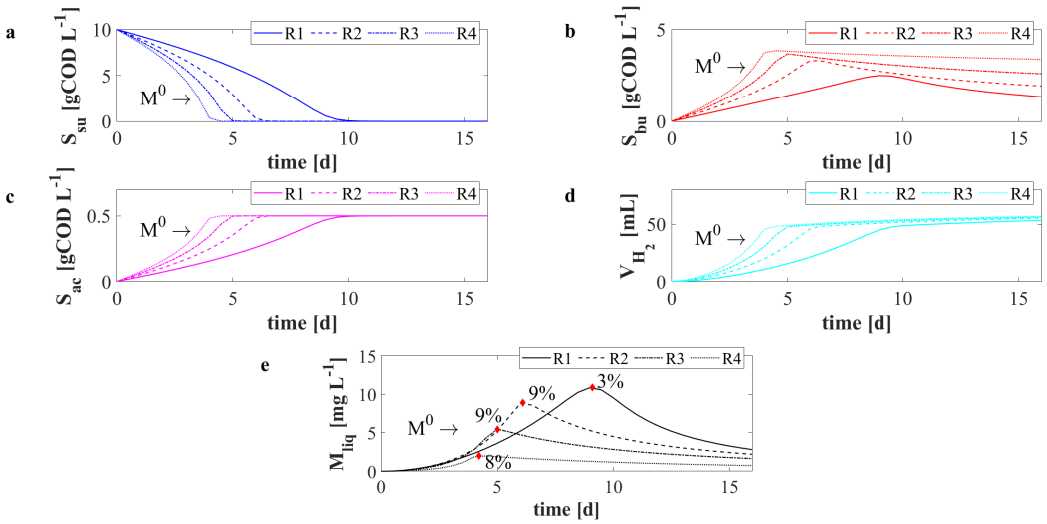


Figure 2.5: $NS1$ - Evolution over time of simulated values of glucose $S_{su}$ (a), butyric acid $S_{bu}$ (b), acetic acid $S_{ac}$ (c) concentrations, cumulative hydrogen production $V_{H_2}$ (d), and concentration of metal in solution $M_{liq}$ (e) for different initial concentration of metal $M^0$. $R1$: $M^0 = 6.5\ g\ L^{-1}$; $R2$: $M^0 = 3\ g\ L^{-1}$; $R3$: $M^0 = 1.5\ g\ L^{-1}$; $R4$: $M^0 = 0.5\ g\ L^{-1}$. Initial concentration of sugar and sugar fermenters: $S^0_{su} = 10\ gCOD\ L^{-1}$ and $X^0_{su} = 5\ gCOD\ L^{-1}$. Red rhombus represents the maximum removal efficiency.

(except for the butyric acid) approximately reached the same concentration when the residual concentrations of glucose were close to zero. The butyric acid (Fig. 2.5b), which is directly involved in the leaching reactions, reached its maximum value when the lowest concentration of metal was fed to the reactor ($R4$). Of course, in this condition the residual concentration of butyric acid was higher due to the limited presence of the metal. Finally, when a smaller amount of E-waste was added to the bioreactor, the inhibition effect was less intense and the butyric acid was faster produced. Figure 2.5e shows the results related to the metal dissolution. As expected, the leaching process led to a higher metal concentration in dissolved form in $R1$ but in a longer time. Nevertheless, the maximum removal efficiency (Fig. 2.5e - red rhombus) obtained in each simulation was lower than $9\%$. When the initial concentration of metal in solid form was equal to $6.5\ g\ L^{-1}$ ($R1$), the dissolved metal concentration initially increased with the highest rate. Nevertheless, around day $3$, a rapid increment was observed in the cases of initial solid metal of $R2$ and $R3$. Indeed, the leaching rate depends lin-

early on the metal concentration and quadratically on butyric acid concentration. At the beginning of the numerical experiments, the butyric acid concentration was low as the complete glucose degradation was not reached. Successively, the butyric acid increased, allowing for the dissolution of the metal.

### 2.5.2 NS2 and NS3 - Effects of F/M ratio on DF process

The $F/M$ ratio plays a fundamental role in the dark fermentation, especially when the process is devoted to hydrogen production [50]. To avoid methane generation and maximize hydrogen production, high $F/M$ ratios (generally higher than $1$) are used for the DF process. For this reason, a numerical study $NS2$ was conducted to investigate the effect of the $F/M$ ratio ($S^0_{su}/X^0_{su}$ in the mathematical model) on the DF evolution. Specifically, $10$ simulations were carried out with different initial concentrations of glucose $S^0_{su}$ (5, 10, 15, 20, 25, 30, 35, 40, 45, and 50 $gCOD\ L^{-1}$). The same initial condition of sugar fermenters and metal concentration were used: $X^0_{su} = 5\ gCOD\ L^{-1}$ and $M = 6.5\ g\ L^{-1}$. Consequently, the value of $F/M$ ratio used in the numerical simulations varied from $1$ to $10\ gCOD_{substrate}\ gVS^{-1}_{inoculum}$. The remaining initial conditions set for this numerical study were the same used in the calibration phase.

The results of $NS2$ are summarized in Fig. 2.6. When $F/M$ ratio increased from $1$ to $4\ gCOD_{substrate}\ gVS^{-1}_{inoculum}$, all the biological process rates increased. Thus, glucose (Fig. 2.6a) was completely consumed at day $4$, and high concentrations of VFAs (Figs. 2.6b and 2.6c) and hydrogen (Fig. 2.6d) were obtained at the end of the biological process. Nevertheless, for $F/M$ ratios greater than $4$ the process was inhibited, and the glucose was not completely degraded. Indeed, when the initial concentration of glucose was higher than $20\ gCOD\ L^{-1}$, the biological environment was characterized by inhibiting pH levels due to high VFAs concentrations. By setting the initial glucose concentration $S^0_{su}$ from $25$ to $50\ gCOD\ L^{-1}$, the residual concentration of glucose at $t = 8\ d$ increased, and similar VFAs and hydrogen productions were observed. From

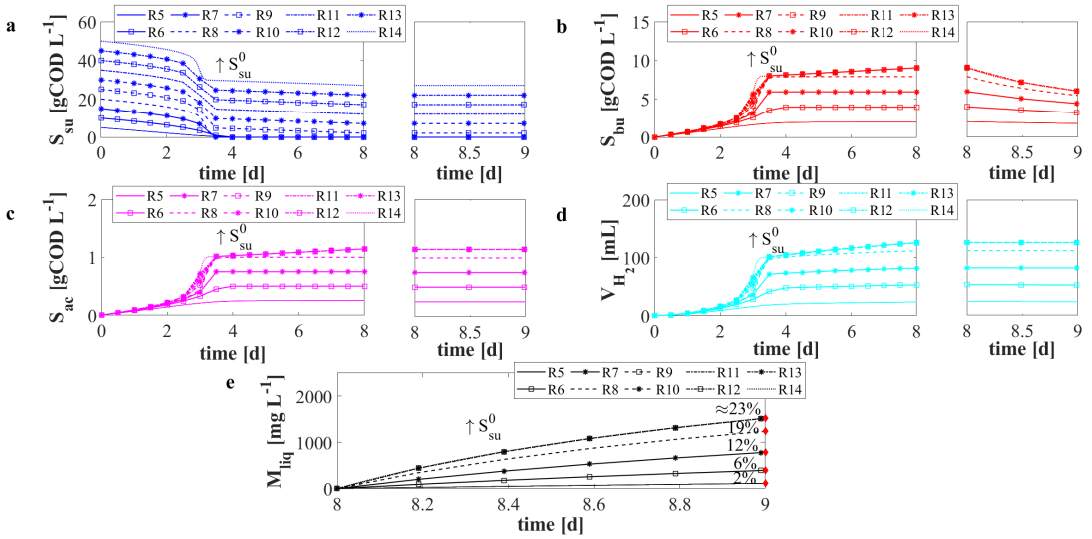


Figure 2.6: $NS2$ - Evolution over time of simulated values of glucose $S_{su}$ (a), butyric acid $S_{bu}$ (b), acetic acid $S_{ac}$ (c) concentrations, cumulative hydrogen production $V_{H_2}$ (d), and concentration of metal in solution $M_{liq}$ (e) for different initial concentration of sugar $S^0_{su}$. $R5$: $S^0_{su} = 5\ gCOD\ L^{-1}$; $R6$: $S^0_{su} = 10\ gCOD\ L^{-1}$; $R7$: $S^0_{su} = 15\ gCOD\ L^{-1}$; $R8$: $S^0_{su} = 20\ gCOD\ L^{-1}$; $R9$: $S^0_{su} = 25\ gCOD\ L^{-1}$; $R10$: $S^0_{su} = 30\ gCOD\ L^{-1}$; $R11$: $S^0_{su} = 35\ gCOD\ L^{-1}$; $R12$: $S^0_{su} = 40\ gCOD\ L^{-1}$; $R13$: $S^0_{su} = 45\ gCOD\ L^{-1}$; $R14$: $S^0_{su} = 50\ gCOD\ L^{-1}$. Initial concentration of sugar fermenters and metal concentration: $X^0_{su} = 5\ gCOD\ L^{-1}$ and $M = 6.5\ g\ L^{-1}$. Red rhombus represents the removal efficiency after 24 hours.

day 8 to 9, a second reactor with the same volume was considered, and the composition of the liquid environment was dictated by the DF effluent composition in terms of dissolved compounds. The butyric acid consumption was immediately observed due to the metal addition (Fig. 2.6b). The higher was the butyric acid concentration at the end of the DF stage (from day 0 to day 8), the faster was its consumption in the second stage (from day 8 to day 9). Indeed, the leaching rate quadratically depends on acid concentration. The trend of dissolved metal is reported in Fig. 2.6e. As explained above, the removal efficiency was computed after 24 hours (Fig. 2.6e - red rhombus). The removal efficiency after 24 hours reached higher values when increasing the $F/M$ ratio from 1 to 4. When the initial glucose concentration was set from 20 to 25 $gCOD\ L^{-1}$, the removal efficiency increased about 5%. When values of $F$ greater than 25 $gCOD\ L^{-1}$ were adopted, the concentration of the leached metal was constant, as the same concentration of butyric acid was predicted in the reactor. This result is confirmed by several

studies [44, 66, 80], showing that the increase of acidic concentrations over specific thresholds does not affect the leaching efficiency in the case of both organic and inorganic acids. In conclusion, the optimal $F/M$ ratio $4\ gCOD_{substrate}\ gVS^{-1}_{inoculum}$ was obtained.

To improve VFAs and hydrogen production, and consequently the metal removal efficiency, the numerical study $NS3$ was performed. Again $10$ different numerical experiments were carried out with different initial conditions of glucose $S^0_{su}$ ($5$, $10$, $15$, $20$, $25$, $30$, $35$, $40$, $45$, and $50\ gCOD\ L^{-1}$), with the same metal concentration ($M = 6.5\ g\ L^{-1}$), but with an initial sugar fermenters concentration $X^0_{su}$ equal to $10$ $gCOD\ L^{-1}$. This choice was aimed at decreasing the degradation and production time of the biological compartment to enhance the metal recovery efficiency. The initial condition of inorganic carbon and inorganic nitrogen were doubled as well with respect to the numerical study $NS2$. The $F/M$ ratios used in this numerical study varied from $0.5$ to $5\ gCOD_{substrate}\ gVS^{-1}_{inoculum}$. The remaining initial conditions set for this numerical study were the same used in the calibration phase.

The results related to $NS3$ are reported in Fig. 2.7. These confirmed that the increase of $F/M$ ratio favoured the biological process evolution. Nevertheless, when $F/M$ ratio greater than 4 (i.e. $S^0_{su}$ greater than $40\ gCOD\ L^{-1}$) were used, the process was inhibited by the pH level, and the glucose was not completely consumed by microorganisms. Thus, a residual concentration of glucose was observed, but the same amount of VFAs and hydrogen were produced. In the second reactor (day $8$), butyric acid was consumed (Fig. 2.7b), and contextually the concentration of metal in solution quickly increased (Fig. 2.7e). By increasing the initial glucose concentration $S^0_{su}$, the predicted concentration of butyric acid increased. Consequently, the dissolution rate was faster and the removal efficiency after $24$ hours increased (Fig. 2.7e - red rhombus). In accordance with the previous numerical study, $F/M$ ratios greater than $4$ did not lead to a beneficial effect on the leaching efficiency. The optimal $F/M$ ratio was again $4$ in terms of VFAs and hydrogen productions. In addition, using $40$ and $10\ gCOD\ L^{-1}$

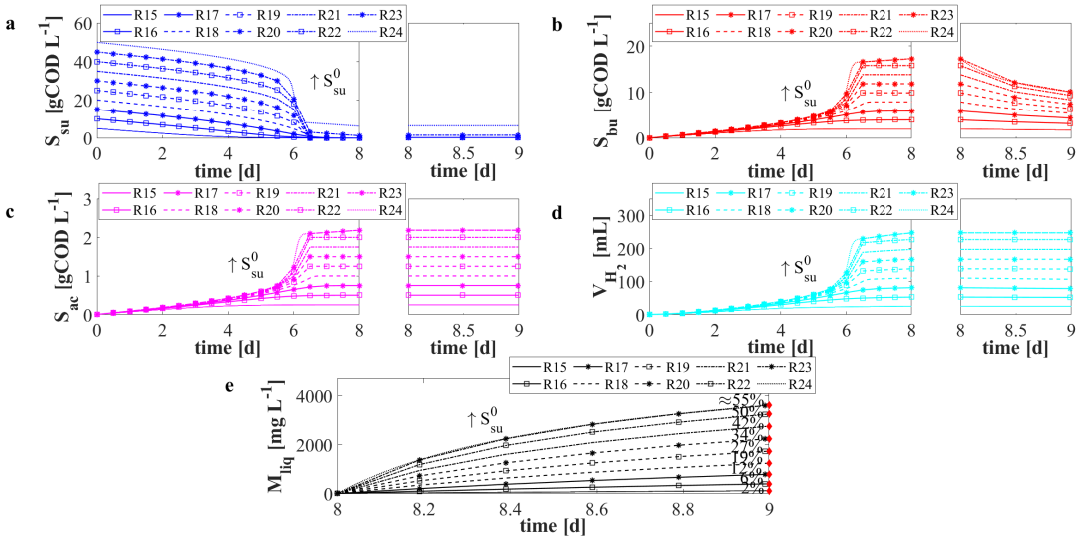


Figure 2.7: $NS3$ - Evolution over time of simulated values of glucose $S_{su}$ (a), butyric acid $S_{bu}$ (b), acetic acid $S_{ac}$ (c) concentrations, cumulative hydrogen production $V_{H_2}$ (d), and concentration of metal in solution $M_{liq}$ (e) for different initial concentration of sugar $S^0_{su}$. $R15$: $S^0_{su} = 5\ gCOD\ L^{-1}$; $R16$: $S^0_{su} = 10\ gCOD\ L^{-1}$; $R17$: $S^0_{su} = 15\ gCOD\ L^{-1}$; $R18$: $S^0_{su} = 20\ gCOD\ L^{-1}$; $R19$: $S^0_{su} = 25\ gCOD\ L^{-1}$; $R20$: $S^0_{su} = 30\ gCOD\ L^{-1}$; $R21$: $S^0_{su} = 35\ gCOD\ L^{-1}$; $R22$: $S^0_{su} = 40\ gCOD\ L^{-1}$; $R23$: $S^0_{su} = 45\ gCOD\ L^{-1}$; $R24$: $S^0_{su} = 50\ gCOD\ L^{-1}$. Initial concentration of sugar fermenters and metal concentration: $X^0_{su} = 10\ gCOD\ L^{-1}$ and $M = 6.5\ g\ L^{-1}$. Red rhombus represents the removal efficiency after $24$ hours.

of glucose and digestate, respectively, the leached metal concentration in the solution significantly increased, due to the increased butyric acid concentration produced in the first stage. The obtained removal efficiency was about $50\%$. This result is in accordance with experimental evidences in which the leaching process was catalyzed by organic acids [66, 45]. Nevertheless, other experimental works reported a leaching efficiency of about $90\%$ [44, 41]. This suggests that the leaching process strictly depends on the type of metal and organic acid investigated. However, the obtained removal efficiency is relatively low if compared with data related to processes performed with inorganic acids used as leaching agents [47, 80].

### 2.5.3 NS4 - Effects of metal concentration on leaching process

Many experimental works focused on metals recovery efficiency using different ratios between concentrations of metals and organic acids [41, 49]. To identify the optimum leaching conditions, the numerical study $NS4$ was performed. Six numerical simulations were carried out with different concentrations of solid metal $M$ (10, 6.5, 3, 1, 0.5, and 0.1 $g\ L^{-1}$). The optimal initial concentrations of glucose and sugar fermenters were used: $S^0_{su} = 40\ gCOD\ L^{-1}$ and $X^0_{su} = 10\ gCOD\ L^{-1}$. Consequently, the value of $F/M$ ratio used in the numerical simulations was set to $4\ gCOD_{substrate}\ gVS^{-1}_{inoculum}$. The remaining initial conditions set for this numerical study were the same used in the calibration phase.

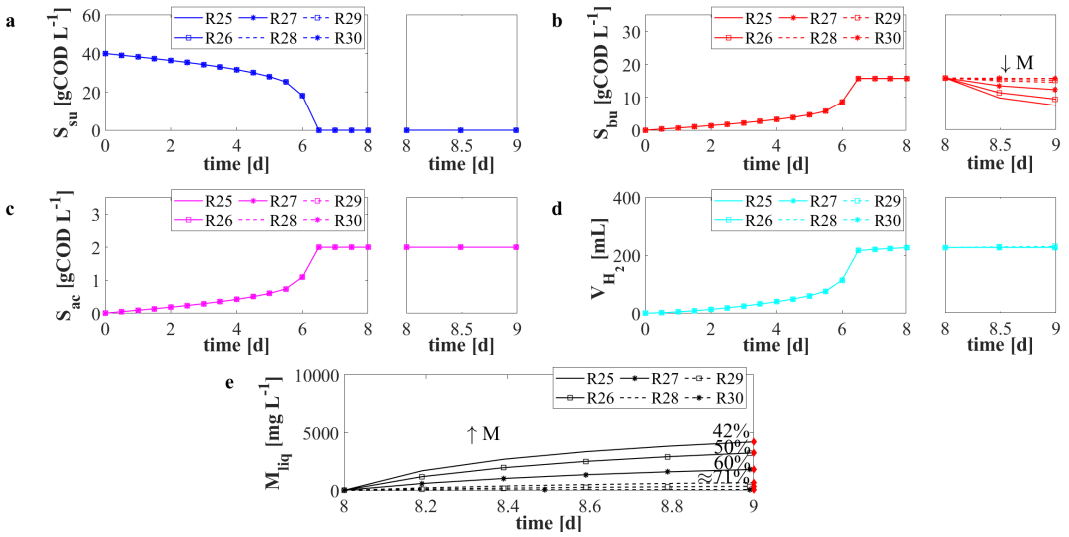


Figure 2.8: $NS4$ - Evolution over time of simulated values of glucose $S_{su}$ (a), butyric acid $S_{bu}$ (b), acetic acid $S_{ac}$ (c) concentrations, cumulative hydrogen production $V_{H_2}$ (d), and concentration of metal in solution $M_{liq}$ (e) for different concentration of metal $M(t_W)$. $R25$: $M = 10\ g\ L^{-1}$; $R26$: $M = 6.5\ g\ L^{-1}$; $R27$: $M = 3\ g\ L^{-1}$; $R28$: $M = 1\ g\ L^{-1}$; $R29$: $M = 0.5\ g\ L^{-1}$; $R30$: $M = 0.1\ g\ L^{-1}$. Initial concentration of sugar and sugar fermenters: $S^0_{su} = 40\ gCOD\ L^{-1}$ and $X^0_{su} = 10\ gCOD\ L^{-1}$. Red rhombus represents the removal efficiency after 24 hours.

$NS4$ results are shown in Fig. 2.8. In the DF phase, all simulations gave the same results in terms of glucose, VFAs and hydrogen, since a common initial condition related to the biological process was used. Once the E-waste was added to the DF effluent,

different butyric acid trends (Fig. 2.8b) were observed. Increasing the amount of the waste, its consumption was faster and its residual concentration at $t = 9\ d$ was lower than those obtained in all the other cases. The trend of the dissolved metal is reported in Fig. 2.8e. Similarly, when the metal concentration in solid form increased, the metal dissolution was faster, but the leaching efficiency at $24$ hours (Fig. 2.8e - red rhombus) decreased. The numerical results showed that the leaching efficiency decreases when an increasing metal concentration and a fixed acid amount are considered. This confirmed the experimental evidences achieved in the case of organic and inorganic acids [44, 46]. Obviously, this result suggests that the leaching process is even more rapid, although less efficient, when a higher amount of the waste is added. This leads to conclude that the butyric acid is not a limiting factor, and a longer time is required to leach a greater amount of E-waste.

## 2.6 Conclusions

A mathematical model able to account for the biological conversion and physico-chemical phenomena involved in the DF and the leaching processes has been presented. The model was successfully calibrated with ad-hoc DF experiments carried out using a synthetic solution of glucose, digestate and spent button batteries. Further numerical studies were presented to investigate the optimal conditions to favour the biological conversion of glucose and the leaching process. Specifically, the inhibition of the DF process due to the metal concentration, the effect of the $F/M$ ratio, and the removal efficiency of the leaching process were investigated by using the model as an experimental tool for the development of the processes in different conditions. In conclusions, the model gave valuable information in terms of: the organic acid concentration required for the leaching process, the amount of leached metal, and the time required for the dissolution process with respect to the amount of E-waste treated in the reactor. Some significant aspects should be further investigated. Specific experimental studies focused

on the leaching process of specific metals or metals mixtures in anaerobic environments, and on the effect of leaching by-products on the DF process are still required. The proposed mathematical model could be further improved with additional physico-chemical processes, involving the chemical compounds contained in the E-waste. Indeed, different leaching reactions of other metals contained in the E-waste can be further included. However, the metal recovery efficiency and the residence time can be optimized to study the sustainability of the integrated DF-leaching process at a larger scale.

## 2.7 Appendix A

The experimental campaigns were carried out using serum bottles with a volume of $120\ mL$ for DF-leaching experiments. The reactors were immersed in a thermostatic bath at $35^{\circ}$C$\pm 1^{\circ}$C to ensure mesophilic conditions. The microbial inoculum was obtained from an anaerobic digestion real-scale plant operating the bioconversion of buffalo manure to biogas. The anaerobic digestate was characterized in terms of Total Solids (TS) and Volatile Solids (VS) to estimate their organic content before to start the experiments according to Standard Methods [81]. In particular, the volatile solids (VS) content of the digestate was $70,67\ gCOD\ L^{-1}$. The inoculum was thermally pretreated for $1\ h$ at $105^{\circ}$C to ensure methanogenic microorganisms inhibition [50]. The working volume of the serum bottles was set to $70\ mL$ and was constituted by:

- $5\ mL$ of thermally pretreated inoculum;
- $60\ mL$ of distilled water;
- $5\ mL$ of glucose solution ($141,34\ gCOD\ L^{-1}$);
- $1\ g$ of waste extracted from spent batteries.

The Food/Microorganisms ratio was close to $2\ gCOD_{substrate}\ gVS^{-1}_{inoculum}$ to inhibit metabolic activities of hydrogen consumers and to ensure DF process evolution[50].

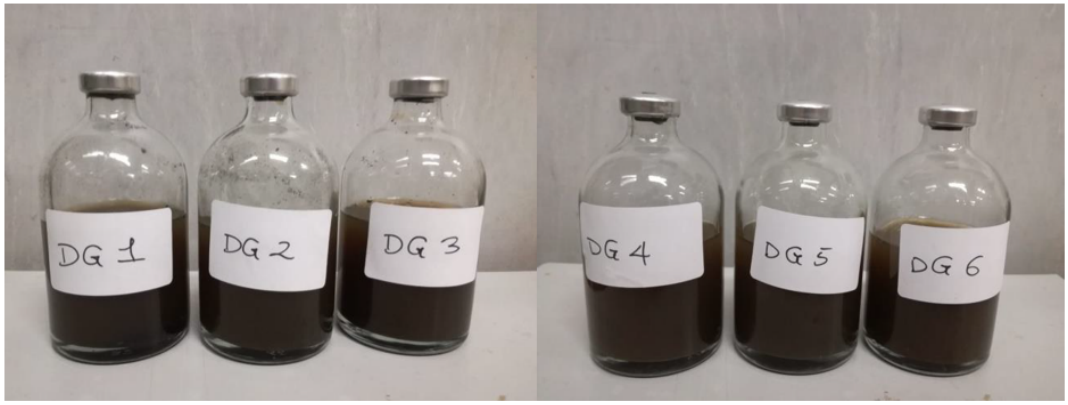


Figure 2.9: Experimental campaigns bioreactors.

Spent button lithium-ion batteries (LIBs) were used as E-waste to investigate the leaching process of metals. LIBs are a common E-waste as they are extensively employed in many anthropic activities due to their superior performance, such as high working voltage, high energy density, small size, low self-discharge rate, and long life-cycle [38]. LIBs contain high concentrations of lithium (Li), cobalt (Co), nickel (Ni), manganese (Mn) and aluminum (Al) [38, 39, 82]. In particular, spent button batteries were chosen for the experimental campaign as the internal part is already in powder form, no crushing process is required, and they can be manually disassembled to separate the plastic elements and metallic shells. According to Russo et al. (2022) [67], the overall content of metals in the tested E-waste was evaluated. The internal part of batteries was mineralized with an aqua-regia solution in a START-D microwave oven (Milestone, USA). Mineralized samples were opportunely diluted, filtered at $0.45\ \mu m$ through cellulose acetate filter and finally analyzed through ICP-MS (PerkinElmer Nexion 350, USA) operating in dual detector mode. Due to its high concentration, Mn content was evaluated through atomic adsorption spectrometry (AAS) using a Varian Model 55B SpectrAA (F-AAS). The internal part of batteries was mainly composed by: Manganese $(45.0\%)$, Lithium $(9.45\%)$, Silicon $(0.18\%)$, Iron $(0.11\%)$, Sodium $(0.13\%)$, Calcium $(0.05\%)$, Magnesium $(0.04\%)$, Potassium $(0.03\%)$, Nickel $(0.01\%)$, Aluminium $(0.01\%)$ and Chromium $(0.01\%)$. The bioreactors were hermetically closed

by using specific metal/rubber caps to ensure sampling procedures and anaerobic conditions. Different experimental tests were carried out (Fig. 2.9), using the same amount of waste and changing the E-waste addition time: i) by adding the waste at the beginning of the biological process, and ii) with waste addition at the end of the hydrogen production phase.

During the experiments, liquid and gas samples were taken every day from each bioreactor. The extracted liquid and gas samples were characterized in terms of metals, glucose and organic acids concentrations and hydrogen production. Manganese concentration in the liquid phase was evaluated. The manganese concentration was quantified through atomic adsorption spectrometry (AAS) using a Varian Model 55B SpectrAA (F-AAS). The glucose and OAs concentrations were evaluated by high-pressure liquid chromatography (HPLC), using an LC 25 Chromatography Oven (Dionex, Sunnyvale, CA, USA) equipped with an Organic Acids column (Metrohom, Herisau, Switzerland) and a 340U UV detector (Dionex, Sunnyvale, USA). Temperature and pH were measured with analytic probes.

The daily hydrogen production was measured using a volumetric method. For gas sampling, the bioreactors were connected with a gas measurement system. The gas was forced to pass into a bottle filled with $HCl$ solution to trap the produced carbon dioxide before hydrogen evaluation. This procedure allowed for the determination of the produced hydrogen volume. Biogas composition was characterized by gas chromatographic analysis conducted using a Varian Star 3400 gas chromatograph equipped with a ShinCarbon ST 80/100 column and a thermal conductivity detector. Argon as used as gas carrier for gaseous samples.

# Chapter 3

# Multiscale modelling of *de novo* anaerobic granulation

## 3.1 Introduction

Biofilms are complex, dense and compact aggregates comprising microbial cells immobilized in a self-produced matrix of extracellular polymeric substances (EPS) [5]. Many species from several trophic groups may coexist in such structures, where they interact through synergistic and antagonistic activities. Although natural biofilms typically develop as planar layers attached to suitable surfaces, under specific conditions the aggregation occurs due to the self-immobilization of cells into approximately spherical-shaped granules [10]. The process leading to the formation of these aggregates is known as granulation. In particular, the term *de novo* granulation is used when the process is initiated by individual microbial cells and flocs, as opposed to when granulation proceeds from inocula already in a granular form.

This Chapter has been published as: Tenore, A.,Russo, F., Mattei, M.R., D'Acunto, B., Collins, G., Frunzo, L. Multiscale modelling of de novo anaerobic granulation. Bulletin of Mathematical Biology 83, 122 (2021).

In recent years, granular bioreactor systems have become increasingly popular in the field of sustainable, and high-rate, wastewater treatment. Compared to suspended biomass systems, the denser, stronger and more regular structure of the biofilm granules underpins better settling properties [12, 13] allowing for higher concentrations of biomass [14] and reduced bioreactor footprints [12]. Furthermore, and in contrast to other biofilm systems in which the biofilms develop on solid supports, granular systems are based on spherical, and constantly moving, microbial aggregates. The movement and shape mitigate boundary layer resistances, and enhance the mass transfer of substrates across the biofilm granule [14]. For these reasons, granular biofilms have been successfully developed in different bioreactor configurations, for various processes, such as aerobic, anaerobic and partial nitritation-anammox treatments [83].

The main drawback of granular-based systems is represented by the start-up phase, due to the complexity of the mechanisms and phenomena which contribute to the success of the granulation process [84]. Many studies have explored the granulation process and numerous theories have been proposed. Hydrodynamic conditions generated by liquid up-flow velocity, gas production, particle-particle collision, mixing systems and bioreactor geometry are universally recognized as key factors in the granulation process as well as throughout the entire life cycle of the granules [12, 83, 85]. Indeed, suitable hydrodynamic conditions are required to initiate the granulation process by promoting, and improving, the aggregation of planktonic biomass [86]. Moreover, intense hydrodynamic conditions induce high shear forces on the granule surface, influencing size, shape, structure and density of the granules [12, 87], and regulate a continuous process of aggregation and breaking that leads to the formation of an increasing number of granules. High shear forces are thought to stimulate the production of EPS, which represents a further beneficial factor for granulation as it increases cell surface hydrophobicity [83]. Several studies also consider the granulation process to be the result of an organised process driven by pioneering microbial species with specific, key characteristics [88, 89].

Pol et al. (2004) [88] collated various theories concerning anaerobic sludge granulation, the most widespread of which asserts that the process is favoured by key microorganisms, such as *Methanosaeta* [83, 88, 90, 91]. Such acetoclastic methanogens have filamentous structures and good adhering properties, and initiate the granulation process by forming a central nucleus supporting the immobilisation of other methanogens and synergistically functioning bacterial groups [92, 93]. In this context, various studies [84, 94, 95] report that quorum sensing plays an essential role by regulating the transition of some *Methanosaeta* species from short to long, filamentous cells. In the initial phase, the nucleus presents a filamentous appearance and achieves a spherical shape due to the rolling effect of the hydraulic shear forces [83, 88]. In a second phase, the nucleus develops into a granule, and acetogens and acidogens attach on its surface to grow syntrophically with acetoclastic methanogens [83, 88, 92, 96]. The result is a concentrically-layered structure with an archaeal core constituted by *Methanosaeta*. This theory is supported by experimental evidence showing layered structures in anaerobic granules [97, 26, 98]. Nonetheless, the granulation process is still not fully understood and further studies are required to assist in optimising the efficiencies of this process.

In this framework, mathematical modelling represents a valuable tool to describe, explore and study the granulation process, the life cycle of the biofilm granules and the performances of granular-based bioreactor systems. The relevance of those topics in environmental engineering and biotechnology has stimulated interest in modelling of granular biofilm systems. Indeed, numerous models have been proposed to mainly describe aerobic [25], anaerobic [26, 28, 27, 99] and anammox [30, 31, 29] processes involved in such systems. An initial classification may be introduced according to the approach used: continuum models simulate the evolution of the granular biofilm in a quantitative and deterministic way, while discrete models, such as individual-based [99, 100, 101] and cellular automata models [102], can represent the multidimensional structural heterogeneity of granular biofilms but provide results including elements of

randomness and introduce stochastic effects into the solutions [103]. Most models of granular biofilms [26, 28, 27, 30, 31] are based on the continuum approach introduced by Wanner and Gujer (1986) [22] for one-dimensional planar biofilms, and model the granule as a spherical, free boundary domain evolved as a result of the prevailing microbial metabolic processes and mass exchange with the surrounding environment. Among these, most describe the dynamic evolution of the granule fixing the final steady-state size [26, 27, 30, 31].

In any case, several significant aspects of granular biofilm growth are not exhaustively considered by existing models. According to Baeten et al. (2019) [14], only two models [26, 104] consider the attachment process, which plays a key role in the formation and evolution of granular biofilms. None takes into account the invasion process i.e. the colonization of a pre-existing biofilm mediated by motile planktonic cells living in the surrounding environment, which can penetrate the porous matrix of the biofilm and convert to sessile biomass. Moreover, all continuum models fix a non-zero initial size of the domain and this requires the composition of the initial domain to be arbitrarily fixed. Finally, according to the exclusion principle presented in Klapper and Szomolay (2011) [105], all biofilm models based on the approach introduced in Wanner and Gujer (1986) [22] lead to restrictions on ecological structure.

Most studies have focused on system performance by describing the biofilm-mediated removal of soluble substrates from wastewater. Some focus on the biofilm granule, paying attention to the dimensional evolution [28] and to the distribution of sessile biomass within the biofilm at the steady-state [28, 27, 30, 31, 29]. However, no continuous model fully describes the *de novo* granulation process by considering the initial formation and ecology of the biofilm granule. Only the individual-based model introduced by Doloman et al. (2017) [99] focuses on the *de novo* formation of anaerobic granules based on a discrete approach.

In this Chapter, a multiscale model to describe the *de novo* granulation process, and which incorporates the mesoscopic, granular biofilm processes within a continuously-

fed, granular-based bioreactor is proposed. For this purpose, and following the approach proposed by Masic and Eberl (2012, 2014) [106, 107] in the case of one-dimensional planar biofilms, the model couples macroscopic bioreactor mass balances with a mesoscopic granular biofilm model here derived by using a continuum approach [22]. The model accounts for the growth of both granular attached and planktonic biomass, and includes the main microbial exchange processes involved, including attachment, detachment and invasion. The *de novo* granulation process is modelled by assuming that all biomass initially present in the bioreactor is in planktonic form. Mathematically, this corresponds to consider a vanishing initial value of the granule radius representing the free boundary under the assumption of radial symmetry. Biofilm formation is initiated by the attachment process, which leads to consider a space-like free boundary. This mathematical problem has been discussed in D'Acunto et al. (2019) [24] and is applied here for the first time to model the genesis of granular biofilms. Granule formation and expansion are governed by the following processes: microbial growth, attachment, invasion and detachment. Attachment initiates the life of biofilms and is regarded as the complex phenomenon whereby pioneering microbial cells in planktonic form attach to a surface and develop in the form of a sessile aggregate [6]. However, as reported above, the formation of a biofilm granule is the result of the interaction and aggregation of microbial cells and flocs without the involvement of a surface. Therefore, attachment is viewed as the flux of microbial mass that aggregates, switches its phenotype from planktonic to sessile, and initiates the granulation. It is modelled as a linear function of the concentrations of the planktonic species, each of which is characterized by a specific attachment velocity. The invasion process is included for the first time in the modelling of granular biofilms by extending the mathematical formulation proposed in D'Acunto et al. (2015) [23] for one-dimensional planar biofilms to a spherical domain. This allows removal of the restrictions on ecological structure highlighted by Klapper and Szomolay (2011) [105]. Furthermore, the bulk liquid is modelled as a perfectly mixed medium in which soluble substrates and planktonic biomass are found,

and which is influenced by the operational parameters of the bioreactor, the microbial metabolic activities, and the processes of mass exchange with the biofilm. The mathematical model has been derived for a generic, granular-based bioreactor and applied to the anaerobic granulation process to test the model's behaviour and study the genesis, evolution and ecology of anaerobic granules. Various numerical studies have investigated how the granulation properties of planktonic biomass, the biomass density of the granules, the detachment intensity, the number of granules and the composition of the influent wastewater may affect the evolution of the process. The results include the dimensional evolution and ecology of the granule (in terms of biomass distribution and relative abundance), the distribution of soluble substrates within the granule, and the time variation of soluble substrates and planktonic biomass within the bioreactor.

The paper is organised as follows: in Section 3.2, the derivation of the model is carried out by presenting all assumptions, variables, equations, and initial and boundary conditions; Section 3.3 then describes the biological case to which the model is applied. Numerical studies are reported, and discussed in detail, in Sections 3.4 and 3.5, respectively. Finally, the conclusions of the work, and future goals, are outlined in Section 3.6.

## 3.2 Mathematical Model

In this Chapter, the granular biofilm reactor is modelled as a completely mixed, continuously-fed system in which $N_G$ identical biofilm granules are immersed. As shown in Fig. 3.1, two different scales are considered in the model: the bioreactor macroscale and the granule mesoscale. Three components are considered within the granular biofilm: the sessile biomass, which constitutes the solid matrix; the planktonic biomass, which is found in the channels and voids; and the soluble substrates dissolved in the liquid phase. Meanwhile, planktonic biomass and soluble substrates are considered within the bulk liquid of the reactor. These components interact with, and influence, each other

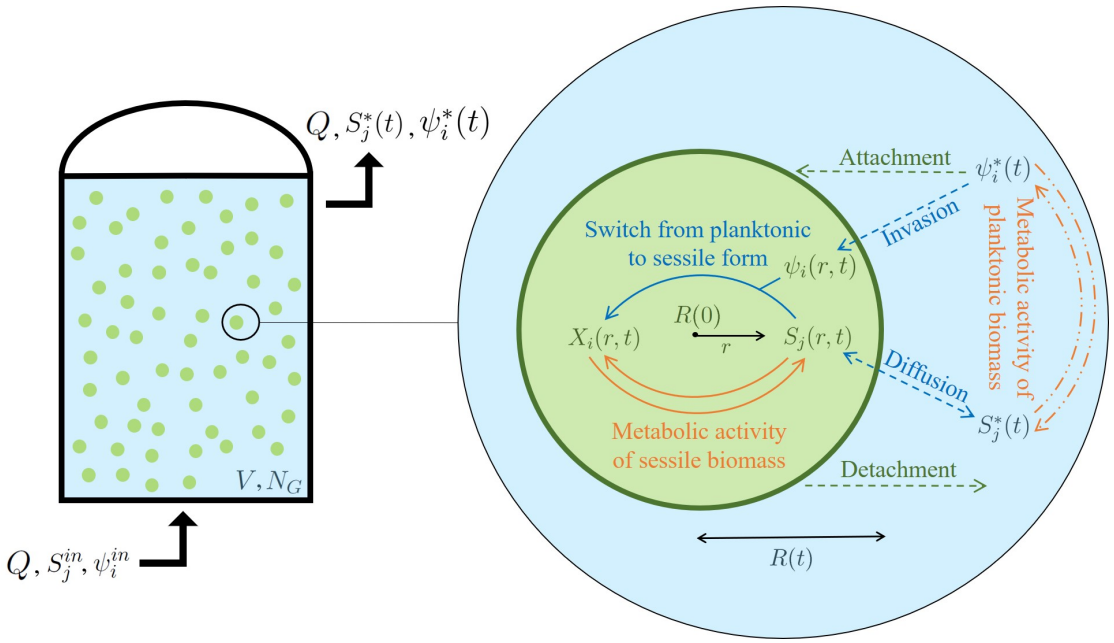


Figure 3.1: Multiscale representation of the model. The bioreactor is modelled as a perfectly mixed continuous system (on the left), having volume $V$, where $N_G$ biofilm granules are immersed. A focus on a single granule is presented on the right, with all processes considered in the model. The granule has a zero initial radius $R(0)$, which varies over time due to the effect of various biological processes. Metabolic processes within the granule are carried out by the sessile biomass $X_i(r,t)$, which grows by converting the substrates dissolved in the biofilm liquid $S_j(r,t)$, while metabolic processes within the bulk liquid are carried out by the planktonic biomasses $\psi_i^*(t)$, which grows by converting the substrates dissolved in the bulk liquid $S_j^*(t)$. The superficial exchange processes of attachment and detachment are considered at the interface granule-bulk liquid. Moreover, invasion processes are modelled: the planktonic biomass $\psi_i(r,t)$ invades the solid matrix of the granule and switches its phenotype from planktonic to sessile. Finally, process of diffusion of substrates across the granule is included in the model. Solid arrows: processes within the granule. Dash-dot arrows: processes within the bulk liquid. Dash arrows: exchange processes between granule and bulk liquid.

as a result of biological, physical and chemical processes. Modelling of both the granule and bioreactor scales is discussed, introducing each of the processes, assumptions, variables, equations, and initial and boundary conditions involved.

### 3.2.1 Modelling granule scale

Under the assumption of radial symmetry, the biofilm granule is modelled as a spherical, free boundary domain whose spatial evolution is completely described by the evo-

lution of the radius $R(t)$. A vanishing initial value $R(0) = 0$ is considered to model the initial granulation. All variables involved in the biofilm modelling are considered as functions of time $t$ and space $r$, where $r$ denotes the radial coordinate. Consequently, the granule centre is located at $r = 0$.

The model takes into account the dynamics of three components, expressed in terms of concentration: $n$ microbial species in sessile form $X_i(r,t)$; $n$ microbial species in planktonic form $\psi_i(r,t)$; $m$ dissolved substrates $S_j(r,t)$.

The volume occupied by planktonic cells is considered negligible due to the small particle size. The density of the granule $\rho$ is assumed to be constant and equal for all microbial species. By dividing sessile species concentration $X_i$ by $\rho$, biomass volume fractions $f_i(r,t)$ are achieved. $f_i$ are constrained to add up to unity [108]. In summary, the model components describing the granular biofilm compartment are:

$$X_i,\ i = 1, ..., n,\ \mathbf{X} = (X_1, ..., X_n), \tag{3.1}$$

$$f_i = \frac{X_i}{\rho},\ i = 1, ..., n,\ \mathbf{f} = (f_1, ..., f_n), \tag{3.2}$$

$$\psi_i,\ i = 1, ..., n,\ \boldsymbol{\psi} = (\psi_1, ..., \psi_n), \tag{3.3}$$

$$S_j,\ j = 1, ..., m,\ \mathbf{S} = (S_1, ..., S_m). \tag{3.4}$$

Based on the continuum approach introduced in Wanner and Gujer (1986) [22] for one-dimensional planar biofilms, a system of partial differential equations (PDEs) in a spherical, free boundary domain is derived from mass balance considerations, under the assumption of radial symmetry. Hyperbolic PDEs model the distribution and growth of sessile biomass $f_i(r,t)$ and parabolic PDEs describe the diffusion and conversion of soluble substrates $S_j(r,t)$. Further parabolic PDEs govern the process of invasion and

conversion of planktonic cells $\psi_i(r,t)$.

Based on the aggregation properties of the planktonic biomass living in the bulk liquid, attachment phenomena govern the initial granulation process, while further biofilm evolution is significantly affected by detachment phenomena. Attachment and detachment contribute to the microbial mass exchange occurring between granules and bulk liquid, and are included in the model as continuous and deterministic processes. Finally, as introduced by D'Acunto et al. (2015) [23], in the case of one-dimensional planar biofilm, the invasion process is considered to describe the phenomena of granule colonization by planktonic cells. Such cells penetrate the porous matrix of the biofilm from the surrounding medium and contribute to the development of the biofilm.

Under the assumption of radial symmetry, the mass balance set up for a generic component in a differential volume of the spherical domain, leads to the following equation:

$$\frac{\partial c(r,t)}{\partial t} + \frac{1}{r^2}\frac{\partial}{\partial r}(r^2 J_r(r,t)) = r_c(r,t), \tag{3.5}$$

where $c(r,t)$ is the concentration of a generic component in the spherical domain, $J_r$ is the advective and/or diffusive flux in the radial direction and $r_c(r,t)$ is the transformation term.

The transport of sessile biomass is modelled as an advective process. Hence, by expressing the advective flux of the $i^{th}$ sessile microbial species in the radial direction as:

$$J_{r,i}(r,t) = u(r,t)X_i(r,t), \tag{3.6}$$

where $u(r,t)$ is the biomass velocity, Eq.(3.5) takes the following form:

$$\frac{\partial X_i(r,t)}{\partial t} + \frac{1}{r^2}\frac{\partial}{\partial r}(r^2 u(r,t)X_i(r,t)) = \rho r_{M,i}(r,t,\mathbf{X},\mathbf{S}) + \rho r_i(r,t,\boldsymbol{\psi},\mathbf{S}),$$

$$i = 1, ..., n, 0 \leq r \leq R(t),\ t > 0, \tag{3.7}$$

where $r_{M,i}(r, t, \mathbf{X}, \mathbf{S})$ and $r_i(r, t, \boldsymbol{\psi}, \mathbf{S})$ are the specific growth rates due to sessile and planktonic species, respectively.

By dividing Eq.(3.7) by $\rho$ and by considering that $f_i = \frac{X_i}{\rho}$ yields

$$\frac{\partial f_i(r,t)}{\partial t} + \frac{1}{r^2}\frac{\partial}{\partial r}(r^2 u(r,t) f_i(r,t)) = r_{M,i}(r, t, \mathbf{f}, \mathbf{S}) + r_i(r, t, \boldsymbol{\psi}, \mathbf{S}),$$

$$i = 1, ..., n, 0 \leq r \leq R(t),\ t > 0, \tag{3.8}$$

$$\frac{\partial f_i(r,t)}{\partial t} + f_i(r,t)\frac{\partial u(r,t)}{\partial r} + \frac{2u(r,t)f_i(r,t)}{r} + u(r,t)\frac{\partial f_i(r,t)}{\partial r} = r_{M,i}(r, t, \mathbf{f}, \mathbf{S}) +$$

$$+ r_i(r, t, \boldsymbol{\psi}, \mathbf{S}),\ i = 1, ..., n, 0 \leq r \leq R(t),\ t > 0. \tag{3.9}$$

Summing Eq.(3.9) over all sessile microbial species $i$ and considering that $\sum_{i=1}^{n} f_i = 1$, it follows:

$$\frac{\partial u(r,t)}{\partial r} = -\frac{2u(r,t)}{r} + G(r, t, \mathbf{f}, \mathbf{S}, \boldsymbol{\psi}, 0 < r \leq R(t),\ t > 0, \tag{3.10}$$

where $G(r, t, \mathbf{f}, \mathbf{S}, \boldsymbol{\psi}) = \sum_{i=1}^{n}(r_{M,i}(r, t, \mathbf{f}, \mathbf{S}) + r_i(r, t, \boldsymbol{\psi}, \mathbf{S}))$. This differential equation governs the evolution of the biomass velocity $u(r, t)$.

By imposing the flux of the $i^{th}$ sessile microbial species equal to $0$ at $r = 0$, it follows from Eq.(3.6) that $u(0, t) = 0$. Considering this result and integrating Eq.(3.10), the integral expression of $u(r, t)$ is achieved:

$$u(r,t) = \frac{1}{r^2}\int_0^r r'^2 G(r', t, \mathbf{f}, \mathbf{S}, \boldsymbol{\psi})dr', 0 < r \leq R(t),\ t > 0. \tag{3.11}$$

Substituting Eq.(3.10) into Eq.(3.9) yields

$$\frac{\partial f_i(r,t)}{\partial t} + u(r,t)\frac{\partial f_i(r,t)}{\partial r} = r_{M,i}(r,t,\mathbf{f},\mathbf{S}) + r_i(r,t,\boldsymbol{\psi},\mathbf{S}) - f_i(r,t)G(r,t,\mathbf{f},\mathbf{S},\boldsymbol{\psi}),$$

$$i = 1,...,n, 0 \leq r \leq R(t),\ t > 0. \tag{3.12}$$

Eq.(3.12) describes the transport and growth of the sessile microbial species $i$ across the granular biofilm under the assumption of radial symmetry.

Compared to the equation reported in Wanner and Gujer (1986) [22] for a planar biofilm, Eq.(3.12) presents a different expression of $u(r,t)$ and the additional reaction term $r_i(r,t,\boldsymbol{\psi},\mathbf{S})$ due to the invasion phenomenon.

Eq.(3.5) can be applied to soluble substrates and planktonic species. In these cases, the transport of planktonic biomass and soluble substrates is modelled as a diffusive flux and expressed as

$$J_{r,\psi_i}(r,t) = -D_{\psi,i}\frac{\partial \psi_i(r,t)}{\partial r}, \tag{3.13}$$

and

$$J_{r,j}(r,t) = -D_{S,j}\frac{\partial S_j(r,t)}{\partial r}, \tag{3.14}$$

where $D_{\psi,i}$ and $D_{S,j}$ denote the diffusivity coefficient of the planktonic species $i$ and the soluble substrate $j$ in the biofilm, respectively.

Then, parabolic diffusion-reaction PDEs are derived from Eq.(3.5):

$$\frac{\partial \psi_i(r,t)}{\partial t} - D_{\psi,i}\frac{\partial^2 \psi_i(r,t)}{\partial r^2} - \frac{2D_{\psi,i}}{r}\frac{\partial \psi_i(r,t)}{\partial r} = r_{\psi,i}(r,t,\boldsymbol{\psi},\mathbf{S}),$$

$$i = 1, ..., n, 0 < r < R(t),\ t > 0, \tag{3.15}$$

$$\frac{\partial S_j(r,t)}{\partial t} - D_{S,j}\frac{\partial^2 S_j(r,t)}{\partial r^2} - \frac{2D_{S,j}}{r}\frac{\partial S_j(r,t)}{\partial r} = r_{S,j}(r,t,\mathbf{f},\mathbf{S}),$$

$$j = 1, ..., m, 0 < r < R(t),\ t > 0, \tag{3.16}$$

where $r_{\psi,i}(r,t,\boldsymbol{\psi},\mathbf{S})$ is the conversion rate of planktonic species $i$ and $r_{S,j}(r,t,\mathbf{f},\mathbf{S})$ is the conversion rate of soluble substrate $j$.

The free boundary evolution is described by the variation of the radius $R(t)$ over time. This is affected by microbial growth and processes of attachment and detachment occurring at the surface of the biofilm. In particular, as proposed by Wanner and Reichert (1996) [109], the attachment flux of the $i^{th}$ planktonic species is formulated as a function linearly dependent on the concentration of the planktonic species $i$ in the bulk liquid $\psi_i^*(t)$ and is expressed as:

$$\sigma_{a,i}(t) = \frac{v_{a,i}\psi_i^*(t)}{\rho},\ i = 1, ..., n, \tag{3.17}$$

where $v_{a,i}$ is the attachment velocity of the planktonic species $i$.

By summing Eq.(3.17) over all planktonic species, the total attachment flux is achieved:

$$\sigma_a(t) = \frac{\sum_{i=1}^{n} v_{a,i}\psi_i^*(t)}{\rho}. \tag{3.18}$$

The detachment is modelled as a quadratic function of the granule radius $R(t)$ [110]:

$$\sigma_d(t) = \lambda R^2(t), \tag{3.19}$$

where $\lambda$ is the detachment coefficient and is supposed to be equal for all microbial species.

The global mass balance on the spherical domain gives:

$$\frac{\partial}{\partial t}\int_0^{R(t)} 4\pi r^2 \rho dr = \rho A(t)(\sigma_a(t) - \sigma_d(t)) + \int_0^{R(t)} 4\pi r^2 \rho G(r, t, \mathbf{f}, \mathbf{S}, \boldsymbol{\psi}) dr, \quad (3.20)$$

where $A(t)$ is the area of the spherical granule and is equal to $4\pi R^2(t)$.

By dividing Eq.(3.20) by $4\pi\rho$ and by considering $u(R(t), r)$ from Eq.(3.11), it follows:

$$\frac{\partial}{\partial t}\int_0^{R(t)} r^2 dr = R^2(t)(\sigma_a(t) - \sigma_d(t)) + \int_0^{R(t)} r^2 G(r, t, \mathbf{f}, \mathbf{S}, \boldsymbol{\psi}) dr, \quad (3.21)$$

$$\frac{1}{3}\frac{\partial R^3(t)}{\partial t} = R^2(t)(\sigma_a(t) - \sigma_d(t)) + R^2(t)u(R(t), t), \quad (3.22)$$

$$\dot{R}(t) = \sigma_a(t) - \sigma_d(t) + u(R(t), t). \quad (3.23)$$

The latter equation governs the time evolution of the free boundary domain.

The total mass of the sessile community and the mass of the $i^{th}$ sessile microbial species within the granule can be calculated as follows:

$$m_i(t) = \int_0^{R(t)} 4\pi r^2 \rho f_i(r, t) dr, \; i = 1, ..., n, \quad (3.24)$$

$$m_{tot}(t) = \sum_{i=1}^{n} m_i(t) = \frac{4}{3}\pi\rho R^3(t). \quad (3.25)$$

### 3.2.2 Modelling reactor scale

As already mentioned, the reactor is modelled as a completely mixed continuous system. Thus, all the quantities referring to the bulk liquid dynamics are equal at every

point and are dependent on time. The variables considered in the bulk liquid are $n$ planktonic biomasses and $m$ soluble substrates, both expressed in terms of concentration ($\psi_i^*(t)$ and $S_j^*(t)$, respectively). Such concentrations vary over time due to biological processes, operational parameters of the reactor and mesoscopic granule processes. In summary, the model components, which describe the bulk liquid compartment, are:

$$\psi_i^*,\ i = 1, ..., n,\ \boldsymbol{\psi}^* = (\psi_1^*, ..., \psi_n^*), \tag{3.26}$$

$$S_j^*,\ j = 1, ..., m,\ \mathbf{S}^* = (S_1^*, ..., S_m^*). \tag{3.27}$$

Accordingly, a system of ordinary differential equations (ODEs) derived from mass balance considerations is considered to describe the dynamics of planktonic biomass and soluble substrates within the bulk liquid:

$$V\dot{\psi}_i^*(t) = Q(\psi_i^{in} - \psi_i^*(t)) - A(t)N_G D_{\psi,i}\frac{\partial \psi_i(R(t),t)}{\partial r} + r_{\psi,i}^*(t, \boldsymbol{\psi}^*, \mathbf{S}^*) +$$

$$-\sigma_{a,i}(t)\rho A(t)N_G,\ i = 1, ..., n\ \ t > 0, \tag{3.28}$$

$$V\dot{S}_j^*(t) = Q(S_j^{in} - S_j^*(t)) - A(t)N_G D_{S,j}\frac{\partial S_j(R(t),t)}{\partial r} + r_{S,j}^*(t, \boldsymbol{\psi}^*, \mathbf{S}^*),$$

$$j = 1, ..., m,\ \ t > 0. \tag{3.29}$$

where $V$ is the volume of the bulk liquid assumed equal to the reactor volume, $Q$ is the continuous flow rate, $\psi_i^{in}$ is the concentration of the planktonic species $i$ in the influent, $S_j^{in}$ is the concentration of the substrate $j$ in the influent, $r_{\psi,i}^*(t, \boldsymbol{\psi}^*, \mathbf{S}^*)$ and

$r^*_{S,j}(t, \boldsymbol{\psi}^*, \mathbf{S}^*)$ are the conversion rates for $\psi^*_i$ and $S^*_j$, respectively.

Eq.(3.28) represents the mass balance of the $i^{th}$ microbial species in planktonic form. In particular, the mass variation within the bioreactor (first member) is due to the continuous mass flow in and out of the bioreactor (first term of the second member), the exchange flux between the bulk liquid and the granular biofilms (second term of the second member), the growth and decay in the bulk liquid (third term of the second member), and the exchange flux related to attachment processes (fourth term of the second member).

Similarly, Eq.(3.29) represents the mass balance of the $j^{th}$ soluble substrate. In this case, the mass variation within the bioreactor (first member) is due to the continuous mass flow in and out of the bioreactor (first term of the second member), the exchange flux between the bulk liquid and the granular biofilms (second term of the second member) and the consumption, and/or production, occurring in the bulk liquid and mediated by the planktonic biomass (third term of second member).

### 3.2.3 Initial and boundary conditions

The processes involved in a granular biofilm reactor are described by Eqs.(3.10), (3.12), (3.15), (3.16), (3.23), (3.28) and (3.29). To integrate such equations, it is necessary to specify initial and boundary conditions.

As mentioned above, *de novo* granulation is modelled by considering an initial configuration whereby only planktonic biomass is supposed to be present in the reactor. Hence, a vanishing initial condition is coupled to Eq.(3.23), which describes the variation of the granule radius over time:

$$R(0) = 0. \tag{3.30}$$

The following initial conditions are considered for Eq.(3.28) and Eq.(3.29):

$$\psi_i^*(0) = \psi_{i,0}^*,\ i = 1, ..., n, \tag{3.31}$$

$$S_j^*(0) = S_{j,0}^*,\ j = 1, ..., m, \tag{3.32}$$

where $\psi_{i,0}^*$ and $S_{j,0}^*$ are the initial concentrations of the $i^{th}$ planktonic species and the $j^{th}$ soluble substrate within the bulk liquid, respectively.

Eqs.(3.10), (3.12), (3.15) and (3.16) refer to the biofilm domain and do not require initial conditions, since the extension of the biofilm domain is zero at $t = 0$.

The boundary condition for Eq.(3.12) at the interface granule-bulk liquid $r = R(t)$ depends on the sign of the mass flux at the interface. When the free boundary is a space-like line ($\sigma_a - \sigma_d > 0$), there is a mass flux from bulk liquid to biofilm, thus the boundary condition depends on the concentration of planktonic biomass in the bulk liquid:

$$f_i(R(t), t) = \frac{v_{a,i}\psi_i^*(t)}{\sum_{i=1}^{n} v_{a,i}\psi_i^*(t)},\ i = 1, ..., n,\ t > 0. \tag{3.33}$$

Meanwhile, when the free boundary is a time-like line ($\sigma_a - \sigma_d < 0$), the biomass concentration at the interface is regulated exclusively by the internal points of the biofilm domain and the condition (3.33) is not required.

For both parabolic systems (3.15) and (3.16), a no-flux condition is fixed at the granule centre $r = 0$, while boundary conditions at the interface biofilm-bulk liquid $r = R(t)$ are related to the solutions of Eq.(3.28) and Eq.(3.29), which represent the concentrations of planktonic species and soluble substrates within the bulk liquid:

$$\frac{\partial \psi_i}{\partial r}(0, t) = 0,\ \psi_i(R(t), t)) = \psi_i^*(t),\ i = 1, ..., n,\ t > 0, \tag{3.34}$$

$$\frac{\partial S_j}{\partial r}(0, t) = 0,\ S_j(R(t), t)) = S_j^*(t),\ j = 1, ..., m,\ t > 0. \tag{3.35}$$

Finally, as previously mentioned, the boundary condition for Eq.(3.10) is given by:

$$u(0,t) = 0,\ t > 0. \tag{3.36}$$

In conclusion, the model is based on Eqs.(3.10), (3.12), (3.15), (3.16), (3.23), (3.28), (3.29), and initial and boundary conditions Eqs.(3.30)-(3.36). All equations, and initial and boundary conditions are summarised in Table 3.1. The reaction terms of these equations depend on the specific biological case considered and describe the complex biological interplay taking place between sessile biomass $X_i(r,t)$, planktonic biomass $\psi_i(r,t)$ and soluble substrates $S_j(r,t)$ within the biofilm and planktonic biomass $\psi_i^*(t)$ and soluble substrates $S_j^*(t)$ within the bulk liquid.

| **Equations** | **Initial condition** | **Boundary condition** | |
|---|---|---|---|
| | $t=0$ | $r=0$ | $r=R(t)$ |
| $\frac{\partial f_i(r,t)}{\partial t}+u(r,t)\frac{\partial f_i(r,t)}{\partial r}=r_{M,i}(r,t,\mathbf{f},\mathbf{S})+r_i(r,t,\boldsymbol{\psi},\mathbf{S})-f_i(r,t)G(r,t,\mathbf{f},\mathbf{S},\boldsymbol{\psi}))$ | | | $f_i(R(t),t)=\frac{v_{a,i}\psi_i^*(t)}{\sum_{i=1}^n v_{a,i}\psi_i^*(t)}$ for $\sigma_a>\sigma_d$ |
| $\frac{\partial \psi_i(r,t)}{\partial t}-D_{\psi,i}\frac{\partial^2\psi_i(r,t)}{\partial r^2}-\frac{2D_{\psi,i}}{r}\frac{\partial\psi_i(r,t)}{\partial r}=r_{\psi,i}(r,t,\boldsymbol{\psi},\mathbf{S})$ | | $\frac{\partial\psi_i}{\partial r}(0,t)=0$ | $\psi_i(R(t),t))=\psi_i^*(t)$ |
| $\frac{\partial S_j(r,t)}{\partial t}-D_{S,j}\frac{\partial^2 S_j(r,t)}{\partial r^2}-\frac{2D_{S,j}}{r}\frac{\partial S_j(r,t)}{\partial r}=r_{S,j}(r,t,\mathbf{f},\mathbf{S}))$ | | $\frac{\partial S_j}{\partial r}(0,t)=0$ | $S_j(R(t),t))=S_j^*(t)$ |
| $\frac{\partial u(r,t)}{\partial r}=-\frac{2u(r,t)}{r}+G(r,t,\mathbf{f},\mathbf{S},\boldsymbol{\psi})$ | | $u(0,t)=0$ | |
| $\dot{R}(t)=\sigma_a(t)-\sigma_d(t)+u(R(t),t)$ | $R(0)=0$ | | |
| $V\dot{\psi}_i^*(t)=Q(\psi_i^{in}-\psi_i^*(t))-A(t)N_GD_{\psi,i}\frac{\partial\psi_i(R(t),t)}{\partial r}+r_{\psi,i}^*(t,\boldsymbol{\psi}^*,\mathbf{S}^*)-\sigma_{a,i}(t)\rho A(t)N_G$ | $\psi_i^*(0)=\psi_{i,0}^*$ | | |
| $V\dot{S}_j^*(t)=Q(S_j^{in}-S_j^*(t))-A(t)N_GD_{S,j}\frac{\partial S_j(R(t),t)}{\partial r}+r_{S,j}^*(t,\boldsymbol{\psi}^*,\mathbf{S}^*)$ | $S_j^*(0)=S_{j,0}^*$ | | |

Table 3.1: Model equations and initial and boundary conditions.

## 3.3 Modelling *de novo* anaerobic granulation

The mathematical model described in the previous section can be applied to any granular biofilm system by defining appropriate variables, parameters, and initial, and boundary, conditions and reaction terms based on the biological processes involved.

In this Chapter, the model is applied to study the process of *de novo* granulation and the ecology of granules in an anaerobic bioreactor. Anaerobic digestion (AD) is a biological process extensively used to manage liquid and solid wastes, and to produce renewable biofuels. AD underpins low-cost environmental biotechnologies underpinned by a complex, multi-step process in which different trophic grous of microbial species convert organic matter to methane-rich biogas. Over the past few decades, the application of AD has been developed in granular biofilm systems, in which the microbial community forms dense biofilm granules offering several operational advantages over conventional, suspended biomass systems [14, 12].

Many studies report the fundamental role played by methanogenic species, which facilitate the formation of the granule nucleus [83, 84, 94, 95]. To model this aspect, different attachment velocities are used depending on the microbial species.

The following variables, expressed in terms of concentrations, are included in the model:

- five sessile microbial components: sugar fermenters $X_{Su}$, butyrate consumers $X_{Bu}$, propionate consumers $X_{Pro}$, acetoclastic methanogens $X_{Ac}$, and inert material $X_I$.
- four planktonic species within the biofilm: sugar fermenters $\psi_{Su}$, butyrate consumers $\psi_{Bu}$, propionate consumers $\psi_{Pro}$, and acetoclastic methanogens $\psi_{Ac}$.
- five soluble compounds within the biofilm: sugar $S_{Su}$, butyrate $S_{Bu}$, propionate $S_{Pro}$, acetate $S_{Ac}$, and methane $S_{CH_4}$.

- four planktonic species within the bulk liquid: sugar fermenters $\psi^*_{Su}$, butyrate consumers $\psi^*_{Bu}$, propionate consumers $\psi^*_{Pro}$, and acetoclastic methanogens $\psi^*_{Ac}$.
- five soluble compounds within the bulk liquid: sugar $S^*_{Su}$, butyrate $S^*_{Bu}$, propionate $S^*_{Pro}$, acetate $S^*_{Ac}$, and methane $S^*_{CH_4}$.

Inert material is not considered in the bulk liquid as it is supposed to play no role in the life cycle of the granular biofilm (inactive biomass is supposed to have neither metabolic activity nor granulation or invasion properties).

The model considers an influent flow comprised exclusively of dissolved substrates. Therefore, disintegration and hydrolysis processes, which lead to the conversion of organic matter into soluble compounds, are neglected. The main intracellular processes are taken into account both in the biofilm and in the bulk liquid: acidogenesis, acetogenesis and methanogenesis. The kinetic expressions of the biological processes involved in the model are taken from Batstone et al. (2002) [1]. In particular, each growth process leads to the formation of new biomass, and consumption and/or production of one or more soluble substrates. Each decay process implies the death of active biomass, which becomes inert material. Within the biofilm, sessile sugar fermenters $X_{Su}$ grow by converting sugar $S_{Su}$ into butyrate $S_{Bu}$, propionate $S_{Pro}$ and acetate $S_{Ac}$ (i.e. acidogenesis). Butyrate $S_{Bu}$ and propionate $S_{Pro}$ are consumed by sessile butyrate consumers $X_{Bu}$ and sessile propionate consumers $X_{Pro}$, respectively, and acetate $S_{Ac}$ is produced (i.e. acetogenesis). Lastly, acetate is converted into methane $S_{CH_4}$ by sessile acetoclastic methanogens $X_{Ac}$ (i.e. methanogenesis). The same biological processes are supposed to occur in the bulk liquid, in which the planktonic biomass $\psi^*_i$ consume or produce the soluble substrates $S^*_j$. Furthermore, the decay of any sessile biomass is considered to produce inert material $X_I$, which represents inactive biomass and accumulates in the biofilm. The decay processes are also considered for planktonic species in the bulk liquid.

The planktonic active species present in the bulk liquid are also modelled in the

granule domain as planktonic cells $\psi_i$, which populate the voids of the solid matrix and contribute to the growth of the corresponding sessile species as a result of invasion phenomena.

Each of the reaction terms of the model equations are listed below. The specific growth rates within the biofilm due to sessile biomass $r_{M,i}$ in Eq.(3.10) and Eq.(3.12) are modelled as Monod-type kinetics:

$$r_{M,i} = f_i(\mu_{\max,i}\frac{S_i}{K_i + S_i} - k_{d,i}),\ i \in I_B, \tag{3.37}$$

where $I_B = \{Su, Bu, Pro, Ac\}$ is the index set, $\mu_{\max,i}$ is the maximum net growth rate for biomass $i$, $K_i$ is the affinity constant of the consumed substrate for biomass $i$ and $k_{d,i}$ is the decay constant for biomass $i$.

The inert formation rate is give by the sum of the decay rates of each active species, modelled as first order kinetic:

$$r_{M,I} = \sum_{i \in I_B} f_i\ k_{d,i}. \tag{3.38}$$

The specific growth rates within the biofilm due to planktonic cells $r_i$ in Eq.(3.10) and Eq.(3.12) are defined as:

$$r_i = k_{col,i}\ \frac{\psi_i}{\rho}\frac{S_i}{K_i + S_i},\ i \in I_B, \tag{3.39}$$

where $k_{col,i}$ is the maximum colonization rate of motile species $i$ and $\rho$ is the granule density.

The conversion rates for planktonic cells due to the invasion process $r_{\psi,i}$ in Eq.(3.15) are expressed by:

$$r_{\psi,i} = -\frac{1}{Y_{\psi,i}} r_i \ \rho, \ i \in I_B, \tag{3.40}$$

where $Y_{\psi,i}$ denotes the yield of non-motile species $i$ on corresponding motile species.

The conversion rates for soluble substrates within the biofilm $r_{S,j}$ in Eq.(3.16), with $j \in \{Su, Bu, Pro, Ac, CH_4\}$, are listed below:

$$r_{S,Su} = -\frac{\mu_{\max,Su}}{Y_{Su}} \frac{S_{Su}}{K_{Su} + S_{Su}} f_{Su} \ \rho, \tag{3.41}$$

$$r_{S,Bu} = -\frac{\mu_{\max,Bu}}{Y_{Bu}} \frac{S_{Bu}}{K_{Bu} + S_{Bu}} f_{Bu} \ \rho \ + \ g_{Su,Bu} \frac{(1 - Y_{Su})}{Y_{Su}} \mu_{\max,Su} \times$$

$$\times \frac{S_{Su}}{K_{Su} + S_{Su}} f_{Su} \ \rho, \tag{3.42}$$

$$r_{S,Pro} = -\frac{\mu_{\max,Pro}}{Y_{Pro}} \frac{S_{Pro}}{K_{Pro} + S_{Pro}} f_{Pro} \ \rho \ + \ g_{Su,Pro} \frac{(1 - Y_{Su})}{Y_{Su}} \mu_{\max,Su} \times$$

$$\times \frac{S_{Su}}{K_{Su} + S_{Su}} f_{Su} \ \rho, \tag{3.43}$$

$$r_{S,Ac} = -\frac{\mu_{\max,Ac}}{Y_{Ac}} \frac{S_{Ac}}{K_{Ac} + S_{Ac}} f_{Ac} \ \rho \ + \ g_{Su,Ac} \frac{(1 - Y_{Su})}{Y_{Su}} \mu_{\max,Su} \frac{S_{Su}}{K_{Su} + S_{Su}} \times$$

$$\times f_{Su} \ \rho \ + g_{Bu,Ac} \frac{(1 - Y_{Bu})}{Y_{Bu}} \mu_{\max,Bu} \frac{S_{Bu}}{K_{Bu} + S_{Bu}} f_{Bu} \ \rho \ + \ g_{Pro,Ac} \frac{(1 - Y_{Pro})}{Y_{Pro}} \times$$

$$\times \mu_{\max,Pro} \frac{S_{Pro}}{K_{Pro} + S_{Pro}} f_{Su} \ \rho, \tag{3.44}$$

$$r_{S,CH_4} = \frac{(1 - Y_{Ac})}{Y_{Ac}} \mu_{\max,Ac} \frac{S_{Ac}}{K_{Ac} + S_{Ac}} f_{Ac}\, \rho, \tag{3.45}$$

where $Y_{Su}$, $Y_{Bu}$, $Y_{Pro}$, $Y_{Ac}$, denote the yields of sugar fermenters, butyrate consumers, propionate consumers and acetoclastic methanogens on the corresponding substrate consumed, $g_{Su,Bu}$, $g_{Su,Pro}$, $g_{Su,Ac}$ are the stoichiometric fractions of butyrate, propionate and acetate produced from sugar, $g_{Bu,Ac}$ and $g_{Pro,Ac}$ are the stoichiometric fractions of acetate produced from butyrate and propionate.

Moreover, the conversion rates of planktonic biomasses $r^*_{\psi,i}$ within the bulk liquid in Eq.(3.28) are defined as:

$$r^*_{\psi,i} = \psi^*_i (\mu_{\max,i} \frac{S^*_i}{K_i + S^*_i} - k_{d,i}),\ i \in I_B, \tag{3.46}$$

while, the conversion rates of soluble substrates $r^*_{S,j}$ within the bulk liquid in Eq.(3.29), with $j \in \{Su, Bu, Pro, Ac, CH_4\}$, are listed below:

$$r^*_{S,Su} = -\psi^*_{Su} \frac{\mu_{\max,Su}}{Y_{Su}} \frac{S^*_{Su}}{K_{Su} + S^*_{Su}}, \tag{3.47}$$

$$r^*_{S,Bu} = -\psi^*_{Bu} \frac{\mu_{\max,Bu}}{Y_{Bu}} \frac{S^*_{Bu}}{K_{Bu} + S^*_{Bu}} + g_{Su,Bu} \frac{(1 - Y_{Su})}{Y_{Su}} \psi^*_{Su} \mu_{\max,Su} \times$$

$$\times \frac{S^*_{Su}}{K_{Su} + S^*_{Su}}, \tag{3.48}$$

$$r^*_{S,Pro} = -\psi^*_{Pro} \frac{\mu_{\max,Pro}}{Y_{Pro}} \frac{S^*_{Pro}}{K_{Pro} + S^*_{Pro}} + g_{Su,Pro} \frac{(1 - Y_{Su})}{Y_{Su}} \psi^*_{Su} \mu_{\max,Su} \times$$

$$\times \frac{S^*_{Su}}{K_{Su} + S^*_{Su}}, \tag{3.49}$$

$$r^*_{S,Ac} = -\psi^*_{Ac}\frac{\mu_{\max,Ac}}{Y_{Ac}}\frac{S^*_{Ac}}{K_{Ac}+S^*_{Ac}} + g_{Su,Ac}\frac{(1-Y_{Su})}{Y_{Su}}\psi^*_{Su}\mu_{\max,Su}\frac{S^*_{Su}}{K_{Su}+S^*_{Su}} +$$

$$g_{Bu,Ac}\frac{(1-Y_{Bu})}{Y_{Bu}}\psi^*_{Bu}\mu_{\max,Bu}\frac{S^*_{Bu}}{K_{Bu}+S^*_{Bu}} + g_{Pro,Ac}\frac{(1-Y_{Pro})}{Y_{Pro}}\psi^*_{Pro}\mu_{\max,Pro}\times$$

$$\times\frac{S^*_{Pro}}{K_{Pro}+S^*_{Pro}}, \tag{3.50}$$

$$r^*_{S,CH_4} = \frac{(1-Y_{Ac})}{Y_{Ac}}\psi^*_{Ac}\mu_{\max,Ac}\frac{S^*_{Ac}}{K_{Ac}+S^*_{Ac}}. \tag{3.51}$$

The values used for all stoichiometric and kinetic parameters are reported in Table 3.2.

| Parameter | Definition | Unit | Value | Ref |
|---|---|---|---|---|
| $\mu_{max,Su}$ | Maximum specific growth rate for sugar fermenters | $d^{-1}$ | 3 | (a) |
| $\mu_{max,Bu}$ | Maximum specific growth rate for butyrate consumers | $d^{-1}$ | 1.2 | (a) |
| $\mu_{max,Pro}$ | Maximum specific growth rate for propionate consumers | $d^{-1}$ | 0.52 | (a) |
| $\mu_{max,Ac}$ | Maximum specific growth rate for acetoclastic methanogens | $d^{-1}$ | 0.4 | (a) |
| $k_{d,Su}$ | Decay-inactivation rate for sugar fermenters | $d^{-1}$ | 0.02 | (a) |
| $k_{d,Bu}$ | Decay-inactivation rate for butyrate consumers | $d^{-1}$ | 0.02 | (a) |
| $k_{d,Pro}$ | Decay-inactivation rate for propionate consumers | $d^{-1}$ | 0.02 | (a) |
| $k_{d,Ac}$ | Decay-inactivation rate for acetoclastic methanogens | $d^{-1}$ | 0.02 | (a) |
| $K_{Su}$ | Sugar half saturation constant sugar fermenters | $gCOD\ m^{-3}$ | 500 | (a) |
| $K_{Bu}$ | Butyrate half saturation constant butyrate consumers | $gCOD\ m^{-3}$ | 300 | (a) |
| $K_{Pro}$ | Propionate half saturation constant propionate consumers | $gCOD\ m^{-3}$ | 300 | (a) |
| $K_{Ac}$ | Acetate half saturation constant acetoclastic methanogens | $gCOD\ m^{-3}$ | 150 | (a) |
| $Y_{Su}$ | Yield of sugar fermenters on sugar | $--$ | 0.10 | (a) |
| $Y_{Bu}$ | Yield of butyrate consumers on butyrate | $--$ | 0.06 | (a) |
| $Y_{Pro}$ | Yield of propionate consumers on propionate | $--$ | 0.04 | (a) |
| $Y_{Ac}$ | Yield of acetoclastic methanogens on acetate | $--$ | 0.05 | (a) |
| $g_{Su,Bu}$ | Fraction of butyrate from sugar | $--$ | 0.13 | (a) |
| $g_{Su,Pro}$ | Fraction of propionate from sugar | $--$ | 0.27 | (a) |
| $g_{Su,Ac}$ | Fraction of acetate from sugar | $--$ | 0.41 | (a) |
| $g_{Bu,Ac}$ | Fraction of acetate from butyrate | $--$ | 0.80 | (a) |
| $g_{Pro,Ac}$ | Fraction of acetate from propionate | $--$ | 0.57 | (a) |
| $D_{S,Su}$ | Diffusion coefficient of sugar in biofilm | $m^2\ d^{-1}$ | $4.63 \cdot 10^{-5}$ | (b) |
| $D_{S,Bu}$ | Diffusion coefficient of butyrate in biofilm | $m^2\ d^{-1}$ | $6.01 \cdot 10^{-5}$ | (b) |
| $D_{S,Pro}$ | Diffusion coefficient of propionate in biofilm | $m^2\ d^{-1}$ | $7.33 \cdot 10^{-5}$ | (b) |
| $D_{S,Ac}$ | Diffusion coefficient of acetate in biofilm | $m^2\ d^{-1}$ | $8.36 \cdot 10^{-5}$ | (b) |
| $D_{S,CH_4}$ | Diffusion coefficient of methane in biofilm | $m^2\ d^{-1}$ | $10.3 \cdot 10^{-5}$ | (b) |
| $k_{col,i}$ | Maximum colonization rate of $i^{th}$ planktonic species | $d^{-1}$ | 0.001 | (c) |
| $Y_{\psi,i}$ | Yield of non-motile microorganisms on motile species | $--$ | 0.001 | (c) |
| $D_{\psi,i}$ | Diffusion coefficient of $i^{th}$ planktonic species in biofilm | $m^2\ d^{-1}$ | $10^{-5}$ | (c) |
| $v_{a,Su}$ | Attachment velocity of planktonic species $\psi_{Su}$ | $m\ d^{-1}$ | $3 \cdot 10^{-3}$ | (c) |
| $v_{a,Bu}$ | Attachment velocity of planktonic species $\psi_{Bu}$ | $m\ d^{-1}$ | $3 \cdot 10^{-3}$ | (c) |
| $v_{a,Pro}$ | Attachment velocity of planktonic species $\psi_{Pro}$ | $m\ d^{-1}$ | $3 \cdot 10^{-3}$ | (c) |
| $v_{a,Ac}$ | Attachment velocity of planktonic species $\psi_{Ac}$ | $m\ d^{-1}$ | $150 \cdot 10^{-3}$ | (c) |
| $\rho$ | Biofilm density | $gCOD\ m^{-3}$ | 120000 | (c) |
| $\lambda$ | Detachment coefficient | $m^{-1}\ d^{-1}$ | 10 | (c) |
| $V$ | Reactor volume | $m^3$ | 400 | (c) |
| $Q$ | Volumetric flow rate | $m^3\ d^{-1}$ | 600 | (c) |
| $N_G$ | Number of granules in the reactor | $--$ | $2.4 \cdot 10^{10}$ | (c) |

(a) Batstone et al. (2002) [1]; (b) Stewart (2003) [111]; (c) Assumed.

Table 3.2: Kinetic, stoichiometric and operating parameters used for numerical simulations.

| **Parameter** | **NS1** | **NS2** | **NS3** | **NS4** | **NS5** | **NS6** |
|---|---|---|---|---|---|---|
| | RUN1 | RUN2 - RUN4 | RUN5 - RUN13 | RUN14 - RUN17 | RUN18 - RUN25 | RUN26 - RUN30 |
| $S_{Su}^{in}$ $[gCOD\,m^{-3}]$ | 3500 | $varied^1$ | 3500 | 3500 | 3500 | 3500 |
| $S_{Bu}^{in}$ $[gCOD\,m^{-3}]$ | 0 | $varied^1$ | 0 | 0 | 0 | 0 |
| $S_{Pro}^{in}$ $[gCOD\,m^{-3}]$ | 0 | $varied^1$ | 0 | 0 | 0 | 0 |
| $S_{Ac}^{in}$ $[gCOD\,m^{-3}]$ | 0 | $varied^1$ | 0 | 0 | 0 | 0 |
| $S_{CH_4}^{in}$ $[gCOD\,m^{-3}]$ | 0 | $varied^1$ | 0 | 0 | 0 | 0 |
| $\psi_{Su,0}^{*}$ $[gCOD\,m^{-3}]$ | 300 | $varied^1$ | 300 | 300 | 300 | 300 |
| $\psi_{Bu,0}^{*}$ $[gCOD\,m^{-3}]$ | 50 | $varied^1$ | 50 | 50 | 50 | 50 |
| $\psi_{Pro,0}^{*}$ $[gCOD\,m^{-3}]$ | 50 | $varied^1$ | 50 | 50 | 50 | 50 |
| $\psi_{Ac,0}^{*}$ $[gCOD\,m^{-3}]$ | 100 | $varied^1$ | 100 | 100 | 100 | 100 |
| $v_{a,Su}$ $[m\,d^{-1}]$ | $3 \cdot 10^{-3}$ | $3 \cdot 10^{-3}$ | $varied^1$ | $3 \cdot 10^{-3}$ | $3 \cdot 10^{-3}$ | $3 \cdot 10^{-3}$ |
| $v_{a,Bu}$ $[m\,d^{-1}]$ | $3 \cdot 10^{-3}$ | $3 \cdot 10^{-3}$ | $varied^1$ | $3 \cdot 10^{-3}$ | $3 \cdot 10^{-3}$ | $3 \cdot 10^{-3}$ |
| $v_{a,Pro}$ $[m\,d^{-1}]$ | $3 \cdot 10^{-3}$ | $3 \cdot 10^{-3}$ | $varied^1$ | $3 \cdot 10^{-3}$ | $3 \cdot 10^{-3}$ | $3 \cdot 10^{-3}$ |
| $v_{a,Ac}$ $[m\,d^{-1}]$ | $150 \cdot 10^{-3}$ | $150 \cdot 10^{-3}$ | $varied^1$ | $150 \cdot 10^{-3}$ | $150 \cdot 10^{-3}$ | $150 \cdot 10^{-3}$ |
| $\rho$ $[gCOD\,m^{-3}]$ | 120000 | 120000 | 120000 | $varied^1$ | 120000 | 120000 |
| $\lambda$ $[m^{-1}\,d^{-1}]$ | 10 | 10 | 10 | 10 | $varied^1$ | 10 |
| $N_G$ $[--]$ | $2.4 \cdot 10^{10}$ | $2.4 \cdot 10^{10}$ | $2.4 \cdot 10^{10}$ | $2.4 \cdot 10^{10}$ | $2.4 \cdot 10^{10}$ | $varied^1$ |
| $T$ $[d]$ | 300 | 300 | 300 | 300 | 300 | 300 |

[1]The values used are reported in the text

Table 3.3: Initial and boundary conditions and operating parameters adopted in numerical studies.

## 3.4 Numerical simulations and results

The model has been integrated numerically by developing an original code in MatLab platform. Hyperbolic PDEs (Eq. (3.12)) have been integrated by using the method of characteristics, applied for the first time in the biofilm context by D'Acunto and Frunzo (2011) [32], while the method of lines has been adopted for the diffusion-reaction PDEs (Eqs. (3.15) and (3.16)). The ordinary differential equations for $\psi_i^*$ and $S_j^*$ (Eqs. (3.28) and (3.29)) have been integrated by using the MatLab routine ode45, based on a Runge-Kutta method. The time to compute the values of the unknown variables is in the order of hours and depends on the specific target simulation time.

Numerical simulations are performed to describe the formation and evolution of anaerobic granular biofilms, to study the ecological succession occurring in the granule and explore the effects of the main factors on the process. In particular, five numerical studies are carried out: the first numerical study (NS1) describes the *de novo* granulation process in a bioreactor fed with an influent wastewater rich in sugar; the second study (NS2) investigates the effect of influent composition on granule evolution and ecology; the third study (NS3) explores the role of the attachment phenomenon on granule evolution; the fourth study (NS4) investigates the effects of the biomass density on the transport of soluble substrates and, consequently, on the growth and stratification of biomass within the granule; and the fifth study (NS5) simulates the effects of different detachment regimes on granule size and dynamics. Lastly, a sixth study (NS6) analyses the effects of the number of granules on the process. The values used for the parameters under study are presented in Table 3.3 for all numerical studies.

The initial concentration of the soluble substrates in the bulk liquid $S_{j,0}^*$ is assumed the same as the influent wastewater. No microbial biomass is present in the influent flow ($\psi_i^{in} = 0$), while non-null initial concentrations of planktonic biomasses in the bulk liquid $\psi_{i,0}^*$ are set to simulate the reactor inoculated with an anaerobic sludge. In particular, it is considered that the granular reactor is inoculated with the sludge coming

from a suspended-based anaerobic reactor and fed with the same influent wastewater. Therefore, the initial concentrations of planktonic species in the bulk liquid (representative of the inoculum) are derived from numerical results of an ADM1-based model [1].

In granular bioreactors, intense hydrodynamic conditions will improve the aggregation of planktonic cells and the formation of granules. Consequently, for all the simulations reported in this Chapter, the bioreactor volume $V$ and the influent flow rate $Q$ are assumed constant and equal to $400\ m^3$ and $600\ m^3 d^{-1}$, respectively, leading to high hydrodynamic velocities and a very low hydraulic retention time (HRT = $0.667\ d$). Such values are within the range of hydraulic retention times (HRT) values typical of granular biofilm systems [112]. Moreover, the organic loading rate (OLR), defined as the amount of daily organic matter treated per unit reactor volume, is set equal to $5.25\ kg\ m^{-3}\ d^{-1}$. The number of granules $N_G$ has been selected through an iterative procedure which involved the detachment coefficient $\lambda$, with the aim to guarantee a $25\%$ filling ratio [30, 28] by considering $1mm$ as steady-state particle radius, an average size representative of these anaerobic granular communities [83, 26, 27].

Diffusivity of soluble substrates in biofilm is assumed to be $80\%$ of diffusivity in water [22]. The diffusion coefficients in water for all soluble substrates are taken from Stewart (2003) [111], see Table 3.2.

The simulation time $T$ is fixed to $300\ d$ for all simulations. This time interval guarantees to achieve the steady-state configuration for all model variables: concentration of soluble substrates $S_j^*(t)$ and planktonic biomasses $\psi_i^*(t)$ in the bulk liquid; granule size $R(t)$; sessile biomass fractions $f_i(r,t)$, concentration of soluble substrates $S_j(r,t)$ and planktonic species $\psi_i(r,t)$ within the biofilm.

### 3.4.1 NS1 - Anaerobic granulation process

The first numerical study (NS1) describes the *de novo* granulation process occurring in a granular reactor fed with sugar: $S_{Su}^{in} = 3500\ g\ m^{-3}$, $S_{Bu}^{in} = S_{Pro}^{in} = S_{Ac}^{in} = S_{CH_4}^{in} = 0$ (RUN1). The initial concentration of the planktonic biomasses (reactor inoculum) is derived from an ADM1-based model following the procedure introduced above: $\psi_{Su,0}^{*} = 300\ g\ m^{-3}$, $\psi_{Bu,0}^{*} = \psi_{Pro,0}^{*} = 50\ g\ m^{-3}$, $\psi_{Ac,0}^{*} = 100\ g\ m^{-3}$.

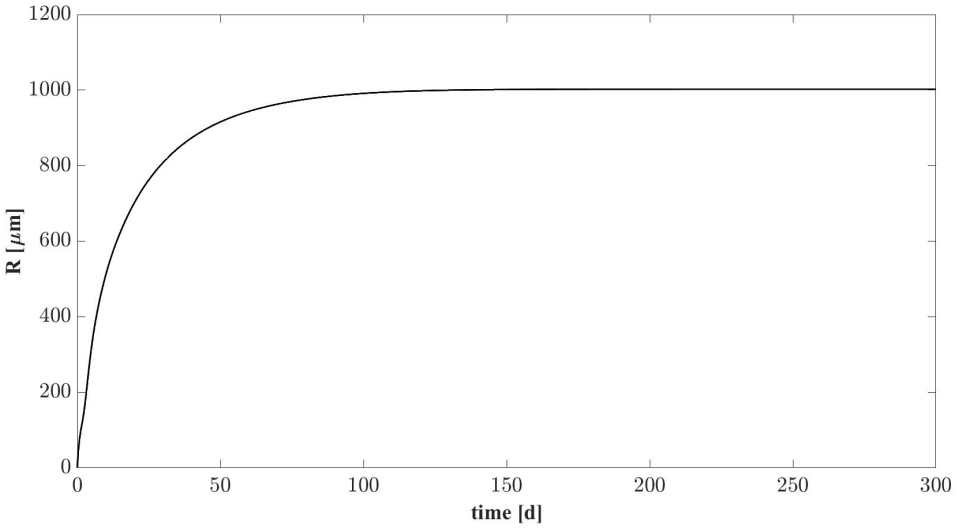


Figure 3.2: NS1 - Biofilm radius evolution over time. Influent wastewater composition: $S_{Su}^{in} = 3500\ g\ m^{-3}$ (Sugar), $S_{Bu}^{in} = 0$ (Butyrate), $S_{Pro}^{in} = 0$ (Propionate), $S_{Ac}^{in} = 0$ (Acetate), $S_{CH_4}^{in} = 0$ (Methane).

Numerical results are summarised in Figs. 3.2-3.6. In Fig. 3.2 the evolution of the granule radius $R(t)$ over time is reported. A vanishing initial value is assigned to $R(t)$ at $t = 0$ ($R(0) = 0$). During the first days, the granulation process has its maximum intensity and the granule size increases. The variation of $R(t)$ is almost exhausted during the first 70-100 days, after which it reaches a steady-state value of about $1\ mm$.

In Fig. 3.3 the distribution of sessile species within the granule is shown at different times. After $5\ d$ the granule has a radius of about $0.3\ mm$ and is constituted mostly by acidogens (blue) which are favoured by the high concentration of sugar initially present in the bulk liquid. However, the granule core is also composed of methanogens (red) which have high propensity to attach due to their filamentous structures and aggrega-

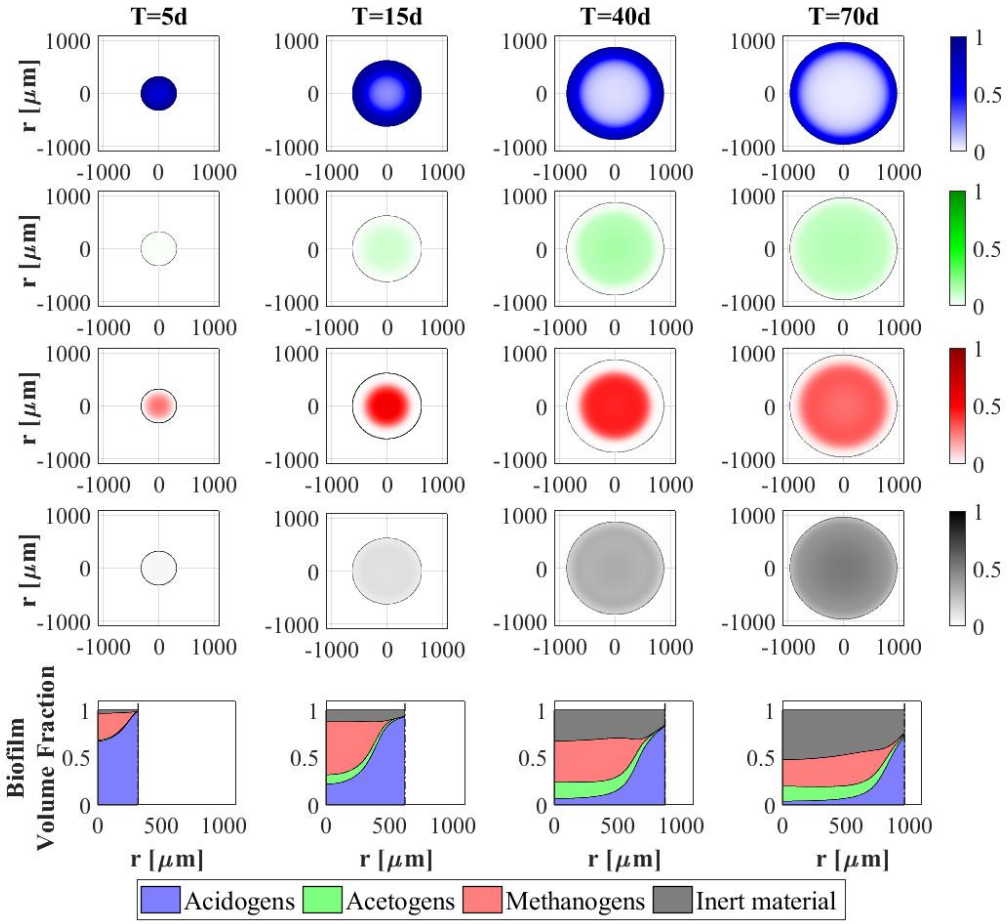


Figure 3.3: NS1 - Microbial species distribution in the diametrical section and across the radius of the granule, at $T = 5\ d$, $T = 15\ d$, $T = 40\ d$ and $T = 70\ d$. Influent wastewater composition: $S_{Su}^{in} = 3500\ g\ m^{-3}$ (Sugar), $S_{Bu}^{in} = 0$ (Butyrate), $S_{Pro}^{in} = 0$ (Propionate), $S_{Ac}^{in} = 0$ (Acetate), $S_{CH_4}^{in} = 0$ (Methane).

tion properties. At $T = 15\ d$, the consumption of sugar and the production of volatile fatty acids (VFAs) in large amount by acidogenesis affects the biomass distribution: the methanogenic core grows while the acidogens occupy the outer layer of the granule, and the acetogens (green) and inert (black) fractions become be visible. For later times (40-70 $d$), the radius almost reaches the steady-state value, a significant amount of inert material accumulates (especially in the innermost part of the domain), and homogeneous fractions of methanogens and acetogens are found throughout the granule - except the outermost part, where a thin layer of acidogens is established. This stratification is due to the distribution of soluble substrate concentrations along the radius of the granule, shown at $T = 300\ d$ in Fig. 3.4. The concentration of sugar in the outer-

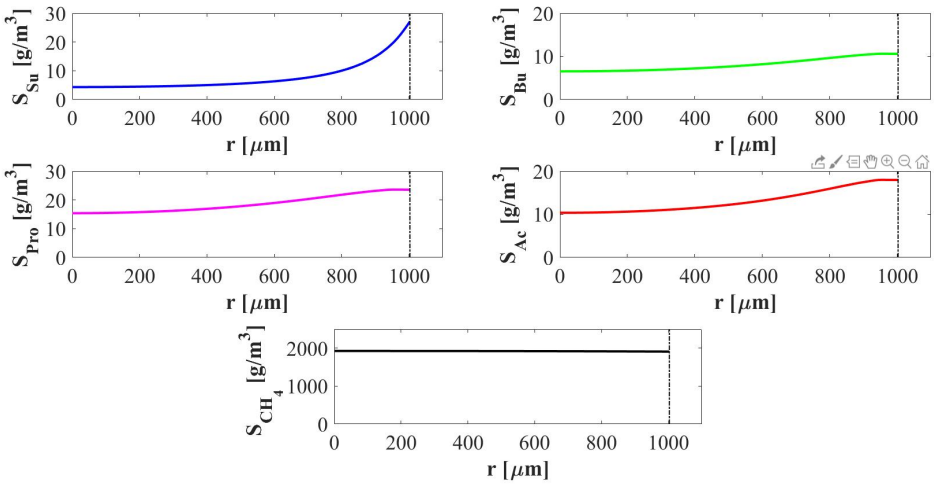


Figure 3.4: NS1 - Distribution of soluble substrates along the granule radius at $T = 300\ d$. $S_{Su}$: Sugar, $S_{Bu}$: Butyrate, $S_{Pro}$: Propionate, $S_{Ac}$: Acetate, $S_{CH_4}$: Methane. Influent wastewater composition: $S^{in}_{Su} = 3500\ g\ m^{-3}$ (Sugar), $S^{in}_{Bu} = 0$ (Butyrate), $S^{in}_{Pro} = 0$ (Propionate), $S^{in}_{Ac} = 0$ (Acetate), $S^{in}_{CH_4} = 0$ (Methane).

most layers promotes the growth of acidogens, which have a higher maximum growth rate than the other species. Otherwise, the substrate concentrations reduce towards the centre of the granule. Shortage of substrates affects acidogens more than other species, due to their high sugar half saturation constant (see Table 3.2). Then, since the acetate half saturation constant for methanogens is very low, they are able to grow even under low substrate concentrations and prevail in this central area.

Fig. 3.5 presents the trend of each microbial species within the granule over time. This result confirms the microbial succession described above. The biofilm is initially constituted predominantly by acidogens $m_{Su}$ (blue) and methanogens $m_{Ac}$ (red). Their mass within the biofilm achieves a maximum and then decreases to a steady-state value when the substrates required by their metabolism (sugar and acetate, respectively) are limited and the decay process prevails. The growth process of acetogens $m_{Bu} + m_{Pro}$ and the accumulation of inert $m_I$ are slower and take place over a longer period. However, all microbial species exhibit steady-state values 150-170 days after granule genesis. Furthermore, the total microbial mass $m_{tot}$ (dashed black line) follows the trend of the radius reported in Fig. 3.2. Indeed, assuming a constant density $\rho$, the variation of

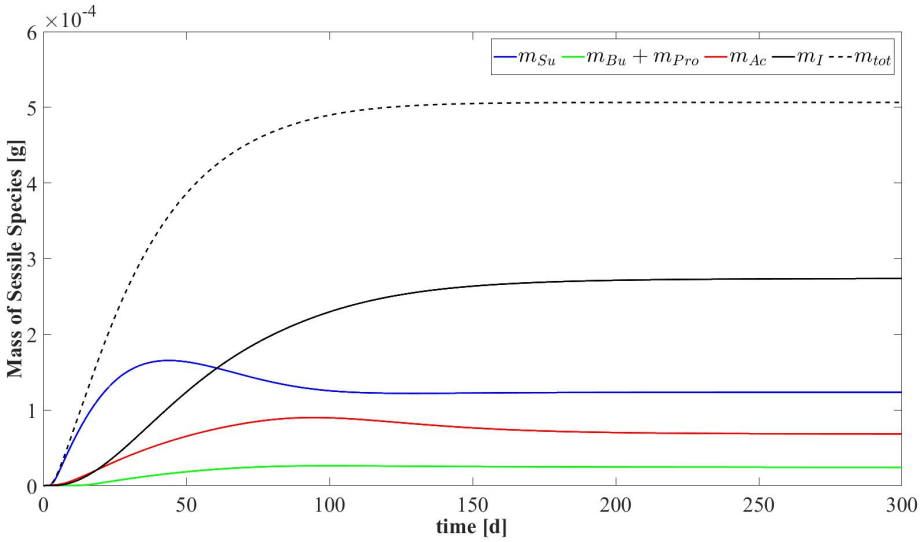


Figure 3.5: NS1 - Evolution of mass of sessile species within the reactor. $m_{Su}$: mass of sugar fermenters, $m_{Bu}$: mass of butyrate consumers, $m_{Pro}$: mass of propionate consumers, $m_{Ac}$: mass of acetoclastic methanogens, $m_{tot}$: total sessile mass. Influent wastewater composition: $S_{Su}^{in} = 3500\ g\ m^{-3}$ (Sugar), $S_{Bu}^{in} = 0$ (Butyrate), $S_{Pro}^{in} = 0$ (Propionate), $S_{Ac}^{in} = 0$ (Acetate), $S_{CH_4}^{in} = 0$ (Methane).

mass within the granule is related to the variation of volume.

Lastly, the trends of soluble substrates and planktonic biomass within the bulk liquid are shown in Fig. 3.6. In the initial phase, the biofilm granules are small, and the consumption and production of soluble substrates are governed by planktonic biomass. In particular, planktonic sugar fermenters $\psi_{Su}^*$ (blue in Fig. 3.6-bottom) degrade sugar $S_{Su}^*$ (blue in Fig. 3.6-top) and produce volatile fatty acids (VFAs): i.e. butyrate $S_{Bu}^*$ (green in Fig. 3.6-top), propionate $S_{Pro}^*$ (magenta in Fig. 3.6-top) and acetate $S_{Ac}^*$ (red in Fig. 3.6-top). Meanwhile, the concentration of all planktonic biomass within the bulk liquid is reduced due to two distinct phenomena: part is converted in sessile biomass during the granulation process and part is rapidly washed out due to the hydrodynamic conditions (i.e. low HRTs in 'high rate' bioreactors). For these reasons, no microbial species in planktonic form is present within the reactor after 5-7 days. After the washout of the planktonic biomass, the substrates trend is influenced exclusively by the sessile metabolic activity: the residual sugar $S_{Su}^*$ and VFAs ($S_{Bu}^*$, $S_{Pro}^*$ and $S_{Ac}^*$) are consumed with different velocities according to the consumption rate of the corresponding sessile

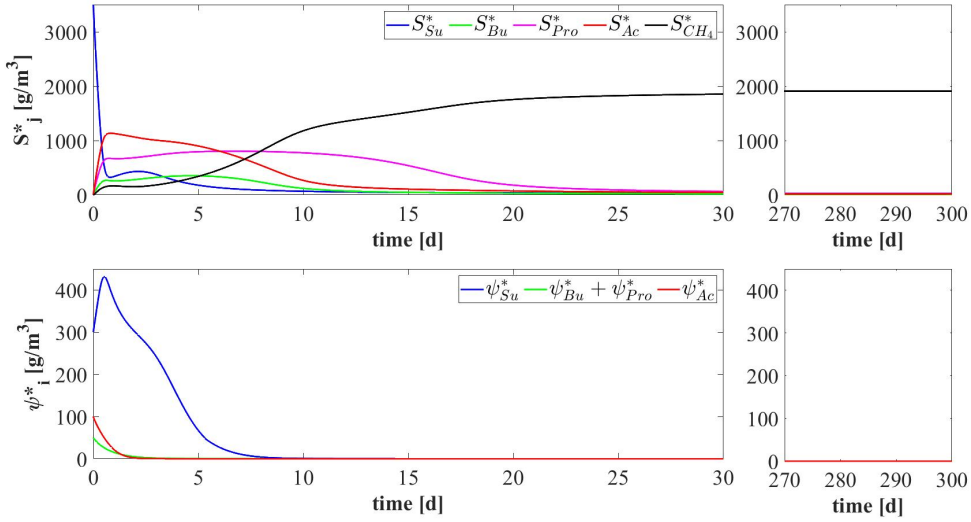


Figure 3.6: NS1 - Evolution of soluble substrates (top) and planktonic biomass (bottom) concentrations within the bulk liquid. $S^*_{Su}$: Sugar, $S^*_{Bu}$: Butyrate, $S^*_{Pro}$: Propionate, $S^*_{Ac}$: Acetate, $S^*_{CH_4}$: Methane, $\psi^*_{Su}$: Sugar fermenters, $\psi^*_{Bu}$: Butyrate consumers, $\psi^*_{Pro}$: Propionate consumers, $\psi^*_{Ac}$: Acetoclastic methanogens. Influent wastewater composition: $S^{in}_{Su} = 3500\ g\ m^{-3}$ (Sugar), $S^{in}_{Bu} = 0$ (Butyrate), $S^{in}_{Pro} = 0$ (Propionate), $S^{in}_{Ac} = 0$ (Acetate), $S^{in}_{CH_4} = 0$ (Methane).

microbial species and significant amount of methane $S^*_{CH_4}$ (black in Fig. 3.6-top) is produced. After 30 days substrates concentrations within the bulk liquid reach a steady-state value. High concentrations of methane (the end product of the AD process), and negligible concentrations of sugar and VFAs, are found in the bioreactor and in the effluent.

### 3.4.2 NS2 - Effects of influent wastewater composition

The results presented in the previous section describe the dynamic evolution and the steady-state configuration of anaerobic granular biofilms growing in a sugar-fed bioreactor. However, the composition of the influent wastewater affects the granulation process and regulates the ecological succession and the growth of individual species. Since the influent wastewater treated in anaerobic granular systems originates from any one of various applications and sources, and thus presents variable compositions of the organic load, it is interesting to compare the model results for different types of influent

wastewater. In particular, in this study (NS2) different influent compositions and bioreactor inocula are set as model input: (RUN2: $S_{Su}^{in} = 2000\ g\ m^{-3}$, $S_{Bu}^{in} = S_{Pro}^{in} = S_{Ac}^{in} = 500\ g\ m^{-3}$, $S_{CH_4}^{in} = 0$, $\psi_{Su,0}^{*} = 170\ g\ m^{-3}$, $\psi_{Bu,0}^{*} = \psi_{Pro,0}^{*} = 40\ g\ m^{-3}$, $\psi_{Ac,0}^{*} = 100\ g\ m^{-3}$; RUN3: $S_{Su}^{in} = S_{Bu}^{in} = S_{Pro}^{in} = S_{Ac}^{in} = 880\ g\ m^{-3}$, $S_{CH_4}^{in} = 0$, $\psi_{Su,0}^{*} = 70\ g\ m^{-3}$, $\psi_{Bu,0}^{*} = 50\ g\ m^{-3}, \psi_{Pro,0}^{*} = 40\ g\ m^{-3}$, $\psi_{Ac,0}^{*} = 110\ g\ m^{-3}$; RUN4: $S_{Su}^{in} = S_{CH_4}^{in} = 0$, $S_{Bu}^{in} = S_{Pro}^{in} = S_{Ac}^{in} = 1170\ g\ m^{-3}$, $\psi_{Su,0}^{*} = 0$, $\psi_{Bu,0}^{*} = 60\ g\ m^{-3}, \psi_{Pro,0}^{*} = 40\ g\ m^{-3}$, $\psi_{Ac,0}^{*} = 110\ g\ m^{-3}$). These cases have been compared with the case of reactor fed with only sugar (RUN1). The results are summarised in Figs. 3.7-3.11.

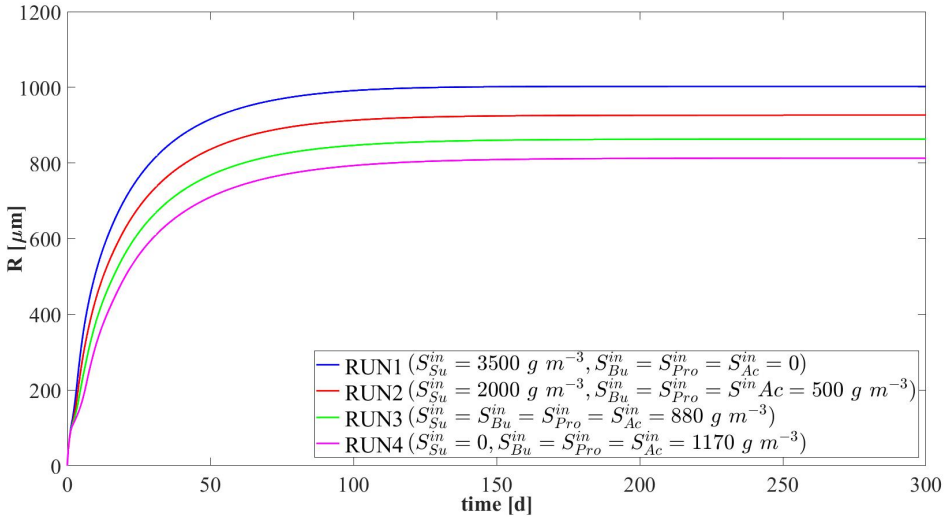


Figure 3.7: NS2 - Biofilm radius evolution over time for different influent wastewater compositions. $S_{Su}^{in}$: Sugar, $S_{Bu}^{in}$: Butyrate, $S_{Pro}^{in}$: Propionate, $S_{Ac}^{in}$: Acetate, $S_{CH_4}^{in}$: Methane.

Fig. 3.7 shows the trend of the granule radius $R(t)$ over time. Granules of different sizes are formed. These differences are related to the sessile biomass growth, which varies according to the substrates present in the influent wastewater. Specifically, sessile growth is affected by anabolic and catabolic pathways of the microbial metabolism: the yield of acidogens on sugar $Y_{Su}$ is higher than the yields of the other species, and thus the amount of acidogenic biomass grown per unit of substrate consumed is higher than the other species. Therefore, the steady-state size of the granule increases with

increasing sugar concentration in the influent $S_{Su}^{in}$. For $S_{Su}^{in} = 0$ (RUN4), the granule achieves the smallest size.

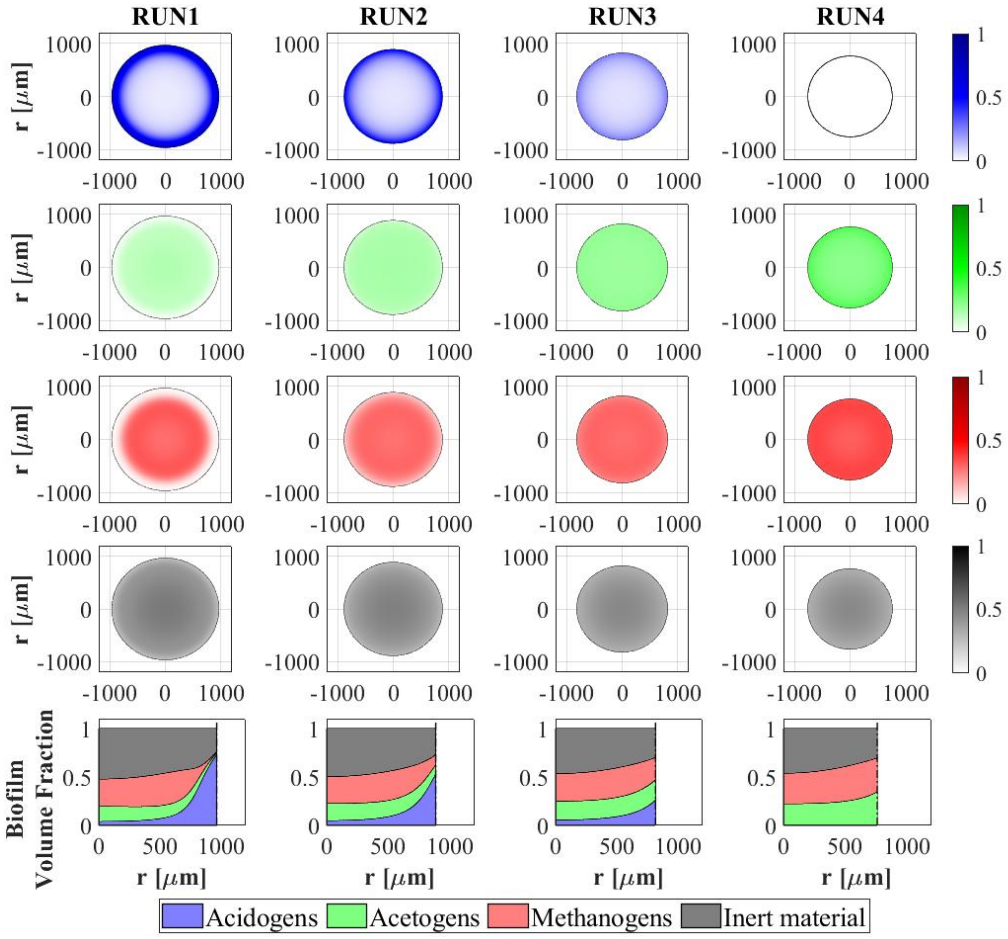


Figure 3.8: NS2 - Microbial species distribution in the diametrical section and across the radius of the granule at $T = 70\ d$, for different influent wastewater compositions. RUN1: $S_{Su}^{in} = 3500\ g\ m^{-3}$, $S_{Bu}^{in} = S_{Pro}^{in} = S_{Ac}^{in} = S_{CH_4}^{in} = 0$; RUN2: $S_{Su}^{in} = 2000\ g\ m^{-3}$, $S_{Bu}^{in} = S_{Pro}^{in} = S_{Ac}^{in} = 500\ g\ m^{-3}$, $S_{CH_4}^{in} = 0$; RUN3: $S_{Su}^{in} = S_{Bu}^{in} = S_{Pro}^{in} = S_{Ac}^{in} = 880\ g\ m^{-3}$, $S_{CH_4}^{in} = 0$; RUN4: $S_{Su}^{in} = 0$, $S_{Bu}^{in} = S_{Pro}^{in} = S_{Ac}^{in} = 1170\ g\ m^{-3}$, $S_{CH_4}^{in} = 0$. $S_{Su}^{in}$: Sugar, $S_{Bu}^{in}$: Butyrate, $S_{Pro}^{in}$: Propionate, $S_{Ac}^{in}$: Acetate, $S_{CH_4}^{in}$: Methane.

The distribution of sessile biomass within the granule in the four cases is reported in Fig. 3.8, at $T = 70\ d$. As the sugar concentration in the influent $S_{Su}^{in}$ increases, the fraction of acidogens $f_{Su}$ (blue) increases, especially in the outer part of the granule, where there is maximum availability of substrate. When the sugar concentration $S_{Su}^{in}$ decreases from $3500\ g\ m^{-3}$ (RUN1) to $880\ g\ m^{-3}$ (RUN3), the acidogenic fraction

present in the external part of the biofilm significantly reduces. Obviously, no acidogens are found within the granule when sugar is absent in the influent wastewater (RUN4). In addition, as the concentration of butyrate $S_{Bu}^{in}$, propionate $S_{Pro}^{in}$ and acetate $S_{Ac}^{in}$ in the influent increases going from RUN1 to RUN4, an increase in the fractions of acetogens $f_{Bu} + f_{Pro}$ (green) and methanogens $f_{Ac}$ (red) is observed.

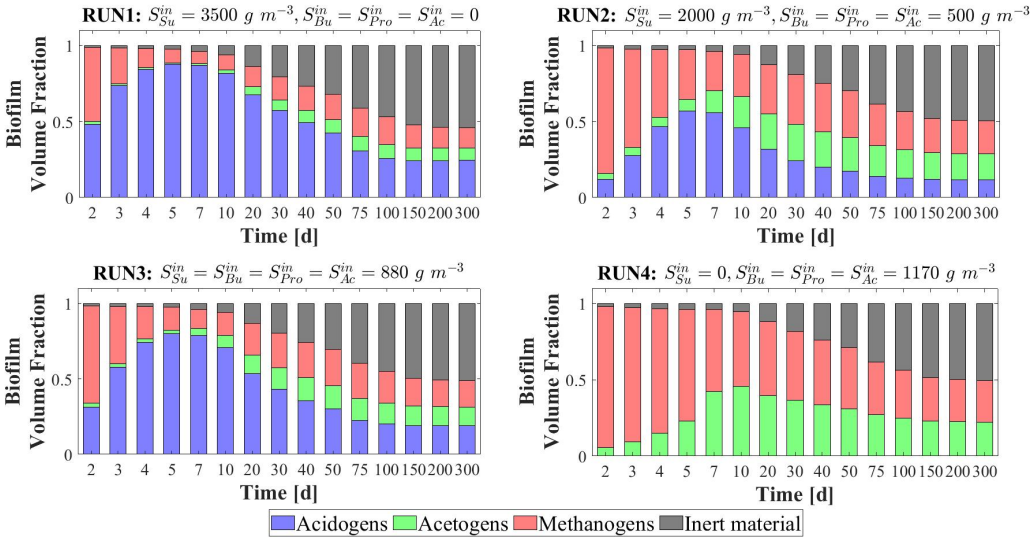


Figure 3.9: NS2 - Relative abundances of microbial species within the granule at several times under different influent wastewater compositions. $S_{Su}^{in}$: Sugar, $S_{Bu}^{in}$: Butyrate, $S_{Pro}^{in}$: Propionate, $S_{Ac}^{in}$: Acetate, $S_{CH_4}^{in}$: Methane.

The relative abundance of sessile microbial species is reported for different simulation times in Fig. 3.9. When sugar is present in the influent (RUN1, RUN2, RUN3), the initial phase of the granulation is governed by acidogens (which have a higher growth rate) and methanogens (which have high attachment velocities). The acidogenic fraction (blue) reaches a maximum after 7 $d$ and then decreases when the availability of sugar in the bulk liquid reduces. When sugar is not present in the influent (RUN4), the granulation process is dominated by methanogens (red) and acetogens in small amounts (green). In all four cases, the maximum fraction of methanogens is observed at the beginning of the process due to their granulation properties. Then, the methanogenic fraction reduces due to the decay process and the competition with acidogens and acetogens. Furthermore, the acetogenic fraction is negligible in all cases during the initial

phase of the granulation and grows when other microbial species become less competitive, and sugar is converted to butyrate and propionate. The microbial relative abundances related to the steady-state value confirm the results introduced in Fig. 3.8: the fraction of acidogens increases with the increase of the sugar in the influent; the fractions of methanogens and acetogens increase with increasing VFAs in the influent; in all cases, inactive biomass (black) represents approximately 50% of the total sessile biomass within the granule.

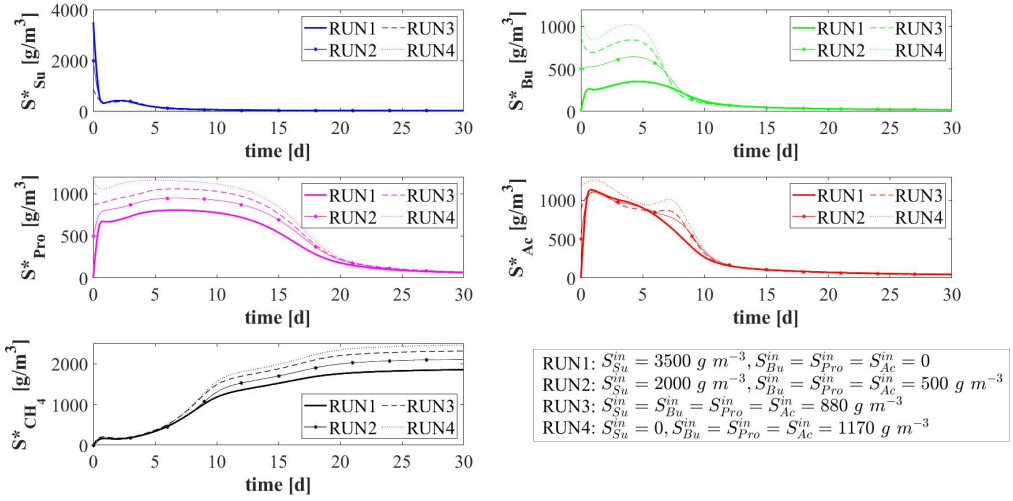


Figure 3.10: NS2 - Evolution of soluble substrates concentrations within the bulk liquid for different influent wastewater compositions. $S^*_{Su}$: Sugar, $S^*_{Bu}$: Butyrate, $S^*_{Pro}$: Propionate, $S^*_{Ac}$: Acetate, $S^*_{CH_4}$: Methane.

The model results related to the bulk liquid are summarised in Fig. 3.10 and Fig. 3.11, which show how the concentration of soluble substrates and planktonic biomass changes over time. As reported in Fig. 3.10, the composition of the influent wastewater affects the trend of the substrates mostly in the initial phase. In all cases, the AD process is completed in about 30 days: sugar (blue), butyrate (green), propionate (magenta) and acetate (red) are totally consumed and the concentration of methane (black) achieves a steady-state value. Notably, different productions of methane are observed as the composition of the influent changes. Concerning the concentration of planktonic biomass shown in Fig. 3.11, the concentration of acidogens (blue) is affected by the composition

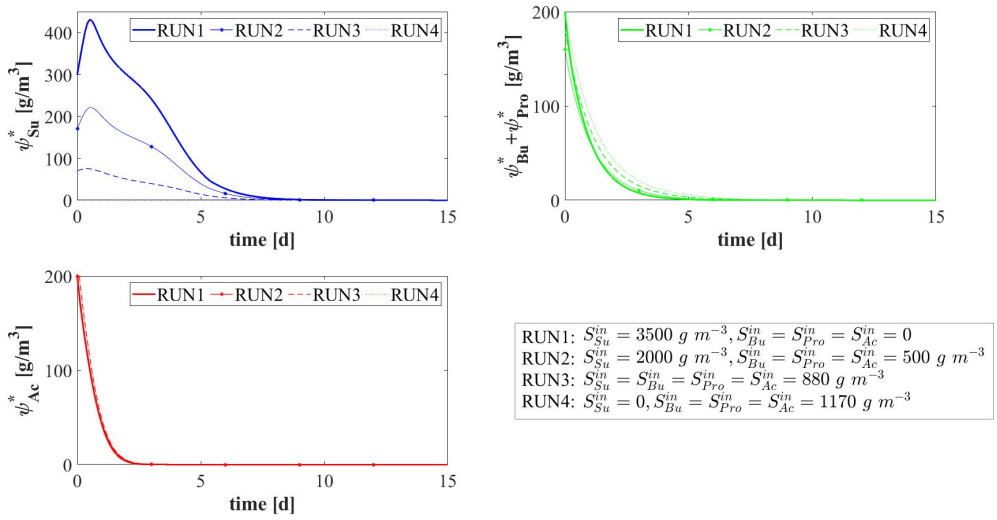


Figure 3.11: NS2 - Evolution of planktonic biomass concentrations within the bulk liquid for different influent wastewater compositions. $\psi^*_{Su}$: Sugar fermenters, $\psi^*_{Bu}$: Butyrate consumers, $\psi^*_{Pro}$: Propionate consumers, $\psi^*_{Ac}$: Acetoclastic methanogens.

of the influent in the initial phase of the granulation process (0-7 days). Conversely, the concentration of acetogens (green) and methanogens (red) in planktonic form have low growth rates and are washed out due to the dilution phenomenon even when significant concentrations of VFAs are present in the influent.

### 3.4.3 NS3 - Effects of granulation properties

The characteristics of the microbial community play a fundamental role in the anaerobic granulation process. In particular, it is affected by the granulating properties of the planktonic biomass present in the bioreactor. In the management of full-scale bioreactors, several strategies are pursued to improve the aggregation properties of the microbial community, reduce the time required for granulation and improve the efficiency of the wastewater treatment process. For example, the direct addition of the quorum sensing molecule acyl homoserine lactone (AHL) during granule formation might remarkably improve the granulation process in granular bioreactors [84, 94, 113]. Equally, bioaugmentation is regarded as a promising method to improve granulation and reduce the start-up in full-scale plants [114, 115, 116]. The addition to bioreactors of selected

microbial cultures depth in self-aggregation has been described [117]. Overall, such strategies positively alter the granulation properties of planktonic microbial communities.

In this framework, a numerical study (NS3) is conducted to investigate the effects on granulation of the granulating properties of the biomass. For this purpose, nine simulations (RUN5 - RUN13) are carried out with different attachment velocities $v_{a,i}$. The nine values of $v_{a,i}$ used are chosen by increasing and reducing the default values (presented in Table 3.2) through different multiplication factors $(0.05, 0.1, 0.25, 0.5, 1, 2, 3, 4, 5)$. The concentration of soluble substrates in the influent wastewater $S_j^{in}$ and the initial concentration of planktonic biomass in the bioreactor $\psi_{i,0}^*$ set for this numerical study are the same used in NS1 and are reported in Table 3.3.

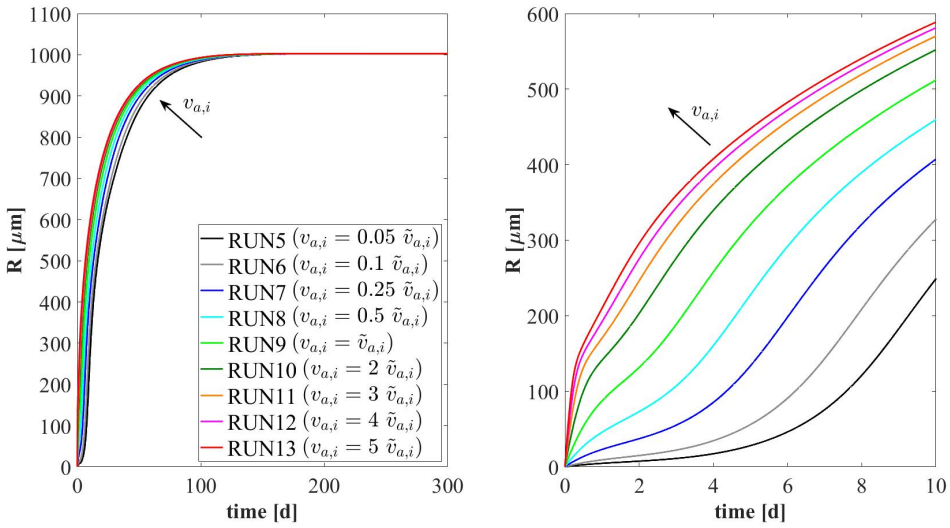


Figure 3.12: NS3 - Biofilm radius evolution over time for different attachment velocities $v_{a,i}$ (left), with a focus on the first 10 days (right). $\tilde{v}_{a,i}$: value of attachment velocity of the $i^{th}$ planktonic species set in RUN1. Influent wastewater composition: $S_{Su}^{in} = 3500\ g\ m^{-3}$ (Sugar), $S_{Bu}^{in} = 0$ (Butyrate), $S_{Pro}^{in} = 0$ (Propionate), $S_{Ac}^{in} = 0$ (Acetate), $S_{CH_4}^{in} = 0$ (Methane).

The results of this study are reported in Figs. 3.12-3.16. The temporal evolution of the granule radius $R(t)$ is shown in Fig. 3.12. From Fig. 3.12 (right) it is clear that different attachment velocities $v_{a,i}$ lead to different growth rates of the granule in the initial phase of the process: when the inoculated microbial community is more inclined

to grow in sessile form, the granulation process occurs faster and the granule reaches the steady-state size sooner. However, such steady-state size is not dependent on the attachment velocity. Indeed, the profiles of $R(t)$ for different $v_{a,i}$ get closer over time and reach the same steady-state value.

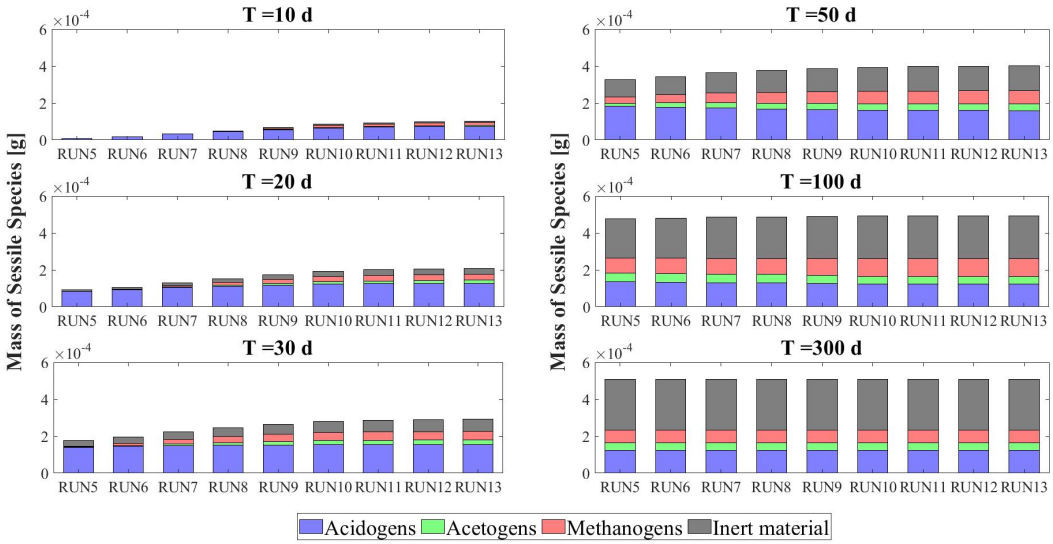


Figure 3.13: NS3 - Mass of microbial species within the granule at $T = 10\ d$, $T = 20\ d$, $T = 30\ d$, $T = 50\ d$, $T = 100\ d$ and $T = 300\ d$ under different attachment velocities $v_{a,i}$. RUN5: $v_{a,i} = 0.05\ \tilde{v}_{a,i}$, RUN6: $v_{a,i} = 0.1\ \tilde{v}_{a,i}$, RUN7: $v_{a,i} = 0.25\ \tilde{v}_{a,i}$, RUN8: $v_{a,i} = 0.5\ \tilde{v}_{a,i}$, RUN9: $v_{a,i} = \tilde{v}_{a,i}$, RUN10: $v_{a,i} = 2\ \tilde{v}_{a,i}$, RUN11: $v_{a,i} = 3\ \tilde{v}_{a,i}$, RUN12: $v_{a,i} = 4\ \tilde{v}_{a,i}$, RUN13: $v_{a,i} = 5\ \tilde{v}_{a,i}$. $\tilde{v}_{a,i}$: value of attachment velocity of the $i^{th}$ planktonic species set in RUN1. Influent wastewater composition: $S_{Su}^{in} = 3500\ g\ m^{-3}$ (Sugar), $S_{Bu}^{in} = 0$ (Butyrate), $S_{Pro}^{in} = 0$ (Propionate), $S_{Ac}^{in} = 0$ (Acetate), $S_{CH_4}^{in} = 0$ (Methane).

Fig. 3.13 and Fig. 3.14 report the mass and the relative abundance of the different sessile microbial species within the granule, respectively. Again, relevant differences concern the initial phase ($T =$ 10-20 $d$), when the total sessile mass, proportional to the granule size, is higher in the case of more intense attachment process. However, after long times both the total sessile mass and the relative abundance of individual microbial species within the granule are no longer affected by $v_{a,i}$ and all simulations achieve the same steady-state configuration.

Other interesting results refer to the effects that the granulation process has on the planktonic biomass $\psi_i^*$ (Fig. 3.15) and soluble substrates $S_j^*$ (Fig. 3.16) within the

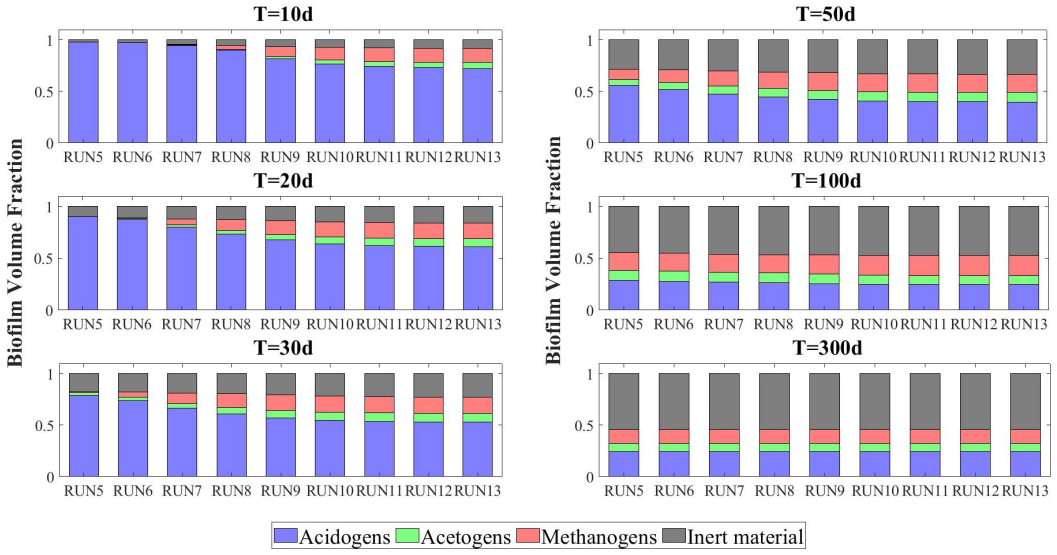


Figure 3.14: NS3 - Relative abundances of microbial species within the granule at $T = 10\ d$, $T = 20\ d$, $T = 30\ d$, $T = 50\ d$, $T = 100\ d$ and $T = 300\ d$ under different attachment velocities $v_{a,i}$. RUN5: $v_{a,i} = 0.05\ \tilde{v}_{a,i}$, RUN6: $v_{a,i} = 0.1\ \tilde{v}_{a,i}$, RUN7: $v_{a,i} = 0.25\ \tilde{v}_{a,i}$, RUN8: $v_{a,i} = 0.5\ \tilde{v}_{a,i}$, RUN9: $v_{a,i} = \tilde{v}_{a,i}$, RUN10: $v_{a,i} = 2\ \tilde{v}_{a,i}$, RUN11: $v_{a,i} = 3\ \tilde{v}_{a,i}$, RUN12: $v_{a,i} = 4\ \tilde{v}_{a,i}$, RUN13: $v_{a,i} = 5\ \tilde{v}_{a,i}$. $\tilde{v}_{a,i}$: value of attachment velocity of the $i^{th}$ planktonic species set in RUN1. Influent wastewater composition: $S^{in}_{Su} = 3500\ g\ m^{-3}$ (Sugar), $S^{in}_{Bu} = 0$ (Butyrate), $S^{in}_{Pro} = 0$ (Propionate), $S^{in}_{Ac} = 0$ (Acetate), $S^{in}_{CH_4} = 0$ (Methane).

bioreactor. The concentration profiles of the planktonic acetogens $\psi^*_{Bu} + \psi^*_{Pro}$ (green) and methanogens $\psi^*_{Ac}$ (red) in the bulk liquid, as shown in Fig. 3.15, are not very sensitive to the variation of $v_{a,i}$. Indeed, the reduction of the planktonic biomass $\psi^*_i$ depends on two phenomena: attachment and dilution. The reduction of $\psi^*_{Bu}, \psi^*_{Pro}$ and $\psi^*_{Ac}$ occurs in the initial phase of the process, when the granules are small and the attachment flux of planktonic biomass (proportional to the granule surface $A(t)$) has limited effects on the properties of the bulk liquid. On the other hand, the dilution process is prominent: the hydrodynamic conditions (i.e. high flow rate, low HRT) and slow metabolic growth (due to low maximum growth rates and limited substrate) lead to washout of planktonic acetogens and methanogens. This dilution process is not affected by granulation properties and therefore leads to similar profiles by varying $v_{a,i}$. Conversely, the planktonic acidogens $\psi^*_{Su}$ (blue) have higher growth rates and optimal conditions to grow (sugar-rich influent). Hence, they are retained in the bioreactor for longer and

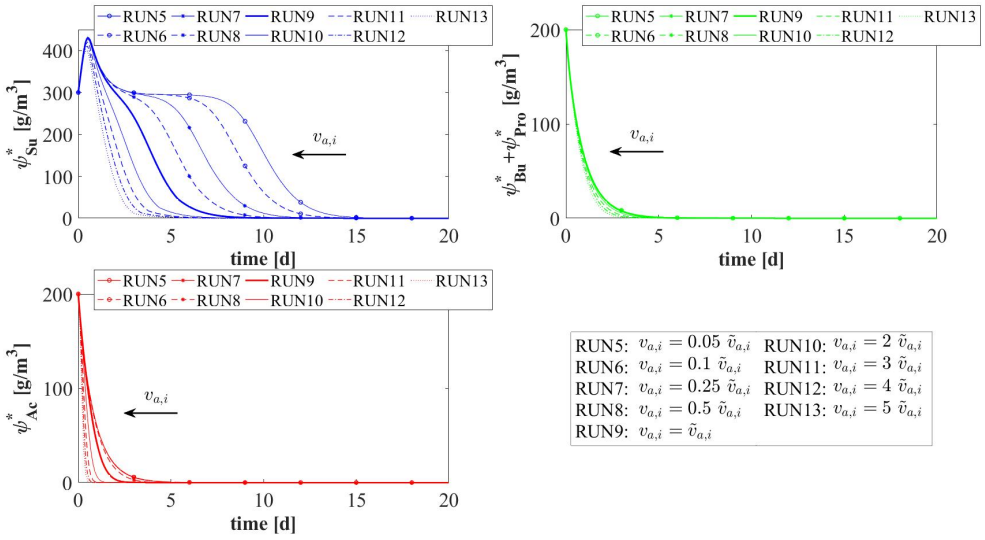


Figure 3.15: NS3 - Evolution of planktonic biomass concentrations within the bulk liquid for different attachment velocities $v_{a,i}$. $\psi^*_{Su}$: Sugar fermenters, $\psi^*_{Bu}$: Butyrate consumers, $\psi^*_{Pro}$: Propionate consumers, $\psi^*_{Ac}$: Acetoclastic methanogens. $\tilde{v}_{a,i}$: value of attachment velocity of the $i^{th}$ planktonic species set in RUN1. Influent wastewater composition: $S^{in}_{Su} = 3500\ g\ m^{-3}$ (Sugar), $S^{in}_{Bu} = 0$ (Butyrate), $S^{in}_{Pro} = 0$ (Propionate), $S^{in}_{Ac} = 0$ (Acetate), $S^{in}_{CH_4} = 0$ (Methane).

are depopulated mainly due to the granulation process, which is strongly influenced by $v_{a,i}$. Consequently, different values of $v_{a,i}$ correspond to different profiles of planktonic acidogens $\psi^*_{Su}$: the higher $v_{a,i}$, the faster the reduction of the concentration $\psi^*_{Su}$ in the bulk liquid.

Fig. 3.16 shows the trend of soluble substrates within the bioreactor. As just mentioned, in the first few days the granules have a small size and the consumption and production of soluble substrates mainly depend on the metabolic activity of the planktonic biomass. Consequently, in the initial phase the trends of soluble substrates are not affected by attachment conditions. For later times, the granule size and the amount of sessile biomass in the bioreactor increase, and the trend of the substrates becomes more sensitive to $v_{a,i}$: for small values of $v_{a,i}$ the concentrations of soluble substrates reach steady-state conditions in 40-50 days while for high values of $v_{a,i}$ half the time is required to reach a steady-state configuration.

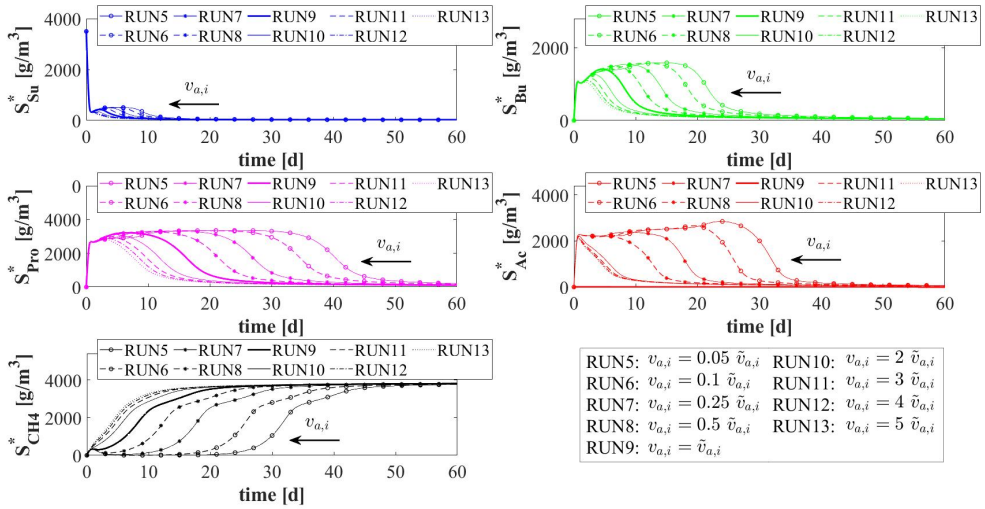


Figure 3.16: NS3 - Evolution of soluble substrates concentrations within the bulk liquid for different attachment velocities $v_{a,i}$. $S^*_{Su}$: Sugar, $S^*_{Bu}$: Butyrate, $S^*_{Pro}$: Propionate, $S^*_{Ac}$: Acetate, $S^*_{CH_4}$: Methane. $\tilde{v}_{a,i}$: value of attachment velocity of the $i^{th}$ planktonic species set in RUN1. Influent wastewater composition: $S^{in}_{Su} = 3500\ g\ m^{-3}$ (Sugar), $S^{in}_{Bu} = 0$ (Butyrate), $S^{in}_{Pro} = 0$ (Propionate), $S^{in}_{Ac} = 0$ (Acetate), $S^{in}_{CH_4} = 0$ (Methane).

### 3.4.4 NS4 - Effects of biomass density

Biomass density of the granules involved in granular biofilm systems is highly variable due to several factors, such as hydrodynamic conditions, shear forces and production. Firstly, high shear forces lead to stronger and denser granules, while weaker and more porous granule structures develop under lower shear forces [12, 87, 118]. Moreover, EPS production is generally thought to increase cell surface hydrophobicity and promote the formation of a sticky matrix favouring granulation of new cells or flocs [83]. Thus, EPS positively influences the granulation process, contributing to the maintenance of the structural integrity of the biofilm matrix and improved biomass density. Biomass density is a crucial property of granular biofilms because it regulates the mass transfer, the consumption of soluble substrates within the granules and, consequently, the growth of microbial cells and the dynamics of the granules. As a result, granules of different densities typically have different sizes and are characterized by different microbial stratifications.

In this context, a numerical study (NS4) is performed to describe the evolution of biofilm granules with different biomass densities. Four simulations (RUN14 - RUN17) are carried out using four different values of biomass density $\rho$ (RUN14: $\rho = 20000\ g\ m^{-3}$, RUN15: $\rho = 70000\ g\ m^{-3}$, RUN16: $\rho = 120000\ g\ m^{-3}$, RUN17: $\rho = 170000\ g\ m^{-3}$). The concentration of soluble substrates in the influent wastewater $S_j^{in}$ and the initial concentration of planktonic biomasses within the reactor $\psi_{i,0}^*$ set for this numerical study are the same used in NS1 and are reported in Table 3.3. Numerical results are summarised in Figs. 3.17-3.19.

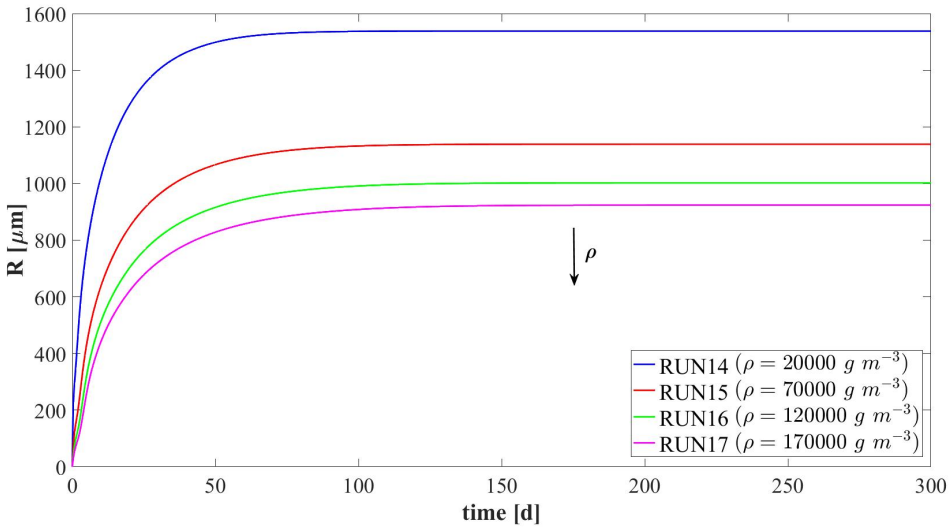


Figure 3.17: NS4 - Biofilm radius evolution over time for different biomass densities $\rho$. Influent wastewater composition: $S_{Su}^{in} = 3500\ g\ m^{-3}$ (Sugar), $S_{Bu}^{in} = 0$ (Butyrate), $S_{Pro}^{in} = 0$ (Propionate), $S_{Ac}^{in} = 0$ (Acetate), $S_{CH_4}^{in} = 0$ (Methane).

The evolution of the granule radius $R(t)$ over time is shown in Fig. 3.17. It is clear that the higher the biomass density of the granule, the smaller the steady-state radius achieved. This is due to different mass transfer conditions occurring within the granule: higher biomass densities entail higher fluxes of soluble substrates exchanged between the bulk liquid and granules. For this reason, for higher densities, the substrates in the bulk liquid are consumed faster and the metabolic growth rates driving the growth of the granule are, on average, lower. This leads to smaller granules, in accordance with Liu and Tay (2002) [12].

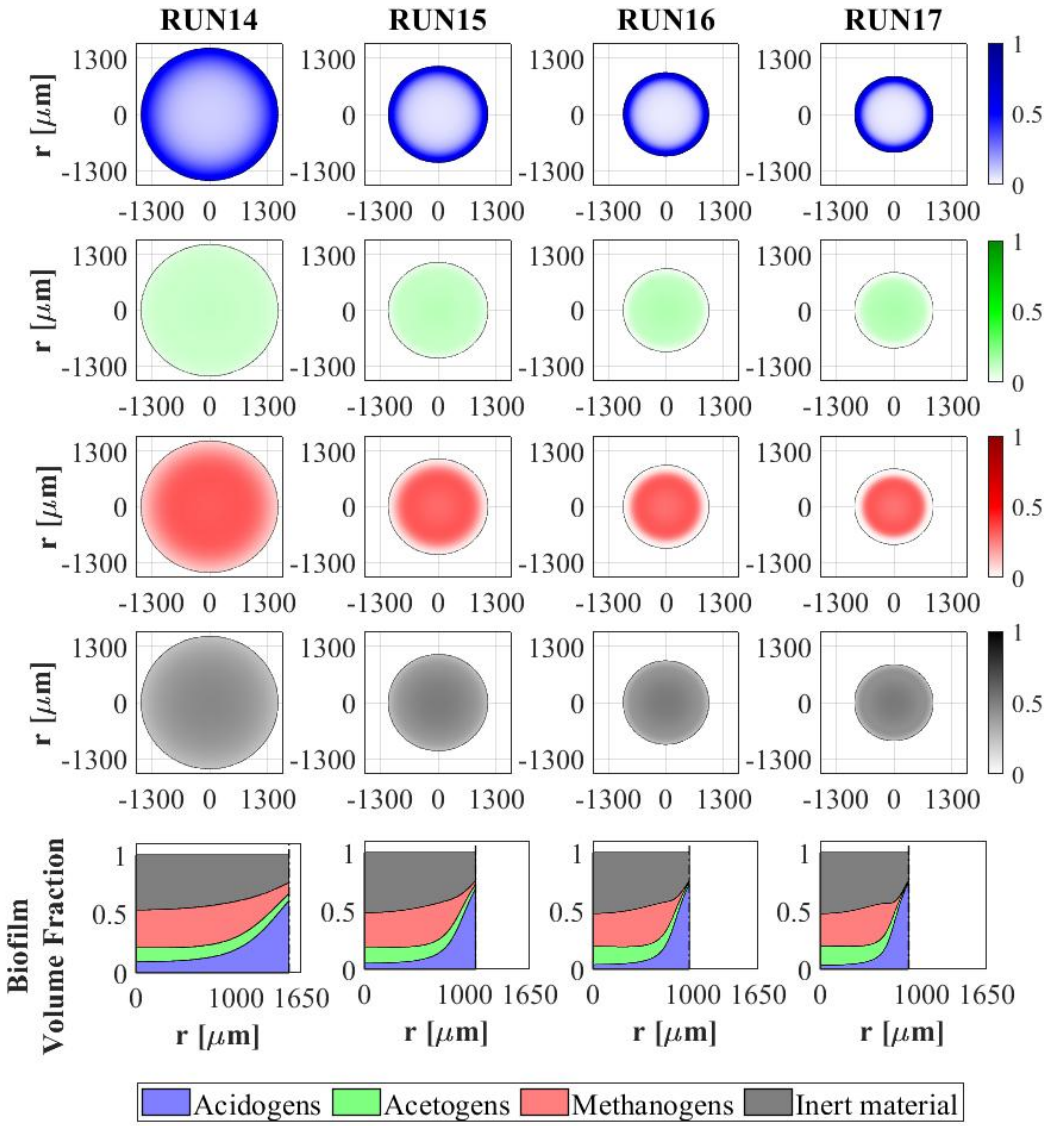


Figure 3.18: NS4 - Microbial species distribution in the diametrical section and across the radius of the granule at $T = 70\ d$, for different biomass densities. RUN14: $\rho = 20000\ g\ m^{-3}$, RUN15: $\rho = 70000\ g\ m^{-3}$, RUN16: $\rho = 120000\ g\ m^{-3}$, RUN17: $\rho = 170000\ g\ m^{-3}$. Influent wastewater composition: $S_{Su}^{in} = 3500\ g\ m^{-3}$ (Sugar), $S_{Bu}^{in} = 0$ (Butyrate), $S_{Pro}^{in} = 0$ (Propionate), $S_{Ac}^{in} = 0$ (Acetate), $S_{CH_4}^{in} = 0$ (Methane).

The microbial ecology for the four values of $\rho$ and at $T = 70\ d$ is reported in Fig. 3.18. As can be seen, granules with different densities have different microbial distributions. In particular, when $\rho = 20000\ g\ m^{-3}$ (RUN14) an homogeneous distribution is observed: although acidogens (blue) have a tendency to gather in the outermost layers and methanogens (red) and acetogens (green) have the tendency to populate the internal part, the microbial distribution within the granule is fairly homogeneous. This is due to

the mass transfer of the soluble substrates within the granule: low biomass density leads to small gradients of soluble substrates across the granule and an homogeneous growth of the different microbial species is observed throughout the biofilm. As the density of the biofilm increases (RUN15-RUN17), the gradient of soluble substrates across the biofilm increases and the layered distribution of the biomass is clearer and more visible: acidogens are strictly confined in the outer layer, while acetogens and methanogens are mostly present in the inner part. These results are in agreement with the experimental evidence reported by Batstone et al. (2004) [26].

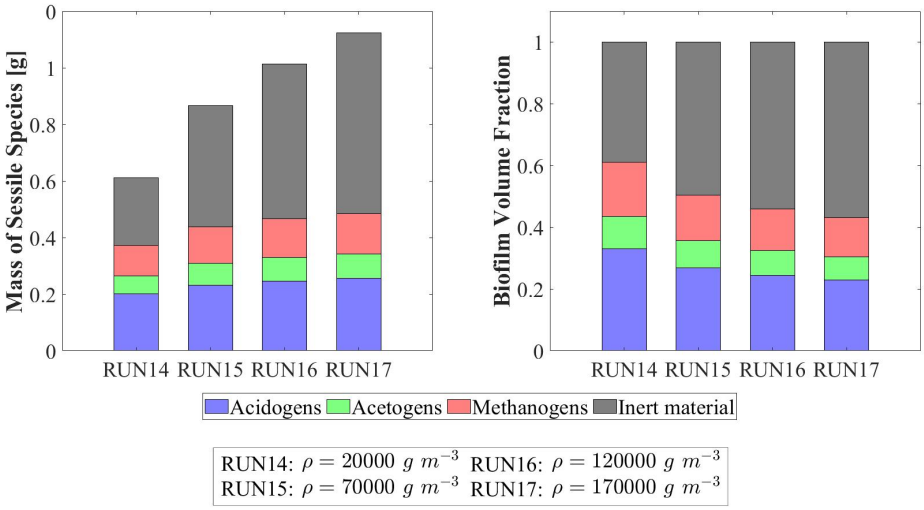


Figure 3.19: NS4 - Mass (left) and relative abundances (right) of microbial species within the granule at $T = 300\ d$ for different biomass densities $\rho$. Influent wastewater composition: $S_{Su}^{in} = 3500\ g\ m^{-3}$ (Sugar), $S_{Bu}^{in} = 0$ (Butyrate), $S_{Pro}^{in} = 0$ (Propionate), $S_{Ac}^{in} = 0$ (Acetate), $S_{CH_4}^{in} = 0$ (Methane).

In Fig. 3.19 the mass (left) and the relative abundance (right) of the sessile microbial species within the biofilm are shown at the steady-state condition ($T = 300\ d$). Higher biomass density leads higher amount (left) and fractions (right) of dead biomass accumulated as inert (black).

### 3.4.5 NS5 - Effects of erosive detachment

The evolution of the granule size is the result of a dynamic equilibrium between biomass growth, attachment of new biomass, and detachment processes. The detachment flux is essentially related to the erosion process occurring on the granule surface, due to the effect of the hydrodynamic shear forces developing in the bioreactor [119]. These forces are highly variable due to the influence of several factors, such as liquid upflow velocity, gas production, particle-particle collision, eventual mixing systems, and the geometry of the bioreactor [12, 118].

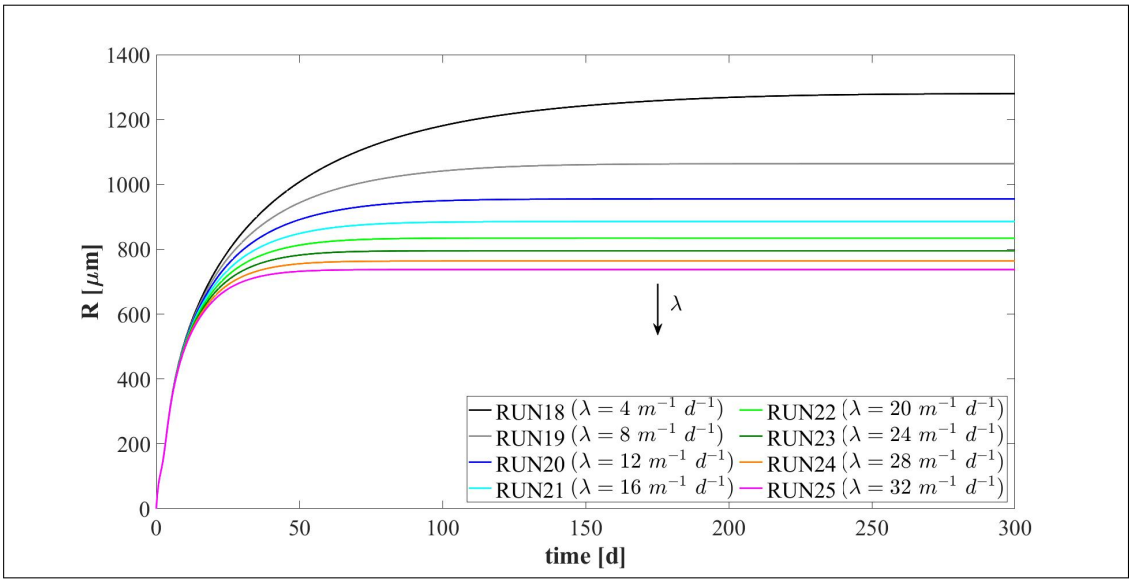


Figure 3.20: NS5 - Biofilm radius evolution over time for different detachment coefficients $\lambda$. Influent wastewater composition: $S_{Su}^{in} = 3500\ g\ m^{-3}$ (Sugar), $S_{Bu}^{in} = 0$ (Butyrate), $S_{Pro}^{in} = 0$ (Propionate), $S_{Ac}^{in} = 0$ (Acetate), $S_{CH_4}^{in} = 0$ (Methane).

Through this perspective, it is interesting to investigate the role of detachment phenomena induced by shear stress on the anaerobic granulation process, and to study their effects on granule size and, consequently, on the distribution, amount and relative abundance of sessile biomass within the granule. For this purpose, the fifth and last study (NS5) is carried out based on eight simulations (RUN18 - RUN25) with eight different values of the detachment coefficient $\lambda$, to simulate different shear stress conditions. The values used are $\lambda = 4, 8, 12, 16, 20, 24, 28, 32\ m^{-1}\ d^{-1}$. The concentration of solu-

ble substrates in the influent wastewater $S_j^{in}$ and the initial concentration of planktonic biomasses within the reactor $\psi_{i,0}^*$ set for this numerical study are the same used in NS1 and are reported in Table 3.3.

It should be noted that, contrary to the attachment, the detachment phenomenon increases as the biofilm size increases and has a negligible effect on the initial phase of granulation ($\sigma_d(t) = \lambda R^2(t)$). For this reason, the study does not focus on initial biofilm formation but investigates the long-term effects of the detachment process.

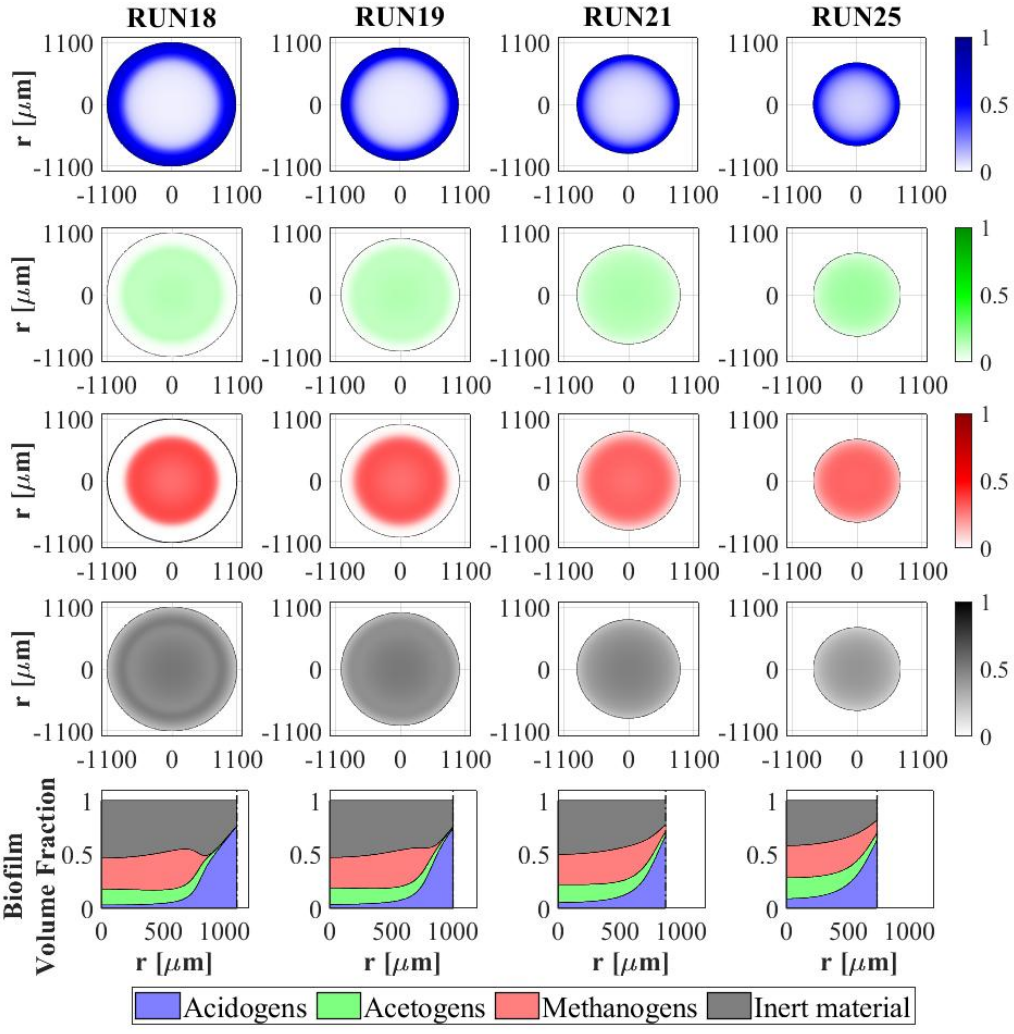


Figure 3.21: NS5 - Microbial species distribution in the diametrical section and across the radius of the granule at $T = 70\ d$, for different detachment coefficients. RUN18: $\lambda = 4\ m^{-1}\ d^{-1}$, RUN19: $\lambda = 8\ m^{-1}\ d^{-1}$, RUN21: $\lambda = 16\ m^{-1}\ d^{-1}$, RUN25: $\lambda = 32\ m^{-1}\ d^{-1}$. Influent wastewater composition: $S_{Su}^{in} = 3500\ g\ m^{-3}$ (Sugar), $S_{Bu}^{in} = 0$ (Butyrate), $S_{Pro}^{in} = 0$ (Propionate), $S_{Ac}^{in} = 0$ (Acetate), $S_{CH_4}^{in} = 0$ (Methane).

Fig. 3.20 summarises the effects that different detachment conditions have on the variation of the granule radius $R(t)$ over time and on the granule steady-state size. As explained above, the formation and the initial evolution of the granule are not affected by the detachment phenomenon. Indeed, it is clear that the trend of $R(t)$ is not influenced by $\lambda$ until $T = 10$-$20\ d$. When the granule reaches a $600\ \mu m$ radius, it becomes very sensitive to the detachment coefficient: as $\lambda$ increases, the erosion phenomenon increases, and a smaller steady-state granule size is achieved. However, the steady-state granule radius has a less than linear behaviour with increasing $\lambda$. Furthermore, in the case of positive attachment flux, steady-state $R(t)$ tends asymptotically to $0$ for $\lambda$ tending towards an infinite value. Indeed, when $R(t) = 0$ the detachment flux is null (see Eq.3.19) and any positive value of attachment flux is enough to trigger the expansion of the spherical free boundary domain.

Fig. 3.21 presents the distribution of sessile biomasses within the granule under four different detachment conditions ($\lambda = 4, 8, 16, 32\ m^{-1}\ d^{-1}$), at $T = 70\ d$. As $\lambda$ increases, an increase in the active biomass fraction $f_{Su} + f_{Bu} + f_{Pro} + f_{Ac}$ and a reduction in the inert material $f_I$ occur within the granule. Moreover, for all $\lambda$ values the granule is mainly comprised of acidogens (blue) in the external layers, and methanogens (red) and acetogens (green) at the nucleus. This distribution appears more evident when the granule is larger (low $\lambda$) and there are higher gradients of soluble substrates along the radius.

Finally, Fig. 3.22 reports the steady-state mass (top) and the relative abundance (bottom) of sessile microbial species within the granule under different detachment conditions, at $T = 300\ d$. Since the density is constant and equal in all simulations, the total sessile mass within the granule is directly proportional to the granule size. Then, a higher value of detachment coefficient $\lambda$ leads to a smaller granule, and consequently, a smaller sessile mass both overall and for individual species (Fig. 3.22-top). The relative abundances shown in Fig. 3.22 (bottom) confirm the results presented in Fig. 3.21: higher erosion conditions lead to smaller granules which are characterized by a

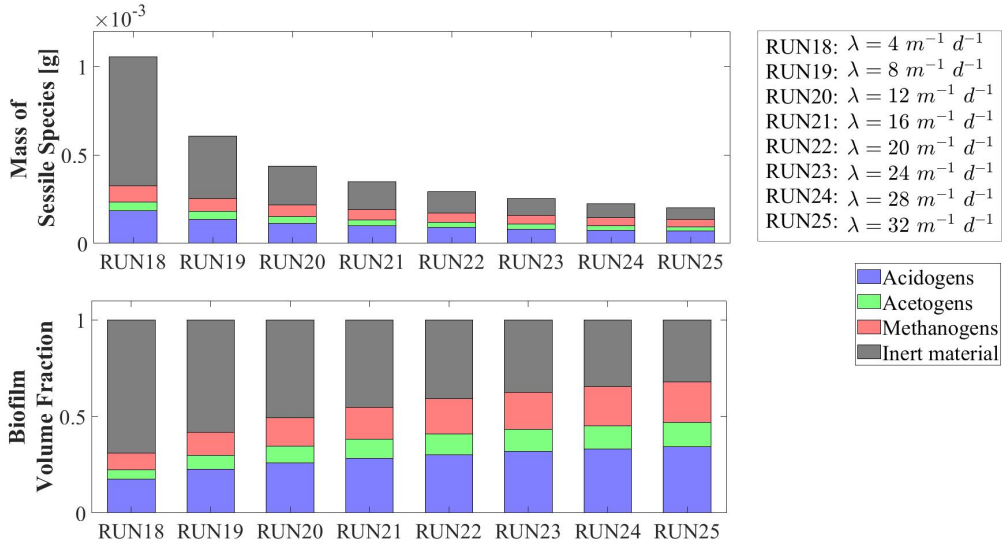


Figure 3.22: NS5 - Mass (top) and relative abundances (bottom) of microbial species within the granule at $T = 300\ d$ for different detachment coefficients $\lambda$. Influent wastewater composition: $S_{Su}^{in} = 3500\ g\ m^{-3}$ (Sugar), $S_{Bu}^{in} = 0$ (Butyrate), $S_{Pro}^{in} = 0$ (Propionate), $S_{Ac}^{in} = 0$ (Acetate), $S_{CH_4}^{in} = 0$ (Methane).

higher fraction of active biomass.

### 3.4.6 NS6 - Effects of number of granules

The latest numerical study (NS6) has been developed with the aim of investigating the effects of the parameter $N_G$ (number of granules) on the process. For this purpose, five simulations (RUN26 - RUN30) have been carried out with different values of $N_G$ (RUN26: $N_G = 2.4e9$, RUN27: $N_G = 7.4e9$, RUN28: $N_G = 2.4e10$, RUN29: $N_G = 7.4e10$, RUN30: $N_G = 2.4e11$). The concentration of soluble substrates in the influent wastewater $S_j^{in}$ and the initial concentration of planktonic biomasses within the bioreactor $\psi_{i,0}^*$ are set equal to NS1 and are reported in Table 3.3. The results of this study are shown in Figs. 3.23-3.27.

Fig. 3.23 shows the evolution of the granule radius over time. The steady-state granule size appears to be strongly affected by $N_G$. In particular, higher $N_G$ leads to smaller granules. This result is intuitive: indeed, the availability of substrates for the single granule reduces when $N_G$ increases, and this leads to a lower metabolic growth

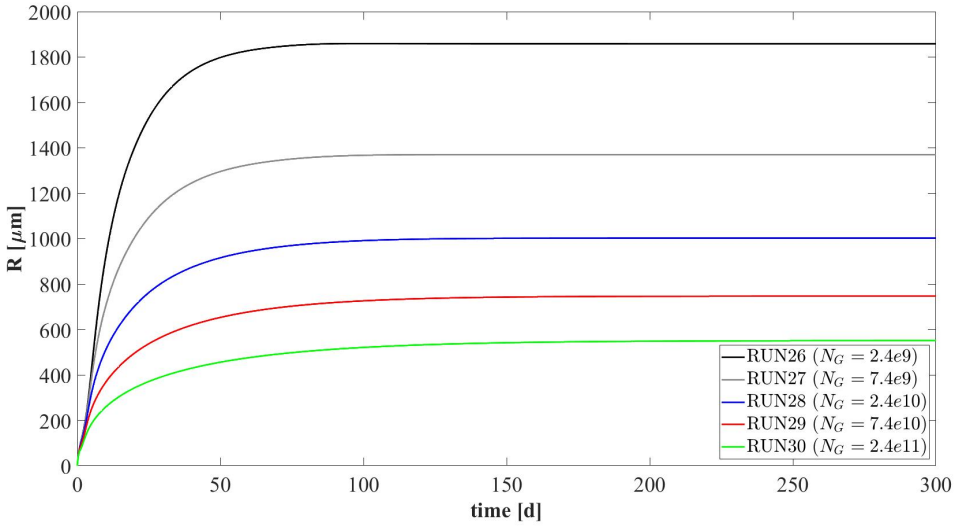


Figure 3.23: NS6 - Biofilm radius evolution over time for different numbers of granules $N_G$. Influent wastewater composition: $S_{Su}^{in} = 3500\ g\ m^{-3}$ (Sugar), $S_{Bu}^{in} = 0$ (Butyrate), $S_{Pro}^{in} = 0$ (Propionate), $S_{Ac}^{in} = 0$ (Acetate), $S_{CH_4}^{in} = 0$ (Methane).

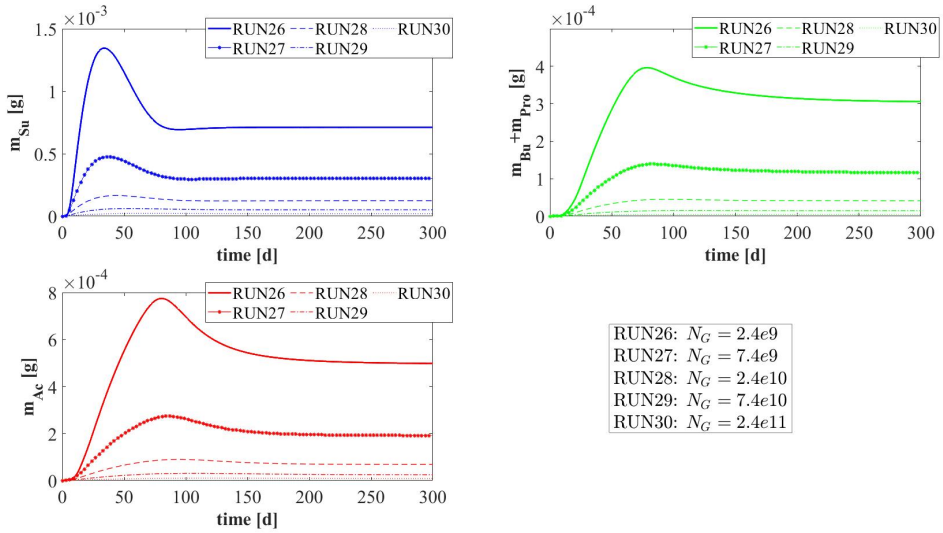


Figure 3.24: NS6 - Evolution of mass of sessile species within the reactor. $m_{Su}$: mass of sugar fermenters, $m_{Bu}$: mass of butyrate consumers, $m_{Pro}$: mass of propionate consumers, $m_{Ac}$: mass of acetoclastic methanogens. Influent wastewater composition: $S_{Su}^{in} = 3500\ g\ m^{-3}$ (Sugar), $S_{Bu}^{in} = 0$ (Butyrate), $S_{Pro}^{in} = 0$ (Propionate), $S_{Ac}^{in} = 0$ (Acetate), $S_{CH_4}^{in} = 0$ (Methane).

of sessile biomass.

Although the size and mass of the single granule decrease as $N_G$ increases, an increase in the overall mass of sessile species within the bioreactor is observed, as shown

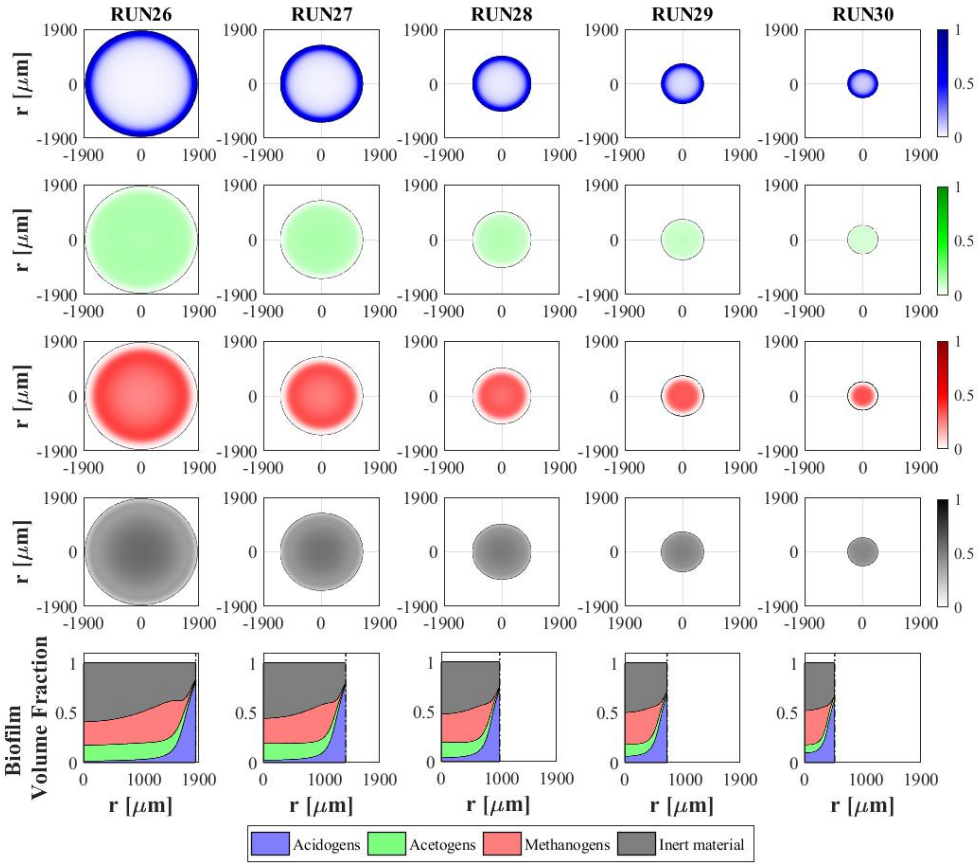


Figure 3.25: NS6 - Microbial species distribution in the diametrical section and across the radius of the granule at $T = 70\ d$, for different numbers of granules $N_G$. RUN26: $N_G = 2.4e9$, RUN27: $N_G = 7.4e9$, RUN28: $N_G = 2.4e10$, RUN29: $N_G = 7.4e10$, RUN30: $N_G = 2.4e11$. Influent wastewater composition: $S_{Su}^{in} = 3500\ g\ m^{-3}$ (Sugar), $S_{Bu}^{in} = 0$ (Butyrate), $S_{Pro}^{in} = 0$ (Propionate), $S_{Ac}^{in} = 0$ (Acetate), $S_{CH_4}^{in} = 0$ (Methane).

in Fig. 3.24. This results in an increase in the filling ratio (biomass volume over reactor volume): going from RUN26 ($N_G = 2.4e9$) to RUN30 ($N_G = 2.4e11$), the filling proportion increases from $16\%$ to $42\%$.

The microbial distribution within the granules for the five values of $N_G$, at $T = 70\ d$, is reported in Fig. 3.25. From this figure it is clear that $N_G$ does not significantly influence the microbial stratification of the granules. This occurs because the higher gradient of substrates concentration within the larger granules is balanced by the higher availability of substrates for the single granule (lower $N_G$).

The difference in the trend of sessile masses over time affects the trend of the sub-

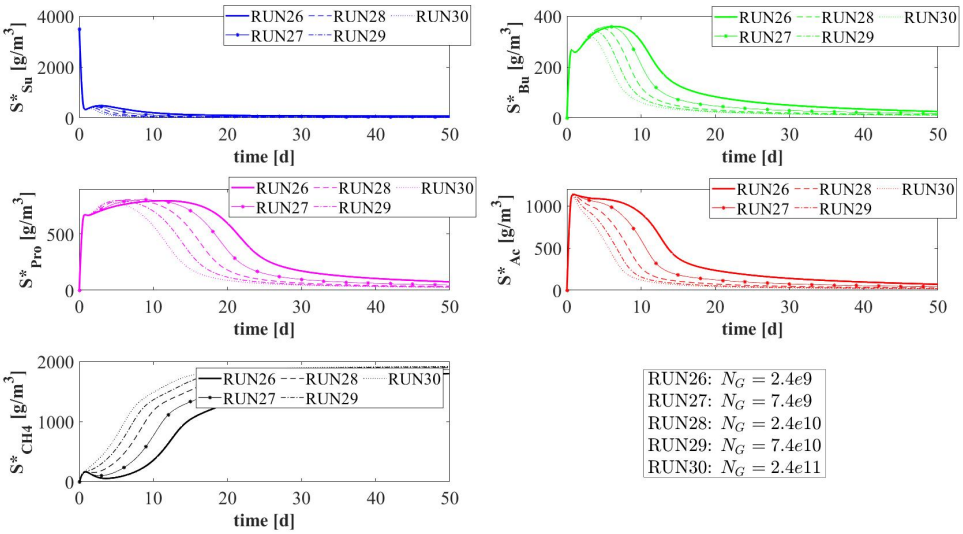


Figure 3.26: NS6 - Evolution of soluble substrates concentrations within the bulk liquid for different numbers of granules $N_G$. $S^*_{Su}$: Sugar, $S^*_{Bu}$: Butyrate, $S^*_{Pro}$: Propionate, $S^*_{Ac}$: Acetate, $S^*_{CH_4}$: Methane. Influent wastewater composition: $S^{in}_{Su} = 3500\ g\ m^{-3}$ (Sugar), $S^{in}_{Bu} = 0$ (Butyrate), $S^{in}_{Pro} = 0$ (Propionate), $S^{in}_{Ac} = 0$ (Acetate), $S^{in}_{CH_4} = 0$ (Methane).

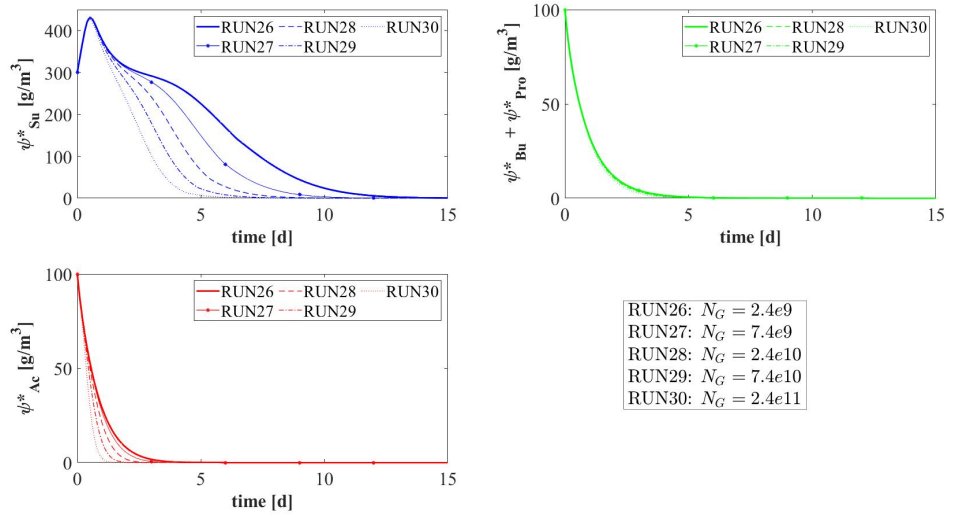


Figure 3.27: NS6 - Evolution of planktonic biomass concentrations within the bulk liquid for different numbers of granules $N_G$. $\psi^*_{Su}$: Sugar fermenters, $\psi^*_{Bu}$: Butyrate consumers, $\psi^*_{Pro}$: Propionate consumers, $\psi^*_{Ac}$: Acetoclastic methanogens. Influent wastewater composition: $S^{in}_{Su} = 3500\ g\ m^{-3}$ (Sugar), $S^{in}_{Bu} = 0$ (Butyrate), $S^{in}_{Pro} = 0$ (Propionate), $S^{in}_{Ac} = 0$ (Acetate), $S^{in}_{CH_4} = 0$ (Methane).

strates concentration within the reactor, as shown in Fig. 3.26. When $N_G$ is higher, sessile masses in the reactor are greater throughout the process and consequently the

influent substrate and its products are consumed more rapidly. In addition, small differences are also observed in the equilibrium values: when $N_G$ is lower, the amount of biomass present in the bioreactor is not able to complete the degradation of sugar, butyrate, propionate and acetate, which are present even at the steady-state condition, albeit at small concentrations. This leads to slightly different efficiencies in terms of methane production.

Finally, the overall attachment flux occurring from the bulk liquid to the granules in the first days clearly increases as the number of granules $N_G$ increases. Then, a more rapid reduction in the concentration of planktonic species is observed (Fig. 3.27).

## 3.5 Discussion

### 3.5.1 Model assumptions

An anaerobic granular biofilm reactor is an extremely complex and heterogeneous, multiphase, biological system, characterized by properties that vary over time and space. This system is constituted by a liquid medium where an assorted microbial meta-community is immersed. Most of this community is organised into granular aggregates: individual, spherical, biological structures with variable densities and comprised of species representing several different microbial trophic groups in sessile form which enhance the spatial heterogeneity. The life cycle of the *de novo* granules includes an initial phase of granulation, which leads to granule formation; a maturation phase, in which the granule size increases; and a final phase of breaking [120]. The pieces of biofilm deriving from the breaking of a granule may, in turn, originate new granules. During this evolution, the granule is affected by complex phenomena, which radically influence its structure and suddenly change its properties: granulation processes of planktonic biomass; metabolic growth and decay of sessile biomass; particle-particle interactions; EPS secretion; gas production; invasion processes by planktonic cells; and detachment processes induced

by intense hydrodynamic conditions and shear stress. The combination of these factors leads to a biological community consisting of many granules that co-exist in parallel, and vary, over time, and which differ from one another in size, density and microbial distribution. In addition, the location inside the bioreactor influences the characteristics of the granules. Indeed, due to the geometry and the hydrodynamic conditions of these systems, gradients in the concentrations of soluble substrates establish along the bioreactor and amplify the differences between granules located at different points throughout the system. However, in some cases mixing devices are added to the system, to enhance the circulation of the sludge granules and to reduce the gradients without the need to increase the flow rates and velocity.

Given its physical and biological complexity, the mathematical modelling of an anaerobic granular-based system necessarily requires the introduction of some model assumptions. In this perspective, the model presented in this Chapter describes the anaerobic granular system as a domain having a constant liquid volume where a fixed number of granules is immersed. All granules are assumed to have identical evolution and properties (same size, same density, same constituents). The single granule is modelled as a spherical, free boundary domain having a biomass density constant in time and space. Under the assumption of perfect mixing, the properties of the bulk liquid, in particular the concentration of soluble substrates and planktonic biomass, are supposed to be the same at every point and vary only over time. The attachment is modelled as a continuous, deterministic process which depends linearly on the concentration of the planktonic biomass. The detachment process is modelled as a continuous mass flux that detaches from the granule due to the effect of shear-induced erosion. No contribution by detachment to planktonic or attached biomass is considered in this model. Indeed, the detached biomass has different characteristics from both sessile and planktonic biomass and needs several hours to return to the planktonic state [121, 122, 123]. Since the HRT of this bioreactor is very low, the detached biomass does not have enough time to convert. Anyway, modelling the detached species within the bioreactor as a new set of

variables, able to grow and convert the soluble substrates, was found to have a negligible effect on the biological dynamics involved (data not shown). The process of invasion by planktonic cells present in the bulk liquid is modelled as a diffusive transport across the granule. This eliminates the restrictions on the granule's ecological structure that could be generated in particular cases, and guarantees the growth of each sessile microbial species where optimal metabolic conditions prevail. Finally, suspended substrates in the influent wastewater, gas transfer processes and EPS production are neglected as they are not significant for the purposes of the numerical investigation presented in this Chapter: qualitatively studying the anaerobic granulation process, the evolution of the granules over time and the related ecological succession.

It is emphasized that all assumptions introduced are consistent and do not compromise the objectives of the model: describing the genesis, evolution and ecology of anaerobic granules and the biological treatment process of an anaerobic granular-based bioreactor.

### 3.5.2 Size, microbial distribution, and ecology of biofilm granules, and the evolution of bulk liquid characteristics

The dimensional evolution of the granule is described through the expansion of a spherical, free boundary domain, whose radius varies over time. In particular, the *de novo* granulation process is modelled starting from an initial condition where all the biomass present in the reactor is in planktonic form and there are no biofilm granules. Subsequently, the aggregation of planktonic cells leads to granule formation. The evolution of the granule over time is governed by the positive contributions of sessile metabolic growth and attachment flux of planktonic biomass and by the negative contribution of the erosive detachment flux. In the initial phase of the process, the size of the granule grows exponentially due to the high availability of substrates. This leads to high rates of sessile metabolic growth, and the high attachment flux induced by the pres-

ence of planktonic biomass within the bulk liquid and the negligible detachment flux, proportional to the granule size ($\sigma_d(t) = \lambda R^2(t)$). Later, the concentrations of soluble substrates and the planktonic biomass within the bulk liquid reduce. This leads to a reduction in metabolic growth and attachment flux. In addition, the detachment flux intensifies as a result of the granule size increase. Consequently, the growth of the granule decreases until it reaches a steady-state value regulated by the balance between the positive source from sessile growth and the negative detachment flux.

The numerical studies show that the evolution of the granule size and its equilibrium value are deeply influenced by some factors, such as the erosion intensity, the mass transfer of soluble substrates, the composition of the influent, the granulation properties of the planktonic biomass present in the inoculum and the number of granules within the system. The model results presented in NS5 report that the granule size is governed by the erosive detachment: intense detachment forces on the granule surface limits its growth. This qualitative result is in agreement with previous observations [12, 118, 119].

As reported in NS2, the composition of the influent can affect the size of the granule due to the anabolic pathway of the species involved in the process. For example, the consumption of sugar induces more growth of sessile biomass compared to the consumption of the other substrates. As a result, for equal OLRs, an influent with higher sugar concentrations leads to the growth of more sessile biomass and larger granules. NS4 reports that more soluble substrate is consumed in denser granules, per unit of volume, and that the metabolic growth rates therefore decrease faster and lead to smaller equilibrium sizes, in accordance with Liu and Tay (2002) [12]. NS3 suggests that the granulation properties of the planktonic biomass regulate the evolution of the granule, especially in the initial phase of biofilm formation. More precisely, when the planktonic biomass is more prone to form biofilm structures and to grow in sessile form, the granulation process is more intense, and the granules grow faster. Finally, NS6 shows that the number of granules present in the system affects the steady-state granule size

by influencing the substrates dynamics within the bulk liquid.

In addition, the model describes the microbial ecology that develops in the granule and shows the distribution of the different microbial species. In the initial phase, the granulation process is governed by acidogenic and methanogenic species. This is in agreement with several studies [83, 88, 90] reporting that methanogens play a fundamental role in the formation of the initial nucleus of the granule. Indeed, some methanogenic cells have a filamentous morphology [83] and the ability to employ quorum sensing strategies [84, 94, 95] to improve their granulating properties and increase granulation efficiency. At the same time, acidogens have higher growth rates than other species, and are therefore abundant in the granule from the beginning of the process. Acidogens and methanogens exhibit the tendency to grow in different areas of the granule: the first in the outermost layer and the second in the inner part. This distribution becomes more evident over time. In particular, when the granule is mature, it is constituted by a large internal part populated by methanogens shielded by a thin external layer of acidogens. This happens because the growth rate of acidogens is higher than other species in the presence of adequate concentrations of substrate (external layers), while methanogens are able to adapt better than other species to shortage of substrates (internal layers). For extended periods, an homogeneous growth of acetogens, and the presence of inert material deriving from biomass decay, is also observed. Many experimental studies [97, 26] show a microbial distribution within anaerobic granules similar to the results proposed by the model.

However, the model suggests that some factors, such as the composition of the influent, the biomass density, and the erosive detachment intensity can radically affect the microbial distribution. For example, NS2 shows that in the case of higher sugar concentrations within the influent wastewater, the granules that develop during the process have more acidogenic biomass. Conversely, when only VFAs are present in the influent, acidogens do not develop, and methanogens and acetogens dominate the granule. Furthermore, the model qualitatively reproduces the microbial distribution observed

by Batstone et al. (2004) [26] in granules of different densities (study NS4). The biomass density deeply influences the mass transfer of the soluble substrates and, thus, the microbial ecology. Accordingly, low densities lead to small gradients of soluble substrates across the granule, and an homogeneous distribution of the microbial species is observed throughout the biofilm. More pronounced gradients develop within denser granules, leading to a more stratified distribution of biomass. According to the NS5 study, the detachment intensity appears to be an additional factor affecting the microbial distribution in an anaerobic granule, especially affecting the amount of active and inactive biomass: as mentioned above, intense erosion results in the formation of small granules where there is high availability of substrates, and active biomass prevails over inactive biomass; meanwhile, weaker erosion induces the formation of larger granules populated by more inactive biomass accumulating in the innermost zone of the granule due to the limitation of soluble substrates.

Furthermore, the model describes how the granulation process influences the characteristics of the bulk liquid and the effluent, in particular the concentration of planktonic biomasses and soluble substrates. The planktonic biomasses are present in the inoculum initially introduced in the bioreactor and represent the microbial community that initiates the granulation process. In the first few days, the concentration of planktonic biomass decreases rapidly as a consequence of attachment and dilution. The first concerns the aggregation of planktonic biomass, which converts to sessile form and contributes to the establishment of granular structures. The second is the result of the short HRT of the bioreactor. Indeed, as already reported, the HRT of granular-based systems is fixed short enough to guarantee hydrodynamic conditions and shear forces optimal for the granulation process. Such HRTs are highly unfavourable for planktonic biomass, which has insufficient time to grow and is consequently diluted [88]. In agreement with this, after a few days the planktonic biomass is completely washed out. Planktonic acidogens remain in the bulk liquid longer than other species due to their higher growth rate. Soluble substrates are produced, or consumed, in the bulk liquid

due to the effect of planktonic and sessile biomass. In the initial phase, the granules are small and the substrates are converted mainly by planktonic biomass. Subsequently, when the size of the granules increases, and the planktonic biomass has already been washed out, the trend of the substrates in the bulk liquid is governed by the granular biomass. Note that soluble substrates and planktonic biomass achieve the steady-state values over a shorter time than sessile biomass in the granule. The effluent appears to be purified at the steady-state, with the complete conversion of sugar and VFAs into methane.

Obviously, the trend of planktonic biomass and soluble substrates within the bulk liquid is influenced by the influent composition (study NS2). Furthermore, NS3 shows that the granulation properties of the planktonic microbial community initially present in the bioreactor deeply affect the velocity of the *de novo* granulation process. When the granulation process occurs faster, the conversion rate of substrates is higher, and the process reaches the steady-state sooner. Accordingly, the model results confirm that improving granulation properties of the microbial community allows for the process to be expedited and long bioreactor start-up times [84] be reduced, which represents a critical issue in the operation of granular-based systems. Finally, the number of granules present in the bioreactor influences both the dynamics of the planktonic species and the bioreactor performance (NS6). A higher number of granules implies an overall higher attachment flux and, therefore, a faster reduction of planktonic species. At the same time, a higher number of granules leads to higher sessile masses and, consequently, to faster and more effective conversion of sugars and VFAs into biomethane.

## 3.6 Conclusions

In this Chapter, a mathematical model able to reproduce the *de novo* granulation process involved in a generic, granular biofilm system has been introduced. The work presents the derivation of the model equations, which govern the expansion of the granule; the

growth of sessile biomass; and the transport of substrates and planktonic cells within the granule, under the assumption of radial symmetry. Such equations have been derived from mass balances considerations in the framework of continuum mechanics. Processes of growth, and decay, of attached and planktonic biomass; attachment from bulk liquid to biofilm; detachment from biofilm to bulk liquid; invasion of planktonic cells; and conversion, and diffusion, of soluble substrates are modelled. The model has been applied to anaerobic granular systems to test its qualitative behaviour and study the process for a case of biological and engineering interest. The model takes into account the different contributions that individual microbial trophic groups can provide to the granulation process. Specifically, in the case of the anaerobic digestion pathway, the model is able to consider the fundamental role that some species of methanogens play in granulation by setting appropriate values of attachment velocity. The results shown describe exhaustively the anaerobic granulation process; the main properties of the granules, such as dimensional evolution, ecology, biomass distribution, microbial relative abundance and distribution of soluble substrates; and the evolution of the bulk liquid characteristics (soluble substrates and planktonic biomass). Finally, further numerical studies have been carried out to investigate the effects on the process of key factors.

The most interesting observations resulting from the numerical studies include:

- The anaerobic granule presents a typical microbial stratification: methanogens and acetogens populate the innermost layers of the granule, and are shielded by a thin external layer of acidogens; the thickness of these layers depends on multiple factors (e.g. composition of the influent wastewater, biomass density, detachment forces).

- Intense flow rates and short HRTs, typical of granular biofilm systems, limit the growth of planktonic biomass, which is washed out.

- The influent wastewater composition affects the evolution, ecology and microbial

stratification of the granules.

- The granulation properties of the planktonic biomass considerably influence the start-up period of the system. Strategies, such as controlling hydrodynamic conditions, stimuling quorum sensing stimulation, and bioaugmentation may reduce the duration of this stage and enhance the efficiency of bioreactor start-up.

- The density of biomass regulates the mass transfer of soluble substrates and, consequently, the distribution of microorganisms within the granule: denser granules have a more layered structure whilst less dense granules have a more homogeneous structure.

- The detachment erosion has a large impact on the granule size and the ratio of active to inactive biomass: more erosion leads to smaller granules constituted by larger fractions of active biomass.

- The number of granules can significantly affect the granulation process (with respect to granule size) and slightly impact on bioreactor performance (with respect to substrate conversion and methane production).

Most of the results shown are qualitatively in accordance with the experimental evidence from the literature. Accordingly, this model is able to correctly simulate both the formation and maturation of anaerobic granules by focusing on both the transient and the steady state. From an engineering point of view, this allow us to conclude that the model proves to be a useful tool in studying both the start-up and the routine treatment processes of anaerobic granular biofilm systems. Furthermore, the model can be applied to any biological process proceeding in a granular-based system by choosing suitable model variables and kinetic expressions.

In any case, some model parameters, such as the values of the attachment velocities of the planktonic biomass, are introduced here for the first time and should be calibrated, and validated, on the basis of experimental data. Finally, with a view to future work, the

detachment process leading to the breaking of granules and the consequent formation of further, new granules, could be included in the model, to describe the entire life cycle of biofilm granules.

# Chapter 4

# Spherical free boundary problem for the initial phase of multispecies granular biofilm growth

## 4.1 Introduction

In most natural and human environments, microorganisms do not live as pure cultures of dispersed single cells, but are frequently embedded in a self-produced matrix of extracellular polymeric substances ($EPS$), forming complex, dense and compact biofilms [4, 5]. Many species from several trophic groups may coexist in such microbial consortia, where they interact through synergistic and antagonistic activities. Although natural biofilms typically develop as planar layers attached to suitable surfaces, in some engineering systems the aggregation occurs due to the self-immobilization of cells into approximately spherical-shaped biofilms [10]. Differently from the free-swimming planktonic cells, bacteria living in a biofilm benefit from interspecies cooperation, showing

This Chapter will be submitted as: Russo, F., Tenore, A., Mattei, M.R., Frunzo, L. Spherical free boundary problem for the initial phase of multispecies granular biofilm growth.

higher resistance capacities to toxic substances and antibiotics [103].

Biofilm formation, both in the case of planar and granular biofilms, is a dynamic and complex process which consists of several stages resulting from physical (substrate transport, invasion, attachment, detachment, etc.) and biochemical factors (microbial growth, substrate conversion, etc.) [103]. The qualitative trend of this process is illustrated in Fig. 4.1. The formation process of granular biofilms (known as granula-

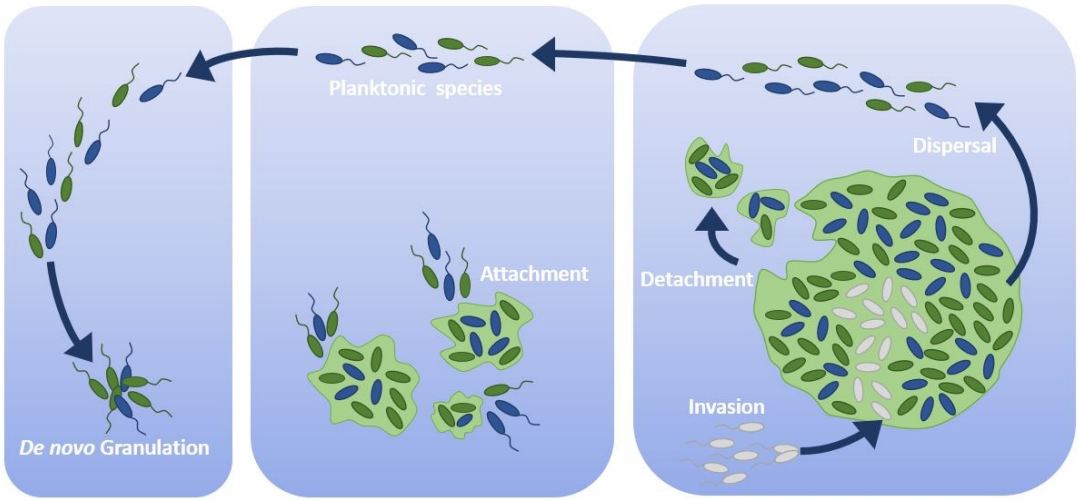


Figure 4.1: Biofilm lifecycle. (I) *De novo* granulation: biofilm formation by self-immobilization of planktonic species. (II) Granular biofilm growth: switch of mode of growth from planktonic to sessile; EPS production; attachment phenomena by planktonic species. (III) Granular biofilm maturation: invasion phenomena by planktonic species; detachment and dispersal phenomena.

tion process) is initiated by pioneering planktonic cells, which attach with each other through an initial attachment process. Such cells switch their mode of growth from planktonic to sessile and constitute the first sessile microbial colony [6]. Once attached, bacteria proliferate and secrete $EPS$, and the biofilm expands over time as a result of microbial metabolic activities. During the maturation stage, several extremely heterogeneous microenvironments form within the granular biofilm, leading to new biological conditions which can promote the microbial invasion phenomena. Thus, the biofilm is colonized by motile planktonic cells which penetrate the biofilm matrix and proliferate as a new sessile biomass, where ideal conditions for their metabolic activities occur.

Furthermore, external shear forces, nutrients depletion and biomass decay lead to the detachment of cells from the biofilm into the surrounding medium. Conversely, detachment can be initiated internally, leading to the dispersion of individual planktonic cells.

Despite the large number of mathematical works on multispecies biofilms growth and formation developed in the framework of continuum mathematical modelling both in the case of planar [124, 125, 126] and granular biofilms [27, 28, 30], most of them completely neglect the attachment process in the initial phase of the biofilm formation. Indeed, usually the initial conditions of location, size, and biofilm composition at the onset of the simulations are arbitrarily assigned. Only the $1D$ biofilm model and the granular biofilm model introduced by D'Acunto et al. (2019, 2021) [24, 127] and Tenore et al. (2021) [128] focus on the *de novo* formation of biofilms, by considering a vanishing initial domain.

According to D'Acunto et al. (2019, 2021) [24, 127], the present Chapter mainly deals with the modelling of the flux of planktonic species moving from the bulk liquid to the granular biofilm surface, which seems to be the main regulating mechanism for biofilm early stage attachment [6]. The mathematical model presented in this Chapter considers the initial biofilm formation mediated by pioneering planktonic cells as well as the colonization process. Specifically, it considers two state variables representing the planktonic and sessile phenotypes and the conversion from the first to the second during the granulation process. Attachment is modelled as a continuous deterministic process which depends on the concentrations of the planktonic species in the surrounding medium [24, 127], while the invasion process is modelled by considering an additional reaction term, which depends on the concentration of planktonic species within the biofilm [23]. Note, that modelling the attachment phenomenon does not require the definition of any initial conditions as the initial biofilm domain is supposed to be equal to zero and the species composition is modelled according to the environmental conditions.

The Chapter is organized as follows. Section 4.2 presents the spherical free boundary value problem that models the attachment process in the initial phase of multispecies granular biofilm formation in the framework of continuous models [22]. The spherical free boundary is represented by the granular biofilm radius under the assumption of radial symmetry, and is governed by a first order differential equation that depends on: microbial growth, attachment, invasion and detachment. Biofilm formation is initiated by the attachment process, which leads to consider an initial vanishing domain of the granular biofilm. The growth of the attaching species is governed by non-linear hyperbolic partial differential equations (PDEs). During the first instants of the biofilm formation, the free boundary velocity is greater than the characteristic velocity of such hyperbolic system, and, consequently, it is a space-like line [24, 127]. The initial-boundary conditions for the microbial concentrations are assigned on this line, and they are equal to the microbial species relative abundances in the biomass which attach on the granule-bulk liquid interface. Moreover, the attachment flux is modelled as a linear function of the planktonic species concentration, each of which is characterized by a specific attachment velocity [24, 128, 127]. The free boundary value problem is completed by a system of semi-linear elliptic PDEs that governs the quasi-static diffusion of substrates. Moreover, it has been proved that equations describing the growth and transport of sessile biomass hold for $r = 0$ in Section 4.2. Section 4.2.2 introduces the characteristic coordinates that allow for the conversion of the differential equations into integral equations. The complete integral version of the original differential free boundary problem is provided in Section 4.3. An existence and uniqueness theorem of solutions is shown in Section 4.4 in the class of continuous functions. Finally, the conclusions of the work are outlined in Section 4.5.

## 4.2 Modelling the initial phase of multispecies granular biofilm growth

The free boundary approach introduced in D'Acunto et al. (2021) [127] for modeling the initial phase of the multispecies $1D$ biofilm formation and growth in the framework of Wanner-Gujer model [22] is here applied to the case of multispecies granular biofilm. The growth of multispecies granular biofilm is governed by the following system of non-linear hyperbolic partial differential equations:

$$\frac{\partial X_i(r,t)}{\partial t} + \frac{1}{r^2}\frac{\partial}{\partial r}(r^2 u(r,t) X_i(r,t)) = \rho_i r_{M,i} + \rho_i r_i,\ i = 1, ..., n, \tag{4.1}$$

where $X_i(r,t)$ denotes the concentration of the $i^{th}$ microbial species; $t$ and $r$ indicate time and space variables, respectively; $u(r,t)$ denotes the velocity of the microbial mass; $r_{M,i}$ and $r_i$ are the specific growth rates due to sessile and planktonic species, respectively; $\rho_i$ is the constant density. The granular biofilm center is located in $r = 0$.

The function $r_{M,i}$ depends on sessile species $X_i$ , $i = 1, ..., n$, and substrates $S_j$, $j = 1, ..., m$, while the function $r_i$ depends on planktonic species $\psi_i$ , $i = 1, ..., n$, and substrates $S_j$, $j = 1, ..., m$:

$$r_{M,i} = r_{M,i}(\mathbf{X}(r,t), \mathbf{S}(r,t)), \tag{4.2}$$

$$r_i = r_i(\boldsymbol{\psi}(r,t), \mathbf{S}(r,t)), \tag{4.3}$$

where $\mathbf{X} = (X_1, ..., X_n)$, $\boldsymbol{\psi} = (\psi_1, ..., \psi_n)$, $\mathbf{S} = (S_1, ..., S_m)$.

$u(r,t)$ is governed by the following equation:

$$\frac{\partial u(r,t)}{\partial r} = -\frac{2u(r,t)}{r} + \sum_{i=1}^{n}(r_{M,i} + r_i),\ u(0,t) = 0. \tag{4.4}$$

The diffusion of substrates and colonizing species within the biofilm is governed by

semi-linear parabolic partial differential equations that are usually considered in quasi-static conditions:

$$-D_{S,j}\frac{1}{r^2}\frac{\partial}{\partial r}\left(r^2\frac{\partial S_j}{\partial r}\right) = r_{S,j}(\mathbf{X}(r,t),\mathbf{S}(r,t)),\ j=1,...,m, \tag{4.5}$$

$$-D_{\psi,i}\frac{1}{r^2}\frac{\partial}{\partial r}\left(r^2\frac{\partial \psi_i}{\partial r}\right) = r_{\psi,i}(\boldsymbol{\psi}(r,t),\mathbf{S}(r,t)),\ i=1,...,n, \tag{4.6}$$

where $r_{S,j}$ denotes the conversion rate of the $j^{th}$ substrate and $r_{\psi,j}$ indicates the conversion rate due to the switch of the mode of growth from planktonic to sessile; and $D_{S,i}$ and $D_{\psi,i}$ are the diffusivity coefficients of the substrates and the planktonic species within the biofilm, respectively.

The biofilm size $R(t)$ (the radius of the biofilm granule) represents the spherical free boundary of the mathematical problem. Its evolution is governed by the following equation [22, 24, 127]:

$$\dot{R}(t) = u(R(t),t) + \sigma_a(t) - \sigma_d(t), \tag{4.7}$$

where $\sigma_a$ denotes the attachment velocity of biomass from bulk liquid to biofilm and $\sigma_d$ denotes the detachment velocity of biomass from biofilm to bulk liquid. The function $\sigma_a$ linearly depends on the concentrations of the microbial species in planktonic form $\psi_i^*$, $i=1,...,n$, $\boldsymbol{\psi}^* = (\psi_1^*,...,\psi_n^*)$, suspended in the bulk liquid [22, 24, 107, 127], each of which is characterized by a specific attachment velocity $v_{a,i}$:

$$\sigma_a(t) = \sum_{i=1}^{n}\sigma_{a,i}(t) = \frac{\sum_{i=1}^{n} v_{a,i}\psi_i^*(t)}{\rho_i}. \tag{4.8}$$

The attachment velocities can be assigned constant or can be considered as functions of the environmental conditions affecting biofilm growth, that is substrates concentrations, biofilm composition itself, electrostatic and mechanical properties of the surface. Meanwhile, the function $\sigma_d$ is modelled through a continuous flux from granule to bulk

liquid, which is a quadratic function of the granule radius $R(t)$ [110]:

$$\sigma_d(t) = \delta R^2(t), \tag{4.9}$$

where $\delta$ depends on the mechanical properties of the biofilm. In the initial phase of biofilm formation, the attachment process prevails and the detachment process is very small, since so is $R^2$ . Therefore, as shown by D'Acunto et al. (2021) [127] in this circumstances it is $\sigma_a - \sigma_d > 0$ and the free boundary velocity is greater than the characteristic velocity ($\dot{R}(t) > u(R,t)$). Thus, the spherical free boundary is a space-like line. For mature biofilms the spherical free boundary $R$ becomes greater, the detachment is the prevailing process ($\sigma_a - \sigma_d < 0$) and the free boundary is a time-like line. The initial-boundary conditions for Eqs. (4.1), (4.5)-(4.7) are the following [24, 127]:

$$X_i(R(t),t) = X_{i,0}(t),\ i = 1, ..., n, \tag{4.10}$$

$$\frac{\partial S_j}{\partial r}(0,t) = 0,\ S_j(R(t),t) = S_j^*(t),\ j = 1, ..., m, \tag{4.11}$$

$$\frac{\partial \psi_i}{\partial r}(0,t) = 0,\ \psi_i(R(t),t)) = \psi_i^*(t),\ i = 1, ..., n, \tag{4.12}$$

$$L(0) = 0. \tag{4.13}$$

In Eq. (4.10), $X_{i,0}(t)$ is the relative abundance of the $i^{th}$ species in the biomass attached to the granule-bulk liquid interface [127]. More precisely, $X_{i,0}(t)$ can be evaluated as [127]:

$$X_{i,0}(t) = \frac{v_{a,i}\psi_i^*(t)}{\sum_{i=1}^{n} v_{a,i}\psi_i^*(t)}\rho_i,\ i = 1, ..., n, \tag{4.14}$$

According to Eq. (4.14), the concentration of the microbial species at the granule-

bulk liquid interface $X_i(R(t),(t))$, for a multispecies granular biofilm under attachment regime, depends on the concentrations of the species in planktonic form present in the bulk liquid and its attachment capacity. Note that, when all microbial species in the bulk liquid are characterized by the same attachment velocity, Eq. (4.14) reduces to:

$$\frac{X_{i,0}(t)}{\rho_i} = \frac{\psi_i^*(t)}{\sum_{i=1}^{n} \psi_i^*(t)},\ i = 1, ..., n, \tag{4.15}$$

that is the volume fraction of the $i^{th}$ microbial species at the granule-bulk liquid interface assumes the same value of the volume fraction within the bulk liquid. This reproduces the case of a granular biofilm that will be initially constituted by all microbial species inhabiting the surrounding liquid environment. However, going on with time the biofilm composition is affected by other factors such as substrate availability, specific microbial growth rate, invasion phenomena, detachment flux. Regarding the diffusion of substrates and planktonic species, the boundary conditions $(4.11)_1$ and $(4.12)_1$ are the no flux conditions at the granule center ($r = 0$). While, the boundary conditions $(4.11)_2$ and $(4.12)_2$ are Dirichlet conditions, which state that the values of the substrates and planktonic species on the free boundary are the same as in the bulk liquid. The functions $S_j^*(t)$ and $\psi_j^*(t)$ are prescribed functions in general.

An equivalent expression of Eq. (4.1) can be obtained by using the volume fractions $f_i$ defined as $f_i(r,t) = X_i(r,t)/\rho_i$, $i = 1, ..., n$, subjected to the constraint: $\sum_{i=1}^{n} f_i = 1$. Considering $f_i$ in Eq. (4.1) yields:

$$\frac{\partial f_i(r,t)}{\partial t} + \frac{1}{r^2}\frac{\partial}{\partial r}(r^2 u(r,t) f_i(r,t)) = r_{M,i} + r_i,\ i = 1, ..., n, \tag{4.16}$$

In this case, the initial condition (4.10) is replaced by:

$$f_i(R(t),t) = f_{i,0}(t), i = 1, ..., n, \tag{4.17}$$

where:

$$f_{i,0}(t) = \frac{X_{i,0}(t)}{\rho_i}. \tag{4.18}$$

In summary, the attachment process in the initial phase of multispecies granular biofilm growth is expressed by the following spherical free boundary problem:

$$\frac{\partial X_i}{\partial t} + \frac{1}{r^2}\frac{\partial}{\partial r}(r^2 u X_i) = \rho_i r_{M,i}(\mathbf{X}, \mathbf{S}) + \rho_i r_i(\boldsymbol{\psi}, \mathbf{S}), 0 \leq r \leq R(t),\ t > 0,\ i = 1, ..., n, \tag{4.19}$$

$$X_i(R(t), t) = X_{i,0}(t),\ t > 0,\ i = 1, ..., n, \tag{4.20}$$

$$\dot{R}(t) = u(R(t), t) + \sigma_a(\boldsymbol{\psi}^*),\ t > 0,\ R(0) = 0 \tag{4.21}$$

$$\frac{\partial u(r,t)}{\partial r} = -\frac{2u(r,t)}{r} + G(\mathbf{X}(r,t), \mathbf{S}(r,t), \boldsymbol{\psi}(r,t)),\ 0 < r \leq R(t),\ u(0,t) = 0, \tag{4.22}$$

where:

$$G(\mathbf{X}(r,t), \mathbf{S}(r,t), \boldsymbol{\psi}(r,t)) = \sum_{i=1}^{n}(r_{M,i} + r_i), \tag{4.23}$$

$$-D_{S,j}\frac{1}{r^2}\frac{\partial}{\partial r}\left(r^2\frac{\partial S_j}{\partial r}\right) = r_{S,j}(\mathbf{X}(r,t), \mathbf{S}(r,t)),\ 0 < r < R(t),\ t > 0,\ j = 1, ..., m, \tag{4.24}$$

$$\frac{\partial S_j}{\partial r}(0,t) = 0,\ S_j(R(t), t) = S_j^*(t),\ t > 0,\ j = 1, ..., m, \tag{4.25}$$

$$-D_{\psi,i}\frac{1}{r^2}\frac{\partial}{\partial r}\left(r^2\frac{\partial \psi_i}{\partial r}\right) = r_{\psi,i}(\boldsymbol{\psi}(r,t),\mathbf{S}(r,t)),\ 0<r<R(t),\ t>0,\ \ i=1,...,n, \tag{4.26}$$

$$\frac{\partial \psi_i}{\partial r}(0,t)=0,\ \psi_i(R(t),t)=\psi_i^*(t),\ t>0,\ i=1,...,n. \tag{4.27}$$

Note that Eq. (4.21) refers to the initial phase of biofilm formation, when the detachment flux $\sigma_d$ is negligible compared to $\sigma_a$. The spherical free boundary $R(t)$ is a space-like line and Eq. (4.20) provides the initial conditions for the microbial species in sessile form on the free boundary.

### 4.2.1 Remark 1

Eq. (4.19) has an apparent singularity for $r=0$. In this Section, it has been proved that Eq. (4.19) holds also for $r=0$, as the singularity may be eliminated.

Eq. (4.19) can be rewritten as:

$$\frac{\partial X_i(r,t)}{\partial t}+X_i(r,t)\frac{\partial u(r,t)}{\partial r}+\frac{2u(r,t)X_i(r,t)}{r}+u(r,t)\frac{\partial X_i(r,t)}{\partial r}=\rho_i r_{M,i}+\rho_i r_i,$$

$$i=1,...,n. \tag{4.28}$$

Consider the Taylor's series expansion of $u(r,t)$ about $r=0$:

$$u(r,t)=u(0,t)+\frac{\partial u(0,t)}{\partial r}r+... \tag{4.29}$$

Taking into account the boundary condition in Eq. (4.22), it follows:

$$\lim_{r\to 0}\frac{u(r,t)}{r}=\frac{\partial u(0,t)}{\partial r}. \tag{4.30}$$

By considering Eq. (4.30), Eqs. (4.22) and (4.28) for $r=0$ may be replaced by:

$$\frac{\partial u(0,t)}{\partial r}=\frac{G(\mathbf{X}(0,t),\mathbf{S}(0,t),\boldsymbol{\psi}(0,t))}{3}, \tag{4.31}$$

$$\frac{\partial X_i(0,t)}{\partial t}+3X_i(0,t)\frac{\partial u(0,t)}{\partial r}=\rho_i r_{M,i}+\rho_i r_i. \tag{4.32}$$

Substituting Eq. (4.31) in Eq. (4.32) yields:

$$\frac{\partial X_i(0,t)}{\partial t}=\rho_i r_{M,i}+\rho_i r_i-X_i(0,t)G(\mathbf{X}(0,t),\mathbf{S}(0,t),\boldsymbol{\psi}(0,t)). \tag{4.33}$$

Eq. (4.33) replaces Eq. (4.28) for $r=0$ and confirms that Eq. (4.19) holds also for $r=0$.

### 4.2.2 Characteristic coordinates

Consider the characteristic-like lines $r=r(t)$ of system (4.1). They are defined by the differential equation:

$$\frac{\partial r(t)}{\partial t}=u(r(t),t). \tag{4.34}$$

Since they also depend on the starting point $t_0$, we will use the notation $r(t)=c(t_0,t)$. Therefore, more precisely, the characteristics are defined by the following initial value problem:

$$\frac{\partial c}{\partial t}(t_0,t)=u(c(t_0,t),t),\ \ c(t_0,t_0)=R(t_0). \tag{4.35}$$

In particular, for $t_0=0$ we have:

$$\frac{\partial c}{\partial t}(0,t) = u(c(0,t),t), \;\; c(0,0) = 0, \tag{4.36}$$

since $R(0) = 0$. The initial value problem (4.36) admits the solution $c(0,t) = 0$ because of condition in Eq. (4.22).

In characteristic coordinates, the integral form of Eq. (4.22) can be written as:

$$u(c(t_0,t),t) = \frac{1}{c^2(t_0,t)} \int_0^{t_0} c^2(\tau,t) G(\mathbf{X}(c(\tau,t),t), \mathbf{S}(c(\tau,t),t), \boldsymbol{\psi}(c(\tau,t),t)) \frac{\partial}{\partial \tau} c(\tau,t) d\tau. \tag{4.37}$$

Consider Eq. (4.21) for $R$ written for $t = t_0$:

$$\dot{R}(t_0) = \sigma_a(\boldsymbol{\psi}^*(t_0)) + u(R(t_0),t_0), \; R(0) = 0, \; (\sigma_a > 0). \tag{4.38}$$

Since $u(R(t_0),t_0) = u(c(t_0,t_0),t_0)$, we can use Eq. (4.37) in Eq. (4.38) to obtain:

$$\dot{R}(t_0) = \sigma_a(\boldsymbol{\psi}^*(t_0))$$

$$+ \frac{1}{c^2(t_0,t_0)} \int_0^{t_0} c^2(\tau,t_0) G(\mathbf{X}(c(\tau,t_0),t_0), \mathbf{S}(c(\tau,t_0),t_0), \boldsymbol{\psi}(c(\tau,t_0),t_0)) \frac{\partial}{\partial \tau} c(\tau,t_0) d\tau, \tag{4.39}$$

After, integrating over $(0,t_0)$ we obtain:

$$R(t_0) = \int_0^{t_0} \sigma_a(\boldsymbol{\psi}^*(\theta)) d\theta$$

$$+ \int_0^{t_0} \frac{1}{c^2(\theta,\theta)} d\theta \int_0^{\theta} c^2(\tau,\theta) G(\mathbf{X}(c(\tau,\theta),\theta), \mathbf{S}(c(\tau,\theta),\theta), \boldsymbol{\psi}(c(\tau,\theta),\theta)) \frac{\partial}{\partial \tau} c(\tau,\theta) d\tau. \tag{4.40}$$

Equation (4.40) is the desired integral equation for $R$ in characteristic coordinates. Note the function $R$ defined by Eq. (4.40) satisfies the differential equation in $(4.38)_1$ and the initial condition $(4.38)_2$. Therefore, the integral equation (4.40) is equivalent to the differential initial value problem (4.38).

Substituting Eq. (4.37) in Eq. (4.35), it follows:

$$\frac{\partial}{\partial t}c(t_0,t) = \frac{1}{c^2(t_0,t)}\int_0^{t_0} c^2(\tau,t)G(\mathbf{X}(c(\tau,t),t),\mathbf{S}(c(\tau,t),t),\boldsymbol{\psi}(c(\tau,t),t))\frac{\partial c}{\partial \tau}(\tau,t)d\tau, \tag{4.41}$$

Let us integrate over $(t_0,t)$:

$$c(t_0,t) - c(t_0,t_0)$$

$$= \int_{t_0}^{t} \frac{1}{c^2(t_0,\theta)}d\theta \int_0^{t_0} c^2(\tau,\theta)G(\mathbf{X}(c(\tau,\theta),\theta),\mathbf{S}(c(\tau,\theta),\theta),\boldsymbol{\psi}(c(\tau,\theta),\theta))\frac{\partial}{\partial \tau}c(\tau,\theta)d\tau, \tag{4.42}$$

$$c(t_0,t) = R(t_0)$$

$$+ \int_{t_0}^{t} \frac{1}{c^2(t_0,\theta)}d\theta \int_0^{t_0} c^2(\tau,\theta)G(\mathbf{X}(c(\tau,\theta),\theta),\mathbf{S}(c(\tau,\theta),\theta),\boldsymbol{\psi}(c(\tau,\theta),\theta))\frac{\partial}{\partial \tau}c(\tau,\theta)d\tau, \tag{4.43}$$

Lastly, substituting expression (4.40) of $R(t_0)$ in Eq. (4.43) yields:

$$c(t_0,t) = \int_0^{t_0} \sigma_a(\boldsymbol{\psi}^*(\theta))d\theta$$

$$+\int_0^{t_0}\frac{1}{c^2(\theta,\theta)}d\theta\int_0^{\theta}c^2(\tau,\theta)G(\mathbf{X}(c(\tau,\theta),\theta),\mathbf{S}(c(\tau,\theta),\theta),\boldsymbol{\psi}(c(\tau,\theta),\theta))\frac{\partial c}{\partial\tau}(\tau,\theta)d\tau$$

$$+\int_{t_0}^{t}\frac{1}{c^2(t_0,\theta)}d\theta\int_0^{t_0}c^2(\tau,\theta)G(\mathbf{X}(c(\tau,\theta),\theta),\mathbf{S}(c(\tau,\theta),\theta),\boldsymbol{\psi}(c(\tau,\theta),\theta))\frac{\partial c}{\partial\tau}(\tau,\theta)d\tau. \tag{4.44}$$

Equation (4.44) is the desired integral equation for the characteristics. Note that the function $c(t_0,t)$ defined by (4.44) satisfies the differential equation in $(4.35)_1$ and the initial condition $(4.35)_2$. Therefore, the integral equation (4.44) is equivalent to the differential initial value problem (4.35).

In addition, the partial derivative of $c(t_0,t)$ with respect to $t_0$ satisfies the following integral equation:

$$\frac{\partial}{\partial t_0}c(t_0,t)=\sigma_a(\boldsymbol{\psi}^*(t_0))+\int_{t_0}^{t}G(\mathbf{X}(c(t_0,\theta),\theta),\mathbf{S}(c(t_0,\theta),\theta),\boldsymbol{\psi}(c(t_0,\theta),\theta))\frac{\partial}{\partial t_0}c(t_0,\theta)d\theta. \tag{4.45}$$

The previous equation is needed as $\partial c/\partial t_0$ appears in the integral equations (4.44) and (4.40).

Consider system (4.19) rewritten in characteristic coordinates:

$$\frac{dX_i}{dt}(c(t_0,t),t)=\rho_i r_{M,i}(\mathbf{X}(c(t_0,t),t),\mathbf{S}(c(t_0,t),t))+\rho_i r_i(\boldsymbol{\psi}(c(t_0,t),t),\mathbf{S}(c(t_0,t),t))$$

$$-X_i(c(t_0,t),t)G(\mathbf{X}(c(t_0,t),t),\mathbf{S}(c(t_0,t),t),\boldsymbol{\psi}(c(t_0,t),t)),0\le t_0<t\le T,\ i=1,...,n, \tag{4.46}$$

where Eq. (4.22) was used. The initial conditions for $t = t_0$ are derived from (4.20):

$$X_i(c(t_0, t_0), t_0) = X_i(R(t_0), t_0) = X_{i,0}(t_0),\ i = 1, ..., n. \tag{4.47}$$

From (4.46), it follows:

$$\frac{dX_i}{dt}(c(t_0,t),t) = F_i(\mathbf{X}(c(t_0,t),t), \mathbf{S}(c(t_0,t),t), \boldsymbol{\psi}(c(t_0,t),t)), 0 \le t_0 < t \le T, i = 1, ..., n, \tag{4.48}$$

where:

$$F_i = \rho_i r_{M,i} + \rho_i r_i - X_i G,\ i = 1, ..., n. \tag{4.49}$$

Integrating Eq. (4.48) over $(t_0, t)$ yields:

$$X_i(c(t_0,t),t) = X_{i,0}(t_0)$$

$$+ \int_{t_0}^{t} F_i(\mathbf{X}(c(t_0,\tau),\tau), \mathbf{S}(c(t_0,\tau),\tau), \boldsymbol{\psi}(c(t_0,\tau),\tau))d\tau,\ 0 \le t_0 < t \le T,\ i = 1, ..., n. \tag{4.50}$$

The equation above is the desired integral equation for $X_i$ in characteristic coordinates. Note that the integral equation (4.50) is equivalent to the differential initial value problem (4.46)-(4.47).

Consider Eq. (4.24) rewritten in characteristic coordinates:

$$D_{S,j} \frac{1}{c^2(t_0,t)} \frac{\partial}{\partial r}\left(c^2(t_0,t) \frac{\partial S_j}{\partial r}(c(t_0,t),t)\right) = -r_{S,j}(\mathbf{X}(c(t_0,t),t), \mathbf{S}(c(t_0,t),t)), j = 1, ..., m. \tag{4.51}$$

The boundary conditions (4.25) for (4.51) assume the following expressions in char-

acteristic coordinates:

$$\frac{\partial S_j}{\partial r}(0,t) = \frac{\partial S_j}{\partial r}(c(0,t),t) = 0,\ S_j(R(t),t) = S_j(c(t,t),t)) = S_j^*(t), \tag{4.52}$$

because of (4.35) and (4.36). From (4.51):

$$D_{S,j}\frac{\partial}{\partial t_0}\left(c^2(t_0,t)\frac{\partial S_j}{\partial r}(c(t_0,t),t)\right) = -c^2(t_0,t)r_{S,j}(\mathbf{X}(c(t_0,t),t),\mathbf{S}(c(t_0,t),t))\frac{\partial}{\partial t_0}c(t_0,t). \tag{4.53}$$

Integrating the equation above over $(0,t_0)$ yields:

$$D_{S,j}c^2(t_0,t)\frac{\partial S_j}{\partial r}(c(t_0,t),t) = -\int_0^{t_0} c^2(\tau,t)r_{S,j}(\mathbf{X}(c(\tau,t),t),\mathbf{S}(c(\tau,t),t))\frac{\partial}{\partial \tau}c(\tau,t)d\tau. \tag{4.54}$$

where the boundary condition $(4.52)_1$ was used. From (4.54):

$$D_{S,j}\frac{\partial}{\partial t_0}S_j(c(t_0,t),t)$$

$$= -\frac{1}{c^2(t_0,t)}\frac{\partial}{\partial t_0}c(t_0,t)\int_0^{t_0} c^2(\tau,t)r_{S,j}(\mathbf{X}(c(\tau,t),t),\mathbf{S}(c(\tau,t),t))\frac{\partial}{\partial \tau}c(\tau,t)d\tau. \tag{4.55}$$

Integrating the equation above over $(t_0,t)$ yields:

$$D_{S,j}S_j(c(t_0,t),t) = D_{S,j}S_j^*(t)$$

$$+\int_{t_0}^{t}\frac{1}{c^2(\theta,t)}\frac{\partial}{\partial \theta}c(\theta,t)d\theta\int_0^{\theta} c^2(\tau,t)r_{S,j}(\mathbf{X}(c(\tau,t),t),\mathbf{S}(c(\tau,t),t))\frac{\partial}{\partial \tau}c(\tau,t)d\tau,$$

$$0 \leq t_0 < t \leq T,\ j = 1, ..., m, \tag{4.56}$$

where the boundary condition $(4.52)_2$ was used. The equation above is the desired integral equation for $S_j$ in characteristic coordinates. Note that the integral equation (4.56) is equivalent to the differential initial value problem (4.51)-(4.52).

Similarly, consider Eq. (4.26) rewritten in characteristic coordinates:

$$D_{\psi,j}\frac{1}{c^2(t_0,t)}\frac{\partial}{\partial r}\left(c^2(t_0,t)\frac{\partial \psi_i}{\partial r}(c(t_0,t),t)\right) = -r_{\psi,i}(\boldsymbol{\psi}(c(t_0,t),t),\mathbf{S}(c(t_0,t),t)), i=1, ..., n, \tag{4.57}$$

The boundary conditions (4.27) for (4.57) assume the following expression in characteristic coordinates:

$$\frac{\partial \psi_i}{\partial r}(0,t) = \frac{\partial \psi_i}{\partial r}(c(0,t),t) = 0,\ \psi_i(R(t),t) = \psi_i(c(t,t),t)) = \psi_i^*(t), \tag{4.58}$$

because of (4.35) and (4.36). From (4.57):

$$D_{\psi,j}\frac{\partial}{\partial t_0}\left(c^2(t_0,t)\frac{\partial \psi_i}{\partial r}(c(t_0,t),t)\right) = -c^2(t_0,t)r_{\psi,i}(\boldsymbol{\psi}(c(t_0,t),t),\mathbf{S}(c(t_0,t),t))\frac{\partial}{\partial t_0}c(t_0,t). \tag{4.59}$$

Integrating the equation above over $(0, t_0)$ yields:

$$D_{\psi,i}c^2(t_0,t)\frac{\partial \psi_i}{\partial r}(c(t_0,t),t) = -\int_0^{t_0} c^2(\tau,t)r_{\psi,i}(\boldsymbol{\psi}(c(\tau,t),t),\mathbf{S}(c(\tau,t),t))\frac{\partial}{\partial \tau}c(\tau,t)d\tau. \tag{4.60}$$

where the boundary condition $(4.58)_1$ was used. From (4.60):

$$D_{\psi,i}\frac{\partial}{\partial t_0}\psi_i(c(t_0,t),t)$$

$$= -\frac{1}{c^2(t_0,t)}\frac{\partial}{\partial t_0}c(t_0,t)\int_0^{t_0} c^2(\tau,t)r_{\psi,i}(\boldsymbol{\psi}(c(\tau,t),t),\mathbf{S}(c(\tau,t),t))\frac{\partial}{\partial \tau}c(\tau,t)d\tau. \quad (4.61)$$

Integrating the equation above over $(t_0,t)$ yields:

$$D_{\psi,i}\psi_i(c(t_0,t),t) = D_{\psi,i}\psi_i^*(t)$$

$$+\int_{t_0}^{t}\frac{1}{c^2(\theta,t)}\frac{\partial}{\partial \theta}c(\theta,t)d\theta\int_0^{\theta} c^2(\tau,t)r_{\psi,i}(\boldsymbol{\psi}(c(\tau,t),t),\mathbf{S}(c(\tau,t),t))\frac{\partial}{\partial \tau}c(\tau,t)d\tau,$$

$$0 \le t_0 < t \le T,\ i = 1,...,n, \quad (4.62)$$

where the boundary condition $(4.58)_2$ was used. The equation above is the desired integral equation for $\psi_i$ in characteristic coordinates. Note that the integral equation (4.62) is equivalent to the differential initial value problem (4.57)-(4.58).

## 4.3 Spherical free boundary value problem in characteristic coordinates

The integral problem is summarized below by using the following positions:

$$\mathbf{x}(t_0,t) = \mathbf{X}(c(t_0,t),t),\ \ \mathbf{x}(x_1,...,x_n), \quad (4.63)$$

$$\mathbf{s}(t_0,t)=\mathbf{S}(c(t_0,t),t),\ \ \mathbf{s}(s_1,...,s_m), \tag{4.64}$$

$$\mathbf{\Psi}(t_0,t)=\boldsymbol{\psi}(c(t_0,t),t),\ \ \mathbf{\Psi}(\Psi_1,...,\Psi_n), \tag{4.65}$$

The integral equations for $x_i$ follow from (4.50)

$$x_i(t_0,t)=X_{i,0}(t_0)+\int_{t_0}^{t}F_i(\mathbf{x}(t_0,\tau),\mathbf{s}(t_0,\tau),\mathbf{\Psi}(t_0,\tau))d\tau,\ 0\le t_0<t\le T,\ i=1,...,n. \tag{4.66}$$

The integral equations for $s_j$ follow from (4.56)

$$s_j(t_0,t)=S_j^*(t)+\int_{t_0}^{t}d\theta\int_0^{\theta}F_{s,j}(\mathbf{x}(\tau,t),\mathbf{s}(\tau,t),c(\theta,t),c(\tau,t),\frac{\partial c}{\partial\theta}(\theta,t),\frac{\partial c}{\partial\tau}(\tau,t))d\tau,$$

$$0<t_0<t\le T,\ j=1,...,m, \tag{4.67}$$

where $F_{s,j}$ is defined in (4.75) at the end of this Section. Similarly to $\mathbf{s}$, the integral equations for $\psi_i$ follow from (4.62):

$$\Psi_i(t_0,t)=\psi_i^*(t)+\int_{t_0}^{t}d\theta\int_0^{\theta}F_{\psi,i}(\mathbf{\Psi}(\tau,t),\mathbf{s}(\tau,t),c(\theta,t),c(\tau,t),\frac{\partial c}{\partial\theta}(\theta,t),\frac{\partial c}{\partial\tau}(\tau,t))d\tau,$$

$$0<t_0<t\le T,\ i=1,...,n, \tag{4.68}$$

where $F_{\psi,i}$ is defined in (4.76).

The integral equation for $R$ follows from (4.40):

$$R(t_0)=\Sigma(t_0)$$

$$+\int_0^{t_0} d\theta \int_0^{\theta} F_L(\mathbf{x}(\tau,\theta),\mathbf{s}(\tau,\theta),\mathbf{\Psi}(\tau,\theta),c(\theta,\theta),c(\tau,\theta),\frac{\partial c}{\partial \tau}(\tau,\theta))d\tau,\ 0<t_0\leq T, \tag{4.69}$$

with $\Sigma(t_0)$ and $F_L$ defined in (4.77)-(4.78), respectively.

The integral equations for $c(t_0,t)$ and $\partial c/\partial t_0$ can be obtained from (4.44) and (4.45) rewritten in terms of characteristic coordinates:

$$c(t_0,t)=\Sigma(t_0)$$

$$+\int_0^{t_0} d\theta \int_0^{\theta} F_{c,1}(\mathbf{x}(\tau,\theta),\mathbf{s}(\tau,\theta),\mathbf{\Psi}(\tau,\theta),c(\theta,\theta),c(\tau,\theta),\frac{\partial c}{\partial \tau}(\tau,\theta))d\tau$$

$$+\int_{t_0}^{t} d\theta \int_0^{t_0} F_{c,2}(\mathbf{x}(\tau,\theta),\mathbf{s}(\tau,\theta),\mathbf{\Psi}(\tau,\theta),c(t_0,\theta),c(\tau,\theta),\frac{\partial c}{\partial \tau}(\tau,\theta))d\tau,\ 0<t_0<t\leq T, \tag{4.70}$$

$$\frac{\partial c}{\partial t_0}(t_0,t)=\int_{t_0}^{t} F_{c,3}(\mathbf{x}(t_0,\theta),\mathbf{s}(t_0,\theta),\mathbf{\Psi}(t_0,\theta),\frac{\partial c}{\partial t_0}(t_0,\theta))d\theta+\sigma_a(\mathbf{\Psi}^*(t_0)),0<t_0<t\leq T, \tag{4.71}$$

where:

$$F_{c,1}(\mathbf{x}(\tau,\theta),\mathbf{s}(\tau,\theta),\mathbf{\Psi}(\tau,\theta),c(\theta,\theta),c(\tau,\theta),\frac{\partial c}{\partial \tau}(\tau,\theta))$$

$$=\frac{1}{c^2(\theta,\theta)}c^2(\tau,\theta)G(\mathbf{x}(\tau,\theta),\mathbf{s}(\tau,\theta),\mathbf{\Psi}(\tau,\theta))\frac{\partial c}{\partial \tau}(\tau,\theta), \tag{4.72}$$

$$F_{c,2}(\mathbf{x}(\tau,\theta),\mathbf{s}(\tau,\theta),\mathbf{\Psi}(\tau,\theta),c(t_0,\theta),c(\tau,\theta),\frac{\partial c}{\partial \tau}(\tau,\theta))$$

$$= \frac{1}{c^2(t_0,\theta)}c^2(\tau,\theta)G(\mathbf{x}(\tau,\theta),\mathbf{s}(\tau,\theta),\mathbf{\Psi}(\tau,\theta))\frac{\partial c}{\partial \tau}(\tau,\theta), \tag{4.73}$$

$$F_{c,3}(\mathbf{x}(t_0,\theta),\mathbf{s}(t_0,\theta),\mathbf{\Psi}(t_0,\theta),\frac{\partial c}{\partial t_0}(t_0,\theta))$$

$$= G(\mathbf{x}(t_0,\theta),\mathbf{s}(t_0,\theta),\mathbf{\Psi}(t_0,\theta))\frac{\partial c}{\partial t_0}(t_0,\theta). \tag{4.74}$$

The functions introduced in equations (4.67)-(4.69) are defined below

$$F_{s,j}(\mathbf{x}(\tau,t),\mathbf{s}(\tau,t),c(\theta,t),c(\tau,t),\frac{\partial c}{\partial \theta}(\theta,t),\frac{\partial c}{\partial \tau}(\tau,t))$$

$$= D_{S,j}^{-1}\frac{1}{c^2(\theta,t)}c^2(\tau,t)r_{S,j}(\mathbf{x}(\tau,t),\mathbf{s}(\tau,t))\frac{\partial c}{\partial \theta}(\theta,t)\frac{\partial c}{\partial \tau}(\tau,t), \tag{4.75}$$

$$F_{\psi,i}(\mathbf{\Psi}(\tau,t),\mathbf{s}(\tau,t),c(\theta,t),c(\tau,t),\frac{\partial c}{\partial \theta}(\theta,t),\frac{\partial c}{\partial \tau}(\tau,t))$$

$$= D_{\psi,i}^{-1}\frac{1}{c^2(\theta,t)}c^2(\tau,t)r_{\psi,i}(\mathbf{\Psi}(\tau,t),\mathbf{s}(\tau,t))\frac{\partial c}{\partial \theta}(\theta,t)\frac{\partial c}{\partial \tau}(\tau,t), \tag{4.76}$$

$$\Sigma(t_0) = \int_0^{t_0}\sigma_a(\mathbf{\Psi}^*(\theta))d\theta, \tag{4.77}$$

$$F_L(\mathbf{x}(\tau,\theta),\mathbf{s}(\tau,\theta),\mathbf{\Psi}(\tau,\theta),c(\theta,\theta),c(\tau,\theta),\frac{\partial c}{\partial \tau}(\tau,\theta))$$

$$= \frac{1}{c^2(\theta,\theta)}c^2(\tau,\theta)G(\mathbf{x}(\tau,\theta),\mathbf{s}(\tau,\theta),\mathbf{\Psi}(\tau,\theta))\frac{\partial c}{\partial \tau}(\tau,\theta). \tag{4.78}$$

## 4.4 Uniqueness and existence theorem

An existence and uniqueness theorem for the integral problem (4.66)-(4.71) can be proved in the space of the continuous functions as generalization of the results in D'Acunto et al. (2019,2021) [24, 127].

**Theorem 1** *Suppose that:*

*(a)* $x_i(t_0,t), s_j(t_0,t), \Psi_i(t_0,t), c(t_0,t), c_{t_0}(t_0,t) \in C^0([0,\ T_1]\times[0,\ T_1]),\ T_1>0,$ $i=1,...,n,\ j=1,...,m,$ *and* $L(t_0)\in C^0([0,\ T_1]);$

*(b)* $X_{i,0}(t_0), \sigma_a(\boldsymbol{\psi^*}(t_0)), S_j^*(t), \psi_i^*(t)\in C^0([0,\ T_1]),\ i=1,...,n,\ j=1,...,m;$

*(c)* $|x_i - X_{i,0}| \le h_{x,i},\ i=1,...,n;\ |s_j - S_j^*|\le h_{s,j},\ j=1,...,m;\ |\Psi_i - \psi_i^*|\le h_{\psi,i},\ i=1,...,n;\ |L-\Sigma|\le h_L;\ |c-\Sigma|\le h_{c,1};\ |c_{t_0}-\sigma_a|\le h_{c,2},$ *where* $h_{x,i}, h_{s,j}, h_{\psi,i}, h_L, h_{c,1}, h_{c,2}$ *are positive constants;*

*(d)* $F_i, i=1,...,n,\ F_{s,j}, j=1,...,m,\ F_{\psi,i}, i=1,...,n,\ F_L, F_{c,1}, F_{c,2}, F_{c,3}$ *are bounded and Lipschitz continuous with respect to their arguments*

$$M_i=\max|F_i|,\ i=1,...,n,\ M_{s,j}=\max|F_{s,j}|,\ j=1,...,m,$$

$$M_{\psi,i}=\max|F_{\psi,i}|,\ i=1,...,n,\ M_L=\max|F_L|,$$

$$M_{c,1}=\max(|F_{c,1}|,|F_{c,2}|),\ M_{c,2}=\max|F_{c,3}|,$$

$$|F_i(\mathbf{x},\mathbf{s},\boldsymbol{\psi})-F_i(\tilde{\mathbf{x}},\tilde{\mathbf{s}},\tilde{\boldsymbol{\psi}})|$$
$$\le\lambda_i\left[\sum_{k=1}^{n}|x_k-\tilde{x}_k|+\sum_{k=1}^{m}|s_k-\tilde{s}_k|+\sum_{k=1}^{n}|\psi_k-\tilde{\psi}_k|\right],\ i=1,...n,$$
$$|F_{s,j}(\mathbf{x},\mathbf{s},c,c_{t_0})-F_{s,j}(\tilde{\mathbf{x}},\tilde{\mathbf{s}},\tilde{c},\tilde{c}_{t_0})|$$
$$\le\lambda_{s,j}\left[\sum_{k=1}^{n}|x_k-\tilde{x}_k|+\sum_{k=1}^{m}|s_k-\tilde{s}_k|+|c-\tilde{c}|+|c_{t_0}-\tilde{c}_{t_0}|\right],\ j=1,...m,$$
$$|F_{\psi,i}(\boldsymbol{\Psi},\mathbf{s},c,c_{t_0})-F_{\psi,i}(\tilde{\boldsymbol{\Psi}},\tilde{\mathbf{s}},\tilde{c},\tilde{c}_{t_0})|$$

$$\leq \lambda_{\psi,i}\left[\sum_{k=1}^{n}|\Psi_k-\tilde{\Psi}_k|+\sum_{k=1}^{m}|s_k-\tilde{s}_k|+|c-\tilde{c}|+|c_{t_0}-\tilde{c}_{t_0}|\right],\ i=1,...,n,$$

$$|F_L(\mathbf{x},\mathbf{s},\mathbf{\Psi},c,c_{t_0})-F_L(\tilde{\mathbf{x}},\tilde{\mathbf{s}},\tilde{\mathbf{\Psi}},\tilde{c},\tilde{c}_{t_0})|$$

$$\leq \lambda_L\left[\sum_{k=1}^{n}|x_k-\tilde{x}_k|+\sum_{k=1}^{m}|s_k-\tilde{s}_k|+\sum_{k=1}^{n}|\psi_k-\tilde{\psi}_k|+|c-\tilde{c}|+|c_{t_0}-\tilde{c}_{t_0}|\right],$$

$$|F_{c,1}(\mathbf{x},\mathbf{s},\mathbf{\Psi},c,c_{t_0})-F_{c,1}(\tilde{\mathbf{x}},\tilde{\mathbf{s}},\tilde{\mathbf{\Psi}},c,\tilde{c}_{t_0})|$$

$$\leq \lambda_{c,1}\left[\sum_{k=1}^{n}|x_k-\tilde{x}_k|+\sum_{k=1}^{m}|s_k-\tilde{s}_k|+\sum_{k=1}^{n}|\Psi_k-\tilde{\Psi}_k|+|c-\tilde{c}|+|c_{t_0}-\tilde{c}_{t_0}|\right],$$

$$|F_{c,2}(\mathbf{x},\mathbf{s},\mathbf{\Psi},c,c_{t_0})-F_{c,2}(\tilde{\mathbf{x}},\tilde{\mathbf{s}},\tilde{\mathbf{\Psi}},c,\tilde{c}_{t_0})|$$

$$\leq \lambda_{c,2}\left[\sum_{k=1}^{n}|x_k-\tilde{x}_k|+\sum_{k=1}^{m}|s_k-\tilde{s}_k|+\sum_{k=1}^{n}|\psi_k-\tilde{\psi}_k|+|c-\tilde{c}|+|c_{t_0}-\tilde{c}_{t_0}|\right],$$

$$|F_{c,3}(\mathbf{x},\mathbf{s},\mathbf{\Psi},c_{t_0})-F_{c,2}(\tilde{\mathbf{x}},\tilde{\mathbf{s}},\tilde{\mathbf{\Psi}},\tilde{c}_{t_0})|$$

$$\leq \lambda_{c,3}\left[\sum_{k=1}^{n}|x_k-\tilde{x}_k|+\sum_{k=1}^{m}|s_k-\tilde{s}_k|+\sum_{k=1}^{n}|\Psi_k-\tilde{\Psi}_k|+|c_{t_0}-\tilde{c}_{t_0}|\right],$$

*when* $(t_0,t)\in[0,\ T_1]\times[0,\ T_1]$ *and the functions* $x_i$, $s_j$, $\Psi_i$, $L$, $c$, $c_{t_0}$ *satisfy the assumptions (a)-(c).*

*Then, integral system* (4.66)-(4.71) *has a unique solution* $x_i$, $s_j$, $\Psi_i$, $R$, $c$, $c_{t_0}$, $\in C^0([0,\ T]\times[0,\ T])$,

*where*

$$T=\min\left\{T_1,\frac{h_{x,1}}{M_1},...,\frac{h_{x,n}}{M_n},\sqrt{\frac{h_{s,1}}{M_{s,1}}},...,\sqrt{\frac{h_{s,m}}{M_{s,m}}},\sqrt{\frac{h_{\psi,1}}{M_{\psi,1}}},...,\sqrt{\frac{h_{\psi,n}}{M_{\psi,n}}},\sqrt{\frac{h_L}{M_L}},\sqrt{\frac{h_{c,1}}{2M_{c,1}}},\frac{h_{c,2}}{M_{c,2}}\right\}.$$

*Moreover,* $T$ *satisfies the following condition,*

$$aT^2+bT<1, \tag{4.79}$$

*where*

$$a=\sum_{j=1}^{m}\lambda_{s,j}+\sum_{i=1}^{n}\lambda_{\psi,i}+\lambda_L+\lambda_{c,1}+\lambda_{c,2},\ b=\sum_{i=1}^{n}\lambda_i+\lambda_{c,3}. \tag{4.80}$$

**Proof:** Denote by $\Omega$ the space of continuous functions $x_i(t_0,t)$, $s_j(t_0,t)$, $\Psi_i(t_0,t)$, $R(t_0)$, $c(t_0,t)$, $c_{t_0}(t_0,t)$, $t_0 \in [0,\ T]$, $t \in [0,\ T]$, and endow it with the uniform norm

$$||(\mathbf{x}, \mathbf{s}, \mathbf{\Psi}, L, c, c_{t_0})||$$

$$= \sum_{i=1}^{n} \max_{\Omega} |x_i| + \sum_{j=1}^{m} \max_{\Omega} |s_j| + \sum_{i=1}^{n} \max_{\Omega} |\Psi_i| + \max_{\Omega} |R| + \max_{\Omega} |c| + \max_{\Omega} |c_{t_0}|.$$

Consider the map $(\mathbf{x}^*, \mathbf{s}^*, \underline{\mathbf{\Psi}}^*, R^*, c^*, c^*_{t_0}) = A(\mathbf{x}, \mathbf{s}, \mathbf{\Psi}, R, c, c_{t_0})$,

where $(\mathbf{x}^*, \mathbf{s}^*, \underline{\mathbf{\Psi}}^*, R^*, c^*, c^*_{t_0})$ = RHS of equations (4.66)-(4.71). Let us prove that $A$ maps $\Omega$ into itself. Indeed,

$$|x_i^* - X_{i,0}| \le M_i T \le h_{x,i}, \ \ i = 1, ..., n$$

$$|s_j^* - S_j^*| \le M_{s,j} T^2 \le h_{s,j}, \ \ |\underline{\Psi}_i^* - \Psi_i^*| \le M_{\psi,i} T^2 \le h_{\psi,i}, \quad i = 1, ..., n, \ j = 1, ..., m,$$

$$|R^* - \Sigma| \le M_L T^2 \le h_L, \ |c^* - \Sigma| \le 2M_{c,1} T^2 \le h_{c,1}, \ |c^*_{t_0} - \sigma_a| \le M_{c,2} T \le h_{c,2}.$$

Consider $(\tilde{\mathbf{x}}, \tilde{\mathbf{s}}, \tilde{\mathbf{\Psi}}, \tilde{R}, \tilde{c}, \tilde{c}_{t_0}) \in \Omega$ and let $(\tilde{\mathbf{x}}^*, \tilde{\mathbf{s}}^*, \tilde{\mathbf{\Psi}}^*, \tilde{R}^*, \tilde{c}^*, \tilde{c}^*_{t_0}) = A(\tilde{\mathbf{x}}, \tilde{\mathbf{s}}, \tilde{\mathbf{\Psi}}, \tilde{R}, \tilde{c}, \tilde{c}_{t_0})$. It is possible to obtain

$$|x_i^* - \tilde{x}_i^*| \le \lambda_i T ||(\mathbf{x}, \mathbf{s}, \mathbf{\Psi}, R, c, c_{t_0}) - (\tilde{\mathbf{x}}, \tilde{\mathbf{s}}, \tilde{\mathbf{\Psi}}, \tilde{R}, \tilde{c}, \tilde{c}_{t_0})||, \ i = 1, ..., n,$$

$$|s_j^* - \tilde{s}_j^*| \le \lambda_{s,j} T^2 ||(\mathbf{x}, \mathbf{s}, \mathbf{\Psi}, R, c, c_{t_0}) - (\tilde{\mathbf{x}}, \tilde{\mathbf{s}}, \tilde{\mathbf{\Psi}}, \tilde{R}, \tilde{c}, \tilde{c}_{t_0})||, \ j = 1, ..., m,$$

$$|\underline{\Psi}_i^* - \tilde{\Psi}_i^*| \le \lambda_{\psi,i} T^2 ||(\mathbf{x}, \mathbf{s}, \mathbf{\Psi}, R, c, c_{t_0}) - (\tilde{\mathbf{x}}, \tilde{\mathbf{s}}, \tilde{\mathbf{\Psi}}, \tilde{R}, \tilde{c}, \tilde{c}_{t_0})||, \ i = 1, ..., n,$$

$$|R^* - \tilde{R}^*| \le \lambda_L T^2 ||(\mathbf{x}, \mathbf{s}, \mathbf{\Psi}, R, c, c_{t_0}) - (\tilde{\mathbf{x}}, \tilde{\mathbf{s}}, \tilde{\mathbf{\Psi}}, \tilde{R}, \tilde{c}, \tilde{c}_{t_0})||,$$

$$|c^* - \tilde{c}^*| \le (\lambda_{c,1} + \lambda_{c,2}) T^2 ||(\mathbf{x}, \mathbf{s}, \mathbf{\Psi}, R, c, c_{t_0}) - (\tilde{\mathbf{x}}, \tilde{\mathbf{s}}, \tilde{\mathbf{\Psi}}, \tilde{R}, \tilde{c}, \tilde{c}_{t_0})||,$$

$$|c^*_{t_0} - \tilde{c}^*_{t_0}| \le \lambda_{c,3} T ||(\mathbf{x}, \mathbf{s}, \mathbf{\Psi}, R, c, c_{t_0}) - (\tilde{\mathbf{x}}, \tilde{\mathbf{s}}, \tilde{\mathbf{\Psi}}, \tilde{R}, \tilde{c}, \tilde{c}_{t_0})||.$$

Therefore,

$$||(\mathbf{x}^*, \mathbf{s}^*, \underline{\mathbf{\Psi}}^*, R^*, c^*, c^*_{t_0}) - (\tilde{\mathbf{x}}^*, \tilde{\mathbf{s}}^*, \tilde{\mathbf{\Psi}}^*, \tilde{R}^*, \tilde{c}^*, \tilde{c}^*_{t_0})||$$

$$\leq \Lambda||(\mathbf{x}, \mathbf{s}, \mathbf{\Psi}, R, c, c_{t_0}) - (\tilde{\mathbf{x}}, \tilde{\mathbf{s}}, \tilde{\mathbf{\Psi}}, \tilde{R}, \tilde{c}, \tilde{c}_{t_0})||,$$

where

$$\Lambda = aT^2 + bT.$$

According to (4.79) $\Lambda < 1$, proving Theorem 1. □

The existence and uniqueness result has been obtained for an arbitrary number of microbial species n and dissolved substrates m, with non-linear reaction terms. The uniqueness result provides a solid base for the further numerical calculations. Moreover, we stress that all hypotheses of the theorem are not suggested by mathematical artefacts, but they are mostly qualitative and naturally derived from biological considerations.

## 4.5 Conclusions

The Chapter presents for the first time the qualitative analysis of the spherical free boundary problem where the initial free boundary value is zero. The presented model considers both the initial attachment phase and the growth of new sessile species within the biofilm mediated by the invasion process. This allows to properly reproduce the evolution of granular biofilms starting from the initial formation and including the establishment and growth of new species. The modeling of the initial phase of granular biofilm formation allows describing the biofilm growth without arbitrarily fixing the initial composition of the biofilm. The existence and uniqueness result has been obtained for an arbitrary number of microbial species $n$ and dissolved substrates $m$, with non-linear reaction terms. The uniqueness result provides a solid base for the further numerical calculations. Moreover, we stress that all hypotheses of the theorem are not suggested by mathematical artefacts, but they are mostly qualitative and naturally derived from biological considerations. The influence of the environmental conditions

on the attachment process represents a key factor in the mathematical modelling of the granular biofilm genesis and attachment phenomenon. This aspect has not been considered in this Chapter, and it requires further investigations.

# Chapter 5

# Multiscale modelling of the start-up process of anammox-based granular reactors

## 5.1 Introduction

In the last decades, granular sludge technologies have completely revolutionized the treatment and valorization of industrial and municipal wastewater as they can be applied for the simultaneous removal of organic, nitrogen and phosphorus compounds and the production of bioenergy [14]. Granular sludge reactors are biofilm systems where biomass grows arranged in granules, dense and compact aggregates with an approximately spherical shape [11]. In contrast to the traditional biofilm systems, where biofilms develop on solid surfaces, biofilm formation in granular sludge reactors occurs due to the self-immobilization of cells without the involvement of a surface, in a process known as granulation. Such process can be initiated from an inoculum in gran-

This Chapter will be submitted as: Russo, F., Tenore, A., Mattei, M.R., Frunzo, L. Multiscale modelling of the start-up process of anammox-based granular reactors.

ular or suspended form. In the latter case, the process is named *de novo* granulation. Conversely to conventional wastewater systems, high amounts of extracellular polymeric substances (EPS) constitute biofilm granules which, consequently, have higher biomass densities, more regular shapes and stronger structures [13]. These characteristics also provide protection for sensitive microbial species which have difficulties to develop in suspended form [88]. Moreover, due to the high settling velocity of granular sludge, solid-liquid separation is facilitated [129] and high biomass concentrations can be achieved in the system [130]. Additionally, the geometry and free movement of granules limit external boundary layer resistances and promote the mass transport of substrates towards the various granule microbial layers [14]. All these features contribute to high removal efficiencies and reduced-footprint systems, and, consequently, specific granular biofilms, such as aerobic, anaerobic and anammox granules, have been adapted for various wastewater treatment processes.

Although the traditional process of nitrification-denitrification (N/D) is commonly used to remove nitrogen compounds from wastewater, it is energy-intensive as it requires dissolved oxygen supply for ammonium oxidation. Moreover, an external carbon source is necessary for the heterotrophic metabolism of denitrifying bacteria, in the case of low carbon-to-nitrogen ratio wastewater. Therefore, in recent years, the combination of partial nitritation and anammox processes (PN/A) has been increasingly studied for the treatment of nitrogenous wastewater. Such process allows the conversion of ammonium into molecular nitrogen: in the first step the partial nitritation takes place and about half of the ammonium present in the wastewater is converted to nitrite by ammonia-oxidizing bacteria ($AOB$); then, in the subsequent anammox step, the nitrite produced and the remaining ammonium are simultaneously converted into nitrogen gas and small amounts of nitrate by anammox bacteria ($AMX$). In the case of suspended biomass, the two processes occur in separate reactors arranged in series as they require aerobic and anoxic conditions. The granular biofilm technology represents a cost-effective and alternative solution, since both processes can be carried out simulta-

neously in a granular sludge reactor. Indeed, the formation of two distinct zones inside the granules is induced by providing a constant and appropriately low oxygen level in the reactor: an external zone where oxygen necessary for partial nitritation is guaranteed and an internal zone where oxygen is not present and ideal anoxic conditions for anammox processes occur.

Compared to the traditional N/D process, PN/A granular process results in lower aeration costs, $CO_2$ emissions and sludge production. Additionally, due to the autotrophic metabolism of anammox bacteria, no external addition of carbon is required. For these reasons, PN/A granular process is considered a promising technology for N-removal. Nevertheless, anammox bacteria are very sensitive to environmental and operating conditions, and are characterized by very low growth rates and cellular yields [131, 132, 133, 134, 135, 136]. Consequently, the start-up of anammox granular sludge reactors is a long and complex process, which represents the main drawback of this technology [132, 135] and deeply impacts the operating strategies and procedures [137].

The start-up process of anammox granular sludge systems can be divided into four phases: cell lysis phase, lag phase, activity elevation phase and stationary phase [131, 132, 133, 134, 138, 139]. The lysis phase occurs frequently when microbial species constituting the granular sludge inoculum find new and unknown environmental conditions and carry out processes of microbial autolysis leading to the disintegration of biofilm granules. A transition period occurs in the successive lag phase, when the biomass begins to adapt to the reactor conditions and new biofilm granules begin to develop. In the elevation phase, the well-adapted biomass grows and a continuous and increasing ammonium and nitrite removal is observed. Finally, in the stationary phase, red mature granules are detected, dominated by anammox bacteria, with the presence of ammonia-oxidizing bacteria and denitrifying heterotrophic bacteria. In this phase, an optimum and stable N-removal efficiency is achieved [132, 138].

Many studies deal with the start-up of PN/A granular sludge systems by focusing on factors which govern the biological processes involved and the growth of anam-

mox bacteria, such as inoculum sludge, hydraulic retention time, dissolved oxygen, temperature, pH, wastewater composition and reactor configuration. Among these, the inoculation procedure appears to be a key element to reduce the start-up period [138, 140]. In experimental works reported in literature, different selected sludges have been used as inocula of lab-, pilot- and full-scale bioreactors, such as anaerobic granular sludge [131, 132, 133, 134, 139], flocculant nitrification sludge [131, 133, 137], flocculant denitrification sludge [131], activated sludge with or without addition of anammox sludge [139]. Anaerobic granular sludge can be a competitive alternative solution, as the biomass is already in granular form and acclimatized to anaerobic conditions. Moreover, the conventional flocculant sludge represents a further alternative, due to its greater availability. The latter two types of inoculum can also be enriched with anammox sludge. In this context, the search for new procedures and strategies that can significantly accelerate the process start-up remains an interesting challenge.

The study of the anammox process and start-up strategies through experimental activities requires high cost and long time, mainly due to very low growth rates of anammox bacteria. Consequently, mathematical modelling appears to be an attractive alternative solution for the description and optimization of PN/A granular sludge reactors, for the understanding and investigation of microbial dynamics which govern the growth of anammox granules, and for testing a wide range of environmental and operational conditions which could influence the process. In the recent years, numerous mathematical models have been proposed to describe anaerobic [26, 27, 28, 141], aerobic [142, 143, 101] and anammox processes [29, 30, 31, 144, 145] in granular-based systems, by considering the evolution of biofilm granules. Depending on the approach used to model the development and the structure of granular biofilms, two types of models can be distinguished: continuum and discrete models. The first ones describe granular biofilms as spherical continuum domains, through a quantitative and deterministic approach [27, 28, 30, 142], while discrete models, such as individual-based models [101, 99], consider microbial cells as discrete entities and introduce elements

of randomness and stochastic effects in the solution. Most of continuous models have been formulated as spherical free boundary problems with radial symmetry. Some of them take into account attachment [26, 104, 128] and invasion [128] processes. Moreover, the initial formation of biofilm granules has been modelled in Tenore et al. (2021) [128] by setting a zero initial granule radius. Continuum models frequently assume one single granule size class [30, 144, 145], while someone takes into account the size distribution of granules within the reactor by considering more size classes [27, 28, 31]. However, some works [28, 31] demonstrate that one single size class allows to correctly describe the global treatment process, while the granule size distribution could be required to investigate more specific aspects, such as the microbial composition and the solute exchange between granules of different sizes. Although most models consider all the biomass in the granular form, a few include both the sessile biomass and the planktonic biomass present in the reactor and model the microbial mass fluxes between granular biofilms and liquid medium [128, 145]. Many free boundary models describe the granules evolution by fixing the steady-state dimension [30, 31, 144, 145], while in other works the steady-state dimension is supposed to be a function of microbial metabolic activities and operating conditions of the system [28, 146]. Except for a few cases [147], almost all models on granular biofilms consider the perfect retention of biofilm granules and, consequently, assume the number of granules in the system as a constant [142, 30].

Among the models on granular biofilms, some focus on processes of partial nitritation and anammox [30, 31, 144], by taking into account the dynamics of main microbial species involved, such as ammonia-oxidizing bacteria ($AOB$), nitrite-oxidizing bacteria ($NOB$), anammox bacteria ($AMX$) and main soluble substrates, such as ammonium, nitrite and nitrate . However, someone includes also the conversion of organic compounds by heterotrophic bacteria [145, 148]. Indeed, when sufficient amounts of organic carbon occur in the system, heterotrophic bacteria can play a negative role in the N-removal process, by proliferating within the granules and competing with $AOB$

and $AMX$.

Models on PN/A granular systems propose some interesting numerical studies, aimed at describing the PN/A process and to look into the effects of some key factors on the reactor performance and microbial composition of granules. Specifically, the effects of the following factors have been investigated: bulk oxygen concentration [30, 29] and aeration pattern [149], granule size [30, 31, 29, 148] and granule size distribution [31], influent concentration of ammonium [30, 29] influent concentration of COD and heterotrophic growth [145, 148]. Furthermore, the impact of the coexistence of microbial flocs and granular biofilm on the reactor performance is studied by Hubaux et al. (2015) [145]. The emission of nitrous oxide ($N_2O$) and nitric oxide ($NO$) occurring in the treatment process is investigated by Vangsgaard et al. (2012) [144], exploring the effects of ammonium load, granule size and temperature. Finally, a model which propose the integration of methane removal in PN/A granular sludge reactors is reported by Castro-Barros et al. (2018) [150].

In this context, the present Chapter proposes a mathematical model aimed at describing and investigating aspects of the PN/A granular sludge bioreactor that have never been addressed in literature, such as the initial formation of anammox granules (anammox *de novo* granulation) and the start-up process. The general framework has been introduced in Tenore et al. (2021) [128] for anaerobic biofilm granules and has been applied here to PN/A processes. The model is formulated as a spherical free boundary value problem under the assumption of radial symmetry. The *de novo* granulation process is modelled by assuming a vanishing initial granule size [24, 127]. This means that all the biomass present in the system at the beginning of the process is in planktonic form (flocculant sludge inoculum). Then, the granules formation is initiated by attachment phenomena. By using a continuum approach [22, 106], the model takes into account the dynamics of soluble substrates and biomasses in planktonic and sessile form. In particular, processes of microbial growth, substrates conversion, microbial invasion, attachment and detachment are included in the model.

This model has been integrated numerically by developing an original code in the MaTLab platform and numerical studies have been carried out for the following purposes: (i) test the model behaviour, (ii) explore the formation, evolution and ecology of anammox granules in PN/A granular sludge systems, (iii) study the autotrophic nitrogen removal through PN/A processes, (iv) investigate and optimize the process start-up of these bioreactors. In particular, numerical simulations have been carried out to investigate how the size and the addition time of the anammox inoculum can affect and optimize the process start-up. The numerical results refer to both the individual biofilm granule and the global reactor performance and include the distribution and relative abundance of active sessile biomasses within the granule, the evolution of granule dimension, and the profiles of soluble substrates and planktonic biomasses within the reactor. This Chapter is organized as follows. The mathematical model is reported in Section 5.2, while the biological context is described in Section 5.3, where model variables and kinetic rate equations are introduced. Numerical studies are presented and discussed in Section 5.4. Finally, the conclusions are outlined in Section 5.5.

## 5.2 Mathematical Model

As mentioned in Section 5.1, the mathematical formulation of granular biofilm reactors presented in Tenore et al. (2021) [128] for anaerobic digestion is applied here to partial nitritation/anammox granular processes. In this Section, the model equations are reported.

A granular-based reactor is an extremely complex multiphase biological system which need the introduction of some assumptions in order to be modelled. It is supposed here to consist of two distinct components: the granular biofilm phase and the bulk liquid phase. These components influence each other through continuous mass exchanges involving sessile and planktonic biomass and soluble substrates. The granular biofilm phase is represented by a fixed number of biofilm granules ($N_G$) immersed within the

bulk liquid and assumed to have identical properties at any instant of time. Specifically, biofilm granules are modelled as spherical free boundary domains with radial symmetry and with a vanishing initial radius. The attachment flux of planktonic biomass from the bulk liquid is accounted to initiate the granulation process. Biofilm granules evolves over time as a result of various processes such as metabolic activities, detachment and transport of sessile biomass, diffusion and conversion of soluble substrates and invasion of planktonic species. The term attachment is used here to indicate the aggregation of planktonic cells, which contributes to the genesis and growth of biofilm granules. Invasion phenomena consist in the colonization of a pre-existing granule mediated by planktonic motile cells living in the surrounding environment, which can penetrate the porous matrix of the biofilm and convert to sessile biomass. Detachment phenomena lead to sessile biomass losses, induced by external shear forces, substrates depletion and biomass decay.

In order to model all these processes, the following model variables have been considered within the granular biofilm domain:

- radius of the biofilm granule: $R(t)$,
- concentration of $n$ sessile species: $X_i(r,t),\ i = 1, ..., n$,
- concentration of $n$ planktonic invading species: $\psi_i(r,t),\ i = 1, ..., n$,
- concentration of $m$ dissolved substrates: $S_j(r,t),\ j = 1, ..., m$.

The free boundary domain is described by the time-dependent granule radius R(t), while all other variables are expressed as functions of the time $t$ and the radial coordinate $r$, where $r = 0$ identifies the granule center. The liquid present in the voids of granules is not included as a model variable, since it is supposed to not play a limiting role in the microbial metabolic activities. Soluble substrates and planktonic cells are supposed to not occupy biofilm volume due to the small particle size and the biofilm volume is constituted just by sessile biomasses. Assuming that all sessile species have

the same constant density $\rho$, the biofilm volume fraction of each individual species $f_i$ can be calculated by dividing $X_i$ by $\rho$. Furthermore, it is assumed that the sum of the biomass volume fractions is equal to one at each location and time, $\sum_{i=1}^{n} f_i = 1$ [108]. Since $X_i$ and $f_i$ are mutually dependent variables, only $f_i$ is included among the model unknowns.

The reactor is modelled as a completely mixed continuous system. Therefore, the properties of the bulk liquid are the same at every point and change over time due to the conversion processes of the planktonic biomass and soluble substrates present in the bulk liquid and due to mass exchanges with the biofilm granules. In order to take into account these aspects, the following model variables have been considered within the bulk liquid:

- concentration of $n$ planktonic biomasses: $\psi_i^*(t),\ i = 1, ..., n$,
- concentration of $m$ dissolved substrates: $S_j^*(t),\ j = 1, ..., m$.

In the following, all model equations and boundary and initial conditions related to the biofilm domain and the bulk liquid domain are reported.

The growth and the transport of the $i^{th}$ sessile species across the granular biofilm is governed by the following hyperbolic partial differential equations (PDEs):

$$\frac{\partial X_i(r,t)}{\partial t} + \frac{1}{r^2}\frac{\partial}{\partial r}(r^2 u(r,t) X_i(r,t)) = \rho r_{M,i}(r,t,\mathbf{X},\mathbf{S}) + \rho r_i(r,t,\boldsymbol{\psi},\mathbf{S}),$$

$$i = 1, ..., n, 0 \leq r \leq R(t),\ t > 0, \tag{5.1}$$

$$X_i(R(t),t) = \frac{v_{a,i}\psi_i^*(t)\rho}{\sum_{i=1}^{n} v_{a,i}\psi_i^*(t)},\ i = 1, ..., n,\ t > 0,\ \sigma_a(t) - \sigma_d(t) > 0, \tag{5.2}$$

where $u(r,t)$ is the biomass velocity, $r_{M,i}(r,t,\mathbf{X},\mathbf{S})$ and $r_i(r,t,\boldsymbol{\psi},\mathbf{S})$ are the specific growth rates due to sessile and planktonic species, respectively, $\mathbf{X} = (X_1,...,X_n)$, $\mathbf{S} = (S_1,...,S_m)$, $\boldsymbol{\psi} = (\psi_1,...,\psi_n)$, $v_{a,i}$ is the attachment velocity of the $i^{th}$ planktonic biomass and $\psi_i^*(t)$ is the concentration of the $i^{th}$ planktonic biomass in the bulk liquid.

When the attachment flux from bulk liquid to granule $\sigma_a(t)$ is higher than detachment flux from granule to bulk liquid $\sigma_d(t)$, the free boundary is a space-like line and the condition (5.2) at the interface granule-bulk liquid $r = R(t)$ is required. Conversely, when $\sigma_a(t)$ is lower than $\sigma_d(t)$, the free boundary is a time-like line and the condition (5.2) is not needed, because the properties of the boundary are regulated by the internal points of the domain.

The function $u(r,t)$ satisfies the following problem:

$$\frac{\partial u(r,t)}{\partial r} = -\frac{2u(r,t)}{r} + G(r,t,\mathbf{f},\mathbf{S},\boldsymbol{\psi}),\ 0 < r \leq R(t),\ t > 0, \tag{5.3}$$

$$u(0,t) = 0,\ t > 0. \tag{5.4}$$

where $G(r,t,\mathbf{f},\mathbf{S},\boldsymbol{\psi}) = \sum_{i=1}^{n}(r_{M,i}(r,t,\mathbf{f},\mathbf{S}) + r_i(r,t,\boldsymbol{\psi},\mathbf{S}))$ and $\mathbf{f} = (f_1,...,f_n)$.

By considering Eq. (5.3), Eqs. (5.1) and (5.2) can be rewritten as follows:

$$\frac{\partial f_i(r,t)}{\partial t} + u(r,t)\frac{\partial f_i(r,t)}{\partial r} = r_{M,i}(r,t,\mathbf{f},\mathbf{S}) + r_i(r,t,\boldsymbol{\psi},\mathbf{S}) - f_i(r,t)G(r,t,\mathbf{f},\mathbf{S},\boldsymbol{\psi}),$$

$$i = 1,...,n, 0 \leq r \leq R(t),\ t > 0, \tag{5.5}$$

$$f_i(R(t),t) = \frac{v_{a,i}\psi_i^*(t)}{\sum_{i=1}^{n} v_{a,i}\psi_i^*(t)},\ i = 1,...,n,\ t > 0,\ \sigma_a(t) - \sigma_d(t) > 0, \tag{5.6}$$

The free boundary evolution is described by the granule radius $R(t)$ and depends on processes of sessile metabolic growth, detachment and attachment. Attachment phenomena dominate the granulation process, while detachment phenomena become predominant as the granule dimension increases. The variation of $R(t)$ is governed by the following ordinary differential equation (ODE), derived from the mass balance on the granule volume:

$$\dot{R}(t) = \sigma_a(t) - \sigma_d(t) + u(R(t), t), \tag{5.7}$$

$$R(0) = 0. \tag{5.8}$$

In particular, attachment process is modelled through a continuous flux from bulk liquid to granule, given by the sum of the attachment fluxes of each planktonic species $\sigma_{a,i}(t)$, which are linearly dependent on the concentration of planktonic biomasses within the bulk liquid $\psi_i^*(t)$ [24, 127]:

$$\sigma_a(t) = \sum_{i=1}^{n} \sigma_{a,i}(t) = \frac{\sum_{i=1}^{n} v_{a,i}\psi_i^*(t)}{\rho}. \tag{5.9}$$

Meanwhile, the detachment process is modelled through a continuous flux from granule to bulk liquid, which is a quadratic function of the granule radius $R(t)$:

$$\sigma_d(t) = \lambda R^2(t), \tag{5.10}$$

where $\lambda$ is the detachment coefficient and is supposed to be equal for all microbial species.

The diffusion and conversion of planktonic cells and soluble substrates within the biofilm granule are governed by the following parabolic PDEs:

$$\frac{\partial \psi_i(r,t)}{\partial t} - D_{\psi,i}\frac{\partial^2 \psi_i(r,t)}{\partial r^2} - \frac{2D_{\psi,i}}{r}\frac{\partial \psi_i(r,t)}{\partial r} = r_{\psi,i}(r, t, \boldsymbol{\psi}, \mathbf{S}),$$

$$i = 1, ..., n, 0 < r < R(t),\ t > 0, \tag{5.11}$$

$$\frac{\partial \psi_i}{\partial r}(0,t) = 0,\ \psi_i(R(t),t)) = \psi_i^*(t),\ i = 1, ..., n,\ t > 0, \tag{5.12}$$

$$\frac{\partial S_j(r,t)}{\partial t} - D_{S,j}\frac{\partial^2 S_j(r,t)}{\partial r^2} - \frac{2D_{S,j}}{r}\frac{\partial S_j(r,t)}{\partial r} = r_{S,j}(r,t,\mathbf{f},\mathbf{S}),$$

$$j = 1, ..., m, 0 < r < R(t),\ t > 0, \tag{5.13}$$

$$\frac{\partial S_j}{\partial r}(0,t) = 0,\ S_j(R(t),t)) = S_j^*(t),\ j = 1, ..., m,\ t > 0, \tag{5.14}$$

where $r_{\psi,i}(r,t,\boldsymbol{\psi},\mathbf{S})$ and $r_{S,j}(r,t,\mathbf{f},\mathbf{S})$ represent the conversion rate of $i^{th}$ invading species and $j^{th}$ substrate, respectively; $D_{\psi,i}$ and $D_{S,j}$ denote the diffusion coefficients in biofilm for the $i^{th}$ planktonic species and $j^{th}$ dissolved substrates, $\psi_i^*(t)$ and $S_j^*(t)$ denote the concentrations of planktonic cells and dissolved substrates within the bulk liquid, respectively. All equations which refer to the biofilm domain do not require initial conditions, since the extension of the biofilm domain is zero at $t = 0$.

$\psi_i^*(t)$ and $S_j^*(t)$ represent the solutions of the following ordinary differential equations (ODEs), which describe the dynamics of planktonic biomass and soluble substrates within the bulk liquid, respectively, and are derived from mass balances on the bulk liquid volume:

$$V\dot{\psi}_i^*(t) = Q(\psi_i^{in} - \psi_i^*(t)) - A(t)N_G D_{\psi,i}\frac{\partial \psi_i(R(t),t)}{\partial r} + r_{\psi,i}^*(t,\boldsymbol{\psi}^*,\mathbf{S}^*) - \sigma_{a,i}(t)\rho A(t),$$

$$i = 1, ..., n\ t > 0, \tag{5.15}$$

$$\psi_i^*(0) = \psi_{i,0}^*,\ i = 1, ..., n, \tag{5.16}$$

$$V\dot{S}_j^*(t) = Q(S_j^{in} - S_j^*(t)) - A(t)N_G D_{S,j}\frac{\partial S_j(R(t),t)}{\partial r} + r_{S,j}^*(t, \boldsymbol{\psi}^*, \mathbf{S}^*),$$

$$j = 1, ..., m,\ \ t > 0, \tag{5.17}$$

$$S_j^*(0) = S_j^{in},\ j = 1, ..., m, \tag{5.18}$$

where $V$ is the volume of the bulk liquid, assumed equal to the reactor volume, $Q$ is the continuous flow rate, $A(t)$ is the area of the granule and is equal to $4\pi R^2(t)$, $\psi_i^{in}$ is the concentration of the planktonic species $i$ in the influent, $S_j^{in}$ is the concentration of the substrate $j$ in the influent, $r_{\psi,i}^*(r, t, \boldsymbol{\psi}^*, \mathbf{S}^*)$ and $r_{S,j}^*(r, t, \boldsymbol{\psi}^*, \mathbf{S}^*)$ are the conversion rates for $\psi_i^*$ and $S_i^*$, $\psi_{i,0}^*$ is the initial concentrations of the $i^{th}$ planktonic species within the bulk liquid, $\mathbf{S}^* = (S_1^*, ..., S_m^*)$, $\boldsymbol{\psi}^* = (\psi_1^*, ..., \psi_n^*)$.

No contribution by detachment to planktonic or detached biomass is considered in this model. Indeed, the detached biomass has different characteristics from both sessile and planktonic biomass, and several hours are required for its conversion into the planktonic form [121, 122, 123]. Moreover, granular-based reactors are typically characterized by high selection pressures (low $HRT$ and high velocities) to promote the biomass aggregation [11]. Under these high selection pressures, granules are retained in the reactor, while planktonic and detached cells are rapidly washed out [88].

The mass of the $i^{th}$ sessile species within the granule can be derived from:

$$m_i(t) = \int_0^{R(t)} 4\pi r^2 \rho f_i(r, t) dr,\ i = 1, ..., n, \tag{5.19}$$

while, the total mass can be calculated as follow:

$$m_{tot}(t) = \sum_{i=1}^{n} m_i(t) = \frac{4}{3}\pi\rho R^3(t). \tag{5.20}$$

## 5.3 Modelling *de novo* anammox granulation

The mathematical model described in the previous Section has been applied to the partial nitritation/anammox process, with the aim of describing the dynamics of anammox granules and investigating the start-up of combined partial nitritation-anammox reactors.

The anaerobic ammonia oxidation process (anammox process) allows to remove nitrogen from wastewater via anaerobic pathways of specific autotrophic microbial species, known as anammox bacteria. Such bacteria use ammonium as electron donor to convert nitrite into nitrogen gas and small fractions of nitrate. However, since nitrite are not commonly present in nitrogenous wastewater, the anammox process is preceded by a partial nitritation step, where the necessary amount of nitrite is produced. As mentioned in Section 5.1, under appropriate operating conditions these two processes can be carried out simultaneously in one single granular sludge reactor, exploiting the coexistence of anoxic and aerobic zones within biofilm granules.

In order to comprehensively model the treatment process and the evolution of granules occurring in these reactors, all the main biological processes, microbial species and soluble substrates have been considered. Specifically, processes of nitritation, anammox, denitrification, organic carbon and nitrite oxidation are supposed to occur in biofilm granules and in the bulk liquid, induced by the metabolic activities of the planktonic and sessile biomass. Hence, the following active microbial species have been considered both in sessile and planktonic form: aerobic ammonia-oxidizing bacteria $AOB$, anaerobic ammonia-oxidizing bacteria $AMX$, aerobic nitrite-oxidizing bacteria $NOB$ and facultative heterotrophic bacteria $HB$. All sessile species are supposed to decay

and produce sessile inactive biomass $I$ which accumulate within the biofilm granules. Conversely, although it is assumed that planktonic biomasses also decay, the inactive biomass in planktonic form has not been included in the model because it is likely to play a negligible role in the development of the successive processes. Moreover, in order to describe the metabolic activity of the active microbial species, the following soluble compounds have been modelled: ammonium $NH_4$, nitrite $NO_2$, nitrate $NO_3$, soluble organic carbon $OC$ and oxygen $O_2$.

During the nitritation process, ammonium-oxidizing bacteria $AOB$ convert ammonium $NH_4$ and oxygen $O_2$ to nitrite $NO_2$ under aerobic conditions, according to the following reaction:

$$NH_4^+ + 1.5O_2 \rightarrow NO_2 + H_2O + 2H^+ \tag{5.21}$$

Under aerobic conditions, nitrite $NO_2$ is oxidized with $O_2$ to form nitrate $NO_3$ by nitrite-oxidizing bacteria $NOB$:

$$NO_2 + 0.5O_2 \rightarrow NO_3 \tag{5.22}$$

During anammox processes, under anoxic conditions, anammox bacteria $AMX$ convert ammonium $NH_4$ and nitrite $NO_2$ in nitrogen gas and little amounts of nitrate $NO_3$, as follows:

$$NH_4^+ + 1.32NO_2^- + 0.066HCO_3^- + 0.13H^+$$

$$\rightarrow 1.02N_2 + 0.256NO_3^- + 0.066CH_2O_{0.5}N_{0.15} + 2.03H_2O \tag{5.23}$$

The model considers metabolic processes of facutative heterotrophic bacteria $HB$ as well. Specifically, $HB$ are supposed to growth both in aerobic and anoxic conditions.

Under aerobic condition, they oxidate organic carbon $OC$ by using free oxygen $O_2$, while they carry out two denitrification reactions under anoxic conditions: in the first they oxidate $OC$ by using the nitrate bound oxygen and $NO_3$ reduces to nitrite $NO_2$; in the second they oxidize $OC$ by using nitrite bound oxygen and $NO_2$ reduces to molecular nitrogen.

In summary, the list of all model variables is reported below:

$$f_i(z,t),\ i \in \{AOB, AMX, NOB, HB, I\}, \tag{5.24}$$

$$\psi_i(z,t),\ i \in \{AOB, AMX, NOB, HB\}, \tag{5.25}$$

$$S_j(z,t),\ j \in \{NH_4, NO_2, NO_3, OC, O_2\}, \tag{5.26}$$

$$\psi_i^*(t),\ i \in \{AOB, AMX, NOB, HB\}, \tag{5.27}$$

$$S_j^*(t),\ j \in \{NH_4, NO_2, NO_3, OC\}. \tag{5.28}$$

As mentioned in Section 5.1, a constant and appropriate oxygen level is maintained in PN/A granular reactors, in order to guarantee distinct zones for ideal growth of both anaerobic and aerobic species. To model this, oxygen concentration is assumed to be variable only within the biofilm $S_{O_2}(z,t)$, where it varies due to microbial consumption and diffusion phenomena. Instead, oxygen concentration in the bulk liquid does not represent a model variable and is fixed at a constant value $S^*_{O_2}(t) = \overline{S}_{O_2}$.

Biological pathways described above have been included in the model through the mathematical formulation of the reaction terms. In particular, specific growth rates due to sessile species $r_{M,i}$ in Eqs. (5.3) and (5.5) are modelled as Monod-type kinetics:

$$r_{M,i} = f_i(\mu_i - k_{d,i}),\ i \in \{AOB, AMX, NOB, HB\}, \tag{5.29}$$

$$\mu_{AOB} = \mu_{max,AOB}\frac{S_{NH_4}}{K_{AOB,NH_4} + S_{NH_4}}\frac{S_{O_2}}{K_{AOB,O_2} + S_{O_2}}, \tag{5.30}$$

$$\mu_{AMX} = \mu_{max,AMX}\frac{K_{AMX,O_2}}{K_{AMX,O_2} + S_{O_2}}\frac{S_{NH_4}}{K_{AMX,NH_4} + S_{NH_4}}\frac{S_{NO_2}}{K_{AMX,NO_2} + S_{NO_2}}, \tag{5.31}$$

$$\mu_{NOB} = \mu_{max,NOB}\frac{S_{NO_2}}{K_{NOB,NO_2} + S_{NO_2}}\frac{S_{O_2}}{K_{NOB,O_2} + S_{O_2}}\frac{S_{NH_4}}{K_{NOB,NH_4} + S_{NH_4}}, \tag{5.32}$$

$$\mu_{HB} = \mu_{HB,1} + \mu_{HB,2} + \mu_{HB,3} =$$

$$= \mu_{max,HB}\frac{S_{OC}}{K_{HB,OC} + S_{OC}}\frac{S_{O_2}}{K_{HB,O_2} + S_{O_2}}\times$$

$$\times\frac{S_{NH_4}}{K_{HB,NH_4} + S_{NH_4}} + \beta_1\mu_{max,HB}\frac{K_{HB,O_2}}{K_{HB,O_2} + S_{O_2}}\frac{S_{OC}}{K_{HB,OC} + S_{OC}}\frac{S_{NO_3}}{K_{HB,NO_3} + S_{NO_3}}\times$$

$$\times\frac{S_{NO_3}}{S_{NO_2} + S_{NO_3}}\frac{S_{NH_4}}{K_{HB,NH_4} + S_{NH_4}} + \beta_2\mu_{max,HB}\frac{K_{HB,O_2}}{K_{HB,O_2} + S_{O_2}}\frac{S_{OC}}{K_{HB,OC} + S_{OC}}\times$$

$$\times\frac{S_{NO_2}}{K_{HB,NO_2} + S_{NO_2}}\frac{S_{NO_2}}{S_{NO_2} + S_{NO_3}}\frac{S_{NH_4}}{K_{HB,NH_4} + S_{NH_4}}, \tag{5.33}$$

where $\mu_{\max,i}$ is the maximum growth rate for biomass $i$, $K_i$ is the affinity constant of

the consumed substrate for biomass $i$ and $k_{d,i}$ is the decay constant for biomass $i$, $\beta_1$ and $\beta_2$ are the reduction factors for denitrification.

The formation rate of inactive biomass is given by the sum of decay rates of each active species, modelled as first order kinetics:

$$r_{M,I} = \sum_i f_i \, k_{d,i}, \; i \in \{AOB, AMX, NOB, HB\}. \tag{5.34}$$

The specific growth rates due to planktonic species $r_i$ in Eqs. (5.3) and (5.5), with $i \in \{AOB, AMX, NOB, HB\}$, are defined as:

$$r_{AOB} = k_{col,AOB} \, \frac{\psi_{AOB}}{\rho} \frac{S_{NH_4}}{K_{AOB,NH_4} + S_{NH_4}} \frac{S_{O_2}}{K_{AOB,O_2} + S_{O_2}}, \tag{5.35}$$

$$r_{AMX} = k_{col,AMX} \, \frac{\psi_{AMX}}{\rho} \frac{K_{AMX,O_2}}{K_{AMX,O_2} + S_{O_2}} \frac{S_{NH_4}}{K_{AMX,NH_4} + S_{NH_4}} \frac{S_{NO_2}}{K_{AMX,NO_2} + S_{NO_2}}, \tag{5.36}$$

$$r_{NOB} = k_{col,NOB} \, \frac{\psi_{NOB}}{\rho} \frac{S_{NO_2}}{K_{NOB,NO_2} + S_{NO_2}} \frac{S_{O_2}}{K_{NOB,O_2} + S_{O_2}} \frac{S_{NH_4}}{K_{NOB,NH_4} + S_{NH_4}}, \tag{5.37}$$

$$r_{HB} = k_{col,HB} \, \frac{\psi_{HB}}{\rho} \Bigg( \frac{S_{OC}}{K_{HB,OC} + S_{OC}} \frac{S_{O_2}}{K_{HB,O_2} + S_{O_2}} \frac{S_{NH_4}}{K_{HB,NH_4} + S_{NH_4}} +$$

$$+ \frac{S_{NO_3}}{S_{NO_2} + S_{NO_3}} \frac{K_{HB,O_2}}{K_{HB,O_2} + S_{O_2}} \frac{S_{OC}}{K_{HB,OC} + S_{OC}} \frac{S_{NO_3}}{K_{HB,NO_3} + S_{NO_3}} \times$$

$$\times \frac{S_{NH_4}}{K_{HB,NH_4} + S_{NH_4}} + \frac{S_{NO_2}}{S_{NO_2} + S_{NO_3}} \frac{K_{HB,O_2}}{K_{HB,O_2} + S_{O_2}} \frac{S_{OC}}{K_{HB,OC} + S_{OC}} \times$$

$$\times \frac{S_{NO_2}}{K_{HB,NO_2} + S_{NO_2}} \frac{S_{NH_4}}{K_{HB,NH_4} + S_{NH_4}} \Bigg), \tag{5.38}$$

where $k_{col,i}$ is the maximum colonization rate of motile species $i$.

The conversion rates of planktonic species $r_{\psi,i}$ in Eq. (5.11) are expressed by:

$$r_{\psi,i} = -\frac{1}{Y_{\psi,i}} r_i \ \rho, \ i \in \{AOB, AMX, NOB, HB\}, \tag{5.39}$$

where $Y_{\psi,i}$ denotes the yield of non-motile species $i$ on the corresponding motile species.

While, the conversion rates for soluble substrates within the biofilm $r_{S,j}$ in Eq.(5.13), with $j \in \{NH_4, NO_2, NO_3, OC, O_2\}$, are listed below:

$$r_{S,NH_4} = \Bigg( \Bigg( - \frac{1}{Y_{AOB}} - i_{N,B} \Bigg) \mu_{AOB} f_{AOB} + \Bigg( - \frac{1}{Y_{AMX}} - i_{N,B} \Bigg) \mu_{AMX} f_{AMX} +$$

$$- i_{N,B} \Bigg( \mu_{NOB} f_{NOB} + \mu_{HB,1} f_{HB} + \mu_{HB,2} f_{HB} + \mu_{HB,3} f_{HB} \Bigg) \Bigg) \ \rho, \tag{5.40}$$

$$r_{S,NO_2} = \left( \frac{1}{Y_{AOB}} \mu_{AOB} f_{AOB} - \left( \frac{1}{Y_{AMX}} + \frac{1}{1.14} \right) \mu_{AMX} f_{AMX} - \frac{1}{Y_{NOB}} \mu_{NOB} f_{NOB} + \right.$$

$$\left. - \left( 1 - \frac{1}{Y_{HB}} \right) \frac{1}{1.14} \mu_{HB,2} f_{HB} + \left( 1 - \frac{1}{Y_4} \right) \frac{1}{1.72} \mu_{HB,3} f_{HB} \right) \rho, \tag{5.41}$$

$$r_{S,NO_3} = \left( \frac{1}{1.14} \mu_{AMX} f_{AMX} + \frac{1}{Y_{NOB}} \mu_{NOB} f_{NOB} + \left( 1 - \frac{1}{Y_{HB}} \right) \frac{1}{1.14} \mu_{HB,2} f_{HB} \right) \rho, \tag{5.42}$$

$$r_{S,OC} = -\frac{1}{Y_{HB}} \left( \mu_{HB,1} f_{HB} + \mu_{HB,2} f_{HB} + \mu_{HB,3} f_{HB} \right) \rho, \tag{5.43}$$

$$r_{S,O_2} = \left(\left(1-\frac{3.43}{Y_{AOB}}\right)\mu_{AOB}f_{AOB}+\left(1-\frac{1.14}{Y_{NOB}}\right)\mu_{NOB}f_{NOB}+\left(1-\frac{1}{Y_{HB}}\right)\mu_{HB,1}f_{HB}\right)\rho, \tag{5.44}$$

where $Y_{AOB}$ is the yield of $AOB$ on $NH_4$, $Y_{AMX}$ is the yield of $AMX$ on $NH_4$, $Y_{NOB}$ is the yield of $NOB$ on $NO_2$ and $Y_{HB}$ is the yield of $HB$ on $OC$.

Moreover, the conversion rates of planktonic biomasses $r^*_{\psi,i}$ within the bulk liquid in Eq. (5.15) are defined as:

$$r^*_{\psi,i} = \psi^*_i(\mu^*_i - k_{d,i}),\ i \in \{AOB, AMX, NOB, HB\}, \tag{5.45}$$

$$\mu^*_{AOB} = \mu_{max,AOB}\frac{S^*_{NH_4}}{K_{AOB,NH_4}+S^*_{NH_4}}\frac{\overline{S}_{O_2}}{K_{AOB,O_2}+\overline{S}_{O_2}}, \tag{5.46}$$

$$\mu^*_{AMX} = \mu_{max,AMX}\frac{K_{AMX,O_2}}{K_{AMX,O_2}+\overline{S}_{O_2}}\frac{S^*_{NH_4}}{K_{AMX,NH_4}+S^*_{NH_4}}\frac{S^*_{NO_2}}{K_{AMX,NO_2}+S^*_{NO_2}}, \tag{5.47}$$

$$\mu^*_{NOB} = \mu_{max,NOB}\frac{S^*_{NO_2}}{K_{NOB,NO_2}+S^*_{NO_2}}\frac{\overline{S}_{O_2}}{K_{NOB,O_2}+\overline{S}_{O_2}}\frac{S^*_{NH_4}}{K_{NOB,NH_4}+S^*_{NH_4}}, \tag{5.48}$$

$$\mu^*_{HB} = \mu^*_{HB,1}+\mu^*_{HB,2}+\mu^*_{HB,3} =$$

$$= \mu_{max,HB}\frac{S^*_{OC}}{K_{HB,OC}+S^*_{OC}}\frac{\overline{S}_{O_2}}{K_{HB,O_2}+\overline{S}_{O_2}}\frac{S^*_{NH_4}}{K_{HB,NH_4}+S^*_{NH_4}}+$$

$$+\beta_1\mu_{max,HB}\frac{S^*_{NO_3}}{S^*_{NO_2}+S^*_{NO_3}}\frac{K_{HB,O_2}}{K_{HB,O_2}+\overline{S}_{O_2}}\frac{S^*_{OC}}{K_{HB,OC}+S^*_{OC}}\frac{S^*_{NO_3}}{K_{HB,NO_3}+S^*_{NO_3}}\times$$

$$\times \frac{S^*_{NH_4}}{K_{HB,NH_4} + S^*_{NH_4}} + \beta_2 \mu_{max,HB} \frac{S^*_{NO_2}}{S^*_{NO_2} + S^*_{NO_3}} \frac{K_{HB,O_2}}{K_{HB,O_2} + \overline{S}_{O_2}} \frac{S^*_{OC}}{K_{HB,OC} + S^*_{OC}} \times$$

$$\times \frac{S^*_{NO_2}}{K_{HB,NO_2} + S^*_{NO_2}} \frac{S^*_{NH_4}}{K_{HB,NH_4} + S^*_{NH_4}}, \tag{5.49}$$

while, the conversion rates of soluble substrates $r^*_{S,j}$ within the bulk liquid in Eq.(5.17), with $j \in \{NH_4, NO_2, NO_3, OC\}$, are listed below:

$$r^*_{S,NH_4} = \Bigg( \Bigg( - \frac{1}{Y_{AOB}} - i_{N,B} \Bigg) \mu_{AOB} \psi^*_{AOB} + \Bigg( - \frac{1}{Y_{AMX}} - i_{N,B} \Bigg) \mu_{AMX} \psi^*_{AMX} +$$

$$- i_{N,B} \Big( \mu_{NOB} \psi^*_{NOB} + \mu_{HB,1} \psi^*_{HB} + \mu_{HB,2} \psi^*_{HB} + \mu_{HB,3} \psi^*_{HB} \Big) \Bigg), \tag{5.50}$$

$$r^*_{S,NO_2} = \Bigg( \frac{1}{Y_{AOB}} \mu_{AOB} \psi^*_{AOB} - \Bigg( \frac{1}{Y_{AMX}} + \frac{1}{1.14} \Bigg) \mu_{AMX} \psi^*_{AMX} - \frac{1}{Y_{NOB}} \mu_{NOB} \psi^*_{NOB} +$$

$$- \Bigg( 1 - \frac{1}{Y_{HB}} \Bigg) \frac{1}{1.14} \mu_{HB,2} \psi^*_{HB} + \Bigg( 1 - \frac{1}{Y_{HB}} \Bigg) \frac{1}{1.72} \mu_{HB,3} \psi^*_{HB} \Bigg), \tag{5.51}$$

$$r*_{S,NO_3} = \Bigg( \frac{1}{1.14} \mu_{AMX} \psi^*_{AMX} + \frac{1}{Y_{NOB}} \mu_{NOB} \psi^*_{NOB} + \Bigg( 1 - \frac{1}{Y_{HB}} \Bigg) \frac{1}{1.14} \mu_{HB,2} \psi^*_{HB} \Bigg), \tag{5.52}$$

$$r^*_{S,OC} = - \frac{1}{Y_{HB}} \Big( \mu_{HB,1} \psi^*_{HB} + \mu_{HB,2} \psi^*_{HB} + \mu_{HB,3} \psi^*_{HB} \Big), \tag{5.53}$$

The values used for all stoichiometric and kinetic parameters are reported in Table

| Parameter | Definition | Unit | Value | Ref |
|---|---|---|---|---|
| $\mu_{max,AOB}$ | Maximum specific growth rate for $AOB$ | $d^{-1}$ | 2.05 | [151] |
| $\mu_{max,AMX}$ | Maximum specific growth rate for $AMX$ | $d^{-1}$ | 0.08 | [151] |
| $\mu_{max,NOB}$ | Maximum specific growth rate for $NOB$ | $d^{-1}$ | 1.45 | [151] |
| $\mu_{max,HB}$ | Maximum specific growth rate for $HB$ | $d^{-1}$ | 6.0 | [151] |
| $k_{d,AOB}$ | Decay-inactivation rate for $AOB$ | $d^{-1}$ | 0.0068 | [151] |
| $k_{d,AMX}$ | Decay-inactivation rate for $AMX$ | $d^{-1}$ | 0.00026 | [151] |
| $k_{d,NOB}$ | Decay-inactivation rate for $NOB$ | $d^{-1}$ | 0.004 | [151] |
| $k_{d,HB}$ | Decay-inactivation rate for $HB$ | $d^{-1}$ | 0.06 | [151] |
| $K_{AOB,NH_4}$ | $NH_4$ affinity constant for $AOB$ | $gN\ m^{-3}$ | 2.4 | [151] |
| $K_{AOB,O_2}$ | $O_2$ affinity constant for $AOB$ | $gO_2\ m^{-3}$ | 0.6 | [151] |
| $K_{AMX,NH_4}$ | $NH_4$ affinity constant for $AMX$ | $gN\ m^{-3}$ | 0.07 | [151] |
| $K_{AMX,NO_2}$ | $NO_2$ affinity constant for $AMX$ | $gN\ m^{-3}$ | 0.05 | [151] |
| $K_{AMX,O_2}$ | $O_2$ inhibiting constant for $AMX$ | $gO_2\ m^{-3}$ | 0.01 | [151] |
| $K_{NOB,NH_4}$ | $NH_4$ affinity constant for $NOB$ | $gN\ m^{-3}$ | 0.1 | [151] |
| $K_{NOB,NO_2}$ | $NO_2$ affinity constant for $NOB$ | $gN\ m^{-3}$ | 5.5 | [151] |
| $K_{NOB,O_2}$ | $O_2$ affinity constant for $NOB$ | $gO_2\ m^{-3}$ | 2.2 | [151] |
| $K_{HB,NH_4}$ | $NH_4$ affinity constant for $HB$ | $gN\ m^{-3}$ | 0.1 | [151] |
| $K_{HB,NO_2}$ | $NO_2$ affinity constant for $HB$ | $gN\ m^{-3}$ | 0.5 | [151] |
| $K_{HB,NO_3}$ | $NO_3$ affinity constant for $HB$ | $gN\ m^{-3}$ | 0.5 | [151] |
| $K_{HB,OC}$ | $OC$ affinity constant for $HB$ | $gCOD\ m^{-3}$ | 4.0 | [151] |
| $K_{HB,O_2}$ | $O_2$ affinity/inhibiting constant for $HB$ | $gO_2\ m^{-3}$ | 0.2 | [151] |
| $Y_{AOB}$ | $AOB$ yield on $NH_4$ | $gCOD\ gN^{-1}$ | 0.150 | [151] |
| $Y_{AMX}$ | $AMX$ yield on $NH_4$ | $gCOD\ gN^{-1}$ | 0.159 | [151] |
| $Y_{NOB}$ | $NOB$ yield on $NO_2$ | $gCOD\ gN^{-1}$ | 0.041 | [151] |
| $Y_{HB}$ | $HB$ yield on $O_2$ | $gCOD\ gCOD^{-1}$ | 0.63 | [151] |
| $i_{N,B}$ | N content of biomass | $gN\ gCOD^{-1}$ | 0.07 | [151] |
| $\beta_1$ | Reduction factor for denitrification $NO_3 - NO_2$ | $--$ | 0.8 | [151] |
| $\beta_2$ | Reduction factor for denitrification $NO_2 - N_2$ | $--$ | 0.8 | [151] |
| $k_{col,i}$ | Maximum colonization rate of $i^{th}$ planktonic species | $d^{-1}$ | 0.02 | (a) |
| $Y_{\psi,i}$ | Yield of non-motile microorganisms on motile species | $--$ | 0.02 | (a) |
| $D_{S,NH_4}$ | Diffusion coefficient of $NH_4$ in biofilm | $m^2\ d^{-1}$ | $1.49 \cdot 10^{-4}$ | [22] |
| $D_{S,NO_2}$ | Diffusion coefficient of $NO_2$ in biofilm | $m^2\ d^{-1}$ | $1.12 \cdot 10^{-4}$ | [145] |
| $D_{S,NO_3}$ | Diffusion coefficient of $NO_3$ in biofilm | $m^2\ d^{-1}$ | $1.12 \cdot 10^{-4}$ | [145] |
| $D_{S,OC}$ | Diffusion coefficient of $OC$ in biofilm | $m^2\ d^{-1}$ | $0.83 \cdot 10^{-4}$ | [22] |
| $D_{S,O_2}$ | Diffusion coefficient of $O_2$ in biofilm | $m^2\ d^{-1}$ | $1.75 \cdot 10^{-4}$ | [22] |
| $D_{\psi,i}$ | Diffusion coefficient of $i^{th}$ planktonic species in biofilm | $m^2\ d^{-1}$ | $10^{-5}$ | (a) |
| $v_{a,AOB}$ | Attachment velocity of $AOB$ planktonic species | $m\ d^{-1}$ | $3.75 \cdot 10^{-3}$ | (a) |
| $v_{a,AMX}$ | Attachment velocity of $AMX$ planktonic species | $m\ d^{-1}$ | 0 | (a) |
| $v_{a,NOB}$ | Attachment velocity of $NOB$ planktonic species | $m\ d^{-1}$ | $3.75 \cdot 10^{-3}$ | (a) |
| $v_{a,HB}$ | Attachment velocity of $HB$ planktonic species | $m\ d^{-1}$ | $3.75 \cdot 10^{-3}$ | (a) |
| $\rho$ | Biofilm density | $gCOD\ m^{-3}$ | 25000 | (a) |
| $\lambda$ | Detachment coefficient | $m^{-1}\ d^{-1}$ | 25 | (a) |
| $V$ | Reactor volume | $m^3$ | 400 | (a) |
| $Q$ | Volumetric flow rate | $m^3\ d^{-1}$ | 2000 | (a) |
| $N_G$ | Number of granules in the reactor | $--$ | $2.4 \cdot 10^{10}$ | (a) |
| $\overline{S}_{O_2}$ | Oxygen level in the bulk liquid | $gO_2\ m^{-3}$ | 0.75 | (a) |

(a) Assumed

Table 5.1: Kinetic, stoichiometric and operating parameters used for numerical simulations.

5.1.

## 5.4 Numerical studies and results

### 5.4.1 Influent characteristics, reactor configuration and simulation parameters.

Numerical simulations have been carried out to test the model behaviour, simulate the evolution and ecology of anammox granular biofilms and investigate the treatment process occurring in PN/A granular sludge reactors, with a focus on the start-up phase.

The modelled influent wastewater represents a typical high ammonium wastewater treated in PN/A granular sludge reactors. It is characterized by $300\ gN\ m^{-3}$ of ammonium and $50\ gCOD\ m^{-3}$ of soluble organic carbon, while nitrite and nitrate amounts are supposed to be negligible. Specifically, $S^{in}_{NO_2}$ and $S^{in}_{NO_3}$ are set to $0.0001\ gN\ m^{-3}$ in order to avoid numerical errors arising from zero concentrations in the kinetic expressions. The constant oxygen level within the reactor is fixed at $0.75\ gO_2\ m^{-3}$. Microbial biomasses are assumed to be not present in the influent ($\psi^{in}_i = 0$).

The strategy of using two separate inocula is studied: at $t = 0$ the bioreactor is inoculated with the activated sludge coming from a conventional nitrification-denitrification reactor, where anammox biomass is not present. Once the process has started, an anammox inoculum is added at a fixed time instant $t_{AMX}$. Then, the $AMX$ planktonic cells are supposed to colonize the granules through invasion phenomena and grow in sessile form in the innermost part, where anoxic conditions are guaranteed. The parameter $t_{AMX}$ has been varied in the simulations to investigate the effect of granules dimension on anammox growth. The activated sludge inoculum is modelled by setting the initial concentration of planktonic biomasses in the bulk liquid: $\psi^*_{AOB,0} = \psi^*_{NOB,0} = \psi^*_{HB,0} = 300\ gCOD\ m^{-3}$, $\psi^*_{AMX,0} = 0$. Meanwhile, in order to consider the addition of the anammox inoculum at $t_{AMX}$, Eq. (5.15) for $\psi^*_{AMX}$ has been replaced by the following impulsive ordinary differential equation (IDE):

$$V\dot{\psi}^*_{AMX}(t) = Q(\psi^{in}_{AMX} - \psi^*_{AMX}(t)) - A(t)N_G D_{\psi,AMX}\frac{\partial \psi_{AMX}(R(t),t)}{\partial r} +$$

$$+r^*_{\psi,AMX}(t,\boldsymbol{\psi}^*,\mathbf{S}^*) - \sigma_{a,AMX}(t)\rho A(t), \;\; t \neq t_{AMX},\; t > 0, \tag{5.54}$$

$$\Delta\psi^*_{AMX}(t_{AMX}) = \psi^*_{AMX,t_{AMX}} = \psi^*_{AMX}(t^+_{AMX}) - \psi^*_{AMX}(t^-_{AMX}), \tag{5.55}$$

where $\psi^*_{AMX,t_{AMX}}$ is the concentration of anammox planktonic biomass added in the bulk liquid at $t_{AMX}$ and is related to the anammox inoculum size. $\psi^*_{AMX}(t^+_{AMX})$ and $\psi^*_{AMX}(t^-_{AMX})$ are the right and left limits of $\psi^*_{AMX}$ at time $t_{AMX}$. Since the parameters $\psi^*_{AMX,t_{AMX}}$ and $t_{AMX}$ are varied in numerical studies, their values will be provided below, case to case.

| Parameter | Definition | Unit | Value |
|---|---|---|---|
| $S^{in}_{NH_4}$ | Inlet concentration of ammonium | $gN\ m^{-3}$ | 300 |
| $S^{in}_{NO_2}$ | Inlet concentration of nitrite | $gN\ m^{-3}$ | 0.0001 |
| $S^{in}_{NO_3}$ | Inlet concentration of nitrate | $gN\ m^{-3}$ | 0.0001 |
| $S^{in}_{OC}$ | Inlet concentration of organic carbon | $gCOD\ m^{-3}$ | 50 |
| $\psi^*_{AOB,0}$ | Initial concentration of planktonic $AOB$ | $gCOD\ m^{-3}$ | 300 |
| $\psi^*_{NOB,0}$ | Initial concentration of planktonic $NOB$ | $gCOD\ m^{-3}$ | 300 |
| $\psi^*_{HB,0}$ | Initial concentration of planktonic $HB$ | $gCOD\ m^{-3}$ | 300 |
| $\psi^*_{AMX,t_{AMX}}$ | Concentration of $AMX$ sludge added in the reactor at $t_{AMX}$ | $gCOD\ m^{-3}$ | varied[1] |
| $t_{AMX}$ | Addition time of $AMX$ sludge | $d$ | varied[1] |

[1]The values used are reported in the text

Table 5.2: Wastewater influent and inoculum composition.

Reactor volume $V$ is assumed equal to $400\ m^3$ [30, 31, 145] and fed with a constant flow rate $Q$ of $2000\ m^3\ d^{-1}$ (hydraulic retention time $HRT = 0,2\ d$). The detachment contribution to planktonic or detached biomass is neglected, since the $HRT$ is very low. Indeed, the detached biomass has different characteristics from both ses-

sile and planktonic biomass and needs several hours to return to the planktonic state [121, 122, 123]. Moreover, under such hydrodynamics conditions granules are retained in the reactor, while planktonic and detached cells are rapidly washed out. The number of granules $N_G$ has been selected through an iterative procedure which involved the detachment coefficient $\lambda$ [152], with the aim to guarantee a $25\%$ filling ratio [30, 31, 145] by considering $1\ mm$ as steady-state particle radius (an average size representative of the anammox granules [30, 31, 145]). In accordance with [22], diffusivity of soluble substrates in biofilm is assumed to be $80\%$ of diffusivity in water. The values reported above for all operating parameters are characteristic of PN/A granular reactors [153]. All model parameters have been summarized in Table 5.1 and Table 5.2.

Four numerical studies have been performed:

- the first study (S1) presents a reference case to test the model behaviour and explores the *de novo* granulation of anammox granules and the global treatment process of PN/A granular bioreactors;
- the second study (S2) examines the effect of the anammox addition time $t_{AMX}$ on the start-up process and granules evolution;
- the third study (S3) investigates the influence of anammmox inoculum size $\psi^*_{AMX,t_{AMX}}$ on the start-up process and granules evolution;
- the last study (S4) analyzes the combined effects of both the addition time and the size of the anammox inoculum on the start-up process.

### 5.4.2 S1 - Partial nitritation/anammox process in granular-based reactors

In the first numerical study (S1) the *de novo* anammox granulation and the dynamics of solutes and planktonic biomasses within the PN/A granular system are investigated. As mentioned in Section 5.1, the granular sludge reactor is initially inoculated with

activated sludge while an anammox inoculum is added later. Such study concerns a reference case ($RUN1$) where the addition time of anammox inoculum $t_{AMX}$ is set to $10\ d$ and the anammox inoculum size $\psi^*_{AMX,t_{AMX}}$ is set to $500\ gCOD\ m^{-3}$. Numerical results are summarized in Figs. 5.1-5.4.

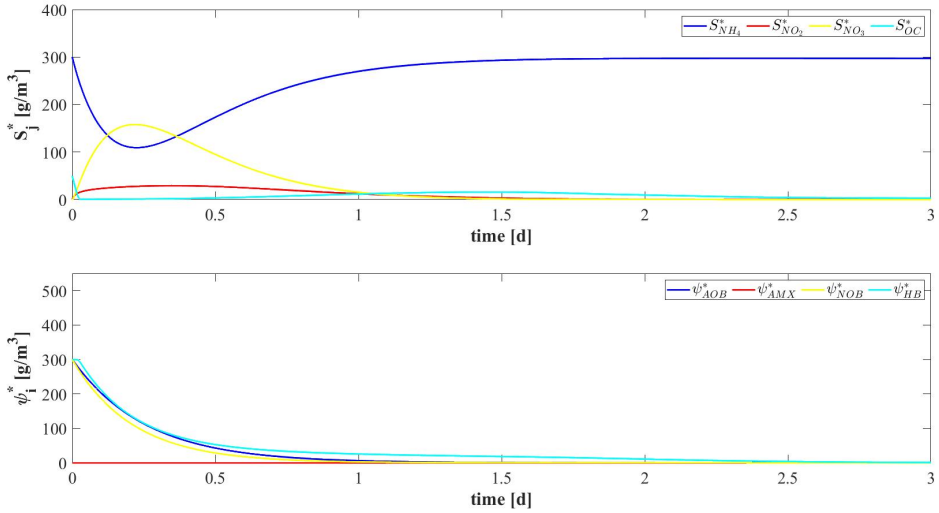


Figure 5.1: S1 - Evolution of soluble substrates (top) and planktonic biomasses (bottom) concentrations within the bulk liquid in the first 3 days. $S^*_{NH_4}$: Ammonium, $S^*_{NO_2}$: Nitrite, $S^*_{NO_3}$: Nitrate, $S^*_{OC}$: Organic carbon, $\psi^*_{AOB}$: Aerobic ammonia-oxidizing bacteria, $\psi^*_{AMX}$: Anaerobic ammonia-oxidizing bacteria, $\psi^*_{NOB}$: Aerobic nitrite-oxidizing bacteria, $\psi^*_{HB}$: Heterotrophic bacteria. Wastewater influent composition: $S^{in}_{NH_4} = 300\ gN\ m^{-3}$ (Ammonium), $S^{in}_{NO_2} = 0.0001\ gN\ m^{-3}$ (Nitrite), $S^{in}_{NO_3} = 0.0001\ gN\ m^{-3}$ (Nitrate), $S^{in}_{OC} = 50\ gCOD\ m^{-3}$ (Organic carbon). Fixed oxygen concentration within the reactor: $S_{O_2} = 0.75\ gO_2\ m^{-3}$. Concentration of $AMX$ bacteria added in the reactor: $\psi^*_{AMX,t_{AMX}} = 500\ gCOD\ m^{-3}$. Addition time of $AMX$ sludge: $t_{AMX} = 10\ d$.

Fig. 5.1 shows the time evolution of soluble substrates and planktonic biomasses within the bulk liquid during the initial 3 days. Initially, biofilm granules have small size and the dynamics of substrates are governed by planktonic biomass. In particular, under aerobic conditions nitritation and $NO_2$ and $OC$ oxidation occur in the reactor due to the metabolic activities of planktonic $AOB$, $NOB$ and $HB$. Ammonium $S^*_{NH_4}$ (blue in Fig. 5.1-top) is consumed and converted into nitrite $S^*_{NO_2}$ (red in Fig. 5.1-top) by planktonic $AOB$ $\psi^*_{AOB}$ (nitritation process), and subsequently nitrite is converted into nitrate $S^*_{NO_3}$ (yellow in Fig. 5.1-top) by planktonic $NOB$ $\psi^*_{NOB}$ (nitrite oxidation). Meantime,

the consumption of organic carbon $S^*_{OC}$ (cyan in Fig. 5.1-top) indicates the activity of planktonic $HB$ $\psi^*_{HB}$. This initial trend is followed by a turnover phase in which the planktonic biomass rapidly decreases (Fig. 5.1-bottom) due to the granulation and the low hydraulic retention time (HRT) and it is replaced by the sessile biomass of growing biofilm granules. Nevertheless, initially the amount of grown sessile biomass is still low to compensate the lost contribution of substrates conversion by planktonic biomass, and sudden increases in ammonium and reductions in nitrite and nitrate are observed. In real granular-based plants, the decrease of planktonic biomass is sometimes slowed down by considering variable HRTs or loading rates [137, 134]. Although these procedures have been not included in the model, this does not compromise its reliability in describing the successive biological processes and substrates dynamics.

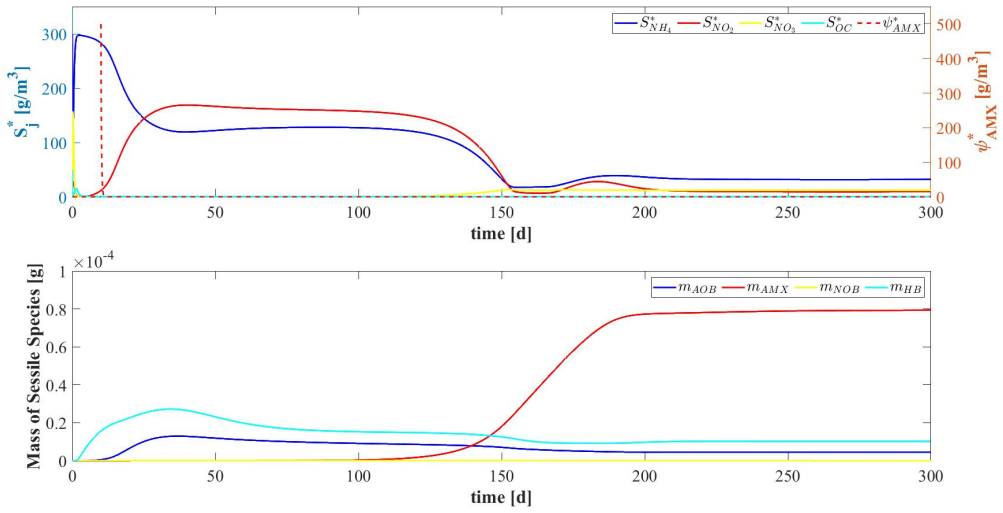


Figure 5.2: S1 - Evolution and steady-state of soluble substrates and $AMX$ planktonic biomass concentrations within the bulk liquid (top) and of mass of active sessile species within the granule (bottom). $S^*_{NH_4}$: Ammonium, $S^*_{NO_2}$: Nitrite, $S^*_{NO_3}$: Nitrate, $S^*_{OC}$: Organic carbon, $\psi^*_{AMX}$: Anaerobic ammonia-oxidizing bacteria, $m_{Su}$: mass of aerobic ammonia-oxidizing bacteria, $m_{Bu}$: mass of anaerobic ammonia-oxidizing bacteria, $m_{Pro}$: mass of aerobic nitrite-oxidizing bacteria, $m_{Ac}$: mass of heterotrophic bacteria. Wastewater influent composition: $S^{in}_{NH_4} = 300\ gN\ m^{-3}$ (Ammonium), $S^{in}_{NO_2} = 0.0001\ gN\ m^{-3}$ (Nitrite), $S^{in}_{NO_3} = 0.0001\ gN\ m^{-3}$ (Nitrate), $S^{in}_{OC} = 50\ gCOD\ m^{-3}$ (Organic carbon). Fixed oxygen concentration within the reactor: $\overline{S}_{O_2} = 0.75\ gO_2\ m^{-3}$. Concentration of $AMX$ bacteria added in the reactor: $\psi^*_{AMX,t_{AMX}} = 500\ gCOD\ m^{-3}$. Addition time of $AMX$ sludge: $t_{AMX} = 10\ d$.

Fig. 5.2 shows the time evolution of soluble substrates and planktonic $AMX$ concentrations, and sessile masses within the system, until a steady-state configuration is reached. After the initial days, the variation of the substrates concentration due to the sessile metabolism begins to be visible. In particular, since granules are still small, aerobic conditions are found in almost all the biofilm domain and dynamics of substrates are governed by aerobic sessile species: $AOB$ convert ammonium (blue in Fig. 5.2-top) into nitrite (red in Fig. 5.2-top) and $HB$ oxidate organic compounds (cyan in Fig. 5.2-top). On the contrary, the conversion of nitrite to nitrate (yellow in Fig. 5.2-top) by $NOB$ is not visible. This happens because $NOB$ have a high $O_2$ affinity constant and are less competitive than $AOB$ and $HB$ at low oxygen levels. Consequently, high masses of sessile $AOB$ and $HB$ and negligible amounts of $NOB$ are observed in the first 30 days (Fig. 5.2-bottom). Furthermore, no anammox biomass is detected in the reactor until $t_{AMX} = 10\ d$, when the anammox inoculum is added and a discontinuity is generated in the graph of planktonic $AMX$ concentration (Fig. 5.2-bottom). Then, planktonic $AMX$ invade the innermost layers of granules, where anoxic conditions optimal for their anaerobic metabolism are found and begin to grow in sessile form. The nitritation process by $AOB$ lead to the partial removal of ammonium, which reaches a temporary equilibrium at about 50% of the influent concentration, while all the organic matter is oxidized aerobically by $HB$. At this moment, a very long transition phase begins, in which ammonium and nitrite concentrations remain almost constant. Granules are fully developed and present anoxic conditions and shortage of organic carbon in the internal layers, which inhibit the $AOB$ and $HB$ growth. At the same time, such anoxic conditions and the simultaneous presence of ammonium and nitrite in the reactor promote the $AMX$ growth. However, as the $AMX$ biomass is characterized by very low growth rates, the further ammonium and nitrite consumption induced by the anammox process begins to be relevant after 100 days. Specifically, a considerable growth of anammox biomass is observed between 100 and 200 days and leads to the consumption of ammonium and nitrite and small production of nitrate. The steady-state configuration

shows a residual ammonium concentration lower than $40 - 50\ gCOD\ m^{-3}$, and very low concentrations of nitrite and nitrate. In conclusion, the system presents an ammonium removal efficiency of about $90\%$, which is achieved through a two-stage treatment process: the first stage is governed by $AOB$ which halve the ammonium concentration and produce nitrite necessary for the successive stage; the second stage is governed by $AMX$ which consume a further relevant amount of ammonium by using nitrite.

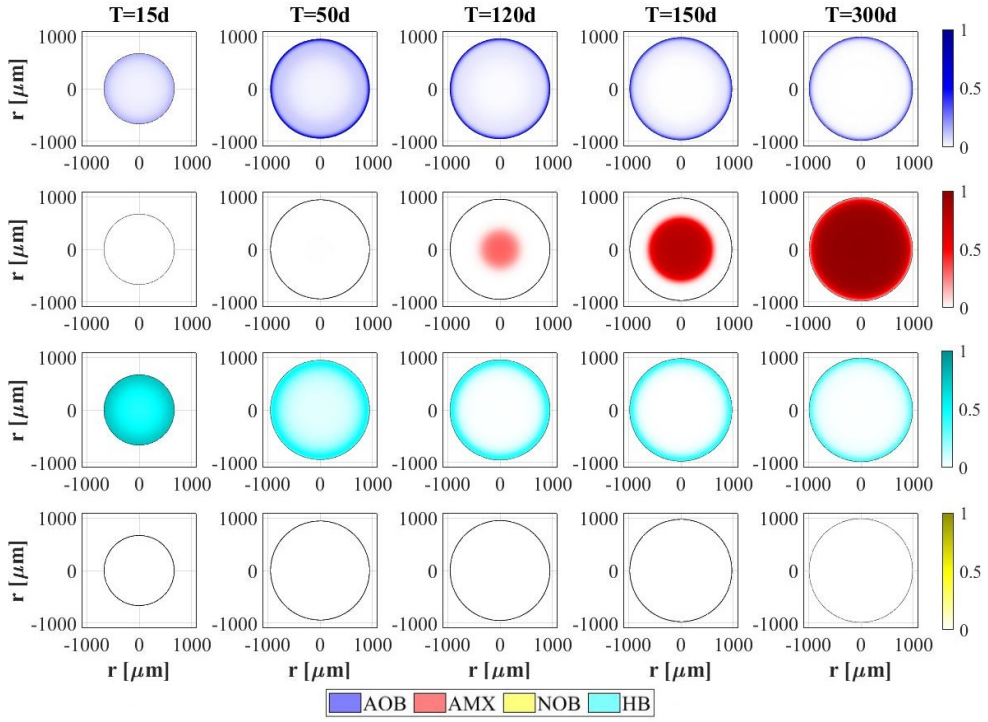


Figure 5.3: S1 - Active microbial species distribution in the diametrical section, at $T = 15\ d$, $T = 50\ d$, $T = 120\ d$, $T = 150\ d$, $T = 300\ d$. Wastewater influent composition: $S^{in}_{NH_4} = 300\ gN\ m^{-3}$ (Ammonium), $S^{in}_{NO_2} = 0.0001\ gN\ m^{-3}$ (Nitrite), $S^{in}_{NO_3} = 0.0001\ gN\ m^{-3}$ (Nitrate), $S^{in}_{OC} = 50\ gCOD\ m^{-3}$ (Organic carbon). Fixed oxygen concentration within the reactor: $\overline{S}_{O_2} = 0.75\ gO_2\ m^{-3}$. Concentration of $AMX$ bacteria added in the reactor: $\psi^*_{AMX,t_{AMX}} = 500\ gCOD\ m^{-3}$. Addition time of $AMX$ sludge: $t_{AMX} = 10\ d$.

In Fig. 5.3, the distribution of sessile species within the granule is shown at 15, 50, 120, 150 and 300 days. At $T = 15\ d$, the granule is constituted mostly by $HB$ (cyan), which have high growth rates, and $AOB$ (blue), favored by the availability of ammonium and oxygen. At $T = 50\ d$, the granule is fully developed and is characterized by internal anoxic zones. Therefore, aerobic $AOB$ and $HB$ accumulate in the

outermost layers of the granule, while $AMX$ (red) grow in the centre. However, due to the low growth rate, a small $AMX$ core only begins to be visible at $T = 120\ d$. Their growth intensifies strongly in the successive phases, up to a steady-state configuration where the granule is dominated by $AMX$ while $AOB$ and $HB$ are limited to the thin outermost layer. The amount of $NOB$ (yellow) present in the granule is negligible throughout the process. Such result is in agreement with [154], which shows that low oxygen levels limit the $NOB$ metabolic pathways. Indeed, as explained above, $NOB$ are less competitive than $AOB$ and $HB$ in the presence of low oxygen concentrations. This is beneficial for the ammonium removal process because $NOB$ metabolic activities would include the consumption of nitrite necessary for the $AMX$ growth.

The microbial distribution and the relative abundance here reported are in agreement with experimental observations in literature [154, 155, 156]. However, they can be influenced by various factors, such as the granule size, the oxygen level in the reactor, the influent composition. First, the $AMX/AOB$ ratio within the granules varies due to the granule size and the oxygen level. Specifically, large granules (described in this study) have more extended anoxic zones and consequently are characterized by an high $AMX/AOB$ ratio, while smaller granules have reduced anoxic cores and lower $AMX/AOB$ ratios [154, 156]. Then, the extension of the anoxic zone and therefore the $AMX/AOB$ ratio increases as the oxygen level set in the reactor decreases [30, 145]. Furthermore, the influent composition can affect the evolution of granules and the relative abundance of individual species. For example, as shown in Mozumder et al. (2014) [148], the presence of organic substance within the influent promotes the heterotrophic growth in the granules.

Lastly, the evolution of the granule radius over time $R(t)$ is reported in Fig. 5.4. $R(t)$ starts from a vanishing initial value and it increases rapidly during the first days, when the granulation process is more intense. It reaches a temporary constant value after 30 days, and increases slightly again due to the anammox growth. The final steady-state value is approximately $1\ mm$.

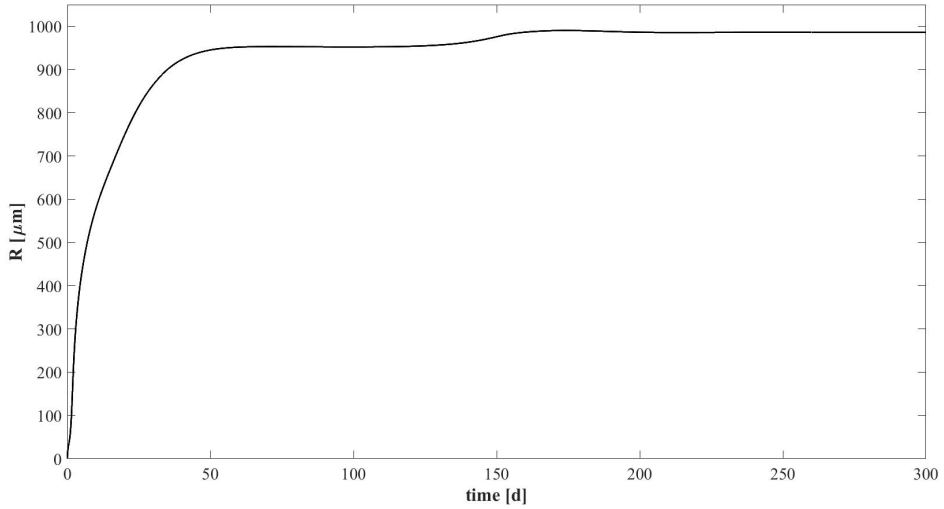


Figure 5.4: S1 - Biofilm radius evolution over time. Wastewater influent composition: $S^{in}_{NH_4} = 300\ gN\ m^{-3}$ (Ammonium), $S^{in}_{NO_2} = 0.0001\ gN\ m^{-3}$ (Nitrite), $S^{in}_{NO_3} = 0.0001\ gN\ m^{-3}$ (Nitrate), $S^{in}_{OC} = 50\ gCOD\ m^{-3}$ (Organic carbon). Fixed oxygen concentration within the reactor: $\overline{S}_{O_2} = 0.75\ gO_2\ m^{-3}$. Concentration of $AMX$ bacteria added in the reactor: $\psi^*_{AMX,t_{AMX}} = 500\ gCOD\ m^{-3}$. Addition time of $AMX$ sludge: $t_{AMX} = 10\ d$.

### 5.4.3 S2 - Effects of the anammox addition time on the process

Results presented in Section 5.4.2 describe the evolution and dynamics of anammox granules in a granular-based reactor inoculated initially with a nitrifying/denitrifying activated sludge and later with an anammox sludge. The addition time of the anammox inoculum appears to be a key element in the process, since the development of the anammox biomass strongly depends on the conditions inside the reactor at the addition time. Specifically, different addition times can lead to different scenarios. In such context, this study (S2) focuses on the effects that the addition time of anammox sludge $t_{AMX}$ has on the growth of anammox granules and on the duration of the start-up period. For this purpose, six simulations ($RUN2 - RUN7$) have been carried out by setting the addition time $t_{AMX}$ equal to 0, 3, 5, 10, 20 and 40 days, respectively. The inoculum size $\psi^*_{AMX,t_{AMX}}$ has been fixed equal to $500\ gCOD\ m^{-3}$ for all simulations. Results are reported in Figs. 5.5-5.9.

Fig. 5.5 shows the oxygen concentration within the granule at $t_{AMX}$ for simulations

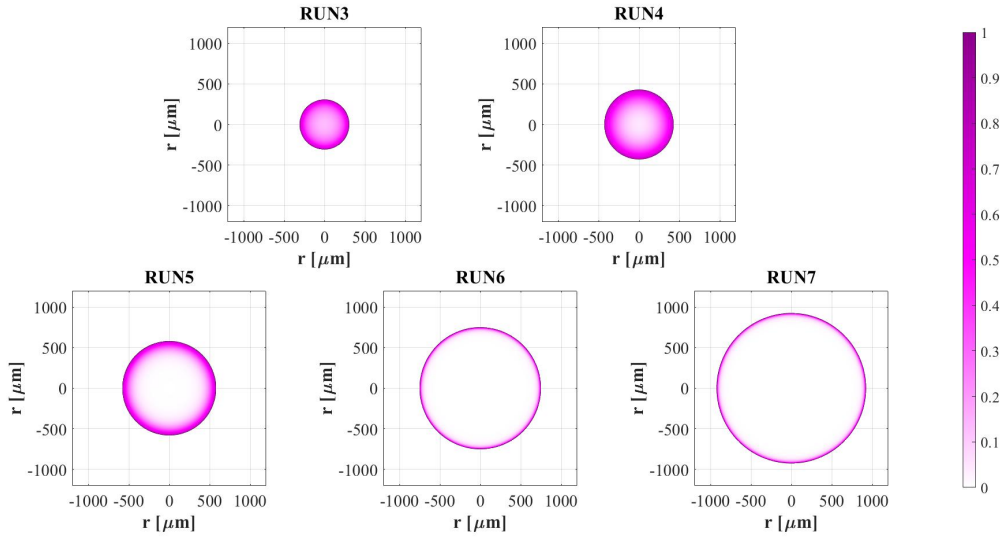


Figure 5.5: S2 - Oxygen concentration within the granule (diametrical section) at the addition time of $AMX$ sludge $t_{AMX}$. Wastewater influent composition: $S^{in}_{NH_4} = 300\ gN\ m^{-3}$ (Ammonium), $S^{in}_{NO_2} = 0.0001\ gN\ m^{-3}$ (Nitrite), $S^{in}_{NO_3} = 0.0001\ gN\ m^{-3}$ (Nitrate), $S^{in}_{OC} = 50\ gCOD\ m^{-3}$ (Organic carbon). $RUN3$: $t_{AMX} = 3\ d$; $RUN4$: $t_{AMX} = 5\ d$; $RUN5$: $t_{AMX} = 10\ d$; $RUN6$: $t_{AMX} = 20\ d$; $RUN7$: $t_{AMX} = 40\ d$. Fixed oxygen concentration within the reactor: $\overline{S}_{O_2} = 0.75\ gO_2\ m^{-3}$. Concentration of $AMX$ bacteria added in the reactor: $\psi^*_{AMX,t_{AMX}} = 500\ gCOD\ m^{-3}$.

$RUN3 - RUN7$. As can be seen, the extension of the anoxic zone increases as $t_{AMX}$ increases. Indeed, when the anammox inoculum is introduced in the initial phase, granules are small and oxygen fully penetrated. On the other hand, when the inoculum is added later, granules are fully developed and almost completely anoxic, except for the most external layers. The extension of the anoxic zone at $t_{AMX}$ affects the invasion and the growth of the anammox biomass.

This is visible in Fig. 5.6, where the distribution of anammox sessile biomass at different times is reported for simulations $RUN2$, $RUN4$, $RUN5$, $RUN7$. When the $AMX$ addition occurs at the beginning of the process ($RUN2$), the invasion process is inhibited by the presence of oxygen throughout the biofilm. Hence the anammox growth is very slow. Conversely, when $t_{AMX}$ is high ($RUN4$, $RUN5$, $RUN7$) anammox cells colonize the anoxic granule core and grow more rapidly in sessile form. Anyway, although the addition of the anammox inoculum can be delayed to promote more intense

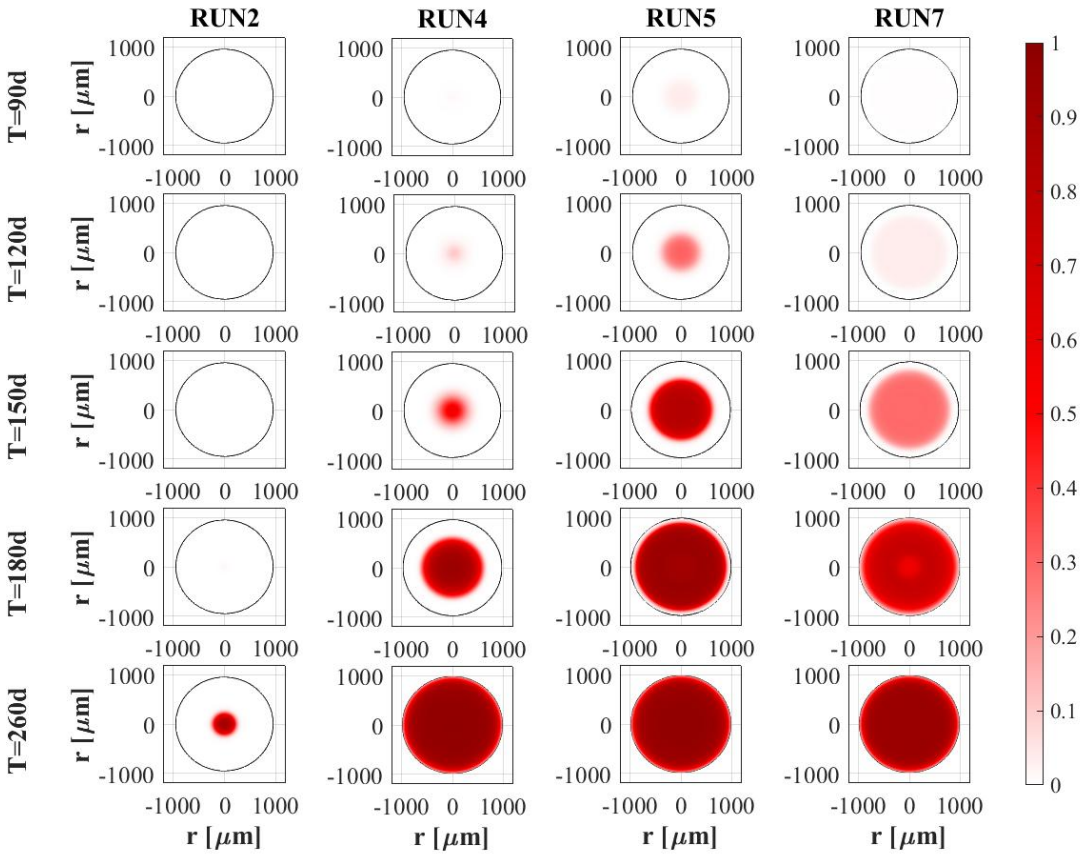


Figure 5.6: S2 - $AMX$ distribution within the granule (diametrical section) at $T = 90\ d$, $T = 120\ d$, $T = 150\ d$, $T = 180\ d$, $T = 260\ d$ for different addition times of $AMX$ sludge $t_{AMX}$. Wastewater influent composition: $S^{in}_{NH_4} = 300\ gN\ m^{-3}$ (Ammonium), $S^{in}_{NO_2} = 0.0001\ gN\ m^{-3}$ (Nitrite), $S^{in}_{NO_3} = 0.0001\ gN\ m^{-3}$ (Nitrate), $S^{in}_{OC} = 50\ gCOD\ m^{-3}$ (Organic carbon). $RUN2$: $t_{AMX} = 0$; $RUN4$: $t_{AMX} = 5\ d$; $RUN5$: $t_{AMX} = 10\ d$; $RUN7$: $t_{AMX} = 40\ d$. Fixed oxygen concentration within the reactor: $\overline{S}_{O_2} = 0.75\ gO_2\ m^{-3}$. Concentration of $AMX$ bacteria added in the reactor: $\psi^*_{AMX,t_{AMX}} = 500\ gCOD\ m^{-3}$.

invasion phenomena, this also leads to a delay in the initiation of the anammox process. This means that the effects of $t_{AMX}$ on the anammox growth are not unique. Indeed, the complete development of the anammox biomass for $t_{AMX} = 10\ d$ ($RUN5$) appears earlier than for $t_{AMX} = 40\ d$ ($RUN7$).

Since $t_{AMX}$ influences the anammox growth, it affects also the rate of the biological processes within the reactor. The concentrations of soluble substrates and $AMX$ planktonic biomass within the reactor are reported in Fig. 5.7. As can be seen, the

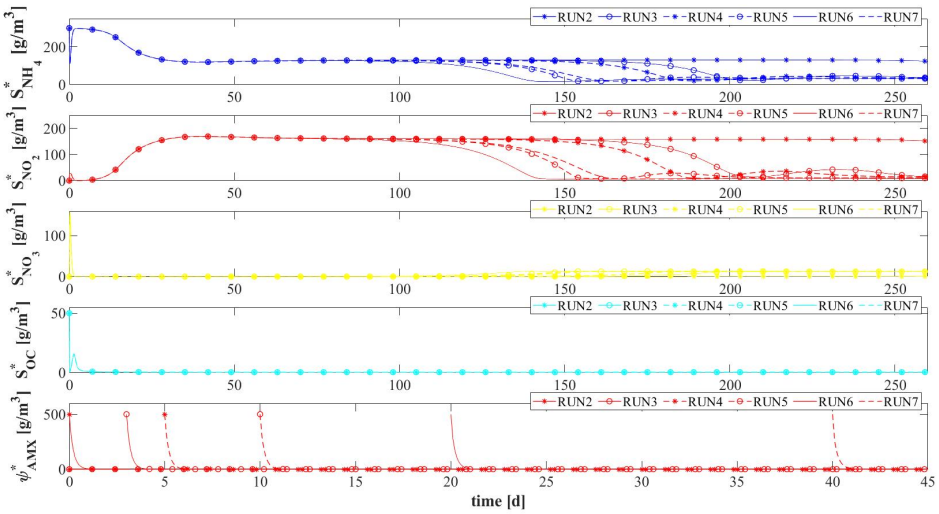


Figure 5.7: S2 - Evolution of soluble substrates and planktonic $AMX$ concentrations within the bulk liquid for different addition times of $AMX$ sludge $t_{AMX}$. $S^*_{NH_4}$: Ammonium, $S^*_{NO_2}$: Nitrite, $S^*_{NO_3}$: Nitrate, $S^*_{OC}$: Organic carbon, $\psi^*_{AMX}$: Anaerobic ammonia-oxidizing bacteria. Wastewater influent composition: $S^{in}_{NH_4} = 300\ gN\ m^{-3}$ (Ammonium), $S^{in}_{NO_2} = 0.0001\ gN\ m^{-3}$ (Nitrite), $S^{in}_{NO_3} = 0.0001\ gN\ m^{-3}$ (Nitrate), $S^{in}_{OC} = 50\ gCOD\ m^{-3}$ (Organic carbon). $RUN2$: $t_{AMX} = 0$; $RUN3$: $t_{AMX} = 3\ d$; $RUN4$: $t_{AMX} = 5\ d$; $RUN5$: $t_{AMX} = 10\ d$; $RUN6$: $t_{AMX} = 20\ d$; $RUN7$: $t_{AMX} = 40\ d$. Fixed oxygen concentration within the reactor: $\overline{S}_{O_2} = 0.75\ gO_2\ m^{-3}$. Concentration of $AMX$ bacteria added in the reactor: $\psi^*_{AMX,t_{AMX}} = 500\ gCOD\ m^{-3}$.

first stage of the process (first 100 days) does not depend on $t_{AMX}$, since the amount of anammox sessile biomass is limited and plays a negligible role. The successive trends of ammonium $S^*_{NH_4}$ (blue) and nitrite $S^*_{NO_2}$ (red) concentrations are influenced by the anammox biomass and, therefore, by $t_{AMX}$, while not significant variations of nitrate $S^*_{NO_3}$ (yellow) and organic matter $S^*_{OC}$ (cyan) occur. When the anammox growth is faster, ammonium and nitrite are more rapidly consumed and the time necessary to reach the steady-state configuration decreases. Specifically, the minimum duration is achieved for $t_{AMX} = 20\ d$, while the start-up in the case of $t_{AMX} = 0$ is not yet completed after 260 days. Furthermore, $t_{AMX}$ does not affect the planktonic $AMX$ wash out after the addition. No variation is observed for planktonic $AOB$, $NOB$ and $HB$ concentrations (data not shown).

Fig. 5.8 displays the relative abundances of active microbial within the granule

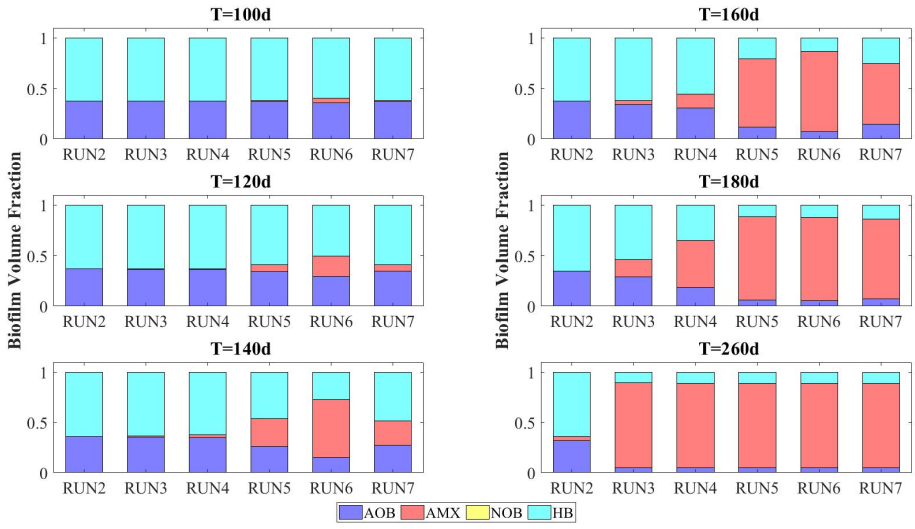


Figure 5.8: S2 - Relative abundances of active microbial species within the granule at $T = 100\ d$, $T = 120\ d$, $T = 140\ d$, $T = 160\ d$, $T = 180\ d$, $T = 260\ d$ for different addition times of $AMX$ sludge $t_{AMX}$. Wastewater influent composition: $S^{in}_{NH_4} = 300\ gN\ m^{-3}$ (Ammonium), $S^{in}_{NO_2} = 0.0001\ gN\ m^{-3}$ (Nitrite), $S^{in}_{NO_3} = 0.0001\ gN\ m^{-3}$ (Nitrate), $S^{in}_{OC} = 50\ gCOD\ m^{-3}$ (Organic carbon). $RUN2$: $t_{AMX} = 0$; $RUN3$: $t_{AMX} = 3\ d$; $RUN4$: $t_{AMX} = 5\ d$; $RUN5$: $t_{AMX} = 10\ d$; $RUN6$: $t_{AMX} = 20\ d$; $RUN7$: $t_{AMX} = 40\ d$. Fixed oxygen concentration within the reactor: $\overline{S}_{O_2} = 0.75\ gO_2\ m^{-3}$. Concentration of $AMX$ bacteria added in the reactor: $\psi^*_{AMX,t_{AMX}} = 500\ gCOD\ m^{-3}$.

at different times. It confirms the results previously described: the growth process of anammox biomass is deeply affected by $t_{AMX}$ and is faster in the case of $t_{AMX} = 20\ d$ ($RUN6$). However, in all cases except $t_{AMX} = 0$ ($RUN2$), the steady-state microbial distribution is reached within the observation period of 260 days.

Lastly, the evolution of the granule radius $R(t)$ over time is shown in Fig. 5.9. $t_{AMX}$ affects the granule evolution in the second stage of the process (Fig. 5.9-right), since the further radius increase around 100-180 days is associated to the $AMX$ growth. However, the steady-state granule dimension achieved is not dependent on $t_{AMX}$.

From all these results, it is clear that the addition time of the anammox inoculum $t_{AMX}$ influences the rate of biological processes related to the $AMX$ biomass and therefore the duration of the start-up period. Anyway, it does not affect the steady-state configuration and the removal efficiency of the process.

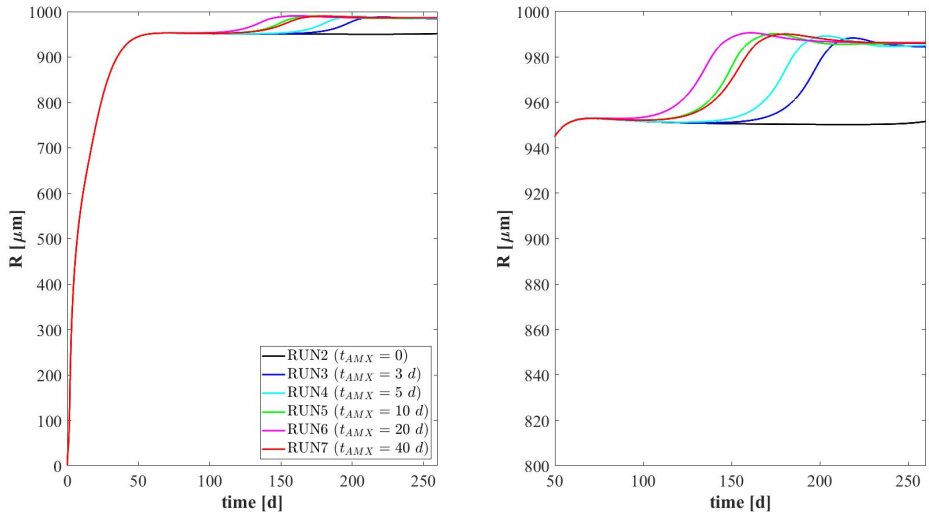


Figure 5.9: S2 - Biofilm radius evolution for different addition times of $AMX$ sludge $t_{AMX}$ (left), with a focus to the last 210 days (right). Wastewater influent composition: $S^{in}_{NH_4} = 300\ gN\ m^{-3}$ (Ammonium), $S^{in}_{NO_2} = 0.0001\ gN\ m^{-3}$ (Nitrite), $S^{in}_{NO_3} = 0.0001\ gN\ m^{-3}$ (Nitrate), $S^{in}_{OC} = 50\ gCOD\ m^{-3}$ (Organic carbon). Fixed oxygen concentration within the reactor: $\overline{S}_{O_2} = 0.75\ gO_2\ m^{-3}$. Concentration of $AMX$ bacteria added in the reactor: $\psi^*_{AMX,t_{AMX}} = 500\ gCOD\ m^{-3}$.

### 5.4.4 S3 - Effects of the anammox inoculum size on the process

As explained in Section 5.1, the most interesting strategy to carry out the start-up of a PN/A granular reactors is based on the use of anammox sludge inocula. However, although this strategy allows to significantly reduce the start-up duration, it has high costs related to the limited availability of anammox biomass around the world.

Therefore, in order to optimize timing and costs, an exhaustive knowledge of effects of anammox inoculum and its size on the process start-up is needed. To this aim, the present study (S3) analyzes numerically the role that the anammox inoculum size $\psi^*_{AMX,t_{AMX}}$ plays in the process and investigates how this size affects the duration of the start-up period. Six simulations ($RUN8 - RUN13$) have been carried out with different values of $\psi^*_{AMX,t_{AMX}}$ ($100, 300, 500, 700, 1000, 1500\ gCOD\ m^{-3}$), while the addition time of anammox sludge $t_{AMX}$ is fixed to $10\ d$. Results are summarized in Figs. 5.10-5.13.

Fig. 5.10 reports the distribution of anammox species within the granule for $\psi^*_{AMX,t_{AMX}}$

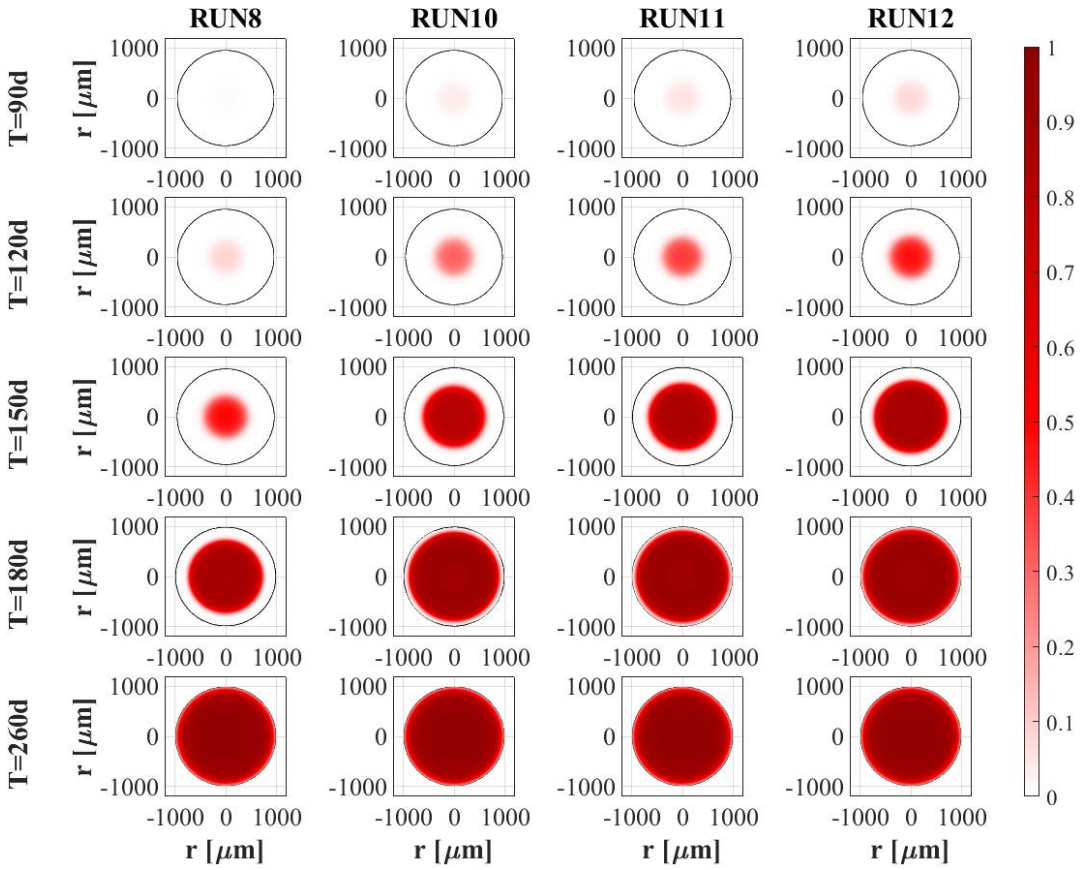


Figure 5.10: S3 - $AMX$ distribution within the granule (diametrical section) at $T = 90\ d$, $T = 120\ d$, $T = 150\ d$, $T = 180\ d$, $T = 260\ d$ for different concentrations of $AMX$ bacteria added in the reactor $\psi^*_{AMX,t_{AMX}}$. Wastewater influent composition: $S^{in}_{NH_4} = 300\ gN\ m^{-3}$ (Ammonium), $S^{in}_{NO_2} = 0.0001\ gN\ m^{-3}$ (Nitrite), $S^{in}_{NO_3} = 0.0001\ gN\ m^{-3}$ (Nitrate), $S^{in}_{OC} = 50\ gCOD\ m^{-3}$ (Organic carbon). $RUN8$: $\psi^*_{AMX,t_{AMX}} = 100\ gCOD\ m^{-3}$; $RUN10$: $\psi^*_{AMX,t_{AMX}} = 500\ gCOD\ m^{-3}$; $RUN11$: $\psi^*_{AMX,t_{AMX}} = 700\ gCOD\ m^{-3}$; $RUN12$: $\psi^*_{AMX,t_{AMX}} = 1000\ gCOD\ m^{-3}$. Fixed oxygen concentration within the reactor: $\overline{S}_{O_2} = 0.75\ gO_2\ m^{-3}$. Addition time of $AMX$ sludge: $t_{AMX} = 10\ d$.

equal to $100, 500, 700, 1000\ gCOD\ m^{-3}$, at different times. Since the invasion process is proportional to the concentration of $AMX$ planktonic biomass, it becomes more intense as the $AMX$ inoculum size increases $\psi^*_{AMX,t_{AMX}}$. Then, by increasing the $AMX$ inoculum size, the anammox sessile biomass grows faster and the steady-state microbial distribution is reached earlier. However, $\psi^*_{AMX,t_{AMX}}$ has no effects on the steady-state configuration.

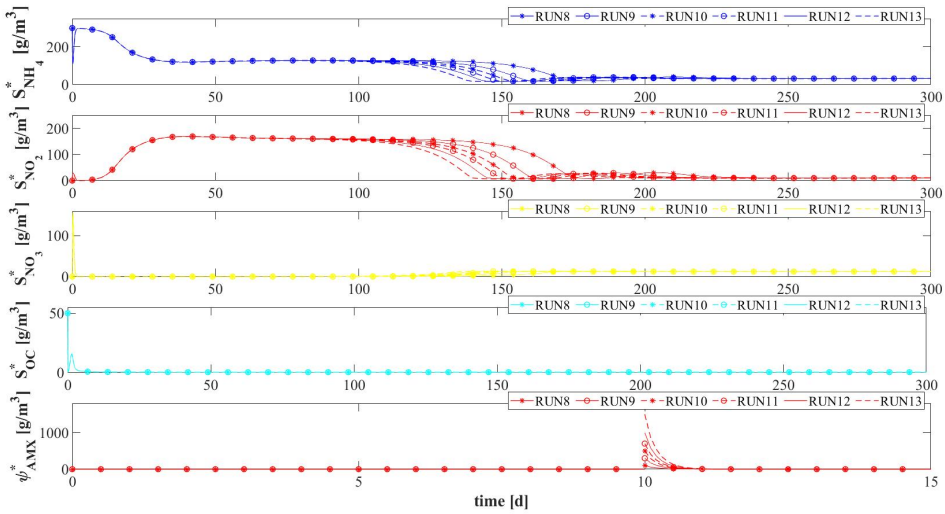


Figure 5.11: S3 - Evolution of soluble substrates and planktonic $AMX$ concentrations within the bulk liquid for different concentrations of $AMX$ bacteria added in the reactor $\psi^*_{AMX,t_{AMX}}$. $S^*_{NH_4}$: Ammonium, $S^*_{NO_2}$: Nitrite, $S^*_{NO_3}$: Nitrate, $S^*_{OC}$: Organic carbon, $\psi^*_{AMX}$: Anaerobic ammonia-oxidizing bacteria. Wastewater influent composition: $S^{in}_{NH_4} = 300\ gN\ m^{-3}$ (Ammonium), $S^{in}_{NO_2} = 0.0001\ gN\ m^{-3}$ (Nitrite), $S^{in}_{NO_3} = 0.0001\ gN\ m^{-3}$ (Nitrate), $S^{in}_{OC} = 50\ gCOD\ m^{-3}$ (Organic carbon). $RUN8$: $\psi^*_{AMX,t_{AMX}} = 100\ gCOD\ m^{-3}$; $RUN9$: $\psi^*_{AMX,t_{AMX}} = 300\ gCOD\ m^{-3}$; $RUN10$: $\psi^*_{AMX,t_{AMX}} = 500\ gCOD\ m^{-3}$; $RUN11$: $\psi^*_{AMX,t_{AMX}} = 700\ gCOD\ m^{-3}$; $RUN12$: $\psi^*_{AMX,t_{AMX}} = 1000\ gCOD\ m^{-3}$; $RUN13$: $\psi^*_{AMX,t_{AMX}} = 1500\ gCOD\ m^{-3}$. Fixed oxygen concentration within the reactor: $\overline{S}_{O_2} = 0.75\ gO_2\ m^{-3}$. Addition time of $AMX$ sludge: $t_{AMX} = 10\ d$.

Trends of soluble substrates and $AMX$ planktonic biomass within the reactor are reported in Fig. 5.11. The $AMX$ inoculum size influences the rate of anammox processes and then, the trend of substrates involved. The first stage seems to be independent of $\psi^*_{AMX,t_{AMX}}$, since anammox processes are negligible and the grown $AMX$ biomass is not still sufficient to significantly affect the substrates concentration. In the second stage, anammox processes intensifies and the consumption rates of ammonium $S^*_{NH_4}$ (blue) and nitrite $S^*_{NO_2}$ (red) varies with the variation of $\psi^*_{AMX,t_{AMX}}$. As the addition time of the $AMX$ inoculum $t_{AMX}$, the $AMX$ inoculum size does not affect the steady-state concentrations of substrates and $AOB$, $NOB$ and $HB$ planktonic biomasses (data not shown).

Fig. 5.12 displays the relative abundances of active microbial species within the

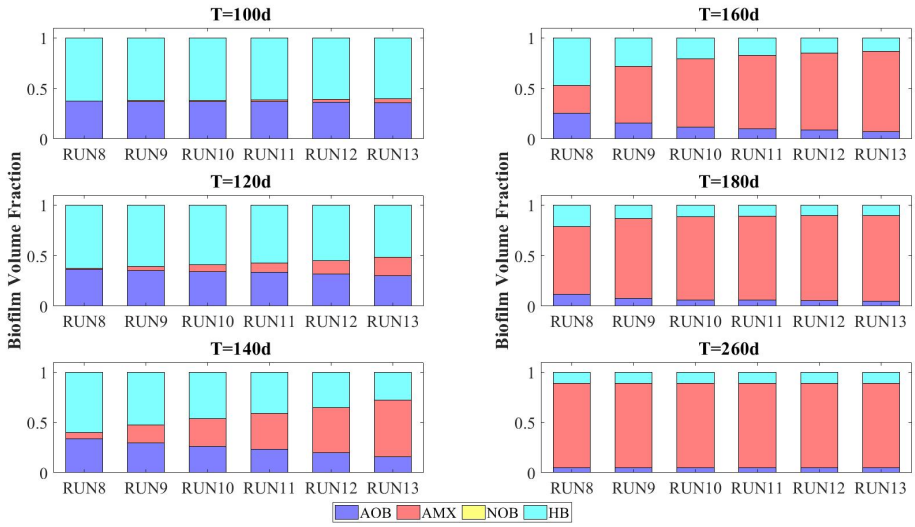


Figure 5.12: S3 - Relative abundances of active microbial species within the granule at $T = 100\ d$, $T = 120\ d$, $T = 140\ d$, $T = 160\ d$, $T = 180\ d$, $T = 260\ d$ for different concentrations of $AMX$ bacteria added in the reactor $\psi^*_{AMX,t_{AMX}}$. Wastewater influent composition: $S^{in}_{NH_4} = 300\ gN\ m^{-3}$ (Ammonium), $S^{in}_{NO_2} = 0.0001\ gN\ m^{-3}$ (Nitrite), $S^{in}_{NO_3} = 0.0001\ gN\ m^{-3}$ (Nitrate), $S^{in}_{OC} = 50\ gCOD\ m^{-3}$ (Organic carbon). $RUN8$: $\psi^*_{AMX,t_{AMX}} = 100\ gCOD\ m^{-3}$; $RUN9$: $\psi^*_{AMX,t_{AMX}} = 300\ gCOD\ m^{-3}$; $RUN10$: $\psi^*_{AMX,t_{AMX}} = 500\ gCOD\ m^{-3}$; $RUN11$: $\psi^*_{AMX,t_{AMX}} = 700\ gCOD\ m^{-3}$; $RUN12$: $\psi^*_{AMX,t_{AMX}} = 1000\ gCOD\ m^{-3}$; $RUN13$: $\psi^*_{AMX,t_{AMX}} = 1500\ gCOD\ m^{-3}$. Fixed oxygen concentration within the reactor: $\overline{S}_{O_2} = 0.75\ gO_2\ m^{-3}$. Addition time of $AMX$ sludge: $t_{AMX} = 10\ d$.

granule at different times. It confirms that as $\psi^*_{AMX,t_{AMX}}$ increases, the anammox growth is faster and the steady-state distribution is achieved earlier.

Fig. 5.13 reports the evolution of the granule radius $R(t)$ over time for different $\psi^*_{AMX,t_{AMX}}$. As noted above, an increase in $\psi^*_{AMX,t_{AMX}}$ leads to a faster anammox growth and thus a faster increase in $R(t)$.

From the results shown it is possible to draw a general conclusion: the $AMX$ growth rate and the duration of the process start-up are directly proportional to the $AMX$ inoculum size. Anyway, it has no effect on the steady-state configuration occurring inside the reactor.

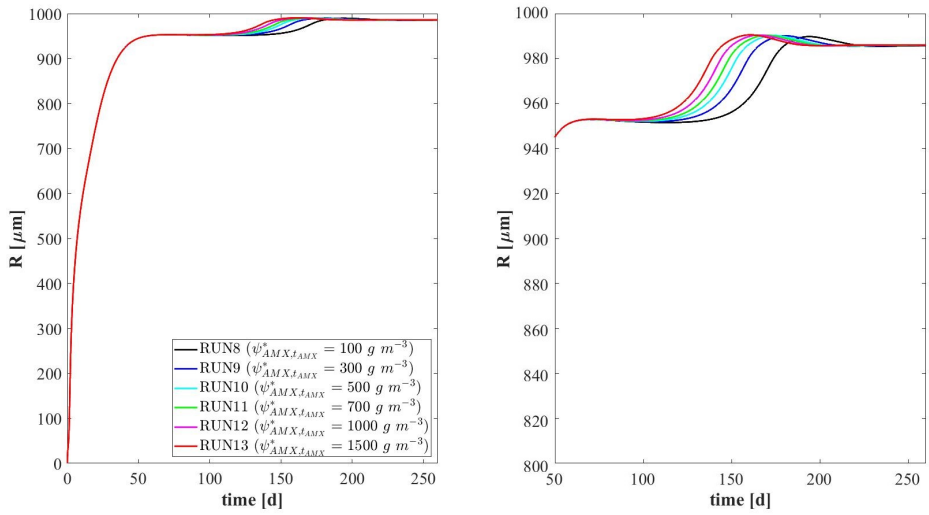


Figure 5.13: S3 - Biofilm radius evolution for different concentrations of $AMX$ bacteria added in the reactor $\psi^*_{AMX,t_{AMX}}$ (left), with a focus to the last 210 days (right). Wastewater influent composition: $S^{in}_{NH_4} = 300\ gN\ m^{-3}$ (Ammonium), $S^{in}_{NO_2} = 0.0001\ gN\ m^{-3}$ (Nitrite), $S^{in}_{NO_3} = 0.0001\ gN\ m^{-3}$ (Nitrate), $S^{in}_{OC} = 50\ gCOD\ m^{-3}$ (Organic carbon). Fixed oxygen concentration within the reactor: $\overline{S}_{O_2} = 0.75\ gO_2\ m^{-3}$. Addition time of $AMX$ sludge: $t_{AMX} = 10\ d$.

### 5.4.5 S4 - Combined effects of anammox addition time and anammox inoculum size

The last numerical study (S4) analyzes the combined effect of the addition time $t_{AMX}$ and the anammox inoculum size $\psi^*_{AMX,t_{AMX}}$ on the biological process, in order to show how the choice of these operating parameters affects the process start-up of PN/A granular bioreactors. For this purpose, 25 simulations are performed by varying $t_{AMX}$ and $\psi^*_{AMX,t_{AMX}}$ (values reported in Table 5.3). The duration of the process start-up is assumed equal to the time necessary to achieve the steady-state ammonium concentration $T^*$.

Fig. 5.14 shows the anammox sessile mass $m_{AMX}$ for different $t_{AMX}$ and $\psi^*_{AMX,t_{AMX}}$. These results are shown for $T = 170\ d$, which is the minimum time, among all the simulations carried out, necessary to reach the steady-state anammox sessile mass ($RUN25$: $t_{AMX} = 20\ d$; $\psi^*_{AMX,t_{AMX}} = 1500\ gCOD\ m^{-3}$). As the $\psi^*_{AMX,t_{AMX}}$ increases, $m_{AMX}$ at $T = 170\ d$ increases. However, $m_{AMX}$ has a less than linear behaviour with increas-

| $\psi^*_{AMX,t_{AMX}}$ $[gCOD\ m^{-3}]$ $\rightarrow$ / $t_{AMX}$ $[d]$ $\downarrow$ | **100** | **300** | **500** | **1000** | **1500** |
|---|---|---|---|---|---|
| **3** | $RUN14$ | $RUN15$ | $RUN3$ | $RUN16$ | $RUN17$ |
| **5** | $RUN18$ | $RUN19$ | $RUN4$ | $RUN20$ | $RUN21$ |
| **10** | $RUN8$ | $RUN9$ | $RUN1$ | $RUN12$ | $RUN13$ |
| **20** | $RUN22$ | $RUN23$ | $RUN6$ | $RUN24$ | $RUN25$ |
| **40** | $RUN26$ | $RUN27$ | $RUN7$ | $RUN28$ | $RUN29$ |

Table 5.3: Values of the parameters investigated in the numerical study S4.

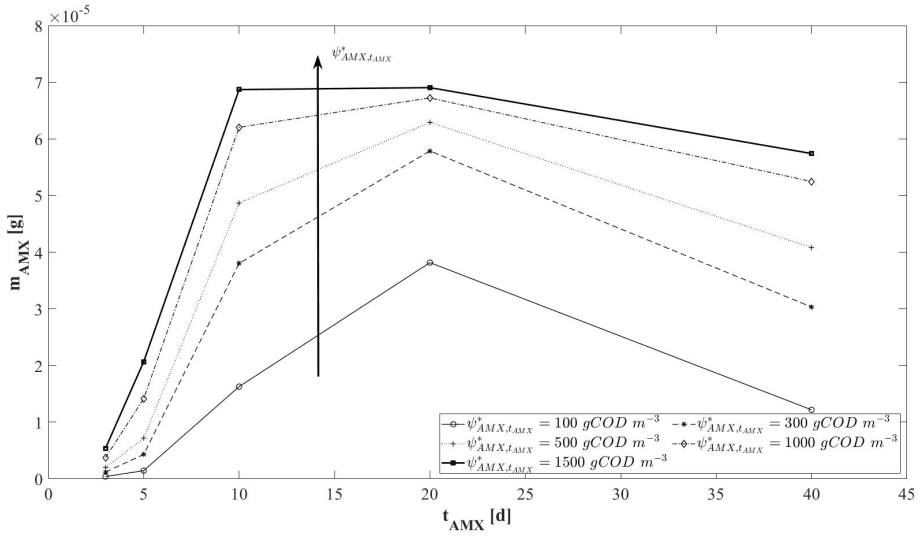


Figure 5.14: S4 - Amount of $AMX$ sessile biomass $m_{AMX}$ at $T = 170\ d$ for different addition times of $AMX$ sludge $t_{AMX}$ [3 - 40 $d$] and different concentrations of $AMX$ bacteria added in the reactor $\psi^*_{AMX,t_{AMX}}$ [100 - 1500 $gCOD\ m^{-3}$]. Wastewater influent composition: $S^{in}_{NH_4} = 300\ gN\ m^{-3}$ (Ammonium), $S^{in}_{NO_2} = 0.0001\ gN\ m^{-3}$ (Nitrite), $S^{in}_{NO_3} = 0.0001\ gN\ m^{-3}$ (Nitrate), $S^{in}_{OC} = 50\ gCOD\ m^{-3}$ (Organic carbon). Fixed oxygen concentration within the reactor: $\overline{S}_{O_2} = 0.75\ gO_2\ m^{-3}$.

ing $\psi^*_{AMX,t_{AMX}}$. On the other hand, $m_{AMX}$ does not present a unique trend as $t_{AMX}$ varies. Specifically, it increases as $t_{AMX}$ increases up to 20 $d$, while it decreases again for $t_{AMX} > 20\ d$ . As explained in Section 5.4.3, this happens because the further delay in the addition of the $AMX$ inoculum prevails over the further acceleration in the process of invasion and anammox growth related to the increase of the anoxic zone within the granule.

The duration of the start-up $T^*$ for different $t_{AMX}$ and $\psi^*_{AMX,t_{AMX}}$ is reported in

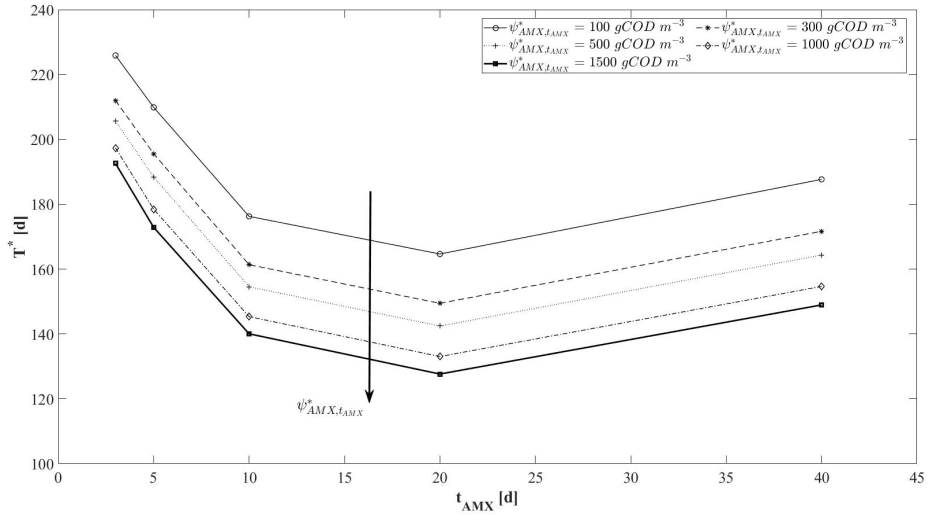


Figure 5.15: S4 - Time necessary to achieve the steady-state ammonium concentration $T^*$ for different addition times of $AMX$ sludge $t_{AMX}$ [3 - 40 $d$] and different concentrations of $AMX$ bacteria added in the reactor $\psi^*_{AMX,t_{AMX}}$ [100 - 1500 $gCOD\ m^{-3}$]. Wastewater influent composition: $S^{in}_{NH_4} = 300\ gN\ m^{-3}$ (Ammonium), $S^{in}_{NO_2} = 0.0001\ gN\ m^{-3}$ (Nitrite), $S^{in}_{NO_3} = 0.0001\ gN\ m^{-3}$ (Nitrate), $S^{in}_{OC} = 50\ gCOD\ m^{-3}$ (Organic carbon). Fixed oxygen concentration within the reactor: $\overline{S}_{O_2} = 0.75\ gO_2\ m^{-3}$.

Fig. 5.15. As expected, $T^*$ presents a behavior inversely proportional to the anammox mass $m_{AMX}$ at $T = 170\ d$. When the invasion and growth of anammox biomass are more intense, $m_{AMX}$ grows faster. As a result, ammonium consumption is faster and the steady state value is achieved earlier.

It seems evident that the duration of the start-up can be reduced by increasing the anammox inoculum size and by adding it when most part of granules is under anoxic conditions. However, some considerations need to be done. First, higher is the anammox inoculum size, higher is the total cost. Furthermore, as can be seen in Fig. 5.15, the time saved for the start-up is reduced as the inoculum size increases. For example, considering a 50% increase of $\psi^*_{AMX,t_{AMX}}$ from 1000 to 1500 $gCOD\ m^{-3}$ (dash-dot line and thick line, respectively), the start-up period reduces only by a few days. Finally, the anammox inoculum should be added into the reactor at the time that maximizes the rates of anammox growth and ammonium removal.

## 5.5 Conclusions

In the present Chapter, a mathematical model on the combined partial nitritation/anammox granular system is proposed. Such model describes the *de novo* anammox granulation through the expansion of a spherical free boundary domain with radial symmetry, and simulates the start-up process of this wastewater system by considering both the biofilm and bulk liquid dynamics. In particular, growth and decay of sessile and planktonic biomasses, diffusion and conversion of substrates, invasion phenomena of planktonic biomass, attachment and detachment phenomena are modelled. A planktonic anammox inoculum is supposed to be added in the system at a specific time. Then, microbial invasion is accounted to initiate the anammox sessile growth.

Numerical results related to both the individual biofilm granule and the reactor start-up phase are presented. The evolution and composition of the biofilm granule mainly depend on oxygen trends. When the granule is small, high oxygen concentration throughout the granule promote the growth of aerobic species ($AOB$ and $HB$ bacteria). On the contrary, when the granule reaches larger dimensions, anoxic conditions arising in the granule center favor the anaerobic metabolic activity of $AMX$ bacteria. In the final steady-state configuration, granules are dominated by $AMX$ bacteria and small amounts of $AOB$ and $HB$ bacteria are detected in the outermost layers. Furthermore, $NOB$ bacteria are negligible throughout the process due to the low oxygen level in the reactor set for all the simulations. Although such results are qualitatively in agreement with experimental evidence, they can vary due to crucial factors, such as the granule size, the oxygen level in the reactor and the influent composition.

Numerical results show that, during the start-up phase, 90% of ammonium is removed from the wastewater influent through a two-stage treatment process: the first stage is governed by the aerobic oxidation of ammonium and organic carbon by $AOB$ and $HB$ bacteria; the second stage is governed by $AMX$ bacteria, which oxidize relevant amounts of ammonium anaerobically, by using the nitrite produced in the first

stage. The long start-up duration ($200 - 220\ d$), measured as the time necessary to achieve a stationary configuration, is due to the slow anammox metabolism.

Moreover, numerical studies have been carried out to investigate the effects of two significant factors influencing the formation and evolution of anammox granules and, consequently, the duration of the start-up period: the anammox inoculum size and the anammox addition time. Such parameters affect the anammox invasion and growth, and then, the time necessary to reach the stady-state condition. As expected, the start-up duration is inversely proportional to the $AMX$ inoculum size, while it does not have a unique trend as the anammox addition time varies. However, it is clear that the best solution to minimize the start-up duration is to add the anammox inoculum when granules are almost fully developed, and their core is under anoxic conditions.

The combined effect of the addition time and the anammox inoculum size on the start-up process is finally investigated, with the aim of providing a numerical support in the choice of the start-up strategy. However, it should be noted that such model results are qualitative, and a calibration procedure should be carried out in order to provide engineering relevance to the model output.

# Chapter 6

# Multiscale modelling of heavy metals adsorption on algal-bacterial photogranules

## 6.1 Introduction

Increased use of metals in process industries has resulted in the production of large quantities of wastewater effluents containing high level of toxic heavy metals [157]. Due to their non-degradable and persistent nature, tendency to accumulate, and hazardous effects on living organisms and environment, heavy metals removal represents a great challenge in the wastewater treatment field [18, 157, 158, 159]. The relevance of these topics in environmental engineering has led to the development of new technologies for removing heavy metals from wastewater. Methods for removing metal ions from aqueous solutions include physical, chemical, and biological processes [160]. Conventional physical/chemical technologies, such as chemical precipitation, ion ex-

This Chapter will be submitted as: Russo, F., Tenore, A., Mattei, M.R., Frunzo, L. Multiscale modelling of heavy metals adsorption on algal-bacterial photogranules.

change, activated carbon adsorption and membrane processes, are often ineffective or expensive in the case of very low metals concentrations [158, 159, 161]. Removal of heavy metals from wastewater through adsorption, particularly biosorption, emerges as a promising alternative technology. Compared with conventional heavy metals removal methods, biosorption has several advantages: utilization of renewable biomaterials; possibility to treat large volumes of wastewater; high selectivity; recovery of bound heavy metals from the biomass; no supplementation of expensive chemical reagents; low production of hazardous waste [159].

Biosorption is a complex combination of processes, consisting of the physical adherence or bonding of ions and molecules (sorbate), dissolved or suspended in a liquid phase (solvent), onto a solid surface (adsorbent) [159, 160, 162, 163, 164]. Until now, a variety of biomaterials and microorganisms have been used as biosorbent for the removal of heavy metals, such as algae, bacteria, fungi, and yeast [159]. Such living or dead organisms are able to bind and concentrate metals, metalloids, radionuclides, and other toxic pollutants from even very dilute aqueous solutions [159, 160, 164, 165]. Several factors can affect the mechanism of metal biosorption, such as the properties of the biomass (living or non-living, type of biomass, phenotype), the presence of other competing ions, and the environmental conditions (pH, temperature, etc.) [158, 159]. Among them, the biomass phenotype may be considered one of the most important factors. The use of freely-suspended microbial biosorbents has some disadvantages, including small particle size, low density, poor mechanical strength, low rigidity, difficulty in separating biomass and effluent, and poor biomass regeneration [159, 160, 163]. For this reason, in recent years immobilized biomass has been regarded an interesting alternative. In addition, cell agglomeration promotes the secretion of extracellular polymeric substances ($EPS$), which further contribute to microorganisms protection and metals biosorption [166, 167, 168].

The simultaneous removal of organic substances and heavy metals from wastewater is still a major engineering problem. Algal-bacterial systems are expected to have a

great potential in removing organic and inorganic compounds in a single treatment step, combining high adsorption capacities of microalgae and cyanobacteria with low process costs [169]. Indeed, microalgae and cyanobacteria show great tendency to produce $EPS$ and high metal binding affinity. Moreover, the photosynthetic activity leads to the production of oxygen and allows the oxidation of carbon and nitrogen compounds by heterotrophic and nitrifying bacteria without external supplementation of oxygen [15, 16]. In this context, self-immobilized granular algal-bacterial consortia, known as oxygenic photogranules (OPGs), are considered as an effective and promising technology for biosorption of inorganic pollutants and degradation of organic compounds from wastewater [17, 18]. In the last years, great attention has been devoted to individual removal of heavy metals [19, 170] or organic compounds [15, 171] in OPGs-based systems. Still, up to the present, there is knowledge lack regarding their contextual removal, although these pollutants usually exist together in industrial wastewater.

In this framework, mathematical modelling represents a useful tool to explore the granulation process of OPGs and the adsorption of heavy metals on the matrix of biofilm granules. Biosorption is usually described through isotherms, which represent the equilibrium relationship between the adsorbate concentration in the liquid phase and the adsorbate concentration onto the adsorbent phase at a given temperature. For the adsorption of a single component, the most widely used isotherm model is the Langmuir-Freundlich model, which is the combination of Langmuir model and Freundlich model [159]. Although biosorption isotherm models have been widely recognized as efficient tools to provide a suitable description of the experimental behavior, kinetic modelling is typically preferred for practical applications and process design. Pseudo-first and pseudo-second order kinetic equations are the most widely used rate equations for the adsorption process [159]. Nevertheless, more comprehensive, and accurate models need to be developed to better explore the complex relationships which establish between the biosorbent and the sorbate. A mathematical model accounting for the biosorption process of heavy metals on the different components of a multispecies biofilm has been

presented by D'Acunto et al. (2018) [162] in the case of planar biofilm. This mono-dimensional biofilm model is conceived in the framework of continuum mathematical modeling of biofilm growth and explicitly accounts for the diffusion and adsorption of heavy metals on the biofilm matrix. Nevertheless, none of the existing models addressed the evolution and dynamics of granular biofilms formation and the adsorption processes on their solid matrix.

In this context, the present Chapter introduces a mathematical model to investigate the mutual interactions between the formation of oxygenic photogranules (biosorbents) and the adsorption of heavy metals (sorbates) on their solid matrix. The *de novo* granulation process of OPGs in a granular-based sequencing batch reactor (SBR) has been addressed by Tenore et al. (2021) [152]. It examines all the main factors influencing the granulation process of algal-bacterial photogranules for the treatment of typical municipal wastewater. In this Chapter, the OPGs model has been extended to explicitly account for heavy metals diffusion from bulk liquid to biofilm and their adsorption on the matrix of biofilm granules. Following the approach proposed by Masic and Eberl (2012, 2014) [106, 107] in the case of one-dimensional planar biofilms, the mesoscopic granular biofilm model has been coupled to the mass balances within the macroscopic bioreactor by using a continuum approach [22]. This multiscale approach leads to model the formation and ecology of the biofilm granules and the performances of the SBR system, considering the interaction between the granules and bulk liquid. The granular biofilm model, derived in Tenore et al. (2021) [128], is formulated as a spherical free boundary value problem under the assumption of radial symmetry. Processes of microbial growth, attachment, and detachment are included to describe the formation and expansion of granules. The *de novo* granulation process is modelled by assuming that all biomass initially present in the bioreactor is in planktonic form. Mathematically, this corresponds to consider a vanishing initial value of the granule radius, using the approach introduced by D'Acunto et al. (2019,2021) [24, 127] in the case of planar biofilm. Attachment is modelled as a continuous flux (from the bulk

liquid to the biofilm) of planktonic species, which aggregate, switch their phenotype from planktonic to sessile and initiate the granulation process. Detachment is modelled as a continuous flux (from the biofilm to the bulk liquid) proportional to the square of the granule radius. The model accounts for the first time the dynamics of the detached biomass and its influence on the biological process. Specifically, detached microbial species are modelled as a new set of variables, and are supposed to grow on soluble substrates and switch to planktonic form. Furthermore, the model includes the diffusion and consumption/production of soluble substrates, due to the metabolic activity of sessile, planktonic and detached biomasses.

The model considers the adsorption of heavy metals on the granular solid matrix. Experimental observations show that each biofilm component is characterized by the presence of specific number of adsorption sites, which are able to adsorb the contaminants present in the wastewater. For this purpose, model equations describing the variation of free binding sites, and diffusion and adsorption of metals have been here derived for the first time in the case of granular biofilm, by following the approach proposed by Tenore et al. (2021) [128]. The variation of free binding sites is assumed to depend on the biofilm growth and adsorption process, and is modelled through a system of hyperbolic partial differential equations (PDEs) [162]. While, the diffusion and consumption of the sorbates is described by a system of parabolic PDEs [162].

All the main components of the OPGs are accounted in the model in sessile and suspended (planktonic and detached) form: phototrophs, facultative heterotrophic bacteria, nitrifying bacteria, $EPS$ and inactive material ($EPS$ and inactive material are accounted only as sessile biomass). Since cyanobacteria (included among phototrophs) play a predominant role in the granulation of oxygenic photogranules due to their filamentous morphology [15, 16, 172], phototrophs are assumed to have better attachment properties and to enhance the attachment of other species [152]. Moreover, the model accounts the diffusion and conversion of inorganic and organic carbon, nitrate, ammonia, oxygen, and metal. The soluble substrates are involved in the metabolism of micro-

bial species, while metal adsorbs on matrix of biofilm granules. Notably, the presence of metals in a such biological system results in a dual effect: it enhances the production of $EPS$ by sessile species [20] and negatively affects the microbial metabolic activities [169]. This is modelled including an inhibition term for metal and a stimulation term for $EPS$ production in all microbial kinetics. Light is included in the model to consider its effects on the metabolic activity of phototrophs. Specifically, light intensity is supposed to be constant in the bulk liquid and vary within the granules due to attenuation phenomena. Various numerical studies have been performed to investigate how the metal concentration and the adsorption properties of the biofilm components may affect the evolution of the process.

The Chapter is organized as follows. The mathematical model is introduced and described in Section 6.2, while the biological context is described in section 6.3. Numerical studies and results are reported in Section 6.4 and discussed in Section 6.5.

## 6.2 Mathematical model

The mathematical model simulates the biosorption process of heavy metals within a granular-based sequencing batch reactor (SBR) with a multiscale approach. The SBR system is modelled as a batch bioreactor having a cyclic configuration, in which $N_G$ identical granules are immersed. For this purpose, two different biological compartments can be identified: the granule mesoscale and the bioreactor macroscale. The model is able to contextually describe the *de novo* granulation process of granular biofilms, SBR performances, and biosorption process. The interactions between the mesoscale and macroscale are accounted in the model, by considering exchange fluxes (from/to bulk liquid and to/from biofilm) of dissolved substances (substrates, products, and heavy metals) and biomasses (in sessile and suspended form). By using a continuum approach, the model accounts all main phenomena involved in the *de novo* granulation process: attachment process by planktonic cells; growth and decay of sessile,

planktonic and detached biomasses; $EPS$ secretion; diffusion of dissolved substrates within the granule; conversion of dissolved substrates within the granules and the bulk liquid; detachment process; conversion of detached biomass into planktonic biomass. Moreover, the biosorption process of heavy metals on granule matrix is included in the model, by considering the diffusion and bioconversion of metals, and the variation of free absorption sites.

Modelling of both the granule mesoscale and bioreactor macroscale is discussed in detail, describing the processes, assumptions, variables, equations, and initial and boundary conditions involved.

### 6.2.1 Granule mesoscale model

The mathematical model describing the *de novo* granulation process derived by Tenore et al. (2021) [128] has been here extended to model the biosorption process of heavy metals on granular biofilms matrix. The granule mesoscale consists of a fixed number of biofilm granules ($N_G$) immersed within the bulk liquid and assumed to be identical at each instant. Specifically, each granule is assumed as constituted by various particulate components (including active microbial species, extracellular polymeric substances, and inactive biomass). The granules expansion depends on growth and decay processes of the various species, attachment flux from the bulk liquid to the biofilm, and detachment flux from the biofilm to the bulk liquid. The growth of microbial species depends on the presence of nutrients necessary for their metabolic activities. The nutrients are modelled as soluble substrates able to diffuse within the granules. Granulation process is initiated by attachment of pioneering planktonic cells, while detachment phenomena lead to the loss of sessile biomass, induced by external shear forces, substrates depletion and biomass decay. Each component of the granules has a specific absorption capacity and is characterized by the presence of a certain number of free binding sites, quantified as volume fractions. The heavy metals (sorbates) are modelled as dis-

solved substances, which diffuse across the granules and are subjected to absorption phenomena on the various biofilm components.

The granular biofilm is modelled as a spherical free boundary domain under the assumption of radial symmetry. The evolution of free boundary domain is described by the variation of the granule radius $R(t)$. A vanishing initial domain ($R(0) = 0$) is considered to fully model the *de novo* granulation process. The center of the granule is located at $r = 0$, where $r$ denotes the radial coordinate. The granule model includes $n$ microbial species in sessile form $X_i(r,t)$, $m_1$ dissolved substrates $S_j(r,t)$, $n$ free binding sites $X_{\theta_i}(r,t)$, $m_2 - m_1$ heavy metals $M_j(r,t)$. All these variables are expressed in terms of concentration and modelled as functions of time $t$ and space $r$. Each microbial species is supposed to have the same biomass density $\rho$, and the same density of binding sites $\rho_\theta$. By dividing sessile species concentrations $X_i(r,t)$ by $\rho$ and the free binding sites concentrations $X_{\theta_i}(r,t)$ by $\rho_\theta$, biofilm volume fractions $f_i(r,t)$ and free binding sites volume fractions $\theta_i(r,t)$ are achieved. Notably, both $f_i(r,t)$ and $\theta_i(r,t)$ (in absence of metals adsorption) are constrained to add up to unity at each location and time ($\sum_{i=1}^{n} f_i$ and $\sum_{i=1}^{n} \theta_i$) [108].

In summary, the model components describing the granular biofilm mesoscale are:

$$X_i,\ i = 1, ..., n,\ \mathbf{X} = (X_1, ..., X_n) \tag{6.1}$$

$$f_i = \frac{X_i}{\rho},\ i = 1, ..., n,\ \mathbf{f} = (f_1, ..., f_n) \tag{6.2}$$

$$S_j,\ j = 1, ..., m_1,\ \mathbf{S} = (S_1, ..., S_{m_1}) \tag{6.3}$$

$$X_{\theta_i},\ i = 1, ..., n,\ \boldsymbol{X_\theta} = (X_{\theta_1}, ..., X_{\theta_n}) \tag{6.4}$$

$$\theta_i = \frac{X_{\theta_i}}{\rho_\theta},\ i = 1, ..., n,\ \boldsymbol{\theta} = (\theta_1, ..., \theta_n) \tag{6.5}$$

$$M_j,\ j = m_1 + 1, ..., m_2,\ \mathbf{M} = (M_{m_1+1}, ..., M_{m_2}) \tag{6.6}$$

Based on the continuum approach introduced in Wanner and Gujer (1986) [22] for one-dimensional planar biofilms, the model equations for granular biofilms were derived in Tenore et al. (2021) [128] under the assumption of radial symmetry from mass balance considerations in a differential volume of a spherical domain.

The growth and the transport of sessile species within the granular biofilm is governed by the following system of non-linear hyperbolic partial differential equations (PDEs):

$$\frac{\partial f_i(r,t)}{\partial t} + u(r,t)\frac{\partial f_i(r,t)}{\partial r} = r_{M,i}(r,t,\mathbf{f},\mathbf{S},\mathbf{M}) - f_i(r,t)\sum_{i=1}^{n} r_{M,i}(r,t,\mathbf{f},\mathbf{S},\mathbf{M}),$$

$$i = 1, ..., n, 0 \leq r \leq R(t),\ t > 0, \tag{6.7}$$

where $r_{Mi}(r,t,\mathbf{f},\mathbf{S},\mathbf{M})$ is the growth rate of the $i^{th}$ sessile microbial species; and $u(r,t)$ is the biomass velocity.

$u(r,t)$ is governed by the following equation:

$$\frac{\partial u(r,t)}{\partial r} = -\frac{2u(r,t)}{r} + \sum_{i=1}^{n} r_{M,i}(r,t,\mathbf{f},\mathbf{S},\mathbf{M}),\ 0 < r \leq R(t),\ t > 0. \tag{6.8}$$

The evolution of the free boundary domain is described by the variation of the biofilm granule radius $R(t)$, according to the following equation derived from global mass balances considerations on the granule volume:

$$\dot{R}(t) = u(R(t), t) + \sigma_a(t) - \sigma_d(t). \tag{6.9}$$

Attachment flux is modelled as a continuous mass flux from the bulk liquid to the granule, given by the sum of the attachment fluxes $\sigma_{a,i}(t)$ of the planktonic microbial species present in the liquid phase. The term $\sigma_{a,i}(t)$ is modelled as a linear function of the concentration of the $i^{th}$ planktonic species in the bulk liquid [24, 127]:

$$\sigma_a(t) = \sum_{i=1}^{n} \sigma_{a,i}(t) = \sum_{i=1}^{n} \frac{v_{a,i}\psi_i^*(t)}{\rho}, \tag{6.10}$$

where $v_{a,i}$ is the attachment velocity of the $i^{th}$ planktonic species; and $\psi_i^*(t)$ is the concentration of the $i^{th}$ planktonic species within the bulk liquid.

While, detachment flux is modelled as a quadratic function of the granule radius [110]. The term $\sigma_{d,i}(t)$ is modelled as the product between the detachment flux and biofilm volume fraction of the $i^{th}$ sessile biomass at the interface biofilm - bulk liquid:

$$\sigma_d(t) = \sum_{i=1}^{n} \sigma_{d,i}(t) = \sum_{i=1}^{n} \lambda R^2(t) f_i(R(t), t) = \lambda R^2(t), \tag{6.11}$$

where $\lambda$ is the detachment coefficient and is supposed to be equal for all microbial species.

Attachment phenomena prevail on detachment phenomena in the initial stage of the *de novo* granulation process, while detachment phenomena become predominant as the granule dimension increases.

The diffusion and conversion of soluble substrates are governed by the following system of parabolic PDEs:

$$\frac{\partial S_j(r,t)}{\partial t} - D_{S,j}\frac{\partial^2 S_j(r,t)}{\partial r^2} - \frac{2D_{S,j}}{r}\frac{\partial S_j(r,t)}{\partial r} = r_{S,j}(r, t, \mathbf{f}, \mathbf{S}, \mathbf{M}),$$

$$j = 1, ..., m_1,\ 0 < r < R(t),\ t > 0, \tag{6.12}$$

where $r_{S,j}(r,t,\mathbf{f},\mathbf{S},\mathbf{M})$ represents the conversion rate of the $j^{th}$ substrate; and $D_{S,j}$ denotes the diffusion coefficient in biofilm for the $j^{th}$ dissolved substrate.

A further system of PDEs in a spherical free boundary domain has been derived under the assumption of radial symmetry to model the variation of free binding sites and diffusion and adsorption of metals. As in the case of sessile species, the transport of free binding sites is modelled as an advective process [162]. Thus, the model equations governing the dynamics of the free binding sites take the following form:

$$\frac{\partial X_{\theta_i}(r,t)}{\partial t}+\frac{1}{r^2}\frac{\partial}{\partial r}(r^2u(r,t)X_{\theta_i}(r,t))=\rho_\theta r_{\theta,i}(r,t,\boldsymbol{X}_\theta,\mathbf{M})+\frac{\rho_\theta}{\rho}\mu_{M,i}(r,t,\mathbf{X},\mathbf{S},\mathbf{M}),$$

$$i=1,...,n,\ 0\leq r\leq R(t),\ t>0, \tag{6.13}$$

where $\mu_{M,i}(r,t,\mathbf{X},\mathbf{S},\mathbf{M})$ is the $i^{th}$ specific growth rate; and $r_{\theta,i}(r,t,\boldsymbol{X}_\theta,\mathbf{M})$ is the consumption rate of the $i^{th}$ sessile species absorption sites. The term $\frac{\rho_\theta}{\rho}\mu_{M,i}(r,t,\mathbf{X},\mathbf{S},\mathbf{M})$ accounts for the increment of free binding sites due to the sessile biomass growth; while, their consumption is related to biosorption and decay processes, which are taken into account through $r_{\theta,i}(r,t,\boldsymbol{X}_\theta,\mathbf{M})$.

Dividing Eq.(6.13) by $\rho_\theta$ and considering Eq. (6.2) and Eq. (6.5) yields:

$$\frac{\partial \theta_i(r,t)}{\partial t}+\frac{1}{r^2}\frac{\partial}{\partial r}(r^2u(r,t)\theta_i(r,t))=r_{\theta,i}(r,t,\boldsymbol{\theta},\mathbf{M})+\mu_{M,i}(r,t,\mathbf{f},\mathbf{S},\mathbf{M}),$$

$$i=1,...,n,\ 0\leq r\leq R(t),\ t>0, \tag{6.14}$$

$$\frac{\partial \theta_i(r,t)}{\partial t}+\theta_i(r,t)\frac{\partial u(r,t)}{\partial r}+\frac{2u(r,t)\theta_i(r,t)}{r}+u(r,t)\frac{\partial \theta_i(r,t)}{\partial r}=$$

$$= r_{\theta,i}(r,t,\boldsymbol{\theta},\mathbf{M}) + \mu_{M,i}(r,t,\mathbf{f},\mathbf{S},\mathbf{M}),$$

$$i = 1,...,n,\ 0 \leq r \leq R(t),\ t > 0. \tag{6.15}$$

Substituting Eq.(6.8) into Eq.(6.15) yields:

$$\frac{\partial \theta_i(r,t)}{\partial t} + u(r,t)\frac{\partial \theta_i(r,t)}{\partial r} =$$

$$r_{\theta,i}(r,t,\boldsymbol{\theta},\mathbf{M}) + \mu_{M,i}(r,t,\mathbf{f},\mathbf{S},\mathbf{M}) - \theta_i(r,t)\sum_{i=1}^{n} r_{M,i}(r,t,\mathbf{f},\mathbf{S},\mathbf{M}),$$

$$i = 1,...,n,\ 0 \leq r \leq R(t),\ t > 0, \tag{6.16}$$

As for soluble substrates, the transport of dissolved heavy metals is modelled as a diffusive process [162], and it is expressed as follows:

$$\frac{\partial M_j(r,t)}{\partial t} - D_{M,j}\frac{\partial^2 M_j(r,t)}{\partial r^2} - \frac{2D_{M,j}}{r}\frac{\partial M_j(r,t)}{\partial r} = r_{A,j}(r,t,\boldsymbol{\theta},\mathbf{M}),$$

$$j = m_1 + 1,...,m_2,\ 0 < r < R(t),\ t > 0, \tag{6.17}$$

where $r_{A,j}(r,t,\boldsymbol{\theta},\mathbf{M})$ and $D_{M,j}$ denote the adsorption rate and diffusion coefficient of the $j^{th}$ dissolved metal within the biofilm.

### 6.2.2 Bioreactor macroscale model

The reactor macroscale is modelled as a sequencing batch reactor in which $N_G$ granules having the same properties are immersed. Specifically, the reactor is characterized by the presence of a number of soluble substrates involved in the biological process and heavy metals taking part in the biosorption process. Besides the sessile biomass (granules), also planktonic and detached biomasses are considered in the bulk liquid.

Planktonic species contribute to the genesis of the granules, while detached biomass is formed as a result of the detachment process. The modelling choice to include planktonic and detached biomass as two different variables derives from the experimental experience that the newly detached biomass has different properties from both sessile and planktonic biomass [121, 122, 123]. Both planktonic and detached biomasses (suspended biomasses) contribute to the conversion of soluble substrates in the bulk liquid. Reconversion of detached biomass into planktonic biomass is also modelled. The bioreactor model is formulated for $n$ microbial species in planktonic form $\psi_i^*(t)$, $n$ microbial species deriving from the detachment process $\psi_{d_i}^*(t)$, $m_1$ dissolved substrates $S_j^*(t)$, and $m_2 - m_1$ heavy metals $M_j^*(t)$. All these variables are expressed in terms of concentration and modelled as functions of time and not of space, since the reactor is modeled as a completely mixed reactor. An SBR is based on a sequence of treatment cycles constituted by four phases:

- filling phase, in which the reactor is fed with a fixed volume of wastewater;
- reaction phase, in which the wastewater volume is biologically treated through the biomass present in the system;
- settling phase, which consists in the solid-liquid separation;
- emptying phase, in which the clarified supernatant is partially removed from the reactor.

The filling, settling and emptying phases are supposed to be instantaneous, and the duration of the reaction phase is supposed to be the same as the cycle duration. $100\%$ settling efficiency is assumed for biofilm granules, while the suspended biomass has a partial settling efficiency. Moreover, since the volume occupied by the biomass in granular and suspended form is neglected, the reactor volume is assumed to be the same as the liquid volume. The cyclic configuration of the SBR is modelled with a system of first order impulsive ordinary differential equations (IDEs) [152, 173]. An IDE is

described by three components: the continuous-time differential equation, which governs the state of the system between impulses; the impulse equation, which describes an impulsive jump and is defined by a jump function at the instant the impulse occurs; and the jump criterion, which defines a set of jump events in which the impulse equation is active.

In summary, the model components describing the bulk liquid are:

$$\psi_i^*,\ i = 1, ..., n,\ \boldsymbol{\psi}^* = (\psi_1^*, ..., \psi_n^*), \tag{6.18}$$

$$\psi_{d_i}^*,\ i = 1, ..., n,\ \boldsymbol{\psi_d}^* = (\psi_{d_1}^*, ..., \psi_{d_n}^*), \tag{6.19}$$

$$S_j^*,\ j = 1, ..., m_1,\ \mathbf{S}^* = (S_1^*, ..., S_{m_1}^*), \tag{6.20}$$

$$M_j^*,\ j = m_1 + 1, ..., m_2,\ \mathbf{M}^* = (M_{m_1+1}^*, ..., M_{m_2}^*), \tag{6.21}$$

while, the system of IDEs is the following:

$$V\dot{\psi}_i^*(t) = -\sigma_{a,i}(t)\rho A(t) + r_{\psi,i}^*(t, \boldsymbol{\psi}^*, \mathbf{S}^*, \mathbf{M}^*) + r_{C,i}^*(t, \boldsymbol{\psi}_d^*),$$

$$t \in [0, T],\ t \neq t_k, i = 1, ..., n\ t > 0, \tag{6.22}$$

$$V\dot{\psi}_{d_i}^*(t) = \sigma_{d,i}(t)\rho A(t) + r_{\psi_d,i}^*(t, \boldsymbol{\psi}_d^*, \mathbf{S}^*, \mathbf{M}^*) - r_{C,i}^*(t, \boldsymbol{\psi}_d^*),$$

$$t \in [0, T],\ t \neq t_k, i = 1, ..., n\ t > 0, \tag{6.23}$$

$$V\dot{S}_j^*(t) = -A(t)N_G D_{S,j}\frac{\partial S_j(R(t),t)}{\partial r} + r_{S,j}^*(t,\boldsymbol{\psi}^*,\boldsymbol{\psi}_d^*,\mathbf{S}^*,\mathbf{M}^*),$$

$$t \in [0,T],\ t \neq t_k,\ j = 1,...,m_1,\ t > 0, \tag{6.24}$$

$$V\dot{M}_j^*(t) = -A(t)N_G D_{M,j}\frac{\partial M_j(R(t),t)}{\partial r},$$

$$t \in [0,T],\ t \neq t_k, j = m_1+1,...,m_2,\ t > 0, \tag{6.25}$$

where V is the volume of the bulk liquid; $A(t)$ is the area of the spherical granule and is equal to $4\pi R^2(t)$; $r_{\psi,i}^*(t,\boldsymbol{\psi}^*,\mathbf{S}^*,\mathbf{M}^*)$ and $r_{\psi_d,i}^*(t,\boldsymbol{\psi}_d^*,\mathbf{S}^*,\mathbf{M}^*)$ are the growth rates for the $i^{th}$ planktonic and detached biomass, respectively; $r_{S,j}^*(t,\boldsymbol{\psi}^*,\boldsymbol{\psi}_d^*,\mathbf{S}^*,\mathbf{M}^*)$ is the conversion rate for the $j^{th}$ soluble substrates; and $r_{C,i}^*(t,\boldsymbol{\psi}_d^*)$ is the reconversion rate of the $i^{th}$ detached biomasses into planktonic form.

The jump functions associated to Eqs. (6.22)-(6.25) are:

$$\Delta\psi_i^*(t_k) = \psi_i^*(t_k^+) - \psi_i^*(t_k^-) = -\gamma\psi_i^*(t_k^-),\ k = 1,...,h,\ i = 1,...,n, \tag{6.26}$$

$$\Delta\psi_{d_i}^*(t_k) = \psi_{d_i}^*(t_k^+) - \psi_{d_i}^*(t_k^-) = -\gamma\psi_{d_i}^*(t_k^-),\ k = 1,...,h,\ i = 1,...,n, \tag{6.27}$$

$$\Delta S_j^*(t_k) = S_j^*(t_k^+) - S_j^*(t_k^-) = -\omega S_j^*(t_k^-) + \omega S_j^{in},\ k = 1,...,h,\ j = 1,...,m_1, \tag{6.28}$$

$$\Delta M_j^*(t_k) = M_j^*(t_k^+) - M_j^*(t_k^-) = -\omega M_j^*(t_k^-) + \omega M_j^{in},\ k = 1, ..., h,\ j = m_1+1, ..., m_2, \tag{6.29}$$

where $\gamma$ is the fraction of suspended biomass removed during the emptying phase; $\omega$ is the emptying/refilling ratio; $S_j^{in}$ and $M_j^{in}$ are the concentrations of the $j^{th}$ substrate and $j^{th}$ metal in the influent; $0 = t_0 < t_1 < ... < t_h < t_{h+1} = T$, $t_{k+1} - t_k = \tau$; $\tau$ is the duration of the cycle; $\psi_i^*(t_k^+)$, $\psi_{d_i}^*(t_k^+)$, $S_j^*(t_k^+)$, $M_j^*(t_k^+)$, $\psi_i^*(t_k^-)$ ,$\psi_{d_i}^*(t_k^-)$, $S_j^*(t_k^-)$, and $M_j^*(t_k^-)$ are the right and left limits of $\psi_i^*$, $\psi_{d_i}^*$, $S_j^*$ and $M_j^*$ at time $t_k$.

Such systems of IDEs are derived from mass balance considerations and describe the dynamics of planktonic and detached biomasses, soluble substrates, and heavy metals within the bulk liquid. Equation (6.22) represents the mass balance of the $i^{th}$ microbial species in planktonic form. In particular, the mass variation over time within the bioreactor (first member) is due to the exchange flux related to the attachment process (first term of the second member), the metabolic activity in the bulk liquid (second term of the second member), and the conversion of the detached biomass into planktonic form (third term of the second member). Similarly, Eq. (6.23) represents the mass balance of the $i^{th}$ detached microbial species. In particular, the mass variation over time within the bioreactor (first member) is due to the exchange flux related to the detachment process (first term of the second member), the metabolic activity in the bulk liquid (second term of the second member), and the conversion of the detached biomass into planktonic form (third term of the second member). Obviously, the attachment flux represents a negative contribution for the planktonic biomasses, while the detachment process is a positive contribution for the detached biomasses. The conversion rate from detached to planktonic state causes two opposite contributions: positive in the equation of planktonic species and negative in the equation of detached biomasses. Eq. (6.24) represents the mass balance of the $j^{th}$ soluble substrate. In this case, the mass variation over time within the bioreactor (first member) is due to the exchange flux between the

bulk liquid and the granular biofilms related to the diffusion phenomenon (first term of the second member) and its consumption and/or production occurring in the bulk liquid and mediated by the planktonic and detached biomasses (second term of second member). Lastly, Eq. (6.25) represents the mass balance of the $j^{th}$ dissolved metal. In this case, the mass variation over time within the bioreactor (first member) is due to only the exchange flux between the bulk liquid and the granular biofilms related to the diffusion phenomenon. Indeed, its consumption in the bulk liquid mediated by the planktonic and detached biomasses is neglected.

### 6.2.3 Initial and boundary conditions

To integrate Eqs. (6.7)-(6.9), (6.12), (6.16), (6.17), (6.22)-(6.25), it is necessary to specify initial and boundary conditions. The *de novo* granulation process is modelled by coupling a vanishing initial condition to Eq. (6.9):

$$R(0) = 0. \tag{6.30}$$

The boundary condition for Eq. (6.8) is given by:

$$u(0,t) = 0,\ t > 0. \tag{6.31}$$

The granule radius $R(t)$ represents the free boundary of the mathematical problem. Its variation, governed by Eq. (6.9), depends on attachment $\sigma_a$ and detachment $\sigma_d$ velocity. In the initial phase, the granule radius is small and, consequently, attachment prevails on detachment. Therefore, it is $\sigma_a - \sigma_d > 0$ and the free boundary is a space-like line. During maturation, the granule dimension increases, and the detachment is the prevailing process. Thus, it is $\sigma_a - \sigma_d < 0$, and the free boundary is a time-like line. When the free boundary is a space-like line, there is a mass flux from bulk liquid to granule, and the biofilm volume fractions at the granule-bulk liquid interface are dependent on characteristics of the bulk liquid. In particular, the volume fractions of

sessile biomass depend on the concentration of planktonic biomass in the bulk liquid:

$$f_i(R(t),t) = \frac{v_{a,i}\psi_i^*(t)}{\sum_{i=1}^{n} v_{a,i}\psi_i^*(t)},\ i = 1,...,n,\ t > 0,\ \sigma_a(t) - \sigma_d(t) > 0, \tag{6.32}$$

while, the volume fractions of the free binding sites are fixed equal to the biofilm volume fractions at the granule-bulk liquid interface:

$$\theta_i(R(t),t) = f_i(R(t),t),\ i = 1,...,n,\ t > 0,\ \sigma_a(t) - \sigma_d(t) > 0. \tag{6.33}$$

When the free boundary is a time-like line, there is a mass flux from the granule to the bulk liquid. Thus, the volume fractions at the interface are regulated exclusively by the internal points of the biofilm domain and conditions (6.32) and (6.33) are not required.

For what concerns substrates and metals diffusion (Eq. (6.12) and Eq. (6.17)), a no flux condition is fixed at the granule center ($r = 0$), and a Dirichlet condition is considered at the granule-bulk liquid interface ($r = R(t)$):

$$\frac{\partial S_j}{\partial r}(0,t) = 0,\ S_j(R(t),t)) = S_j^*(t),\ j = 1,...,m_1,\ t > 0, \tag{6.34}$$

$$\frac{\partial M_j}{\partial r}(0,t) = 0,\ M_j(R(t),t)) = M_j^*(t),\ j = m_1+1,...,m_2,\ t > 0, \tag{6.35}$$

Note that $S_j^*(t)$ and $M_j^*(t)$ are the solutions of Eq. (6.24) and Eq. (6.25), respectively.

Eqs. (6.7), (6.12), (6.16), and (6.17) refer to the biofilm domain and do not require initial conditions, since the extension of the biofilm domain is zero at $t = 0$.

Lastly, the following initial conditions are considered for Eqs. (6.22)-(6.25):

$$\psi_i^*(0) = \psi_{i,0}^*,\ i = 1, ..., n, \tag{6.36}$$

$$\psi_{d_i}^*(0) = \psi_{d_{i,0}}^*,\ i = 1, ..., n, \tag{6.37}$$

$$S_j^*(0) = S_{j,0}^*,\ j = 1, ..., m_1, \tag{6.38}$$

$$M_j^*(0) = M_{j,0}^*,\ j = m_1 + 1, ..., m_2, \tag{6.39}$$

where $\psi_{i,0}^*$, $\psi_{d_i,0}^*$, $S_{j,0}^*$, and $M_{j,0}^*$ are the initial concentrations of the $i^{th}$ planktonic and detached biomass, and the $j^{th}$ soluble substrate and dissolved metal within the bulk liquid, respectively.

## 6.3 Biochemical framework: OPGs granulation and adsorption processes

The mathematical model described above simulates the biosorption process of metals on the matrix of biofilm granules, occurring in a granular-based SBR system, and is able to contextually describe granules genesis and ecology, bioreactor performances, and adsorption process of inorganic compounds. In this Chapter, the model is applied to study the ecology of OPGs and the adsorption process of a metal on their solid matrix.

### 6.3.1 Metabolic kinetics of OPGs

All main biological processes involved in the OPGs lifecycle are included in the mathematical model. For this purpose, phototrophs $PH$, heterotrophic bacteria $H$, and nitri-

fying bacteria $N$ are taken into account as active microbial species. While, the following soluble substrates are considered: inorganic carbon $IC$, organic carbon $DOC$, nitrate $NO_3$, ammonia $NH_3$, and dissolved oxygen $O_2$.

The growth metabolism of phototrophs is affected by light. Two different processes of phototrophic growth in presence of light are taken into account, based on the available nitrogen source. In presence of $NH_3$, phototrophs carry out photosynthesis, consuming $IC$ and $NH_3$ and producing $O_2$ and $DOC$. In absence or shortage of ammonia, phototrophs can grow by using $NO_3$ as nitrogen source. Furthermore, the model takes into account the inhibition induced by the presence of $O_2$ on the photosynthetic activity. In absence of light, $DOC$, $O_2$, and $NH_3$ are consumed by the phototrophs, which produce $IC$. Heterotrophic bacteria use $DOC$ as a source of carbon and energy, and produce inorganic carbon $IC$. They are assumed to grow under aerobic condition directly using $O_2$, as well as anoxic condition using $NO_3$ as oxygen source (denitrification process). As in the previous case, this aspect is modelled using an inhibition term for oxygen in the nitrate-based heterotrophic growth kinetic [174]. Nitrifying bacteria include ammonia-oxidizing bacteria and nitrite-oxidizing bacteria. For this reason, they are responsible for $NH_3$ conversion into $NO_2$, and the subsequent $NO_2$ conversion into $NO_3$. The same biological processes are supposed to occur in the bulk liquid, where planktonic and detached biomasses consume or produce the $j^{th}$ soluble substrate. The mathematical model considers the production of $EPS$ and inactive material only in sessile form. Indeed, the $EPS$ production by suspended biomass has been neglected because it is much lower than sessile production [152], as well as the production of suspended inactive biomass that does not play any role in the biological process. Moreover, phototrophs are regarded as the main $EPS$ contributors [20], and this aspect has been considered in the model by adopting different values of $EPS$ fraction produced by the microbial species.

### 6.3.2 Adsorption process

Compared to conventional physical/chemical technologies, biosorption is effective and less expensive when the metal concentration is below $100\ mg\ L^{-1}$ [18, 157, 158, 159, 161]. Both living and dead (metabolically inactive) biological materials are able to adsorb toxic heavy metals, as various functional groups are found on their cell wall offering strong attraction forces for the metal ions and providing high metal removal efficiency [159]. Specifically, extracellular substances produced by microorganisms have a crucial role in biosorption of metals [168] and are considered the major potential agents in biosorption processes [20]. In metal-stressed conditions microorganisms are induced to produce a higher amount of $EPS$, increasing the adsorption potential of the microbial consortium [20, 21]. Moreover, microorganisms not only regulate the synthesis of $EPS$ in response to toxic elements, but also increase $EPS$ adsorption capacities [20]. These aspects are included in the model by adopting a higher adsorption constant for $EPS$ and considering a stimulation term for $EPS$ production in all microbial kinetics. Also phototrophs and inactive material play an important role in adsorption processes, as they show high metals removal efficiency and can achieve more effective biosorption of metals than bacteria and fungi [21]. Indeed, metal accumulation capacity of phototrophs is comparable or sometimes higher than chemical sorbents [175], and, in addition, as mentioned before they are the main $EPS$ producers [20]. The use of dead biomass could be a preferred alternative, as it offers high metals adsorption capacity, easy recovery of biosorbed metals, absence of toxicity limitations and nutrients requirements for growth [159, 160]. However, in the case in which the solvent consists of industrial wastewater rich in metals, organic and nitrogen compounds, the problem related to the nutrients requirement is overcome and the utilization of algal-bacterial biomass allows to combine the advantages of $EPS$, microalgae and inactive material. Lastly, metals adsorption by suspended biomasses is neglected. Indeed, populations of planktonic and biofilm cells adsorb metals in different ways [176], and it is

experimentally proved that immobilized bacterial cells have much higher biosorption capacities than suspended cells [177]. Moreover, the use of freely-suspended microbial biosorbents has further disadvantages including small particle size, low density, poor mechanical strength, and little rigidity, while the use of biofilms minimize these disadvantages [160].

### 6.3.3 Modelling of heavy metals adsorption on OPGs

In summary, the following variables are included in the model:

- Granule variables:
  - Five sessile microbial species: phototrophs $f_{PH}(r,t)$, heterotrophic bacteria $f_H(r,t)$, nitrifying bacteria $f_N(r,t)$, $EPS$ $f_{EPS}(r,t)$, and inactive biomass $f_I(r,t)$.
  - Five soluble compounds: inorganic carbon $S_{IC}(r,t)$, organic carbon $S_{DOC}(r,t)$, nitrate $S_{NO_3}(r,t)$, ammonia $S_{NH_3}(r,t)$, and dissolved oxygen $S_{O_2}(r,t)$.
  - Five fractions of free binding sites related to: phototrophs $\theta_{PH}(r,t)$, heterotrophic bacteria $\theta_H(r,t)$, nitrifying bacteria $\theta_N(r,t)$, $EPS$ $\theta_{EPS}(r,t)$, and inactive biomass $\theta_I(r,t)$.
  - One heavy metal: $M(r,t)$.
- SBR variables:
  - Three planktonic microbial species: phototrophs $\psi^*_{PH}(t)$, heterotrophic bacteria $\psi^*_H(t)$, and nitrifying bacteria $\psi^*_N(t)$.
  - Three microbial species deriving from biofilm detachment: phototrophs $\psi^*_{d_{PH}}(t)$, heterotrophic bacteria $\psi^*_{d_H}(t)$, and nitrifying bacteria $\psi^*_{d_N}(t)$.
  - Five soluble compounds: inorganic carbon $S^*_{IC}(t)$, organic carbon $S^*_{DOC}(t)$, nitrate $S^*_{NO_3}(t)$, ammonia $S^*_{NH_3}(t)$, and dissolved oxygen $S^*_{O_2}(t)$.

– One heavy metal: $M^*(t)$

In order to account the light dependency of the phototrophic metabolism, light intensity is included as a model variable: $I(r,t)$. I is assumed to be a piecewise-constant function in the bioreactor to simulate the day-night cycle, while it varies across the granule radius due to attenuation phenomena, according to the Lambert-Beer law:

$$I(r,t) = I_0 e^{-k_{tot}(R(t)-r)\rho}, 0 \leq r \leq R(t),\ t > 0, \tag{6.40}$$

where $I_0$ is the light intensity in the bioreactor and $k_{tot}$ is the light attenuation coefficient [178]. Also the negative effect of photoinhibition is accounted in the model [152]. Indeed, excess light can photoinhibit and slow down photosynthesis activity of phototrophs [179]. In accordance with [180], such phenomena is modelled by using the following optimum type expression:

$$\phi_I(r,t) = \frac{I(r,t)}{I_{opt}}\, e^{1-\frac{I(r,t)}{I_{opt}}},\ 0 \leq r \leq R(t),\ t > 0, \tag{6.41}$$

where $I_{opt}$ is the optimum light intensity for phototrophs.

The OPGs granulation process is governed by phototrophs, in planktonic form which are able to aggregate and enclose non-phototrophic biomass in a rigid and spherical structure thanks to their filamentous morphology [15, 171]. As proposed by Tenore et al. (2021) [152], this aspect is taken into account assuming that the attachment velocities of heterotrophic and nitrifying bacteria are functions of the planktonic phototrophs concentration within the bioreactor:

$$\sigma_{a,i}(t) = \frac{v_{a,i}\psi_i^*(t)}{\rho},\ i \in \{PH, H, N\}, \tag{6.42}$$

$$v_{a,i} = v_{a,i}^0,\ i \in \{PH\}, \tag{6.43}$$

$$v_{a,i}(\psi^*_{PH}(t)) = \frac{v^0_{a,i}\psi^*_{PH}(t)}{K_{PH} + \psi^*_{PH}(t)},\ i \in \{H, N\}, \tag{6.44}$$

where $v^0_{a,i}$ is the maximum attachment velocity of the $i^{th}$ suspended species and $K_{PH}$ is the cyanobacteria half saturation constant on the attachment of heterotrophs and nitrifiers.

All reaction terms of the model are reported below. The sessile biomasses growth rates $r_{M,i}$ and conversion rates for soluble substrates within the biofilm $r_{S,j}$, reported in Eq. (6.7), Eq. (6.8), and Eq. (6.12) are modelled as follows:

$$r_{M,i} = \sum_k \alpha_{i,k}\ \nu_k,\ i \in \{PH, H, N, EPS, I\},\ k = 1, ..., m, \tag{6.45}$$

$$r_{S,j} = \sum_k \beta_{j,k}\ \nu_k,\ j \in \{IC, DOC, NO_3, NH_3, O_2\},\ k = 1, ..., m, \tag{6.46}$$

where $m$ denotes the number of biological processes occurring in the biofilm and accounted in the mathematical model; $\alpha_{i,k}$ is the stoichiometric coefficient of the $i^{th}$ biofilm component referred to the $k^{th}$ biological process within the biofilm (Table 6.1); $\beta_{j,k}$ is the stoichiometric coefficient of the $j^{th}$ soluble substrate referred to the $k^{th}$ biological process within the biofilm (Table 6.2); $\nu_k$ represents the kinetic rate of the $k^{th}$ biological process within the biofilm (Table 6.3). Moreover, the conversion rates of planktonic biomasses $r^*_{\psi,j}$, detached biomasses $r^*_{\psi_{d_i}}$ and soluble substrates $r^*_{S,j}$ within the bulk liquid, reported in Eqs. (6.22)-(6.24) are defined as:

$$r^*_{\psi,i} = \sum_k \alpha^*_{i,k}\ \nu^*_k,\ i \in \{PH, H, N\},\ k = 1, ..., m, \tag{6.47}$$

$$r^*_{\psi_{d_i}} = \sum_k \bar{\alpha}^*_{i,k}\ \nu^*_k,\ i \in \{PH, H, N\},\ k = 1, ..., m, \tag{6.48}$$

$$r^*_{S,j} = \sum_k \beta^*_{j,k}\, \nu^*_k,\ j \in \{IC, DOC, NO_3, NH_3\},\ k = 1, ..., m, \tag{6.49}$$

$$r^*_{S,j} = \sum_k \beta^*_{j,k}\, \nu^*_k + k_{La}(S_{j,sat} - S^*_j),\ j \in \{O_2\},\ k = 1, ..., m, \tag{6.50}$$

where $m$ denotes the number of biological processes occurring in the bulk liquid and accounted in the mathematical model; $k_{La}$ and $S_{O_2,sat}$ are the oxygen mass transfer coefficient and the oxygen saturation concentration in the bulk liquid, respectively; $\alpha^*_{i,k}$ is the stoichiometric coefficient of the $i^{th}$ planktonic species referred to the $k^{th}$ biological process within the bulk liquid (Table 6.4); $\bar{\alpha}^*_{i,k}$ is the stoichiometric coefficient of the $i^{th}$ detached species referred to the $k^{th}$ biological process within the bulk liquid (Table 6.4); $\beta^*_{j,k}$ is the stoichiometric coefficient of the $j^{th}$ soluble substrate referred for the $k^{th}$ biological process within the bulk liquid (Table 6.5); $\nu^*_k$ represents the kinetic rate of the $k^{th}$ biological process within the bulk liquid (Table 6.6).

Detached biomass has different characteristics from both sessile and planktonic biomasses [121, 122, 123]. Experimental observations suggest that the surface properties of detached cells clearly differ from those of planktonic and sessile cells for at least the first $48\ h$ after detachment [122]. For this reason, the reconversion rate of the $i^{th}$ detached species into planktonic form, reported in Eq. (6.22) and Eq. (6.23), is modelled as follows:

$$r^*_{C,i} = K_C \psi^*_{d_i}(t), \tag{6.51}$$

where $K_C$ is the conversion constant from detached to planktonic form.

Regarding the adsorption process, the consumption rate of the free binding sites $r_{\theta,i}$ and the specific growth rate of sessile species $\mu_{M,i}$ in Eq. (6.16), and the adsorption rate of the dissolved metal $r_A$ in Eq. (6.17) are listed below:

$$r_{\theta,i} = -(k_{ads,i}M + k_{d,i})\theta_i,\ i \in \{PH, H, N, EPS, I\}, \tag{6.52}$$

$$\mu_{M,i} = \sum_k \alpha_{i,k}\,\nu_k,\ i \in \{PH, H, N, EPS, I\},\ k = 1, ..., \bar{m}, \tag{6.53}$$

$$r_A = -Y_{ads,i}\rho_\theta k_{ads,i} M\theta_i,\ i \in \{PH, H, N, EPS, I\}, \tag{6.54}$$

where $\bar{m}$ denotes the number of growth processes occurring in the biofilm and accounted in the mathematical model; $k_{d,i}$ is the decay-inactivation rate for the $i^{th}$ microbial species; $Y_{ads,i}$ and $k_{ads,i}$ represent the biosorption yield and the adsorption kinetic constant of the $i^{th}$ microbial species; $\rho_\theta$ is the density of the binding sites.

As mentioned above, in metal-stressed conditions microorganisms regulate the synthesis of $EPS$ and are induced to produce more. To include this aspect in the model, $EPS$ fraction produced by each the microbial species is modelled as function of the metal concentration:

$$K_{EPS,i} = \tilde{K}_{EPS,i}\left(1 + \frac{M}{K_{s,i} + M}\right), \tag{6.55}$$

where $\tilde{K}_{EPS,i}$ and $K_{s,i}$ are the $EPS$ fraction produced by the $i^{th}$ microbial species in absence of toxic pollutants and the stimulation constant for $EPS$ of the $i^{th}$ microbial species. The model takes into account also the toxic effect of metals on microbial metabolic processes, by considering an inhibition term in all microbial kinetics:

$$I_M = \frac{K_M^{in}}{K_M^{in} + M}, \tag{6.56}$$

where $K_M^{in}$ is the inhibition coefficient for the generic heavy metal.

The values used for all stoichiometric and kinetic parameters are reported in Table 6.7.

| | $X_{PH}$ | $X_H$ | $X_N$ | $X_{EPS}$ | $X_I$ | **Rate** |
|---|---|---|---|---|---|---|
| 1 | $1-k_{EPS,PH}$ | | | $k_{EPS,PH}$ | | $\nu_1$ |
| 2 | $1-k_{EPS,PH}$ | | | $k_{EPS,PH}$ | | $\nu_2$ |
| 3 | $1-k_{EPS,PH}$ | | | $k_{EPS,PH}$ | | $\nu_3$ |
| 4 | | $1-k_{EPS,H}$ | | $k_{EPS,H}$ | | $\nu_4$ |
| 5 | | $1-k_{EPS,H}$ | | $k_{EPS,H}$ | | $\nu_5$ |
| 6 | | | $1-k_{EPS,N}$ | $k_{EPS,N}$ | | $\nu_6$ |
| 7 | -1 | | | | 1 | $\nu_7$ |
| 8 | | -1 | | | 1 | $\nu_8$ |
| 9 | | | -1 | | 1 | $\nu_9$ |

Table 6.1: Biochemical rate coefficients ($\alpha_{i,k}$) of the biological processes within the biofilm.

| | $S_{IC}$ | $S_{DOC}$ | $S_{NO_3}$ | $S_{NH_3}$ | $S_{O_2}$ | **Rate** |
|---|---|---|---|---|---|---|
| 1 | $-\frac{k_{EPS,PH}+(1-k_{EPS,PH})(k_{DOC}+1.0025)}{32}$ | $k_{DOC}(1-k_{EPS,PH})$ | $-\frac{0.1704}{32}(1-k_{EPS,PH})$ | | $\frac{k_{EPS,PH}+(1-k_{EPS,PH})(k_{DOC}+1)}{32}$ | $\nu_1$ |
| 2 | $-\frac{k_{EPS,PH}+(1-k_{EPS,PH})(k_{DOC}+1.0025)}{32}$ | $k_{DOC}(1-k_{EPS,PH})$ | | $-\frac{0.1704}{32}(1-k_{EPS,PH})$ | $\frac{k_{EPS,PH}+(1-k_{EPS,PH})(k_{DOC}+1.3409)}{32}$ | $\nu_2$ |
| 3 | $\frac{1-1.0025\,Y_{DOC}}{32\,Y_{DOC}}$ | $-\frac{1}{Y_{DOC}}$ | | $-\frac{0.1704}{32\,Y_{DOC}}$ | $-\frac{1-Y_{DOC}}{32\,Y_{DOC}}$ | $\nu_3$ |
| 4 | $\frac{1}{32\,Y_H}-0.02976$ | $-\frac{1}{Y_H}$ | | $-\frac{0.2}{33.6}$ | $-\frac{1}{32\,Y_H}+0.03125$ | $\nu_4$ |
| 5 | $\frac{1}{32\,Y_H}-0.02976$ | $-\frac{1}{Y_H}$ | $-\frac{0.8}{32\,Y_H}+0.02857$ | $-\frac{0.2}{33.6}$ | | $\nu_5$ |
| 6 | $-\frac{1}{33.6}$ | | $\frac{1}{14\,Y_N}$ | $-(0.00593+\frac{1}{14\,Y_N})$ | $-\frac{1}{7\,Y_N}+\frac{1}{32}$ | $\nu_6$ |
| 7 | | | | | | $\nu_7$ |
| 8 | | | | | | $\nu_8$ |
| 9 | | | | | | $\nu_9$ |

Table 6.2: Biochemical rate coefficients ($\beta_{j,k}$) of the biological processes within the biofilm.

| | Process | Kinetic rate expression |
|---|---|---|
| 1 | Growth of $PH$ on $NO_3$ | $\nu_1 = \mu_{max,PH} \frac{S_{IC}}{K_{PH,IC}+S_{IC}} \frac{S_{NO_3}}{K_{PH,NO_3}+S_{NO_3}} \frac{K_{PH,NH_3}}{K_{PH,NH_3}+S_{NH_3}} \frac{K^{in}_{PH,O_2}}{K^{in}_{PH,O_2}+S_{O_2}} \frac{K^{in}_M}{K^{in}_M+M} \frac{I}{I_{opt}} e^{(1-(\frac{I}{I_{opt}})} f_{PH}$ |
| 2 | Growth of $PH$ on $NH_3$ | $\nu_2 = \mu_{max,PH} \frac{S_{IC}}{K_{PH,IC}+S_{IC}} \frac{S_{NH_3}}{K_{PH,NH_3}+S_{NH_3}} \frac{K^{in}_{PH,O_2}}{K^{in}_{PH,O_2}+S_{O_2}} \frac{K^{in}_M}{K^{in}_M+M} \frac{I}{I_{opt}} e^{(1-(\frac{I}{I_{opt}})} f_{PH}$ |
| 3 | Heterotrophic growth of $PH$ | $\nu_3 = \mu^{resp}_{max,PH} \frac{S_{DOC}}{K_{PH,DOC}+S_{DOC}} \frac{S_{O_2}}{K_{PH,O_2}+S_{O_2}} \frac{K^{in}_{PH,I}}{K^{in}_{PH,I}+I} \frac{K^{in}_M}{K^{in}_M+M} f_{PH}$ |
| 4 | Aerobic growth of $H$ | $\nu_4 = \mu_{max,H} \frac{S_{DOC}}{K_{H,DOC}+S_{DOC}} \frac{S_{NH_3}}{K_{H,NH_3}+S_{NH_3}} \frac{S_{O_2}}{K_{H,O_2}+S_{O_2}} \frac{K^{in}_M}{K^{in}_M+M} f_H$ |
| 5 | Anoxic growth of $H$ | $\nu_5 = \mu_{max,H} \frac{S_{DOC}}{K_{H,DOC}+S_{DOC}} \frac{S_{NO_3}}{K_{H,NO_3}+S_{NO_3}} \frac{S_{NH_3}}{K_{H,NH_3}+S_{NH_3}} \frac{K_{H,O_2}}{K_{H,O_2}+S_{O_2}} \frac{K^{in}_M}{K^{in}_M+M} f_H$ |
| 6 | Growth of $N$ | $\nu_6 = \mu_{max,N} \frac{S_{IC}}{K_{N,IC}+S_{IC}} \frac{S_{NH_3}}{K_{H,NH_3}+S_{NH_3}} \frac{S_{O_2}}{K_{H,O_2}+S_{O_2}} \frac{K^{in}_M}{K^{in}_M+M} f_N$ |
| 7 | Death of $PH$ | $\nu_7 = k_{d,PH} f_{PH}$ |
| 8 | Death of $H$ | $\nu_8 = k_{d,H} f_H$ |
| 9 | Death of $N$ | $\nu_9 = k_{d,N} f_N$ |

where $K^{in}_{PH,O_2} = K^{in}_{O_2,max} \frac{\frac{S_{IC}}{S_{O_2}}}{\frac{S_{IC}}{S_{O_2}}+K_{R_{IC/O_2}}}$

Table 6.3: Kinetic rate expressions ($\nu_k$) of the biological processes within the biofilm.

| | $\psi^*_{\mathbf{PH}}$ | $\psi^*_{\mathbf{H}}$ | $\psi^*_{\mathbf{N}}$ | $\psi^*_{\mathbf{d_{PH}}}$ | $\psi^*_{\mathbf{d_H}}$ | $\psi^*_{\mathbf{d_N}}$ | **Rate** |
|---|---|---|---|---|---|---|---|
| 1 | 1 | | | | | | $\nu^*_1$ |
| 2 | 1 | | | | | | $\nu^*_2$ |
| 3 | 1 | | | | | | $\nu^*_3$ |
| 4 | | 1 | | | | | $\nu^*_4$ |
| 5 | | 1 | | | | | $\nu^*_5$ |
| 6 | | | 1 | | | | $\nu^*_6$ |
| 7 | | | | 1 | | | $\nu^*_7$ |
| 8 | | | | 1 | | | $\nu^*_8$ |
| 9 | | | | 1 | | | $\nu^*_9$ |
| 10 | | | | | 1 | | $\nu^*_{10}$ |
| 11 | | | | | 1 | | $\nu^*_{11}$ |
| 12 | | | | | | 1 | $\nu^*_{12}$ |
| 13 | -1 | | | | | | $\nu^*_{13}$ |
| 14 | | -1 | | | | | $\nu^*_{14}$ |
| 15 | | | -1 | | | | $\nu^*_{15}$ |
| 16 | | | | -1 | | | $\nu^*_{16}$ |
| 17 | | | | | -1 | | $\nu^*_{17}$ |
| 18 | | | | | | -1 | $\nu^*_{18}$ |

Table 6.4: Biochemical rate coefficients ($\alpha^*_{i,k}$ and $\bar{\alpha}^*_{i,k}$) of the biological processes within the bulk liquid.

| | $\mathbf{S^*_{IC}}$ | $\mathbf{S^*_{DOC}}$ | $\mathbf{S^*_{NO_3}}$ | $\mathbf{S^*_{NH_3}}$ | $\mathbf{S^*_{O_2}}$ | **Rate** |
|---|---|---|---|---|---|---|
| 1 | $-\frac{k_{DOC}+1.0025}{32}$ | $k_{DOC}$ | $-\frac{0.1704}{32}$ | | $\frac{k_{DOC}+1}{32}$ | $\nu^*_1$ |
| 2 | $-\frac{k_{DOC}+1.0025}{32}$ | $k_{DOC}$ | | $-\frac{0.1704}{32}$ | $\frac{k_{DOC}+1.3409}{32}$ | $\nu^*_2$ |
| 3 | $\frac{1-1.0025\,Y_{DOC}}{32\,Y_{DOC}}$ | $-\frac{1}{Y_{DOC}}$ | | $-\frac{0.1704}{32\,Y_{DOC}}$ | $-\frac{1-Y_{DOC}}{32\,Y_{DOC}}$ | $\nu^*_3$ |
| 4 | $\frac{1}{32\,Y_H}-0.02976$ | $-\frac{1}{Y_H}$ | | $-\frac{0.2}{33.6}$ | $-\frac{1}{32\,Y_H}+0.03125$ | $\nu^*_4$ |
| 5 | $\frac{1}{32\,Y_H}-0.02976$ | $-\frac{1}{Y_H}$ | $-\frac{0.8}{32\,Y_H}+0.02857$ | $-\frac{0.2}{33.6}$ | | $\nu^*_5$ |
| 6 | $-\frac{1}{33.6}$ | | $\frac{1}{14\,Y_N}$ | $-(0.00593+\frac{1}{14\,Y_N})$ | $-\frac{1}{7\,Y_N}+\frac{1}{32}$ | $\nu^*_6$ |
| 7 | $-\frac{k_{DOC}+1.0025}{32}$ | $k_{DOC}$ | $-\frac{0.1704}{32}$ | | $\frac{k_{DOC}+1}{32}$ | $\nu^*_7$ |
| 8 | $-\frac{k_{DOC}+1.0025}{32}$ | $k_{DOC}$ | | $-\frac{0.1704}{32}$ | $\frac{k_{DOC}+1.3409}{32}$ | $\nu^*_8$ |
| 9 | $\frac{1-1.0025\,Y_{DOC}}{32\,Y_{DOC}}$ | $-\frac{1}{Y_{DOC}}$ | | $-\frac{0.1704}{32\,Y_{DOC}}$ | $-\frac{1-Y_{DOC}}{32\,Y_{DOC}}$ | $\nu^*_9$ |
| 10 | $\frac{1}{32\,Y_H}-0.02976$ | $-\frac{1}{Y_H}$ | | $-\frac{0.2}{33.6}$ | $-\frac{1}{32\,Y_H}+0.03125$ | $\nu^*_{10}$ |
| 11 | $\frac{1}{32\,Y_H}-0.02976$ | $-\frac{1}{Y_H}$ | $-\frac{0.8}{32\,Y_H}+0.02857$ | $-\frac{0.2}{33.6}$ | | $\nu^*_{11}$ |
| 12 | $-\frac{1}{33.6}$ | | $\frac{1}{14\,Y_N}$ | $-(0.00593+\frac{1}{14\,Y_N})$ | $-\frac{1}{7\,Y_N}+\frac{1}{32}$ | $\nu^*_{12}$ |
| 13 | | | | | | $\nu^*_{13}$ |
| 14 | | | | | | $\nu^*_{14}$ |
| 15 | | | | | | $\nu^*_{15}$ |
| 16 | | | | | | $\nu^*_{16}$ |
| 17 | | | | | | $\nu^*_{17}$ |
| 18 | | | | | | $\nu^*_{18}$ |

Table 6.5: Biochemical rate coefficients ($\beta^*_{i,k}$) of the biological processes within the bulk liquid.

| | Process | Kinetic rate expression |
|---|---|---|
| 1 | Growth of $PH$ on $NO_3$ | $\nu_1^* = \mu_{max,PH} \frac{S_{IC}^*}{K_{PH,IC}+S_{IC}^*} \frac{S_{NO_3}^*}{K_{PH,NO_3}+S_{NO_3}^*} \frac{K_{PH,NH_3}}{K_{PH,NH_3}+S_{NH_3}^*} \frac{K_{PH,O_2}^{in,*}}{K_{PH,O_2}^{in,*}+S_{O_2}^*} \frac{K_{M^*}^{in}}{K_M^{in}+M^*} \frac{I_0}{I_{opt}} e^{(1-\frac{I_0}{I_{opt}})} \psi_{PH}^*$ |
| 2 | Growth of $PH$ on $NH_3$ | $\nu_2^* = \mu_{max,PH} \frac{S_{IC}^*}{K_{PH,IC}+S_{IC}^*} \frac{S_{NH_3}^*}{K_{PH,NH_3}+S_{NH_3}^*} \frac{K_{PH,O_2}^{in,*}}{K_{PH,O_2}^{in,*}+S_{O_2}^*} \frac{K_{M^*}^{in}}{K_M^{in}+M^*} \frac{I_0}{I_{opt,PH}} e^{(1-\frac{I_0}{I_{opt}})} \psi_{PH}^*$ |
| 3 | Heterotrophic growth of $PH$ | $\nu_3^* = \mu_{max,PH}^{resp} \frac{S_{DOC}^*}{K_{PH,DOC}+S_{DOC}^*} \frac{S_{O_2}^*}{K_{PH,O_2}+S_{O_2}^*} \frac{K_{PH,I}^{in}}{K_{PH,I}^{in}+I_0} \frac{K_{M^*}^{in}}{K_M^{in}+M^*} \psi_{PH}^*$ |
| 4 | Aerobic growth of $H$ | $\nu_4^* = \mu_{max,H} \frac{S_{DOC}^*}{K_{H,DOC}+S_{DOC}^*} \frac{S_{NH_3}^*}{K_{H,NH_3}+S_{NH_3}^*} \frac{S_{O_2}^*}{K_{H,O_2}+S_{O_2}^*} \frac{K_{M^*}^{in}}{K_M^{in}+M^*} \psi_H^*$ |
| 5 | Anoxic growth of $H$ | $\nu_5^* = \mu_{max,H} \frac{S_{DOC}^*}{K_{H,DOC}+S_{DOC}^*} \frac{S_{NO_3}^*}{K_{H,NO_3}+S_{NO_3}^*} \frac{S_{NH_3}^*}{K_{H,NH_3}+S_{NH_3}^*} \frac{K_{H,O_2}}{K_{H,O_2}+S_{O_2}^*} \frac{K_{M^*}^{in}}{K_M^{in}+M^*} \psi_H^*$ |
| 6 | Growth of $N$ | $\nu_6 = \mu_{max,N}^* \frac{S_{IC}^*}{K_{N,IC}+S_{IC}^*} \frac{S_{NH_3}^*}{K_{H,NH_3}+S_{NH_3}^*} \frac{S_{O_2}^*}{K_{H,O_2}+S_{O_2}^*} \frac{K_{M^*}^{in}}{K_M^{in}+M^*} \psi_N^*$ |
| 7 | Growth of $PH_d$ on $NO_3$ | $\nu_7^* = \mu_{max,PH} \frac{S_{IC}^*}{K_{PH,IC}+S_{IC}^*} \frac{S_{NO_3}^*}{K_{PH,NO_3}+S_{NO_3}^*} \frac{K_{PH,NH_3}}{K_{PH,NH_3}+S_{NH_3}^*} \frac{K_{PH,O_2}^{in,*}}{K_{PH,O_2}^{in,*}+S_{O_2}^*} \frac{K_{M^*}^{in}}{K_M^{in}+M^*} \frac{I_0}{I_{opt}} e^{(1-\frac{I_0}{I_{opt}})} \psi_{d_{PH}}^*$ |
| 8 | Growth of $PH_d$ on $NH_3$ | $\nu_8^* = \mu_{max,PH} \frac{S_{IC}^*}{K_{PH,IC}+S_{IC}^*} \frac{S_{NH_3}^*}{K_{PH,NH_3}+S_{NH_3}^*} \frac{K_{PH,O_2}^{in,*}}{K_{PH,O_2}^{in,*}+S_{O_2}^*} \frac{K_{M^*}^{in}}{K_M^{in}+M^*} \frac{I_0}{I_{opt,PH}} e^{(1-\frac{I_0}{I_{opt}})} \psi_{d_{PH}}^*$ |
| 9 | Heterotrophic growth of $PH_d$ | $\nu_9^* = \mu_{max,PH}^{resp} \frac{S_{DOC}^*}{K_{PH,DOC}+S_{DOC}^*} \frac{S_{O_2}^*}{K_{PH,O_2}+S_{O_2}^*} \frac{K_{PH,I}^{in}}{K_{PH,I}^{in}+I_0} \frac{K_{M^*}^{in}}{K_M^{in}+M^*} \psi_{d_{PH}}^*$ |
| 10 | Aerobic growth of $H_d$ | $\nu_{10}^* = \mu_{max,H} \frac{S_{DOC}^*}{K_{H,DOC}+S_{DOC}^*} \frac{S_{NH_3}^*}{K_{H,NH_3}+S_{NH_3}^*} \frac{S_{O_2}^*}{K_{H,O_2}+S_{O_2}^*} \frac{K_{M^*}^{in}}{K_M^{in}+M^*} \psi_{d_H}^*$ |
| 11 | Anoxic growth of $H_d$ | $\nu_{11}^* = \mu_{max,H} \frac{S_{DOC}^*}{K_{H,DOC}+S_{DOC}^*} \frac{S_{NO_3}^*}{K_{H,NO_3}+S_{NO_3}^*} \frac{S_{NH_3}^*}{K_{H,NH_3}+S_{NH_3}^*} \frac{K_{H,O_2}}{K_{H,O_2}+S_{O_2}^*} \frac{K_{M^*}^{in}}{K_M^{in}+M^*} \psi_{d_H}^*$ |
| 12 | Growth of $N_d$ | $\nu_{12}^* = \mu_{max,N}^* \frac{S_{IC}^*}{K_{N,IC}+S_{IC}^*} \frac{S_{NH_3}^*}{K_{H,NH_3}+S_{NH_3}^*} \frac{S_{O_2}^*}{K_{H,O_2}+S_{O_2}^*} \frac{K_{M^*}^{in}}{K_M^{in}+M^*} \psi_{d_N}^*$ |
| 13 | Death of $PH$ | $\nu_{13}^* = k_{d,PH} \psi_{PH}^*$ |
| 14 | Death of $H$ | $\nu_{14}^* = k_{d,H} \psi_H^*$ |
| 15 | Death of $N$ | $\nu_{15}^* = k_{d,N} \psi_N^*$ |
| 16 | Death of $PH_d$ | $\nu_{16}^* = k_{d,PH} \psi_{d_{PH}}^*$ |
| 17 | Death of $H_d$ | $\nu_{17}^* = k_{d,H} + \psi_{d_H}^*$ |
| 18 | Death of $N_d$ | $\nu_{18}^* = k_{d,N} \psi_{d_N}^*$ |

where $K_{PH,O_2}^{in,*} = K_{O_2,max}^{in} \frac{\frac{S_{IC}^*}{S_{O_2}^*}}{\frac{S_{IC}^*}{S_{O_2}^*}+K_{R_{IC/O_2}}}$

Table 6.6: Kinetic rate expressions ($\nu_k^*$) of the biological processes within the bulk liquid.

| Parameter | Definition | Unit | Value | Ref |
|---|---|---|---|---|
| $\mu_{max,PH}$ | Maximum specific growth rate for $PH$ | $d^{-1}$ | 2.368 | [174] |
| $\mu^{resp}_{max,PH}$ | Maximum specific growth rate for $PH$ respiration | $d^{-1}$ | 0.237 | [174] |
| $\mu_{max,H}$ | Maximum specific growth rate for $H$ | $d^{-1}$ | 4.8 | [181] |
| $\mu_{max,N}$ | Maximum specific growth rate for $N$ | $d^{-1}$ | 1 | [181] |
| $k_{d,PH}$ | Decay-inactivation rate for $PH$ | $d^{-1}$ | 0.1 | [174] |
| $k_{d,H}$ | Decay-inactivation rate for $H$ | $d^{-1}$ | 0.1 | [174] |
| $k_{d,N}$ | Decay-inactivation rate for $N$ | $d^{-1}$ | 0.1 | [174] |
| $K_{PH,IC}$ | $IC$ half saturation coeff. for $PH$ | $kmol(IC)\ m^{-3}$ | $10^{-4}$ | [174] |
| $K_{PH,DOC}$ | $DOC$ half saturation coeff. for $PH$ | $kg(COD)\ m^{-3}$ | $5 \cdot 10^{-3}$ | [174] |
| $K_{PH,NO_3}$ | $NO_3$ half saturation coeff. for $PH$ | $kmol(NO_3)\ m^{-3}$ | $1.2 \cdot 10^{-6}$ | [174] |
| $K_{PH,NH_3}$ | $NH_3$ half saturation coeff. for $PH$ | $kmol(NH_3)\ m^{-3}$ | $1.2 \cdot 10^{-6}$ | [174] |
| $K_{PH,O_2}$ | $O_2$ half saturation coeff. for $PH$ | $kmol(O_2)\ m^{-3}$ | $3 \cdot 10^{-4}$ | [174] |
| $K^{in}_{PH,I}$ | Light inhibition coefficient for $PH$ | $kmol(e^-)\ m^{-2}\ d^{-1}$ | $8 \cdot 10^{-5}$ | [174] |
| $K_{H,DOC}$ | $DOC$ half saturation coeff. for $H$ | $kg(COD)\ m^{-3}$ | $4 \cdot 10^{-3}$ | [174] |
| $K_{H,NO_3}$ | $NO_3$ half saturation coeff. for $H$ | $kmol(NO_3)\ m^{-3}$ | $3.6 \cdot 10^{-5}$ | [174] |
| $K_{H,NH_3}$ | $NH_3$ half saturation coeff. for $H$ | $kmol(NH_3)\ m^{-3}$ | $3.6 \cdot 10^{-6}$ | [182] |
| $K_{H,O_2}$ | $O_2$ half saturation coeff. for $H$ | $kmol(O_2)\ m^{-3}$ | $6.25 \cdot 10^{-6}$ | [174] |
| $K_{N,IC}$ | $IC$ half saturation coeff. for $N$ | $kmol(IC)\ m^{-3}$ | $10^{-4}$ | [174] |
| $K_{N,NH_3}$ | $NH_3$ half saturation coeff. for $N$ | $kmol(NH_3)\ m^{-3}$ | $7 \cdot 10^{-5}$ | [174] |
| $K_{N,O_2}$ | $O_2$ half saturation coeff. for $N$ | $kmol(O_2)\ m^{-3}$ | $1.56 \cdot 10^{-5}$ | [174] |
| $K^{in}_{O_2,max}$ | Max inhibition coefficient of $O_2$ on $PH$ | $kmol(O_2)\ m^{-3}$ | $10^{-3}$ | [183] |
| $K_{R_{IC/O_2}}$ | Half saturation coeff. for $O_2$ inhibition | $--$ | 0.35 | [183] |
| $K^{in}_M$ | Inhibition coefficient of $M$ | $kg(M)\ m^{-3}$ | 0.1 | (a) |
| $Y_H$ | Yield of $H$ on $DOC$ | $kg(COD)\ kg(COD)^{-1}$ | 0.63 | [174] |
| $Y_N$ | Yield of $N$ on $NO_3$ | $kg(COD)\ kg(NO_3 - N)^{-1}$ | 0.24 | [174] |
| $Y_{DOC}$ | Yield of $PH$ on $DOC$ | $kg(COD)\ kg(COD)^{-1}$ | 0.5 | (a) |
| $\tilde{k}_{EPS,PH}$ | EPS fraction produced by $PH$ | $--$ | 0.23 | (a) |
| $\tilde{k}_{EPS,H}$ | EPS fraction produced by $H$ | $--$ | 0.18 | [184] |
| $\tilde{k}_{EPS,N}$ | EPS fraction produced by $N$ | $--$ | 0.075 | [184] |
| $k_{DOC}$ | DOC release fraction by $PH$ | $--$ | 0.05 | [178] |
| $k_{La}$ | $O_2$ mass transfer coefficient | $d^{-1}$ | 23.3 | [181] |
| $S_{O_2,sat}$ | $O_2$ saturation concentration in bulk liquid | $kmol(O_2)\ m^{-3}$ | $2.4 \cdot 10^{-4}$ | [181] |
| $I_{opt}$ | Optimum light intensity for $PH$ | $kmol(e^-)\ m^{-2}\ d^{-1}$ | 0.01728 | [185] |
| $I_0$ | Incident light intensity in the reactor | $kmol(e^-)\ m^{-2}\ d^{-1}$ | 0.008 | [152] |
| $k_{tot}$ | Light attenuation coefficient | $m^2\ kg^{-1}$ | 210 | [174] |
| $k_{ads,PH}$ | Sorption constant of $PH$ | $m^3\ kg(M)^{-1}\ d^{-1}$ | $1 \cdot 10^3$ | (a) |
| $k_{ads,H}$ | Sorption constant of $H$ | $m^3\ kg(M)^{-1}\ d^{-1}$ | $2 \cdot 10^1$ | (a) |
| $k_{ads,N}$ | Sorption constant of $N$ | $m^3\ kg(M)^{-1}\ d^{-1}$ | $2 \cdot 10^1$ | (a) |
| $k_{ads,EPS}$ | Sorption constant of $EPS$ | $m^3\ kg(M)^{-1}\ d^{-1}$ | $2 \cdot 10^3$ | (a) |
| $k_{ads,I}$ | Sorption constant of $I$ | $m^3\ kg(M)^{-1}\ d^{-1}$ | $2 \cdot 10^2$ | (a) |
| $K_{s,i}$ | Stimulation constant for $EPS$ | $kg(M)\ m^{-3}$ | 0.05 | (a) |
| $Y_{ads,i}$ | Yield of $M$ on $i^{th}$ microbial species | $kg(M)\ N^{\circ,-1}_{sites}$ | 1 | (a) |
| $D_{S,IC}$ | Diffusion coefficient of $IC$ in biofilm | $m^2\ d^{-1}$ | $1.32 \cdot 10^{-4}$ | [174] |
| $D_{S,DOC}$ | Diffusion coefficient of $DOC$ in biofilm | $m^2\ d^{-1}$ | $0.83 \cdot 10^{-4}$ | [22] |
| $D_{S,NO_3}$ | Diffusion coefficient of $NO_3$ in biofilm | $m^2\ d^{-1}$ | $1.18 \cdot 10^{-4}$ | [174] |
| $D_{S,NH_3}$ | Diffusion coefficient of $NH_3$ in biofilm | $m^2\ d^{-1}$ | $1.49 \cdot 10^{-4}$ | [22] |
| $D_{S,O_2}$ | Diffusion coefficient of $O_2$ in biofilm | $m^2\ d^{-1}$ | $1.75 \cdot 10^{-4}$ | [22] |
| $D_{S,M}$ | Diffusion coefficient of metal in biofilm | $m^2\ d^{-1}$ | $6.05 \cdot 10^{-5}$ | [186] |
| $v^0_{a,PH}$ | Attachment velocity of $\psi^*_{PH}$ | $m\ d^{-1}$ | $3 \cdot 10^{-3}$ | (a) |
| $v^0_{a,H}$ | Attachment velocity of $\psi^*_H$ | $m\ d^{-1}$ | $5 \cdot 10^{-4}$ | (a) |
| $v^0_{a,N}$ | Attachment velocity of $\psi^*_N$ | $m\ d^{-1}$ | $5 \cdot 10^{-4}$ | (a) |
| $K_{PH}$ | Half saturation coeff. of $\psi^*_{PH}$ on $\psi^*_H$, $\psi^*_N$ attachment | $kg(COD)\ m^{-3}$ | $3 \cdot 10^{-2}$ | (a) |
| $K_C$ | Conversion coeff. from detached to planktonic form | $d^{-1}$ | 0.5 | (a) |
| $\rho$ | Biofilm density | $kg(COD)\ m^{-3}$ | 37 | [181] |
| $\rho_\theta$ | Binding sites density | $N^\circ_{sites}\ m^{-3}$ | 20 | (a) |
| $\lambda$ | Constant detachment coefficient | $m^{-1}\ d^{-1}$ | 40 | (a) |
| $V$ | Reactor volume | $m^3$ | 400 | (a) |
| $N_G$ | Number of granules in the reactor | $--$ | $2.4 \cdot 10^{10}$ | (a) |
| $\tau$ | Duration of the cycle | $d$ | 0.25 | (a) |
| $\gamma$ | Fraction of suspended biomass lost in the emptying | $--$ | 0.2 | (a) |
| $\omega$ | Emptying/refilling ratio | $--$ | 0.5 | (a) |
| $t_{light}$ | Time of light condition | $d$ | 0.125 | (a) |
| $t_{dark}$ | Time of dark condition | $d$ | 0.125 | (a) |

(a) Assumed

Table 6.7: Kinetic, stoichiometric and operating parameters used for numerical simulations.

## 6.4 Numerical studies and results

The model has been integrated numerically by developing an original code in MatLab platform. Hyperbolic PDEs (6.7) and (6.16) have been integrated by using the method of characteristics, applied for the first time in the planar biofilm context by D'Acunto and Frunzo (2011) [32]. The method of lines has been used to solve the diffusion-reaction PDEs (6.12) and (6.17). The ODEs for $\psi_i^*$, $\psi_{d_i}^*$, $S_j^*$, and $M_j^*$ (Eqs. (6.22)-(6.25)) have been integrated by using the MatLab routine ode45, based on a Runge-Kutta method. Numerical simulations have been performed to investigate the genesis and evolution of oxygenic photogranules, the microbial species stratification and interaction between the functional trophic groups, and to study the SBR performances in terms of substrates removal and metal adsorption. Specifically, the first study ($SET1$) investigates the treatment process of a typical industrial wastewater containing a low concentration of a generic heavy metal. Both the granules ecology and the process evolution have been investigated, focusing on metal effects on biofilm formation and its removal process. The second study ($SET2$) investigates how the metal concentration affects the OPGs formation and adsorption processes in terms of microbial growth and removal efficiency. Finally, the third study ($SET3$) explores the role of the adsorption capacities of all the microbial species in the adsorption process.

The wastewater influent is supposed to be fed discontinuously in the SBR. As mentioned before, in each cycle the reactor is filled with a fixed volume $V$ of wastewater, and the substrates are biologically degraded in batch conditions. The bioreactor volume $V$ is assumed constant and equal to $400\ m^3$. The number of granules $N_G$ has been selected through an iterative procedure varying the detachment coefficient $\lambda$ [128], with the aim to obtain a $25\%$ filling ratio by considering granules with a steady-state radius of about $1\ mm$ (an average size representative of OPGs [16, 172]). After the reaction phase, the solid-liquid separation occurs in the reactor, whereby perfect settling has been considered for granules (no granule is removed from the reactor during the empty-

ing phase). While the fraction of suspended biomass lost during the emptying phase has been set equal to $20\%$. At the end of each cycle the reactor is only partially emptied and refilled with a new liquid volume to be treated (emptying/refilling ratio $\omega = 50\%$). As explained above, the reaction phase is supposed to be the same as the duration of the cycle $\tau$, and it consists of 3 hours of darkness and 3 hours of light ($t_{dark} = t_{light} = 0.125\ d$ and $\tau = 0.25\ d$) [152, 172]. In the light phase, the reactor is supposed to be homogeneously illuminated and the incident light intensity $I_0$ is fixed at $0.008\ kmol\ m^{-2}\ d^{-1}$ [152].

The same wastewater influent composition is considered for each treatment cycle. It is characterized by $S^{in}_{IC} = 180\ g\ m^{-3}$ (inorganic carbon), $S^{in}_{DOC} = 500\ g\ m^{-3}$ (organic carbon), $S^{in}_{NH_3} = 50\ g\ m^{-3}$ (ammonia), $S^{in}_{NO_3} = 0$ (nitrate), $S^{in}_{O_2} = 0$ (oxygen). Such concentrations reflect the typical wastewater [187] and are usually used in experimental works [19]. The concentration of the heavy metal in the influent $M^{in}$ is varied in the numerical studies, and its values will be provided below, case to case. The initial concentrations of soluble substrates $S^*_{j,0}$ and metal $M^*_0$ in the bulk liquid have been set equal to the concentration within the wastewater influent ($S^{in}_j$ and $M^{in}$). On the contrary, no suspended biomass is supposed to be present in the influent ($\psi^{in}_i = 0$ and $\psi^{in}_{d_i} = 0$), while phototrophic inoculum of suspended phototrophs is considered, where planktonic heterotrophic and nitrifying bacteria are present in smaller amounts: $\psi^*_{PH,0} = 600\ g\ m^{-3}$, $\psi^*_{H,0} = \psi^*_{N,0} = 50\ g\ m^{-3}$ [152]. The initial concentration of detached species $\psi^*_{d_i,0}$ in the bulk liquid has been set equal to zero ($\psi^*_{d_i,0} = 0$). Note that no addition of oxygen is considered ($S^{in}_{O_2} = 0$), since it is provided by photosynthesis of phototrophs.

Since the phototrophs are the major $EPS$ producers in algal-bacterial biofilm, their $EPS$ fraction produced in absence of toxic pollutants is assumed to be higher than heterotrophs ($\tilde{K}_{EPS,H} = 0.18$ [184]) and nitrifiers ($\tilde{K}_{EPS,N} = 0.075$ [184]) and is fixed at $\tilde{K}_{EPS,PH} = 0.23$. Such value is within the range of typical $EPS$ fraction values of phototrophic biomass [174]. Regarding the adsorption kinetic constants of the

biofilm components, $k_{ads,EPS}$, $k_{ads,PH}$ and $k_{ads,I}$ are supposed to be much higher than $k_{ads,H}$ and $k_{ads,N}$, since the adsorption process is predominantly governed by $EPS$, phototrophs and inactive material. Finally, as mentioned above, attachment velocity of phototrophs is assumed to be a constant value and it is set equal to the average value of attachment velocities of microalgae and cyanobacteria used by Tenore et al. (2021) [152]. All parameters used in this model are reported in Table 6.7.

The simulation time $T$ is fixed to $200\ d$ for all simulations. This time interval guarantees to achieve the steady-state configuration in terms of: performance of SBR cycles (including soluble substrates $S_j^*$, metal $M^*$, planktonic species $\psi_i^*$, and detached biomasses $\psi_{d_i}^*$), granule size $R(t)$; microbial composition and distribution within the granules (in terms of fraction $f_i$ and mass $m_i$); volume fractions of free binding sites $\theta_i$; and concentration of free metal $M$ within the biofilm.

### 6.4.1 SET1 - Evaluation of metal removal from industrial wastewater in OPGs-based system

The first set $SET1$ describes the treatment process of a typical industrial wastewater with a low concentration of metal ($M^{in} = 100\ g\ m^{-3}$), occurring in a granular-based sequencing batch reactor (simulation $S1$). The microbial stratification of oxygenic photogranules, nutrients degradation, and metal adsorption are investigated. The $SET1$ results are shown in Figs. 6.1-6.4.

Fig. 6.1 reports the evolution of the overall mass of sessile species $m_i(t)$ (top) and photogranule radius $R(t)$ (bottom) over time. The active sessile biomasses constituting the biofilm matrix (phototrophs, heterotrophs and nitrifiers) grow by converting the nutrients, and decay producing inert material. Such biomasses can interact with each other, cooperating and/or competing. In presence of light, phototrophs produce $O_2$ and $DOC$ consuming $IC$ and $NH_3$ (or $NO_3$), and consequently they promote the heterotrophs and nitrifiers growth. Indeed, heterotrophic bacteria require $O_2$ (or $NO_3$

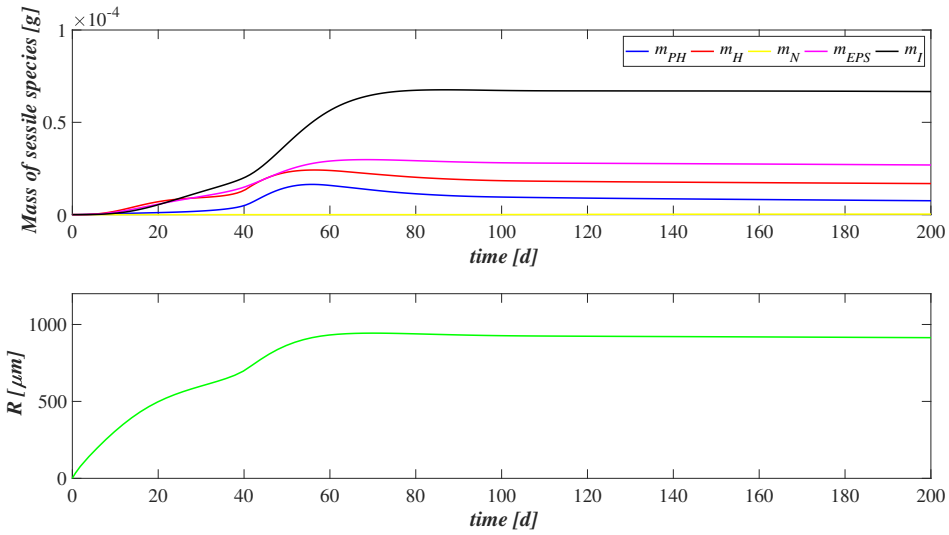


Figure 6.1: $SET1$ - Evolution of biofilm radius and mass of sessile species over time. Wastewater influent composition: $S^{in}_{IC} = 180\ g\ m^{-3}$ (inorganic carbon), $S^{in}_{DOC} = 500\ g\ m^{-3}$ (organic carbon), $S^{in}_{NH_3} = 50\ g\ m^{-3}$ (ammonia), $S^{in}_{NO_3} = 0$ (nitrate), $S^{in}_{O_2} = 0$ (oxygen), $M^{in} = 100\ g\ m^{-3}$ (metal). Incident light intensity: $I_0 = 0.008\ kmol\ m^{-2}\ d^{-1}$. Duration of the cycle: $\tau = 6\ h$. Time of light exposure: $t_{light} = 50\%\ \tau$.

in anoxic condition) and $DOC$ for their metabolic activities. While $NH_3$ and $O_2$ are necessary for nitrifying bacteria, which compete with phototrophs for $IC$. However, nitrifiers produce $NO_3$ necessary for heterotrophs in anoxic condition and for phototrophs in lack or shortage of $NH_3$. Under dark conditions, phototrophs compete with heterotrophs and nitrifiers for $O_2$ and with all heterotrophs for $DOC$. In return, heterotrophic bacteria produce $IC$ necessary for the metabolism of phototrophs in light conditions and nitrifiers. In the initial days, the intense attachment process leads to the formation of photogranules mainly composed by phototrophs. Oxygen production during the photosynthesis promotes the growth of heterotrophic bacteria. Thus, the heterotrophic biomass rapidly increases with respect to the other microbial species, thanks to their high growth rates in presence of elevate availability of $DOC$. It should be noted that the metabolism of all biomasses is initially inhibited, due to the presence of free metal. In this phase the photogranule slowly increases, achieving a radius of about $600\ \mu m$ (Fig. 6.1 - bottom). After $40$ days, when a relevant amount of metal is already

adsorbed on biofilm matrix, a more rapid phototrophs (blue) growth is observed. As consequence, heterotrophs (red) metabolism and production of $EPS$ (magenta) and inert material (black) are favoured. This, in turn, leads to a faster increase of the granule radius. Subsequently, the detachment process becomes more relevant and limits the granule expansion leading to a steady-state dimension of about 920 $\mu m$. A very low mass of nitrifying bacteria (yellow) is observed throughout the process, because they have lower maximum growth rates than heterotrophic bacteria which are more competitive in the use of $O_2$ in presence of $DOC$.

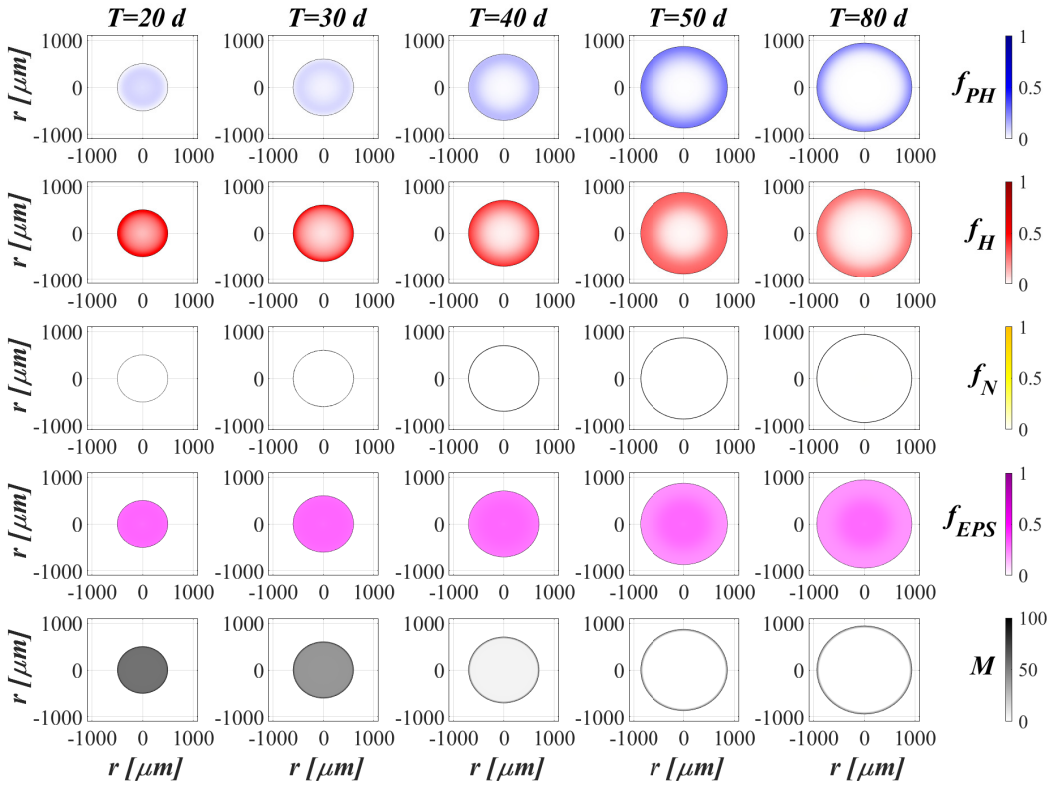


Figure 6.2: $SET1$- Active microbial species distribution and concentration of free metal within the diametrical section of the granule, at $T = 20\ d$, $T = 30\ d$, $T = 40\ d$, $T = 50\ d$, $T = 80\ d$. Wastewater influent composition: $S_{IC}^{in} = 180\ g\ m^{-3}$ (inorganic carbon), $S_{DOC}^{in} = 500\ g\ m^{-3}$ (organic carbon), $S_{NH_3}^{in} = 50\ g\ m^{-3}$ (ammonia), $S_{NO_3}^{in} = 0$ (nitrate), $S_{O_2}^{in} = 0$ (oxygen), $M^{in} = 100\ g\ m^{-3}$ (metal). Incident light intensity: $I_0 = 0.008\ kmol\ m^{-2}\ d^{-1}$. Duration of the cycle: $\tau = 6\ h$. Time of light exposure: $t_{light} = 50\%\ \tau$.

Fig. 6.2 shows the microbial stratification within the granule (from first row to

fourth row) and the free metal concentration (fifth row) at different times. After $20$ and $30$ days, significant fractions of phototrophs (blue) and heterotrophs (red) can be observed throughout the granule. Indeed, phototrophs are responsible for the genesis of the photogranules due to their granulation properties, while heterotrophic bacteria have the highest growth rate. Obviously, in the initial stage of the process the concentration of free metal (black) is still elevate and the metal diffuses throughout the granule inhibiting the microorganisms growth. Passing from $T = 30\ d$ to $T = 40\ d$ the concentration of free metal significantly reduces thanks to the growth of phototrophs (see Fig. 6.4). Indeed, phototrophs have a tendency to secrete $EPS$ higher than other microbial species, and both phototrophs and $EPS$ have higher adsorption capabilities than heterotrophs and nitrifiers. Thanks to the metal consumption, phototrophs are in turn less inhibited and continue to grow. The steady-state of microbial species distribution and free metal concentration is achieved at $T = 80\ d$. Note that phototrophs and $EPS$ are present in relevant amounts and a clear microbial species stratification can be observed: phototrophic biomass accumulates in the outermost layers, where optimal light conditions are guaranteed; heterotrophic bacteria predominantly populate the external part of the granule; $EPS$ (magenta) is homogeneously distributed throughout the granule. In addition, as observed in Fig. 6.1, nitrifying bacteria (yellow) are almost absent. As regard the free metal diffusion, after the complete evolution of the granule, the adsorption process is completed, and a gradient of free metal concentration can be observed across the granule: the free metal concentration goes from low values in a thin external layer to zero in the internal part.

Biofilm volume fractions and free binding sites volume fractions along the granule radius at different times are reported in Fig. 6.3. As shown in fig. 6.1, after $20$ days the granule has achieved a radius of about $500\ \mu m$ and the binding sites of each biofilm component are almost completely consumed. This is ascribed to the combination of different factors: high concentration of metal in the influent wastewater, which is rapidly adsorbed on the granule matrix, granules not completely developed and overall char-

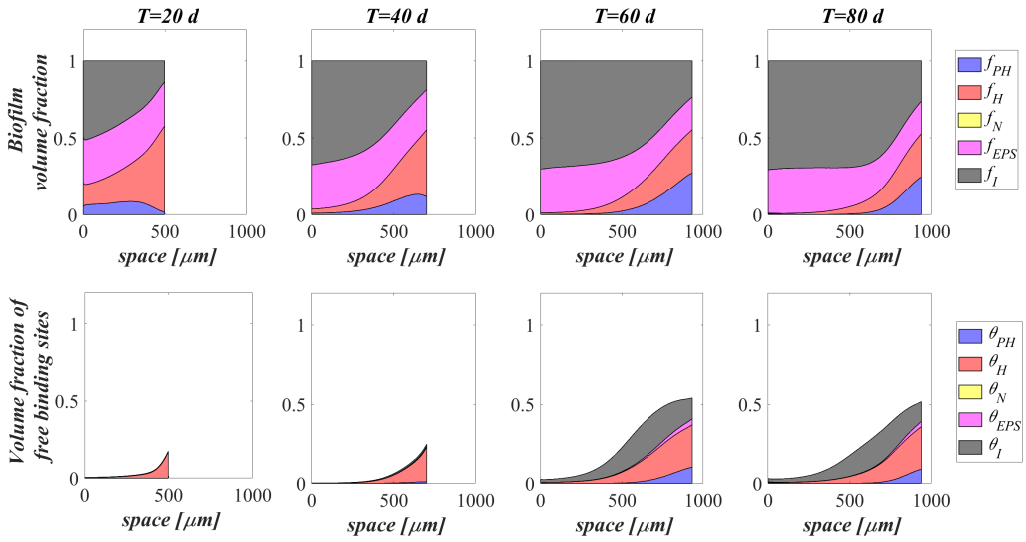


Figure 6.3: $SET1$ - Distribution of microbial species and free binding sites across the radius of the granule, at $T = 20\ d$, $T = 40\ d$, $T = 60\ d$, $T = 80\ d$. Wastewater influent composition: $S^{in}_{IC} = 180\ g\ m^{-3}$ (inorganic carbon), $S^{in}_{DOC} = 500\ g\ m^{-3}$ (organic carbon), $S^{in}_{NH_3} = 50\ g\ m^{-3}$ (ammonia), $S^{in}_{NO_3} = 0$ (nitrate), $S^{in}_{O_2} = 0$ (oxygen), $M^{in} = 100\ g\ m^{-3}$ (metal). Incident light intensity: $I_0 = 0.008\ kmol\ m^{-2}\ d^{-1}$. Duration of the cycle: $\tau = 6\ h$. Time of light exposure: $t_{light} = 50\%\ \tau$.

acterized by a small number of binding sites; low fraction of phototrophs throughout the granule. As shown in Fig. 6.2, when the phototrophs and $EPS$ fractions start to be relevant ($T = 40\ d$), the adsorption process is favoured, microorganisms are less inhibited, and the granule radius increases. As a consequence, new free binding sites are formed and immediately occupied. Passing form $T = 40\ d$ to $T = 60\ d$ the granule radius undergoes a further significant increase (Fig. 6.1), and the residual metal concentration is completely adsorbed (see Fig. 6.4) thanks to the high volume fractions of free binding sites. After $80$ days the granule radius, microbial species distribution and volume fractions of free binding sites have achieved the steady-state configuration. Confirming what has been observed in Fig. 6.2, the granule is mainly composed by $EPS$, phototrophs, inert material, and heterotrophs. The residual binding sites still free indicates the algal-bacterial granules containing in the SBR are perfectly able to remove the metal present in the influent wastewater.

Fig. 6.4 reports the concentration of soluble substrates and metal within the reactor

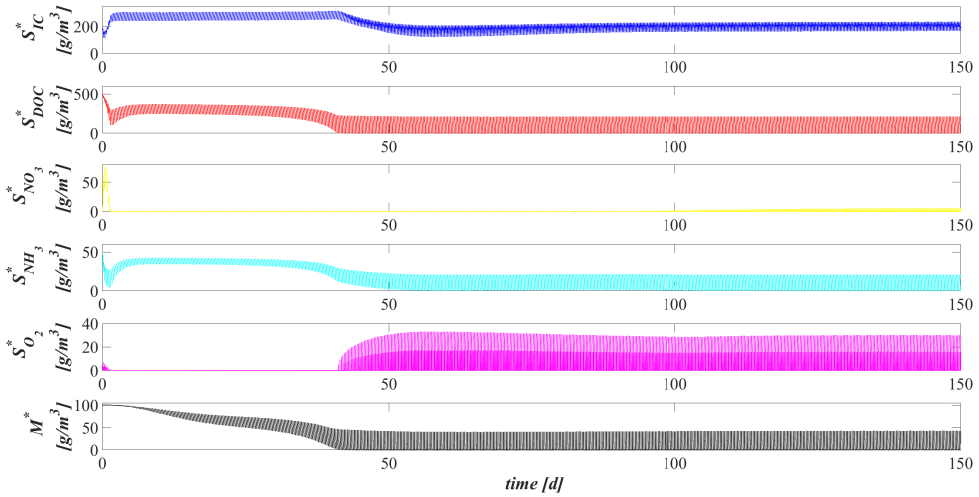


Figure 6.4: $SET1$ - Evolution of soluble substrates and metal concentrations within the reactor. Wastewater influent composition: $S^{in}_{IC} = 180\ g\ m^{-3}$ (inorganic carbon), $S^{in}_{DOC} = 500\ g\ m^{-3}$ (organic carbon), $S^{in}_{NH_3} = 50\ g\ m^{-3}$ (ammonia), $S^{in}_{NO_3} = 0$ (nitrate), $S^{in}_{O_2} = 0$ (oxygen), $M^{in} = 100\ g\ m^{-3}$ (metal). Incident light intensity: $I_0 = 0.008\ kmol\ m^{-2}\ d^{-1}$. Duration of the cycle: $\tau = 6\ h$. Time of light exposure: $t_{light} = 50\%\ \tau$.

over time. The observation period includes the process start-up until the achievement of the steady-state representative of the working configuration of the reactor. It should be noted that such concentrations have a discontinuous trend, due to the SBR configuration. In the initial phase, the biofilm granules are small, and the consumption and production of soluble substrates are governed by planktonic biomass (see Fig. 6.6). Heterotrophic bacteria and phototrophs have higher growth rates than other microbial species. Thus, $DOC$ (red) and $NH_3$ (cyan) consumption and $IC$ (blue) production can be observed. When photogranules dimension increases, biological processes starts to be governed by sessile species. After $10$ days, the oxygen (magenta) produced by phototrophs in presence of light is not sufficient for heterotrophs and nitrifiers, and no $NO_3$ (yellow) is present in the reactor. Thus, a temporary equilibrium in term of soluble substrates characterizes the system from $10$ to $40$ days. In this time frame, the metal (black) is slowly adsorbed on granules matrix and the metal inhibition effect on metabolic microbial activities reduces over time. As observed in Fig. 6.2, this favours

phototrophs growth. Consequently, thanks to $O_2$ production (magenta), heterotrophic bacteria growth is promoted. Moreover, in this phase phototrophs are in turn responsible for more rapid metal adsorption, thanks to their elevate $EPS$ productions and high adsorption capabilities. Metabolic activities of phototrophs and heterotrophs result in the complete $NH_3$ and $DOC$ degradation, $IC$ consumption, and $M$ adsorption after $t = 60\ d$.

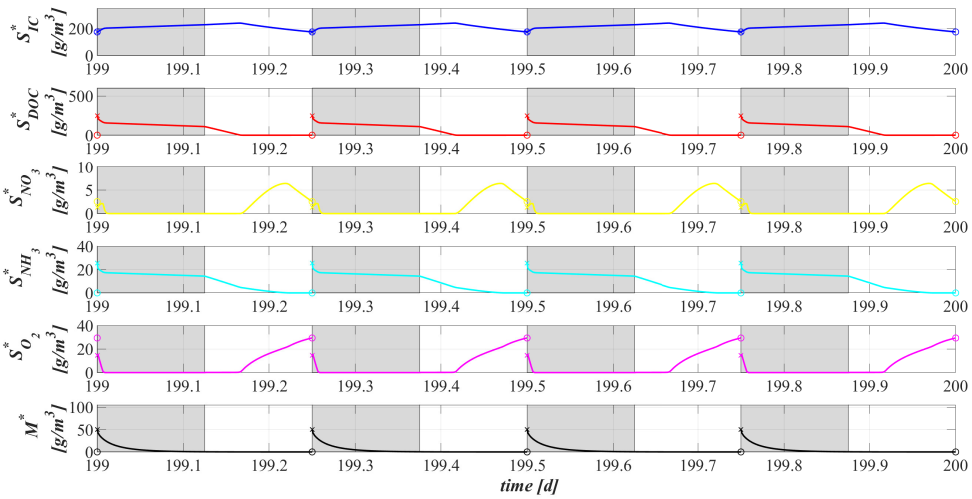


Figure 6.5: $SET1$ - Evolution of soluble substrates and metal concentrations within the reactor, from 199 $d$ to 200 $d$ (four consecutive six-hours treatment cycles). Wastewater influent composition: $S^{in}_{IC} = 180\ g\ m^{-3}$ (inorganic carbon), $S^{in}_{DOC} = 500\ g\ m^{-3}$ (organic carbon), $S^{in}_{NH_3} = 50\ g\ m^{-3}$ (ammonia), $S^{in}_{NO_3} = 0$ (nitrate), $S^{in}_{O_2} = 0$ (oxygen), $M^{in} = 100\ g\ m^{-3}$ (metal). Incident light intensity: $I_0 = 0.008\ kmol\ m^{-2}\ d^{-1}$. Duration of the cycle: $\tau = 6\ h$. Time of light exposure: $t_{light} = 50\%\ \tau$ (grey portions indicate the dark phases, white portions indicate the light phases).

Once the photogranules have reached a steady-state dimension and microbial stratification, the trend of the substrates and metal concentrations are repeated identically in each cycle. Fig. 6.5 shows the evolution of the substrates and metal concentrations over time in the reactor in the period between 199 and 200 days. Note that each cycle identically repeats four times in a single day, and, for this reason, it is representative of the operating conditions of the system, while the substrates and metal concentrations at the end of each cycle are representative of the effluent composition. Solid lines repre-

sent the trends of $IC$ (blue), $DOC$ (red), $NO_3$ (yellow), $NH_3$ (cyan), $O_2$ (magenta), $M$ (black) concentrations during the cycles. Each cycle is constituted by three hours of dark phase (gray parts of the graphs) and three hours of light phase (white parts of the graphs). While the circle and cross markers represent the concentrations of substrates and metal in the effluent and influent, respectively. At the end of each cycle (at $199.25$, $199.50$, $199.75$, and $200$ days) there is a discontinuity between the inlet and outlet concentration values, due to the procedure of emptying and refilling in the reactor. Due to the absence of light, in the first part of each cycle phototrophs and heterotrophs compete for $O_2$ (produced in the previous cycle), $DOC$ and $NH_3$ producing $IC$. Contextually, a small amount of nitrifiers contributes to the conversion of $O_2$, $IC$ and $NH_3$ into $NO_3$. When oxygen is completely consumed, anoxic heterotrophs grow consuming $DOC$ and $NO_3$. When also the concentration of nitrate reaches zero, the trend of substrate concentrations does not show high variations until the end of the dark period. In light conditions, phototrophs carry out photosynthesis, consuming $NH_3$ and $IC$, and producing large amount of $O_2$ necessary for heterotrophs and nitrifiers. Nevertheless, heterotrophic bacteria are more competitive in the use of $O_2$ in presence of $DOC$. As a result, the $DOC$ concentration reduces and $IC$ concentration increases. When the organic carbon ends, oxygen produced by phototrophs is used by nitrifying bacteria. For this reason, $NH_3$ and $IC$ concentrations decreases, and $NO_3$ concentration increases. When also $NH_3$ is completely consumed, phototrophs grow on $NO_3$. At the end of the cycle, $NH_3$, $DOC$ have been completely removed, and a very low concentrations of $NO_3$ (less than $5\ g\ m^{-3}$) and a concentration of about $30\ g\ m^{-3}$ of $O_2$ are observed. Indeed, the biomass of nitrifying bacteria within the granule and their growth rate are very low, therefore the production of $NO_3$ is limited. Regarding the metal adsorption, as already observed in Fig. 6.1 (top) at the steady-state the granule is mainly composed by phototrophs, $EPS$ and inert material which are the major responsible for the adsorption process. Thus, during the day/night cycle the metal is completely adsorbed on granule matrix.

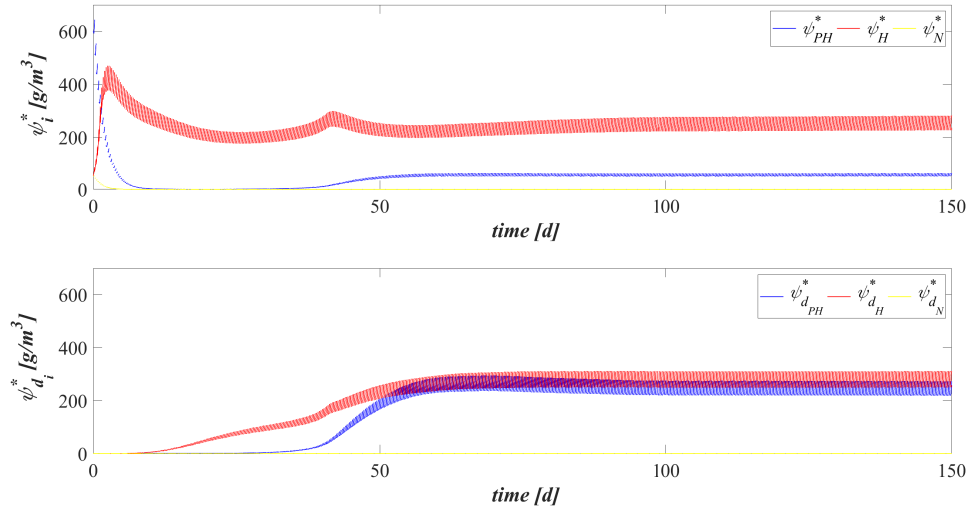


Figure 6.6: $SET1$ - Evolution of planktonic and detached biomasses concentrations within the reactor over time. Wastewater influent composition: $S^{in}_{IC} = 180\ g\ m^{-3}$ (inorganic carbon), $S^{in}_{DOC} = 500\ g\ m^{-3}$ (organic carbon), $S^{in}_{NH_3} = 50\ g\ m^{-3}$ (ammonia), $S^{in}_{NO_3} = 0$ (nitrate), $S^{in}_{O_2} = 0$ (oxygen), $M^{in} = 100\ g\ m^{-3}$ (metal). Incident light intensity: $I_0 = 0.008\ kmol\ m^{-2}\ d^{-1}$. Duration of the cycle: $\tau = 6\ h$. Time of light exposure: $t_{light} = 50\%\ \tau$.

The concentration of planktonic and detached biomasses within the reactor over time is shown in Fig. 6.6. As for soluble substrates and metal (Fig. 6.4), the observation period includes the process start-up until the achievement of the steady-state representative of the working configuration of the reactor. Also in this case, such concentrations have a discontinuous trend, due to cyclic behaviour of the SBR. Several factors can affect the suspended biomasses evolution over time. Attachment phenomena contribute to decrease the concentrations of planktonic species, while detachment phenomena promote the growth of detached biomasses. Both types of biomasses grow on soluble substrates and decay. Moreover, their concentration reduces during the emptying phase due to their non perfect settling properties. Lastly, detached biomasses reconvert into the planktonic cells after $48\ h$ from the detachment. In the initial stage of the process, granules have still small dimension and there is an elevate availability of nutrients. As consequence, the substrates dynamics within the reactor are governed by planktonic biomass. Heterotrophic bacteria have higher growth rate than other mi-

crobial species, and their concentration rapidly increases. When the photogranules dimension increases, biological processes are governed by sessile species. Since then, the amount of substrates available for suspended biomass reduces and the concentration of heterotrophs in planktonic form decreases over time. Other species have low growth rates, and their concentrations decrease over time from the beginning of the process, due to the wash-out and attachment process. After $20$ days, photogranules are already formed and the detachment process becomes relevant. This results in the increment of the concentration of heterotrophic detached biomass. Indeed, as shown in Fig. 6.2 the granule is initially composed by large amount of heterotrophs. After $40$ days, sessile phototrophs grow within the granule and, consequently, the concentration of phototrophic detached biomass increases due to the detachment process. The conversion of heterotrophic and phototrophic detached biomasses into planktonic form causes a further increment of planktonic species. Subsequently, due to the shortage of $DOC$ (Fig. 6.4) a slight reduction of planktonic species concentration within the bulk liquid can be observed again. Overall, after $60$ days all suspended species within the reactor achieve a steady state value.

### 6.4.2 SET2 - Effects of metal concentration on OPGs formation and adsorption processes

Metals in wastewater may increase the sessile production of $EPS$, and, at the same time, may be the cause of stress conditions responsible for the death of microbial cells. More studies are necessary to identify a concentration range that allows microorganisms to grow and secrete $EPS$ maximizing the removal efficiency of metals from wastewater. In this numerical study $SET2$, the efficiency of metal adsorption on the matrix of biofilm granules and the inhibiting effect on OPGs formation are investigated by considering different concentrations of metal. For this purpose, eleven simulations ($S2$ - $S12$) have been carried out by setting the concentration of metal in the influent $M^{in}$

equal to 0, 20, 40, 60, 80, 100, 120, 140, 160, 180, 200 $g\ m^{-3}$. The concentration of soluble substrates in the influent wastewater $S_j^{in}$ and initial concentration of planktonic biomasses within the reactor $\psi_{i,0}^*$ set for this numerical study are the same as in $SET1$. Numerical results are summarized in Figs. 6.7-6.12.

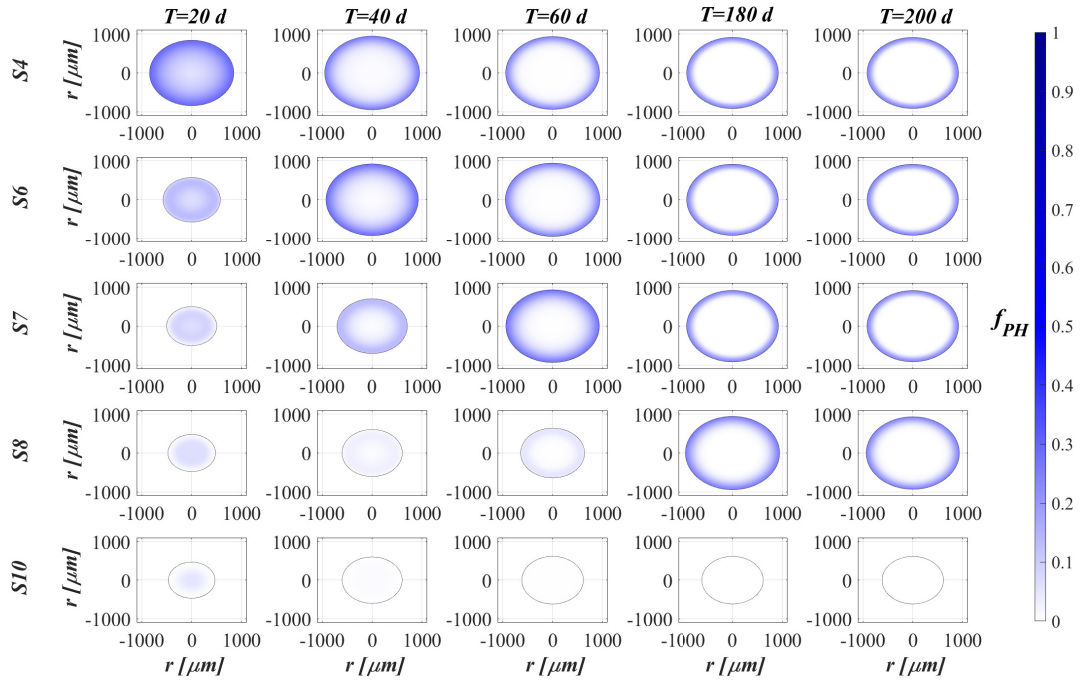


Figure 6.7: $SET2$ - Phototrophs distribution within the granule (diametrical section) at $T = 20\ d, T = 40\ d, T = 60\ d, T = 180\ d, T = 200\ d$ for different metal concentrations in the influent $M^{in}$. Wastewater influent composition: $S_{IC}^{in} = 180\ g\ m^{-3}$ (inorganic carbon), $S_{DOC}^{in} = 500\ g\ m^{-3}$ (organic carbon), $S_{NH_3}^{in} = 50\ g\ m^{-3}$ (ammonia), $S_{NO_3}^{in} = 0$ (nitrate), $S_{O_2}^{in} = 0$ (oxygen). $S4 : M^{in} = 40\ g\ m^{-3}$, $S6 : M^{in} = 80\ g\ m^{-3}$, $S7 : M^{in} = 100\ g\ m^{-3}$, $S8 : M^{in} = 120\ g\ m^{-3}$, $S10 : M^{in} = 160\ g\ m^{-3}$. Incident light intensity: $I_0 = 0.008\ kmol\ m^{-2}\ d^{-1}$. Duration of the cycle: $\tau = 6\ h$. Time of light exposure: $t_{light} = 50\%\ \tau$.

The concentration of metal in the influent affects the adsorption process as well as the microbial species stratification of OPGs. The distribution of the phototrophic sessile biomass at different times is reported in Fig. 6.7 for the following simulations: $S4$ ($M^{in} = 40\ g\ m^{-3}$), $S6$ ($M^{in} = 80\ g\ m^{-3}$), $S7$ ($M^{in} = 100\ g\ m^{-3}$), $S8$ ($M^{in} = 120\ g\ m^{-3}$), $S10$ ($M^{in} = 160\ g\ m^{-3}$). When the metal concentration present in the bioreactor is very low ($S4$), phototrophs are less inhibited and grow faster within the

granule. Conversely, a higher concentration of free metal results in a higher inhibition effect and leads to a slower growth of phototrophs. It means that for wastewater richer in metal the growth of the phototrophic species and the adsorption process occur in a longer time. Thus, the maximum fraction of phototrophs is observed later going from $S4$ to $S8$. However, after long times the phototrophs distribution is no longer affected by $M^{in}$ and all simulations achieve the same steady-state configuration after 200 days, except for $M^{in} = 160\ g\ m^{-3}$. Indeed, in this case ($S10$) the metal concentration is too high, and the biomasses growth and the granule formation are strongly inhibited by the presence of free metal. As a result, the photogranule does not completely develop and the absence of phototrophs is observed throughout the granule at 200 days.

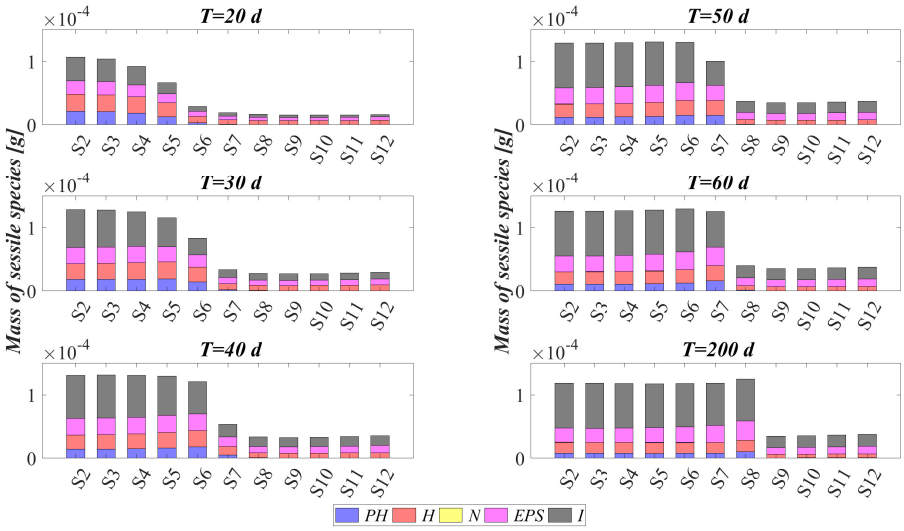


Figure 6.8: $SET2$ - Mass of microbial species within the granule at $T = 20\ d$, $T = 30\ d$, $T = 40\ d$, $T = 50\ d$, $T = 60\ d$, $T = 200\ d$ for different metal concentrations in the influent $M^{in}$. Wastewater influent composition: $S^{in}_{IC} = 180\ g\ m^{-3}$ (inorganic carbon), $S^{in}_{DOC} = 500\ g\ m^{-3}$ (organic carbon), $S^{in}_{NH_3} = 50\ g\ m^{-3}$ (ammonia), $S^{in}_{NO_3} = 0$ (nitrate), $S^{in}_{O_2} = 0$ (oxygen). $S2 : M^{in} = 0$, $S3 : M^{in} = 20\ g\ m^{-3}$, $S4 : M^{in} = 40\ g\ m^{-3}$, $S5 : M^{in} = 60\ g\ m^{-3}$, $S6 : M^{in} = 80\ g\ m^{-3}$, $S7 : M^{in} = 100\ g\ m^{-3}$, $S8 : M^{in} = 120\ g\ m^{-3}$, $S9 : M^{in} = 140\ g\ m^{-3}$, $S10 : M^{in} = 160\ g\ m^{-3}$, $S11 : M^{in} = 180\ g\ m^{-3}$, $S12 : M^{in} = 200\ g\ m^{-3}$. Incident light intensity: $I_0 = 0.008\ kmol\ m^{-2}\ d^{-1}$. Duration of the cycle: $\tau = 6\ h$. Time of light exposure: $t_{light} = 50\%\ \tau$.

This is visible also in Fig. 6.8, where the mass of sessile microbial species within the granule is shown at different times. Relevant differences concern the initial phase of the

process when the total sessile mass is higher for low metal concentrations. However, after long times (when the adsorption process is completed) the sessile mass of the individual microbial species within the granule is no longer affected by the presence of metal for $M^{in}$ lower than $140\ g\ m^{-3}$.

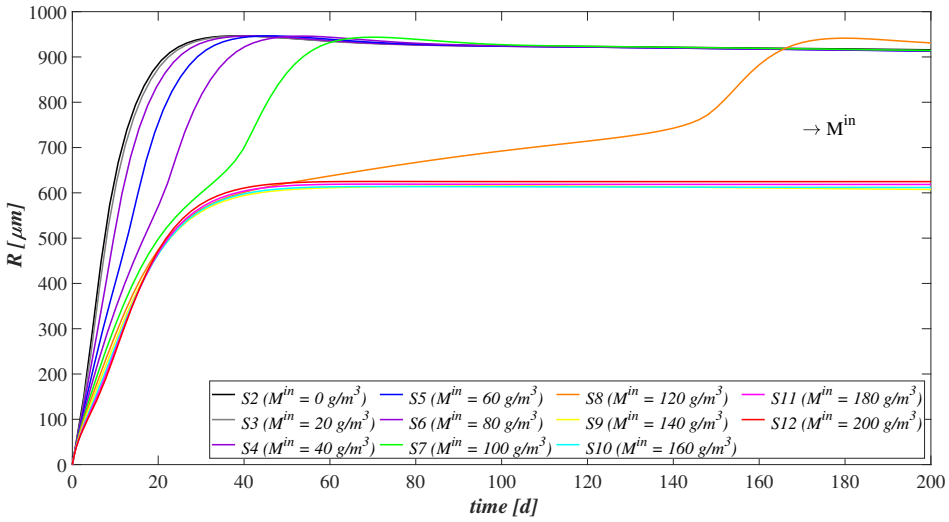


Figure 6.9: $SET2$ - Biofilm radius evolution over time for different metal concentrations in the influent $M^{in}$. Wastewater influent composition: $S^{in}_{IC} = 180\ g\ m^{-3}$ (inorganic carbon), $S^{in}_{DOC} = 500\ g\ m^{-3}$ (organic carbon), $S^{in}_{NH_3} = 50\ g\ m^{-3}$ (ammonia), $S^{in}_{NO_3} = 0$ (nitrate), $S^{in}_{O_2} = 0$ (oxygen). $S2 : M^{in} = 0$, $S3 : M^{in} = 20\ g\ m^{-3}$, $S4 : M^{in} = 40\ g\ m^{-3}$, $S5 : M^{in} = 60\ g\ m^{-3}$, $S6 : M^{in} = 80\ g\ m^{-3}$, $S7 : M^{in} = 100\ g\ m^{-3}$, $S8 : M^{in} = 120\ g\ m^{-3}$, $S9 : M^{in} = 140\ g\ m^{-3}$, $S10 : M^{in} = 160\ g\ m^{-3}$, $S11 : M^{in} = 180\ g\ m^{-3}$, $S12 : M^{in} = 200\ g\ m^{-3}$. Incident light intensity: $I_0 = 0.008\ kmol\ m^{-2}\ d^{-1}$. Duration of the cycle: $\tau = 6\ h$. Time of light exposure: $t_{light} = 50\%\ \tau$.

The evolution of the granule radius $R(t)$ over time is shown in Fig. 6.9. $M^{in}$ affects the granule evolution in the initial stage of the process. For low concentrations of metal, the granule radius increases earlier, small inhibiting effects are observed during the granulation process, and the adsorption process is completed faster. When $M^{in}$ is higher or equal to $100\ g\ m^{-3}$, the granule partially grows, and a further radius increment associated to phototrophs growth can be observed later. Note that passing from $S6$ to $S8$ the phototrophs growth and the subsequent further increment of the granule radius are increasingly slowed down by the presence of free metal, as observed in Fig. 6.7.

Instead, when $M^{in}$ is equal to 140, 160, 180 and 200 $g\ m^{-3}$ the phototrophic biomass growth is totally inhibited. Hence, the absence of phototrophs observed in Fig. 6.7 and Fig. 6.8 is confirmed by the incomplete development of the granule.

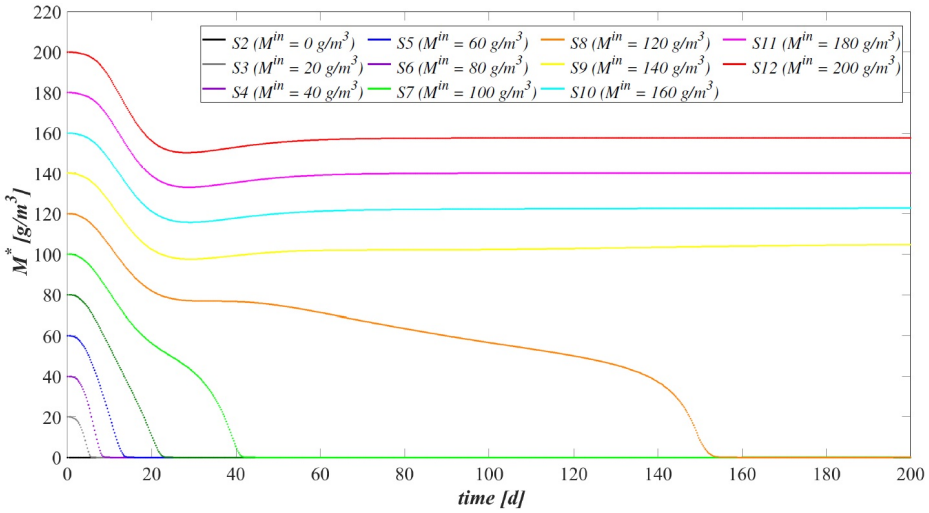


Figure 6.10: $SET2$ - Metal concentration evolution within the reactor for different metal concentrations in the influent $M^{in}$. Wastewater influent composition: $S^{in}_{IC} = 180\ g\ m^{-3}$ (inorganic carbon), $S^{in}_{DOC} = 500\ g\ m^{-3}$ (organic carbon), $S^{in}_{NH_3} = 50\ g\ m^{-3}$ (ammonia), $S^{in}_{NO_3} = 0$ (nitrate), $S^{in}_{O_2} = 0$ (oxygen). $S2 : M^{in} = 0$, $S3 : M^{in} = 20\ g\ m^{-3}$, $S4 : M^{in} = 40\ g\ m^{-3}$, $S5 : M^{in} = 60\ g\ m^{-3}$, $S6 : M^{in} = 80\ g\ m^{-3}$, $S7 : M^{in} = 100\ g\ m^{-3}$, $S8 : M^{in} = 120\ g\ m^{-3}$, $S9 : M^{in} = 140\ g\ m^{-3}$, $S10 : M^{in} = 160\ g\ m^{-3}$, $S11 : M^{in} = 180\ g\ m^{-3}$, $S12 : M^{in} = 200\ g\ m^{-3}$. Incident light intensity: $I_0 = 0.008\ kmol\ m^{-2}\ d^{-1}$. Duration of the cycle: $\tau = 6\ h$. Time of light exposure: $t_{light} = 50\%\ \tau$.

The metal and substrates concentrations in the effluent after each SBR cycle are displayed in Fig. 6.10 and 6.11. Each point represents the concentrations of metal and substrates in the effluent at the end of each cycle. Fig. 6.10 shows that for low metal concentration in the influent wastewater, the adsorption process is rapid and almost linear. When $M^{in}$ is equal to 100 and 120 $g\ m^{-3}$, the removal process slows down at $T = 20\ d$. The phototrophic biomass is characterized by lower growth rate than heterotrophs, and the inhibiting effect related to the presence of free metal further limits their growth process. Later, after 30 days, a considerable growth of phototrophs allows to successfully complete the adsorption process. Specifically, higher is the metal con-

centration in the influent and slower is the adsorption process. This is related to two aspects: the amount of free metal to adsorb is larger, and the phototrophs growth is slower due to the stronger metal inhibition effect. As shown in Fig. 6.8, for $M^{in}$ higher or equal to $140\ g\ m^{-3}$ the granule is not completely developed, and a small amount of $EPS$ and a not visible fraction of phototrophs are present in the granule. Consequently, the adsorption process is not yet completed after $200$ days.

The effluent concentration of soluble substrates is reported in Fig. 6.11. The initial phase of the process, in which $DOC$ and $NH_3$ are consumed and $IC$ is produced, is faster when the metal concentration in the influent is lower. Indeed, the inhibiting effect delays the granulation process and, as consequence, the substrates consumption/production. The subsequent phase is governed by phototrophs, which promote the metabolic activities of the heterotrophic bacteria producing $O_2$. When $M^{in}$ is higher, phototrophs growth is slower, and oxygen is less rapidly produced. As a result, time necessary to reach the complete degradation of $DOC$ and $NH_3$ and the maximum $IC$ reduction increases. Specifically, the same effluent composition both in terms of metal (Fig. 6.10) and substrates (Fig. 6.11) is achieved at the steady-state for $M^{in}$ lower than $140\ g\ m^{-3}$. Indeed, in the latter cases, phototrophs do not grow during the observed simulation period and the degradation of nutrients occurs only partially.

The steady-state configuration of the residual free binding sites within the biofilm granule is reported in Fig. 6.12. Obviously, when no metal is present in the influent wastewater ($S2$), no adsorption site is occupied during the granulation process and the sum of all volume fractions returns 1 at each location and time. The numerical results show that, for values of $M^{in}$ between $20$ and $120\ g\ m^{-3}$, the adsorption process requires a growing number of binding sites. Consequently, a decreasing residual amount of adsorption sites can be observed, although the granule achieves the same steady-state dimension. Lastly, in the cases in which the metal concentration is too high, the adsorption process is not completed (from $S9$ to $S12$), the granule does not completely develop due to the stronger inhibiting effect, and the binding sites are almost occupied.

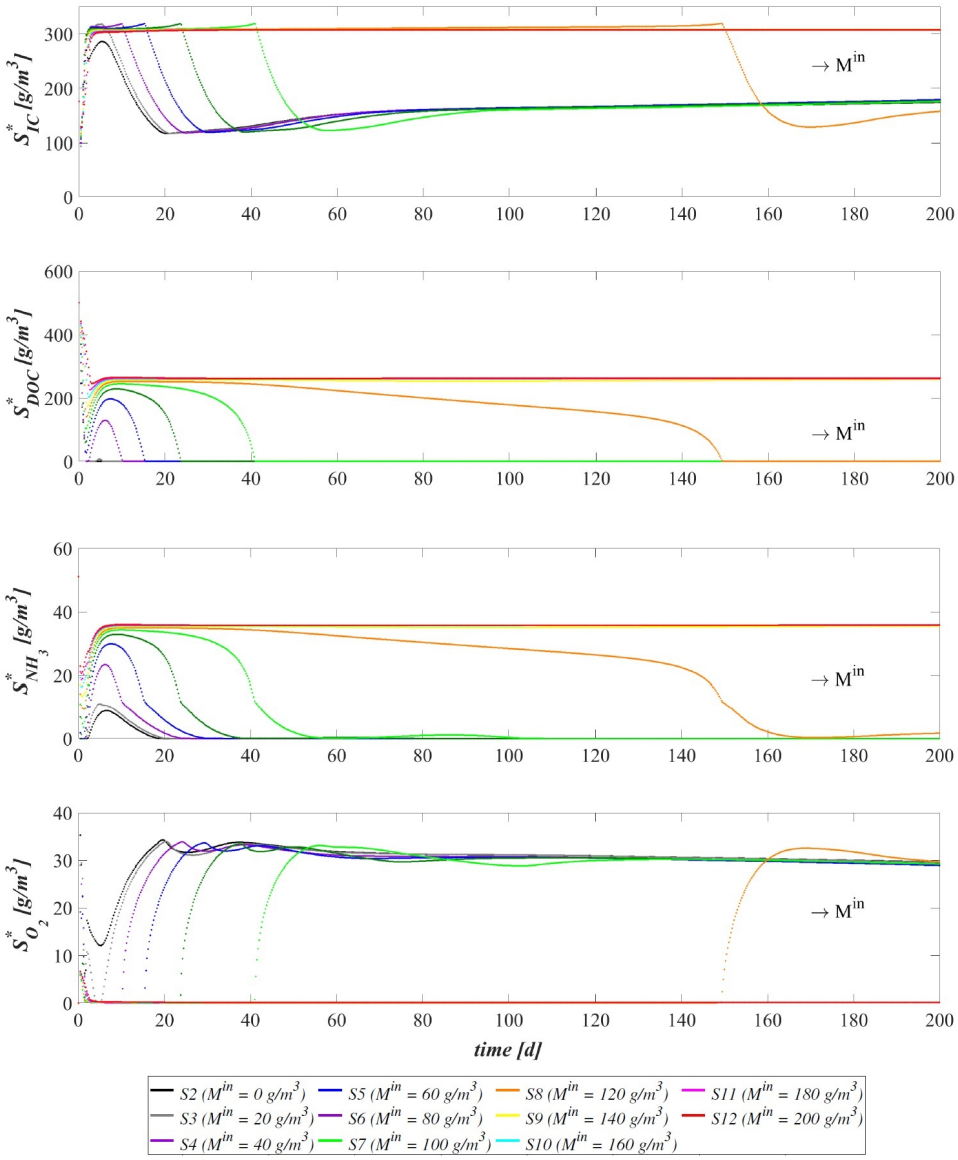


Figure 6.11: $SET2$ - Evolution of soluble substrates concentration within the reactor for different metal concentrations in the influent $M^{in}$. Wastewater influent composition: $S^{in}_{IC} = 180\ g\ m^{-3}$ (inorganic carbon), $S^{in}_{DOC} = 500\ g\ m^{-3}$ (organic carbon), $S^{in}_{NH_3} = 50\ g\ m^{-3}$ (ammonia), $S^{in}_{NO_3} = 0$ (nitrate), $S^{in}_{O_2} = 0\ g\ m^{-3}$ (oxygen). $S2 : M^{in} = 0$, $S3 : M^{in} = 20\ g\ m^{-3}$, $S4 : M^{in} = 40\ g\ m^{-3}$, $S5 : M^{in} = 60\ g\ m^{-3}$, $S6 : M^{in} = 80\ g\ m^{-3}$, $S7 : M^{in} = 100\ g\ m^{-3}$, $S8 : M^{in} = 120\ g\ m^{-3}$, $S9 : M^{in} = 140\ g\ m^{-3}$, $S10 : M^{in} = 160\ g\ m^{-3}$, $S11 : M^{in} = 180\ g\ m^{-3}$, $S12 : M^{in} = 200\ g\ m^{-3}$. Incident light intensity: $I_0 = 0.008\ kmol\ m^{-2}\ d^{-1}$. Duration of the cycle: $\tau = 6\ h$. Time of light exposure: $t_{light} = 50\%\ \tau$.

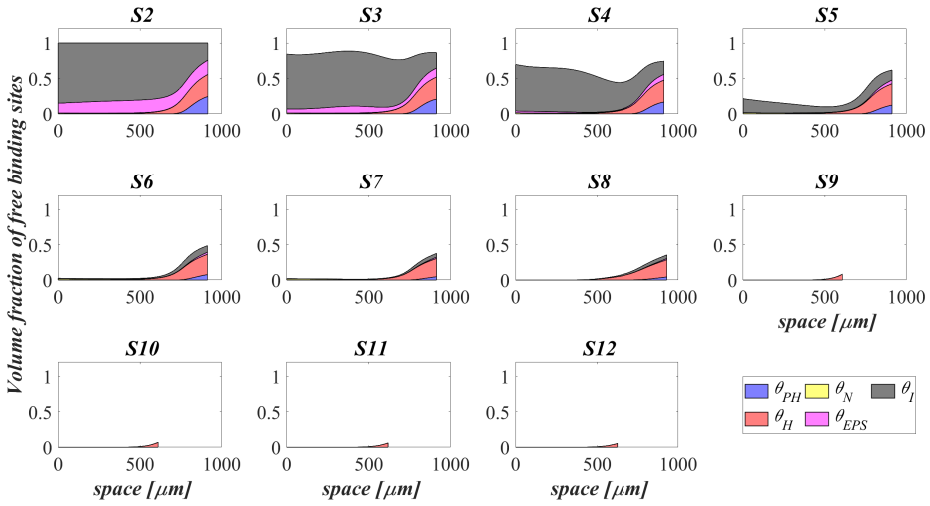


Figure 6.12: $SET2$ - Distribution of the residual free binding site across the radius of the granule for different metal concentrations in the influent $M^{in}$ at $T = 200\ d$. Wastewater influent composition: $S^{in}_{IC} = 180\ g\ m^{-3}$ (inorganic carbon), $S^{in}_{DOC} = 500\ g\ m^{-3}$ (organic carbon), $S^{in}_{NH_3} = 50\ g\ m^{-3}$ (ammonia), $S^{in}_{NO_3} = 0$ (nitrate), $S^{in}_{O_2} = 0$ (oxygen). $S2 : M^{in} = 0$, $S3 : M^{in} = 20\ g\ m^{-3}$, $S4 : M^{in} = 40\ g\ m^{-3}$, $S5 : M^{in} = 60\ g\ m^{-3}$, $S6 : M^{in} = 80\ g\ m^{-3}$, $S7 : M^{in} = 100\ g\ m^{-3}$, $S8 : M^{in} = 120\ g\ m^{-3}$, $S9 : M^{in} = 140\ g\ m^{-3}$, $S10 : M^{in} = 160\ g\ m^{-3}$, $S11 : M^{in} = 180\ g\ m^{-3}$, $S12 : M^{in} = 200\ g\ m^{-3}$. Incident light intensity: $I_0 = 0.008\ kmol\ m^{-2}\ d^{-1}$. Duration of the cycle: $\tau = 6\ h$. Time of light exposure: $t_{light} = 50\%\ \tau$.

### 6.4.3 SET3 - Effects of metal adsorption capabilities on OPGs formation and adsorption processes

Experimental works show that heat or acid pretreatments enhance the metal adsorption potential of algal-bacterial biomass [175]. Metal affinity to the biomass could be manipulated by pretreating the biomass with alkalies, acids, detergents, and heat, which may increase the amount of adsorbed metal and reduce the time necessary for the adsorption process [188]. Indeed, a physical/chemical pretreatment affects the permeability and surface charge of the biomass and makes the adsorption sites more accessible for metal biosorption [159]. In this context, a numerical study ($SET3$) is performed to investigate the pretreatment effect on the evolution of biofilm granules and metal removal. Five simulations ($S13$-$S17$) have been carried out using different values of binding sites densities $\rho_\theta$.

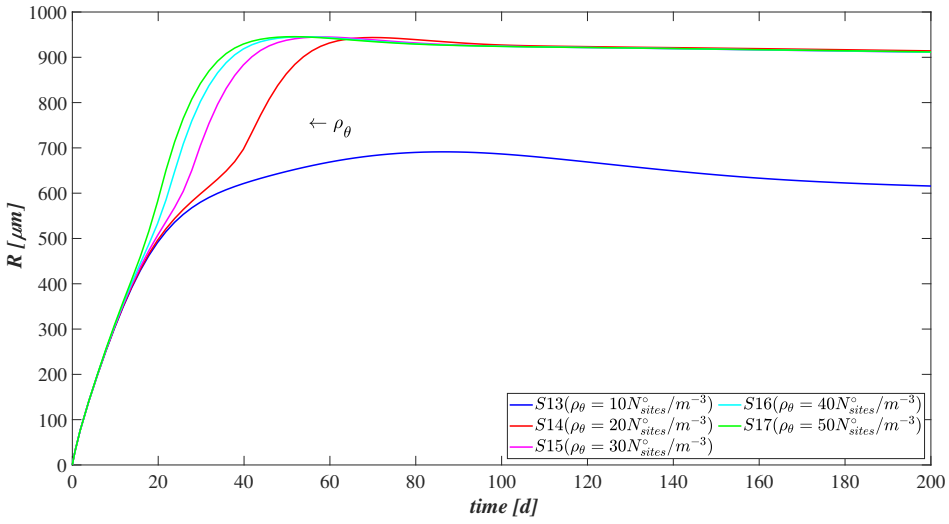


Figure 6.13: $SET3$ - Biofilm radius evolution over time for different densities of binding sites $\rho_\theta$. Wastewater influent composition: $S^{in}_{IC} = 180\ g\ m^{-3}$ (inorganic carbon), $S^{in}_{DOC} = 500\ g\ m^{-3}$ (organic carbon), $S^{in}_{NH_3} = 50\ g\ m^{-3}$ (ammonia), $S^{in}_{NO_3} = 0$ (nitrate), $S^{in}_{O_2} = 0$ (oxygen). $S13 : \rho_\theta = 10\ N^\circ_{sites}\ m^{-3}$, $S14 : \rho_\theta = 20\ N^\circ_{sites}\ m^{-3}$, $S15 : \rho_\theta = 30\ N^\circ_{sites}\ m^{-3}$, $S16 : \rho_\theta = 40\ N^\circ_{sites}\ m^{-3}$, $S17 : \rho_\theta = 50\ N^\circ_{sites}\ m^{-3}$. Incident light intensity: $I_0 = 0.008\ kmol\ m^{-2}\ d^{-1}$. Duration of the cycle: $\tau = 6\ h$. Time of light exposure: $t_{light} = 50\%\ \tau$.

The five values of $\rho_\theta$ used are: 10, 20, 30, 40, 50 $N^\circ_{sites}\ m^{-3}$. The concentration of soluble substrates in the influent wastewater $S^{in}_j$ and initial concentration of planktonic biomasses within the reactor $\psi^*_{i,0}$ set for this numerical study are the same as in $SET1$. Numerical results are summarized in Figs. 6.13-6.18.

The time evolution of the granule radius $R(t)$ is shown in Fig. 6.13. It is clear that different densities of binding sites $\rho_\theta$ affects the granule evolution in the second stage of the process, since the further radius increment around 20-50 days is associated to the phototrophs growth and phototrophs and $EPS$ have better adsorption capabilities. Indeed, when $\rho_\theta$ increases, the granulation process occurs rapidly and the granule reaches the steady-state size quickly. However, such steady-state size is not dependent on the binding sites density. Indeed, the profiles of $R(t)$ get closer over time and reach the same steady-state value, except for $\rho_\theta = 10\ N^\circ_{sites}\ m^{-3}$. It leads to conclude that with very low densities of binding sites the granulation and adsorption process do not

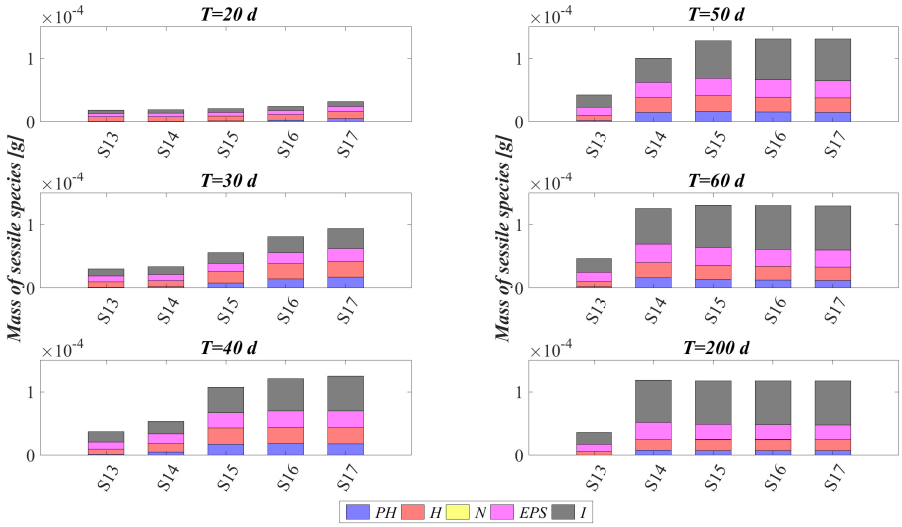


Figure 6.14: $SET3$ - Mass of microbial species within the granule at $T = 20\ d$, $T = 30\ d$, $T = 40\ d$, $T = 50\ d$, $T = 60\ d$, $T = 200\ d$ for different densities of binding sites $\rho_\theta$. Wastewater influent composition: $S_{IC}^{in} = 180\ g\ m^{-3}$ (inorganic carbon), $S_{DOC}^{in} = 500\ g\ m^{-3}$ (organic carbon), $S_{NH_3}^{in} = 50\ g\ m^{-3}$ (ammonia), $S_{NO_3}^{in} = 0$ (nitrate), $S_{O_2}^{in} = 0$ (oxygen). $S13 : \rho_\theta = 10\ N_{sites}^{\circ}\ m^{-3}$, $S14 : \rho_\theta = 20\ N_{sites}^{\circ}\ m^{-3}$, $S15 : \rho_\theta = 30\ N_{sites}^{\circ}\ m^{-3}$, $S16 : \rho_\theta = 40\ N_{sites}^{\circ}\ m^{-3}$, $S17 : \rho_\theta = 50\ N_{sites}^{\circ}\ m^{-3}$. Incident light intensity: $I_0 = 0.008\ kmol\ m^{-2}\ d^{-1}$. Duration of the cycle: $\tau = 6\ h$. Time of light exposure: $t_{light} = 50\%\ \tau$.

completely evolve.

Fig. 6.14 reports the sessile mass of the different microbial species within the granule. Again, relevant differences concern phototrophs growth. The phototrophs mass increases faster when the algal-bacterial consortium have higher binding sites densities. Metal removal and phototrophs growth positively influence each other. A faster metal adsorption enhances the phototrophic growth rate, and phototrophs contribute to accelerate the metal removal process thanks to their high adsorption properties.

This is visible also in Fig. 6.15, where the phototrophic sessile biomass within the granule is shown at different times. Again, relevant differences concern the time frame which goes from 20 to 50 days. By increasing $\rho_\theta$, phototrophic sessile biomass grows faster and the steady-state microbial distribution is reached earlier. However, the steady-state distribution is the same for all values of densities, except for the simulation $S13$, in which no phototrophic biomass is detected throughout the granule.

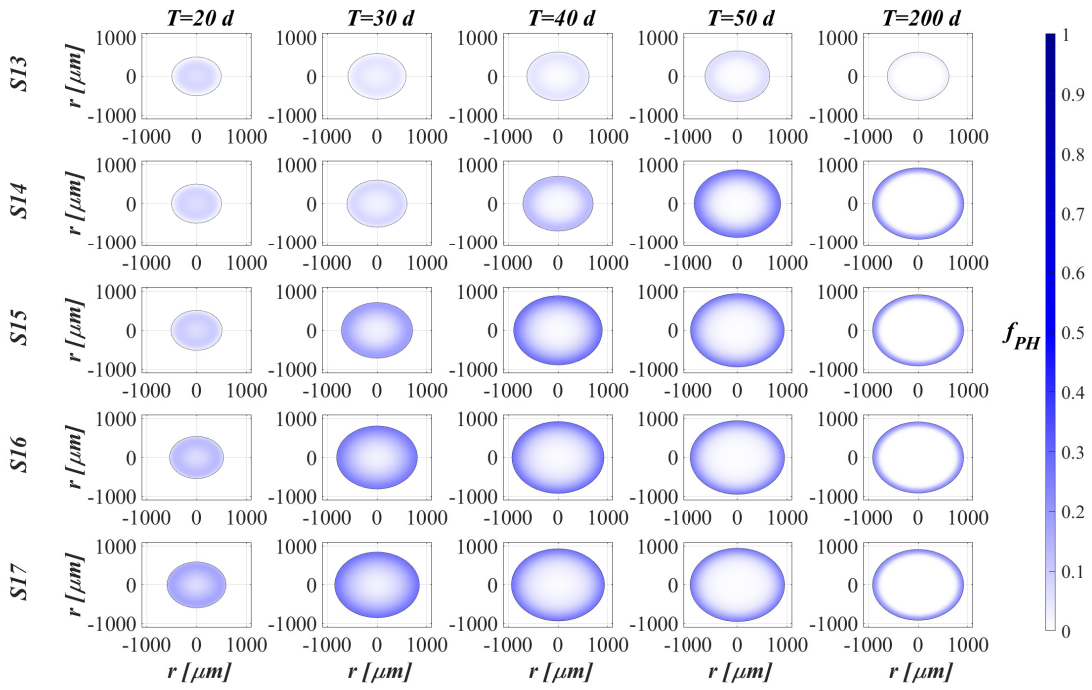


Figure 6.15: $SET3$ - Phototrophs distribution within the granule (diametrical section) at $T = 20\ d$, $T = 30\ d$, $T = 40\ d$, $T = 50\ d$, $T = 200\ d$ for different densities of binding sites $\rho_\theta$. Wastewater influent composition: $S_{IC}^{in} = 180\ g\ m^{-3}$ (inorganic carbon), $S_{DOC}^{in} = 500\ g\ m^{-3}$ (organic carbon), $S_{NH_3}^{in} = 50\ g\ m^{-3}$ (ammonia), $S_{NO_3}^{in} = 0$ (nitrate), $S_{O_2}^{in} = 0$ (oxygen). $S13 : \rho_\theta = 10\ N_{sites}^{\circ}\ m^{-3}$, $S14 : \rho_\theta = 20\ N_{sites}^{\circ}\ m^{-3}$, $S15 : \rho_\theta = 30\ N_{sites}^{\circ}\ m^{-3}$, $S16 : \rho_\theta = 40\ N_{sites}^{\circ}\ m^{-3}$, $S17 : \rho_\theta = 50\ N_{sites}^{\circ}\ m^{-3}$. Incident light intensity: $I_0 = 0.008\ kmol\ m^{-2}\ d^{-1}$. Duration of the cycle: $\tau = 6\ h$. Time of light exposure: $t_{light} = 50\%\ \tau$.

Fig. 6.16 presents the steady-state configuration of the residual free binding sites within the biofilm granule. Obviously, for $\rho_\theta$ equal to $10\ N_{sites}^{\circ}\ m^{-3}$ the adsorption process is not completed ($S13$), the granule does not completely develop due to the stronger inhibiting effect, and the binding sites are almost occupied. On the contrary, for higher values of binding sites density an increasing residual fraction of adsorption sites can be observed ($S14 - S17$).

Fig. 6.17 and 6.18 show the trend of soluble substrates and metal concentrations in the SBR effluent, respectively. each point represents the concentrations of substrates and metal in the effluent at the end of each cycle. As mentioned before, in the initial stage of the process the consumption and production of soluble substrates mainly de-

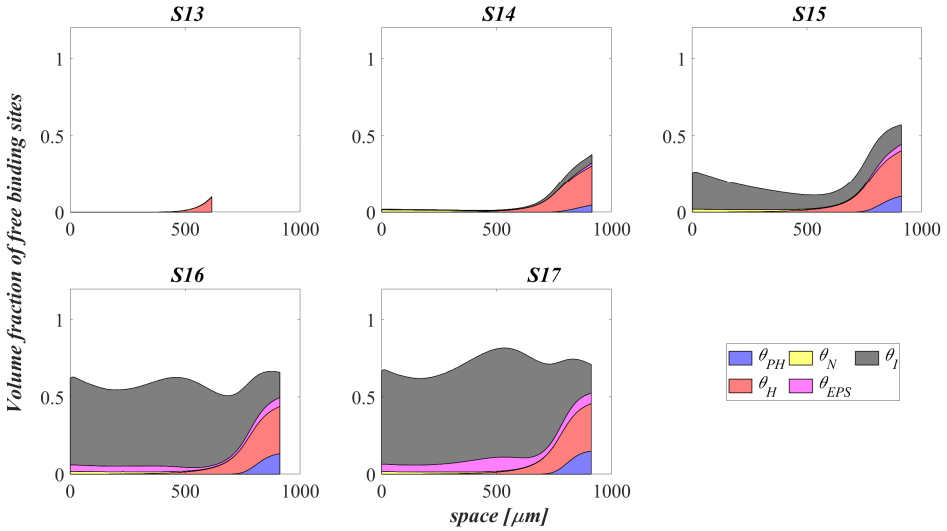


Figure 6.16: $SET3$ - Distribution of the residual free binding site across the radius of the granule for different densities of binding sites $\rho_\theta$ at $T = 200\ d$. Wastewater influent composition: $S^{in}_{IC} = 180\ g\ m^{-3}$ (inorganic carbon), $S^{in}_{DOC} = 500\ g\ m^{-3}$ (organic carbon), $S^{in}_{NH_3} = 50\ g\ m^{-3}$ (ammonia), $S^{in}_{NO_3} = 0$ (nitrate), $S^{in}_{O_2} = 0$ (oxygen). $S13 : \rho_\theta = 10\ N^{\circ}_{sites}\ m^{-3}$, $S14 : \rho_\theta = 20\ N^{\circ}_{sites}\ m^{-3}$, $S15 : \rho_\theta = 30\ N^{\circ}_{sites}\ m^{-3}$, $S16 : \rho_\theta = 40\ N^{\circ}_{sites}\ m^{-3}$, $S17 : \rho_\theta = 50\ N^{\circ}_{sites}\ m^{-3}$. Incident light intensity: $I_0 = 0.008\ kmol\ m^{-2}\ d^{-1}$. Duration of the cycle: $\tau = 6\ h$. Time of light exposure: $t_{light} = 50\%\ \tau$.

pend on the metabolic activity of heterotrophic biomass. Consequently, the trends of soluble substrates are not affected by the variation of $\rho_\theta$, since the role of heterotrophic bacteria in the adsorption process is marginal. For later times, phototrophic biomass starts to grow, and the trend of substrates (Fig. 6.17) and metal (Fig. 6.18) becomes more sensitive to $\rho_\theta$. For high values of $\rho_\theta$, the concentrations of soluble substrates and metal achieve the steady-state values earlier and the time required to completely adsorb the residual metal decreases. For $\rho_\theta = 10\ N^{\circ}_{sites}\ m^{-3}$, the metal adsorption process does not complete, because of the absence of phototrophs and the small amount of $EPS$ observed throughout the granule.

From the numerical results, it is clear that the density of binding sites $\rho_\theta$ influences the adsorption process rate of the free metal, and, therefore, the time necessary for the metal removal. Anyway, it can be concluded that the steady-state configuration in terms of biofilm dimension, microbial species stratification, and metal removal efficiency of

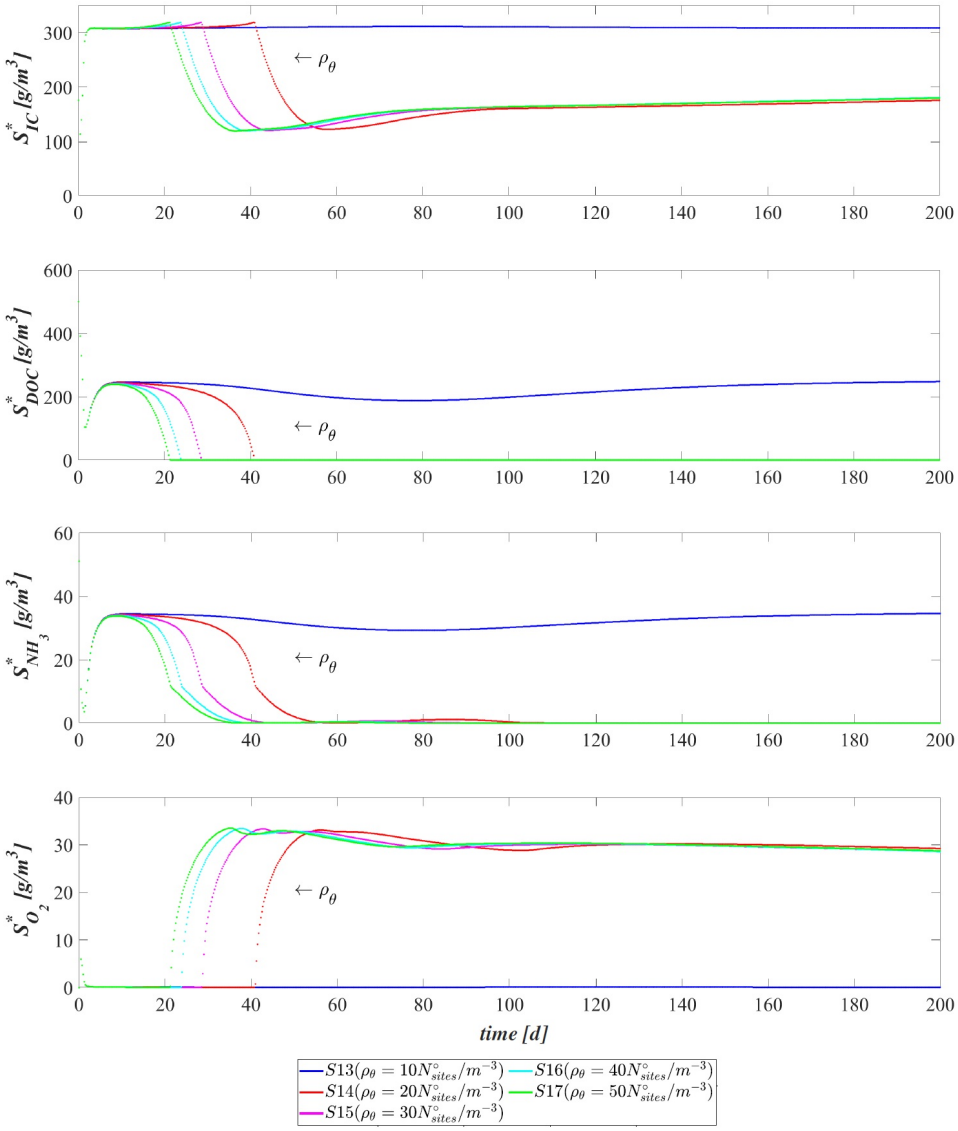


Figure 6.17: $SET3$ - Soluble substrates concentration evolution within the reactor for different densities of binding sites $\rho_\theta$. Wastewater influent composition: $S^{in}_{IC} = 180\ g\ m^{-3}$ (inorganic carbon), $S^{in}_{DOC} = 500\ g\ m^{-3}$ (organic carbon), $S^{in}_{NH_3} = 50\ g\ m^{-3}$ (ammonia), $S^{in}_{NO_3} = 0$ (nitrate), $S^{in}_{O_2} = 0$ (oxygen). $S13 : \rho_\theta = 10\ N^\circ_{sites}\ m^{-3}$, $S14 : \rho_\theta = 20\ N^\circ_{sites}\ m^{-3}$, $S15 : \rho_\theta = 30\ N^\circ_{sites}\ m^{-3}$, $S16 : \rho_\theta = 40\ N^\circ_{sites}\ m^{-3}$, $S17 : \rho_\theta = 50\ N^\circ_{sites}\ m^{-3}$. Incident light intensity: $I_0 = 0.008\ kmol\ m^{-2}\ d^{-1}$. Duration of the cycle: $\tau = 6\ h$. Time of light exposure: $t_{light} = 50\%\ \tau$.

the process are not affected by $\rho_\theta$ above a critical value.

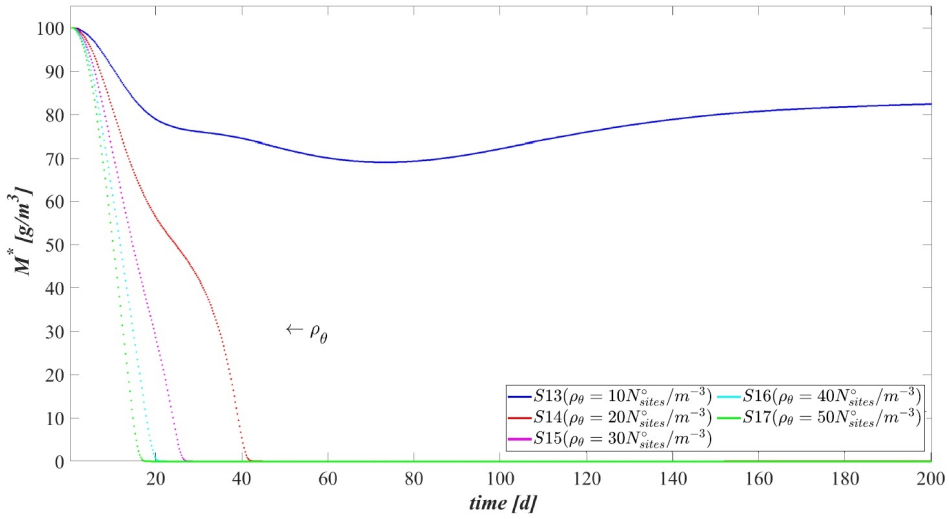


Figure 6.18: $SET3$ - Evolution of metal concentration within the reactor for different densities of binding sites $\rho_\theta$. Wastewater influent composition: $S^{in}_{IC} = 180\ g\ m^{-3}$ (inorganic carbon), $S^{in}_{DOC} = 500\ g\ m^{-3}$ (organic carbon), $S^{in}_{NH_3} = 50\ g\ m^{-3}$ (ammonia), $S^{in}_{NO_3} = 0$ (nitrate), $S^{in}_{O_2} = 0$ (oxygen). $S13 : \rho_\theta = 10\ N^\circ_{sites}\ m^{-3}$, $S14 : \rho_\theta = 20\ N^\circ_{sites}\ m^{-3}$, $S15 : \rho_\theta = 30\ N^\circ_{sites}\ m^{-3}$, $S16 : \rho_\theta = 40\ N^\circ_{sites}\ m^{-3}$, $S17 : \rho_\theta = 50\ N^\circ_{sites}\ m^{-3}$. Incident light intensity: $I_0 = 0.008\ kmol\ m^{-2}\ d^{-1}$. Duration of the cycle: $\tau = 6\ h$. Time of light exposure: $t_{light} = 50\%\ \tau$.

## 6.5 Discussion and conclusions

Biosorption is proving to be a promising alternative to conventional methods for the removal of metals from municipal and industrial effluents, as microorganisms and their derived products have high biosorption capabilities of inorganic compounds. Indeed, conventional physico/chemical methods for metals removal are expensive and inefficient for very low metals concentrations [159, 157, 161, 158]. Biosorption offers several advantages including cost effectiveness, high efficiency, minimization of chemical compounds utilization, and regeneration of biosorbents [159]. Nevertheless, there are practical limitations as living biomass is very sensitive to high metal concentrations [169]. An understanding of metal toxicity effects in biofilms is crucial to the successfully design bioreactors for the contextual removal of organic contaminants and metals. The mathematical model proposed in this Chapter allows to simulate the formation and evolution of oxygenic photogranules within a granular-based sequencing batch reac-

tor and describing the adsorption process of metals on the matrix of biofilm granules. The most interesting observations resulting from the numerical studies are summarized below:

- The adsorption process on oxygenic photogranules matrix shows high removal efficiency. These numerical result is in accordance with experimental works in which more than $99\%$ of metal present in aqueous solutions is absorbed using algal-bacterial granules, thanks to their excellent adsorption capacities [18, 19, 170].

- The results outline the key role of phototrophs and $EPS$ in the metal removal process, as phototrophs are good biosorbents and metals stimulate the production of $EPS$ in greater amount and with higher adsorption capabilities. These results reflect what has been observed in Yang et al. (2020) [19], where a comparison between conventional bacterial granules and algal-bacterial photogranules is performed, demonstrating that algal-bacterial granular biofilms show advantages in both biosorption capacity and granular stability.

- Furthermore, the model confirms that the performances of the adsorption process can be significantly affected by the metals concentration present in the wastewater. Highest removal efficiencies are achieved for low concentrations of metal in the influent [159]. Indeed, higher is the metal concentration in the influent and stronger will be the inhibiting effect on the microbial growth. Although $EPS$ content significantly increases in presence of metals [18], numerical results show that it is not sufficient in case of very high metal concentration. Moreover, as shown by Yang et al. (2015) [18], biomass growth is not or is little inhibited by certain concentrations of heavy metals, confirming that algal biomass could efficiently remove them through intracellular accumulation and extracellular immobilization.

- Lastly, the model results show how a higher density of binding sites, induced by heat or acids pretreatments, may enhance the adsorption process and reduce the time required for the complete degradation of substrates and removal of metals [188].

Most of the results shown are qualitatively in accordance with the experimental evidence reported in literature. Accordingly, this model is able to correctly simulate both the formation and maturation of oxygenic photogranules and removal process of toxic metals. From an engineering point of view, this allows to conclude that the model represents a useful tool in studying the removal processes of both organic and inorganic compounds in granular-based sequencing batch reactor systems.

The present work demonstrates the potential applicability of the algal-bacterial granules towards removal of more than one heavy metal. Nevertheless, their joint removal could be not as easy as the removal of a single contaminant. This could be caused by antagonistic effects between the different metals. Looking forward, research activities should be geared towards ways to minimize the antagonistic effects between contaminants.

# Chapter 7

# Conclusion and future perspectives

Mathematical models and in particular their application to systems for wastewater treatment have been recognized as useful tools to improve the understanding of the fundamental mechanisms regulating biological processes evolution, and to predict systems behaviour and performance under different operational conditions, without relying on build-up specific experimental activities. In this context, the present dissertation proposes novel mathematical models able to widely describe unclear and not well-understood physical and biochemical aspects for some wastewater treatment system.

An original mathematical model for heavy metals removal from electronic waste using dark fermentation combined with the leaching process is proposed in Chapter 2. The integration of the dark fermentation with metals leaching results in a complex biochemical process, mainly due to the interactions between the biological process and chemical reactions. This study is aimed at investigating the utilization of dark fermentation effluent as leaching solution, since it is rich in organic acids with valuable leaching properties. The model is able to describe both the dark fermentation and metal dissolution process, which can contextually or consecutively occur in a batch bioreactor. The mathematical model is calibrated based on experimental data of ad-hoc lab-scale tests: cumulative hydrogen production, glucose degradation, organic acids accumulation, and metals concentration trends. Moreover, further numerical simulations are performed to

analyze the interactions between the fermentation and the leaching processes, and to investigate how metals inhibition affects the biological process and how metals concentration affects the efficiency of the leaching process.

The second part of the thesis deals with the mathematical modelling of granular biofilms. In Chapter 3, a multiscale mathematical model is derived in order to simulate the evolution process of granular biofilms within a continuous reactor. The model predicts the granule formation from the initial granulation process until the achievement of the steady-state configuration. The multiscale approach allows to accurately predict both the formation and growth of biofilm granules and biological treatment process occurring in the system. Furthermore, the model is applied to an anaerobic granular system in order to test its qualitative behavior and to explore the main aspects of the *de novo* anaerobic granulation. Numerical studies are performed to investigate the effects that key factors have on the anaerobic process, such as wastewater influent composition, granulation properties of planktonic species, biomass density, hydrodynamic conditions, and the number of granules. Numerical results show that the attachment process plays an important role on the anaerobic granules formation and that the model is able to well-reproduce the microbial stratification of anaerobic granules observed in the literature.

Chapter 4 presents the spherical free boundary value problem that models the attachment process in the initial phase of multispecies granular biofilm formation in the framework of continuum mechanics. Specifically, the initial attachment phase which leads to the granule formation is modelled by assuming that all biomass initially present in the bioreactor is in planktonic form. Granule formation and expansion is governed by microbial growth, attachment, invasion and detachment processes. Finally, a theorem on the existence and uniqueness of the solutions is presented in the class of continuous functions. Moreover, it is proved that equations describing the growth and transport of sessile biomass, which have an apparent singularity, hold for $r = 0$ (granule center).

In Chapter 5, the multiscale mathematical model introduced in Chapter 3 is applied

to the partial nitritation/anammox process occurring in a continuous granular-based reactor. The aim of this study is to describe and investigate the initial formation of anammox biofilm granules and the main factors influencing the start-up of anammox-based systems. In particular, original numerical studies are performed to examine how the size and the addition time of the anammox inoculum can affect and optimize the start-up process. Numerical results show the partial nitritation and anammox processes evolution over time and granules microbial composition, demonstrating the fundamental role that invasion process of anammox bacteria has on the biological process evolution and system performances.

Finally, in Chapter 6 a modified version of the multiscale model derived in Chapter 3 is applied to study the biosorption process of heavy metals on the matrix of oxygenic photogranules (OPGs) within a granular-based sequencing batch reactor. From the numerical results presented, it can be concluded that the application of algal-bacterial biofilms for detoxification of wastewater rich in organic and inorganic compounds represents an interesting and promising technology. Effects of metals concentrations and adsorption properties of the biofilm components are investigated through a numerical approach. Model results show that microbial interactions between phototrophs (cyanobacteria and microalgae) and heterotrophs and $EPS$ secretion appear to be fundamental factors in the metal adsorption process. Consequently, after being calibrated and validated, the proposed model can be a useful tool for start-up and management activities of future full-scale OPGs-based plants for the contextual removal of nutrients and metals contained in industrial wastewater.

Most of the numerical results shown are qualitatively in accordance with the experimental evidence available in literature and demonstrate the potential of the mathematical models proposed in the present dissertation. However, the calibration of the models to collected data is inevitable and required to effectively use biofilm models in engineering systems design. Further works will be dedicated to activities of sensitivity analysis, calibration and validation of these models.

Detachment, which consists of the release of biofilm clusters, should be investigated in more detail. Detached biomass has different characteristics from both sessile and planktonic biomasses, and needs several hours to return to the planktonic state and take part again in attachment or invasion processes. Nevertheless, experimental observations show that the detached biomasses do not differ from planktonic cells in terms of adhesion properties. In this context, it would be interesting to develop a mathematical model able to account for the formation of further new granules, starting from detached clusters, in order to describe the entire life cycle of biofilm granules [120].

Furthermore, all models proposed in this work consider a constant biofilm density equal for all the biofilm components at each time and location. Starting from this, a future modelling work could include the biofilm porosity and density, as further model variables, with the aim of modelling the pores formation and their evolution over time. Indeed, experimental evidence shows that biofilm density increases with the growth of the biofilm dimension, leading to more compact and denser biofilms, and that higher density limits substrates diffusion within biofilm, since their diffusivity is strictly dependent on the biofilms density [12].

# Bibliography

[1] D. J. Batstone, J. Keller, I. Angelidaki, S. Kalyuzhnyi, S. Pavlostathis, A. Rozzi, W. Sanders, H. Siegrist, V. Vavilin, The iwa anaerobic digestion model no 1 (adm1), Water Science and technology 45 (10) (2002) 65–73.

[2] J. Azeredo, N. F. Azevedo, R. Briandet, N. Cerca, T. Coenye, A. R. Costa, M. Desvaux, G. Di Bonaventura, M. Hébraud, Z. Jaglic, et al., Critical review on biofilm methods, Critical reviews in microbiology 43 (3) (2017) 313–351.

[3] O. Wanner, Mathematical modeling of biofilms, IWA Pub., 2006.

[4] H.-C. Flemming, J. Wingender, U. Szewzyk, P. Steinberg, S. A. Rice, S. Kjelleberg, Biofilms: an emergent form of bacterial life, Nature Reviews Microbiology 14 (9) (2016) 563–575.

[5] H.-C. Flemming, J. Wingender, The biofilm matrix, Nature reviews microbiology 8 (9) (2010) 623–633.

[6] J. Palmer, S. Flint, J. Brooks, Bacterial cell attachment, the beginning of a biofilm, Journal of Industrial Microbiology and Biotechnology 34 (9) (2007) 577–588.

[7] M. G. Trulear, W. G. Characklis, Dynamics of biofilm processes, Journal (Water Pollution Control Federation) (1982) 1288–1301.

[8] B. D'Acunto, L. Frunzo, I. Klapper, M. Mattei, P. Stoodley, Mathematical modeling of dispersal phenomenon in biofilms, Mathematical biosciences 307 (2019) 70–87.

[9] I. W. Sutherland, The biofilm matrix–an immobilized but dynamic microbial environment, Trends in microbiology 9 (5) (2001) 222–227.

[10] A. C. Trego, E. Galvin, C. Sweeney, S. Dunning, C. Murphy, S. Mills, C. Nzeteu, C. Quince, S. Connelly, U. Z. Ijaz, et al., Growth and break-up of methanogenic granules suggests mechanisms for biofilm and community development, Frontiers in microbiology 11 (2020) 1126.

[11] A. C. Trego, S. Mills, G. Collins, Granular biofilms: function, application, and new trends as model microbial communities, Critical Reviews in Environmental Science and Technology 51 (15) (2021) 1702–1725.

[12] Y. Liu, J.-H. Tay, The essential role of hydrodynamic shear force in the formation of biofilm and granular sludge, Water research 36 (7) (2002) 1653–1665.

[13] Y. Liu, J.-H. Tay, State of the art of biogranulation technology for wastewater treatment, Biotechnology advances 22 (7) (2004) 533–563.

[14] J. E. Baeten, D. J. Batstone, O. J. Schraa, M. C. van Loosdrecht, E. I. Volcke, Modelling anaerobic, aerobic and partial nitritation-anammox granular sludge reactors-a review, Water research 149 (2019) 322–341.

[15] A. A. Ansari, A. S. Abouhend, C. Park, Effects of seeding density on photogranulation and the start-up of the oxygenic photogranule process for aeration-free wastewater treatment, Algal Research 40 (2019) 101495.

[16] A. S. Abouhend, K. Milferstedt, J. Hamelin, A. A. Ansari, C. Butler, B. I. Carbajal-González, C. Park, Growth progression of oxygenic photogranules and

its impact on bioactivity for aeration-free wastewater treatment, Environmental science & technology 54 (1) (2019) 486–496.

[17] T. O. Ajiboye, O. A. Oyewo, D. C. Onwudiwe, Simultaneous removal of organics and heavy metals from industrial wastewater: A review, Chemosphere 262 (2021) 128379.

[18] J. Yang, J. Cao, G. Xing, H. Yuan, Lipid production combined with biosorption and bioaccumulation of cadmium, copper, manganese and zinc by oleaginous microalgae chlorella minutissima utex2341, Bioresource technology 175 (2015) 537–544.

[19] X. Yang, Z. Zhao, Y. Yu, K. Shimizu, Z. Zhang, Z. Lei, D.-J. Lee, Enhanced biosorption of cr (vi) from synthetic wastewater using algal-bacterial aerobic granular sludge: Batch experiments, kinetics and mechanisms, Separation and Purification Technology 251 (2020) 117323.

[20] S. Naveed, C. Li, X. Lu, S. Chen, B. Yin, C. Zhang, Y. Ge, Microalgal extracellular polymeric substances and their interactions with metal (loid) s: A review, Critical Reviews in Environmental Science and Technology 49 (19) (2019) 1769–1802.

[21] R. Singh, D. Paul, R. K. Jain, Biofilms: implications in bioremediation, Trends in microbiology 14 (9) (2006) 389–397.

[22] O. Wanner, W. Gujer, A multispecies biofilm model, Biotechnology and bioengineering 28 (3) (1986) 314–328.

[23] B. D'Acunto, L. Frunzo, I. Klapper, M. Mattei, Modeling multispecies biofilms including new bacterial species invasion, Mathematical biosciences 259 (2015) 20–26.

[24] B. D'Acunto, L. Frunzo, V. Luongo, M. Mattei, Free boundary approach for the attachment in the initial phase of multispecies biofilm growth, Zeitschrift für angewandte Mathematik und Physik 70 (3) (2019) 1–16.

[25] M. De Kreuk, C. Picioreanu, M. Hosseini, J. Xavier, M. Van Loosdrecht, Kinetic model of a granular sludge sbr: influences on nutrient removal, Biotechnology and bioengineering 97 (4) (2007) 801–815.

[26] D. J. Batstone, J. Keller, L. Blackall, The influence of substrate kinetics on the microbial community structure in granular anaerobic biomass, Water Research 38 (6) (2004) 1390–1404.

[27] H. Feldman, X. Flores-Alsina, P. Ramin, K. Kjellberg, U. Jeppsson, D. J. Batstone, K. V. Gernaey, Modelling an industrial anaerobic granular reactor using a multi-scale approach, Water research 126 (2017) 488–500.

[28] M. Odriozola, I. López, L. Borzacconi, Modeling granule development and reactor performance on anaerobic granular sludge reactors, Journal of environmental chemical engineering 4 (2) (2016) 1615–1628.

[29] A. K. Vangsgaard, M. Mauricio-Iglesias, K. V. Gernaey, B. F. Smets, G. Sin, Sensitivity analysis of autotrophic n removal by a granule based bioreactor: influence of mass transfer versus microbial kinetics, Bioresource technology 123 (2012) 230–241.

[30] E. Volcke, C. Picioreanu, B. De Baets, M. Van Loosdrecht, Effect of granule size on autotrophic nitrogen removal in a granular sludge reactor, Environmental technology 31 (11) (2010) 1271–1280.

[31] E. Volcke, C. Picioreanu, B. De Baets, M. Van Loosdrecht, The granule size distribution in an anammox-based granular sludge reactor affects the conversion-

implications for modeling, Biotechnology and bioengineering 109 (7) (2012) 1629–1636.

[32] B. D'Acunto, L. Frunzo, Qualitative analysis and simulations of a free boundary problem for multispecies biofilm models, Mathematical and computer modelling 53 (9-10) (2011) 1596–1606.

[33] F. O. Ongondo, I. D. Williams, T. J. Cherrett, How are weee doing? a global review of the management of electrical and electronic wastes, Waste management 31 (4) (2011) 714–730.

[34] S. S. Rath, P. Nayak, P. S. Mukherjee, G. R. Chaudhury, B. Mishra, Treatment of electronic waste to recover metal values using thermal plasma coupled with acid leaching–a response surface modeling approach, Waste management 32 (3) (2012) 575–583.

[35] R. Golmohammadzadeh, F. Faraji, F. Rashchi, Recovery of lithium and cobalt from spent lithium ion batteries (libs) using organic acids as leaching reagents: A review, Resources, Conservation and Recycling 136 (2018) 418–435.

[36] N. Bahaloo-Horeh, S. M. Mousavi, M. Baniasadi, Use of adapted metal tolerant aspergillus niger to enhance bioleaching efficiency of valuable metals from spent lithium-ion mobile phone batteries, Journal of Cleaner Production 197 (2018) 1546–1557.

[37] M. Sethurajan, S. Gaydardzhiev, Bioprocessing of spent lithium ion batteries for critical metals recovery–a review, Resources, Conservation and Recycling 165 (2021) 105225.

[38] Y. Yao, M. Zhu, Z. Zhao, B. Tong, Y. Fan, Z. Hua, Hydrometallurgical processes for recycling spent lithium-ion batteries: a critical review, ACS Sustainable Chemistry & Engineering 6 (11) (2018) 13611–13627.

[39] M. N. Le, M. S. Lee, A review on hydrometallurgical processes for the recovery of valuable metals from spent catalysts and life cycle analysis perspective, Mineral Processing and Extractive Metallurgy Review (2020) 1–20.

[40] J. J. Roy, B. Cao, S. Madhavi, A review on the recycling of spent lithium-ion batteries (libs) by the bioleaching approach, Chemosphere (2021) 130944.

[41] L. Li, J. B. Dunn, X. X. Zhang, L. Gaines, R. J. Chen, F. Wu, K. Amine, Recovery of metals from spent lithium-ion batteries with organic acids as leaching reagents and environmental assessment, Journal of Power Sources 233 (2013) 180–189.

[42] A. H. Kaksonen, X. Deng, T. Bohu, L. Zea, H. N. Khaleque, Y. Gumulya, N. J. Boxall, C. Morris, K. Y. Cheng, Prospective directions for biohydrometallurgy, Hydrometallurgy 195 (2020) 105376.

[43] R. Golmohammadzadeh, F. Rashchi, E. Vahidi, Recovery of lithium and cobalt from spent lithium-ion batteries using organic acids: Process optimization and kinetic aspects, Waste Management 64 (2017) 244–254.

[44] L. Li, E. Fan, Y. Guan, X. Zhang, Q. Xue, L. Wei, F. Wu, R. Chen, Sustainable recovery of cathode materials from spent lithium-ion batteries using lactic acid leaching system, ACS Sustainable Chemistry & Engineering 5 (6) (2017) 5224–5233.

[45] J. Wang, Z. Wang, Z. Zhang, G. Zhang, Zinc removal from basic oxygen steelmaking filter cake by leaching with organic acids, Metallurgical and Materials Transactions B 50 (1) (2019) 480–490.

[46] C. K. Lee, K.-I. Rhee, Reductive leaching of cathodic active materials from lithium ion battery wastes, Hydrometallurgy 68 (1-3) (2003) 5–10.

[47] M. Joulié, R. Laucournet, E. Billy, Hydrometallurgical process for the recovery of high value metals from spent lithium nickel cobalt aluminum oxide based lithium-ion batteries, Journal of power sources 247 (2014) 551–555.

[48] P. Zhang, T. Yokoyama, O. Itabashi, Y. Wakui, T. M. Suzuki, K. Inoue, Hydrometallurgical process for recovery of metal values from spent nickel-metal hydride secondary batteries, Hydrometallurgy 50 (1) (1998) 61–75.

[49] C. E. Halim, J. A. Scott, H. Natawardaya, R. Amal, D. Beydoun, G. Low, Comparison between acetic acid and landfill leachates for the leaching of pb (ii), cd (ii), as (v), and cr (vi) from cementitious wastes, Environmental science & technology 38 (14) (2004) 3977–3983.

[50] A. Ghimire, L. Frunzo, F. Pirozzi, E. Trably, R. Escudie, P. N. Lens, G. Esposito, A review on dark fermentative biohydrogen production from organic biomass: process parameters and use of by-products, Applied Energy 144 (2015) 73–95.

[51] V. Luongo, A. Ghimire, L. Frunzo, M. Fabbricino, G. d'Antonio, F. Pirozzi, G. Esposito, Photofermentative production of hydrogen and poly-$\beta$-hydroxybutyrate from dark fermentation products, Bioresource technology 228 (2017) 171–175.

[52] N. Ren, W. Guo, B. Liu, G. Cao, J. Ding, Biological hydrogen production by dark fermentation: challenges and prospects towards scaled-up production, Current Opinion in Biotechnology 22 (3) (2011) 365–370.

[53] G. Cornelis, S. Poppe, T. Van Gerven, E. Van den Broeck, M. Ceulemans, C. Vandecasteele, Geochemical modelling of arsenic and selenium leaching in alkaline water treatment sludge from the production of non-ferrous metals, Journal of hazardous materials 159 (2-3) (2008) 271–279.

[54] G. Cornelis, T. Van Gerven, C. Vandecasteele, Antimony leaching from mswi bottom ash: modelling of the effect of ph and carbonation, Waste Management 32 (2) (2012) 278–286.

[55] C. E. Halim, S. A. Short, J. A. Scott, R. Amal, G. Low, Modelling the leaching of pb, cd, as, and cr from cementitious waste using phreeqc, Journal of Hazardous Materials 125 (1-3) (2005) 45–61.

[56] G. Costa, A. Polettini, R. Pomi, A. Stramazzo, Leaching modelling of slurry-phase carbonated steel slag, Journal of hazardous materials 302 (2016) 415–425.

[57] C. J. Engelsen, H. A. van der Sloot, G. Wibetoe, G. Petkovic, E. Stoltenberg-Hansson, W. Lund, Release of major elements from recycled concrete aggregates and geochemical modelling, Cement and Concrete Research 39 (5) (2009) 446–459.

[58] C. J. Engelsen, H. A. Van der Sloot, G. Wibetoe, H. Justnes, W. Lund, E. Stoltenberg-Hansson, Leaching characterisation and geochemical modelling of minor and trace elements released from recycled concrete aggregates, Cement and concrete research 40 (12) (2010) 1639–1649.

[59] H. Van der Sloot, D. Kosson, Use of characterisation leaching tests and associated modelling tools in assessing the hazardous nature of wastes, Journal of hazardous materials 207 (2012) 36–43.

[60] J. Wang, W. Wan, Factors influencing fermentative hydrogen production: a review, International journal of hydrogen energy 34 (2) (2009) 799–811.

[61] I. K. Kapdan, F. Kargi, Bio-hydrogen production from waste materials, Enzyme and microbial technology 38 (5) (2006) 569–582.

[62] C. Li, H. H. Fang, Fermentative hydrogen production from wastewater and solid wastes by mixed cultures, Critical reviews in environmental science and technology 37 (1) (2007) 1–39.

[63] A. Ghimire, L. Frunzob, E. Salzanoc, A. Panicod, G. Espositoa, P. N. Lense, F. Pirozzif, Biomass enrichment and scale-up implications for dark fermentation hydrogen production with mixed cultures, CHEMICAL ENGINEERING 43 (2015).

[64] F. R. Hawkes, I. Hussy, G. Kyazze, R. Dinsdale, D. L. Hawkes, Continuous dark fermentative hydrogen production by mesophilic microflora: principles and progress, International journal of hydrogen energy 32 (2) (2007) 172–184.

[65] V. Takahashi, A. B. Junior, D. Espinosa, J. Tenório, Enhancing cobalt recovery from li-ion batteries using grinding treatment prior to the leaching and solvent extraction process, Journal of Environmental Chemical Engineering 8 (3) (2020) 103801.

[66] B. Musariri, G. Akdogan, C. Dorfling, S. Bradshaw, Evaluating organic acids as alternative leaching reagents for metal recovery from lithium ion batteries, Minerals Engineering 137 (2019) 108–117.

[67] F. Russo, R. Veropalumbo, L. Pontoni, C. Oreto, S. A. Biancardo, N. Viscione, F. Pirozzi, M. Race, Sustainable asphalt mastics made up recycling waste as filler, Journal of Environmental Management 301 (2022) 113826.

[68] L. S. Martins, L. F. Guimarães, A. B. B. Junior, J. A. S. Tenório, D. C. R. Espinosa, Electric car battery: An overview on global demand, recycling and future approaches towards sustainability, Journal of Environmental Management 295 (2021) 113091.

[69] D. S. Patil, S. M. Chavan, J. U. K. Oubagaranadin, A review of technologies for manganese removal from wastewaters, Journal of Environmental Chemical Engineering 4 (1) (2016) 468–487.

[70] A. E. Lewis, Review of metal sulphide precipitation, Hydrometallurgy 104 (2) (2010) 222–234.

[71] B. C. Maharaj, M. R. Mattei, L. Frunzo, E. D. van Hullebusch, G. Esposito, A general framework to model the fate of trace elements in anaerobic digestion environments, Scientific Reports 11 (1) (2021) 1–19.

[72] V. Gadhamshetty, Y. Arudchelvam, N. Nirmalakhandan, D. C. Johnson, Modeling dark fermentation for biohydrogen production: Adm1-based model vs. gompertz model, international journal of hydrogen energy 35 (2) (2010) 479–490.

[73] C. Li, H. H. Fang, Inhibition of heavy metals on fermentative hydrogen production by granular sludge, Chemosphere 67 (4) (2007) 668–673.

[74] C.-Y. Lin, S.-H. Shei, Heavy metal effects on fermentative hydrogen production using natural mixed microflora, International Journal of Hydrogen Energy 33 (2) (2008) 587–593.

[75] Y. Arudchelvam, M. Perinpanayagam, N. Nirmalakhandan, Predicting vfa formation by dark fermentation of particulate substrates, Bioresource technology 101 (19) (2010) 7492–7499.

[76] P.-Y. Lin, L.-M. Whang, Y.-R. Wu, W.-J. Ren, C.-J. Hsiao, S.-L. Li, J.-S. Chang, Biological hydrogen production of the genus clostridium: metabolic study and mathematical model simulation, International Journal of Hydrogen Energy 32 (12) (2007) 1728–1735.

[77] P. Janssen, P. Heuberger, Calibration of process-oriented models, Ecological Modelling 83 (1-2) (1995) 55–66.

[78] D. Panaro, L. Frunzo, M. Mattei, V. Luongo, G. Esposito, Calibration, validation and sensitivity analysis of a surface-based adm1 model, Ecological Modelling 460 (2021) 109726.

[79] J. Wang, Z. Wang, Z. Zhang, G. Zhang, Effect of addition of other acids into butyric acid on selective leaching of zinc from basic oxygen steelmaking filter cake, Metallurgical and Materials Transactions B 50 (3) (2019) 1378–1386.

[80] S. Barik, G. Prabaharan, L. Kumar, Leaching and separation of co and mn from electrode materials of spent lithium-ion batteries using hydrochloric acid: Laboratory and pilot scale study, Journal of Cleaner Production 147 (2017) 37–43.

[81] A. P. H. Association, A. W. W. Association, W. P. C. Federation, W. E. Federation, Standard methods for the examination of water and wastewater, Vol. 2, American Public Health Association., 1912.

[82] S. Ghassa, A. Farzanegan, M. Gharabaghi, H. Abdollahi, The reductive leaching of waste lithium ion batteries in presence of iron ions: Process optimization and kinetics modelling, Journal of Cleaner Production 262 (2020) 121312.

[83] A. C. Trego, S. Mills, G. Collins, Granular biofilms: function, application, and new trends as model microbial communities, Critical Reviews in Environmental Science and Technology (2020) 1–24.

[84] L. Li, M. Zheng, H. Ma, S. Gong, G. Ai, X. Liu, J. Li, K. Wang, X. Dong, Significant performance enhancement of a uasb reactor by using acyl homoserine lactones to facilitate the long filaments of methanosaeta harundinacea 6ac, Applied microbiology and biotechnology 99 (15) (2015) 6471–6480.

[85] G. Lettinga, A. Van Velsen, S. d. Hobma, W. De Zeeuw, A. Klapwijk, Use of the upflow sludge blanket (usb) reactor concept for biological wastewater treatment,

especially for anaerobic treatment, Biotechnology and bioengineering 22 (4) (1980) 699–734.

[86] R. Lemaire, R. I. Webb, Z. Yuan, Micro-scale observations of the structure of aerobic microbial granules used for the treatment of nutrient-rich industrial wastewater, The ISME journal 2 (5) (2008) 528–541.

[87] C. Di Iaconi, R. Ramadori, A. Lopez, R. Passino, Influence of hydrodynamic shear forces on properties of granular biomass in a sequencing batch biofilter reactor, Biochemical Engineering Journal 30 (2) (2006) 152–157.

[88] L. H. Pol, S. de Castro Lopes, G. Lettinga, P. Lens, Anaerobic sludge granulation, Water Research 38 (6) (2004) 1376–1389.

[89] W. Wiegant, The spaghetti theory on anaerobic granular sludge formation, or the inevitability of granulation, Granular anaerobic sludge (1988) 146–152.

[90] C. Jian, L. Shi-yi, Study on mechanism of anaerobic sludge granulation in uasb reactors, Water Science and Technology 28 (7) (1993) 171–178.

[91] H. Fang, Microbial distribution in uasb granules and its resulting effects, Water science and technology 42 (12) (2000) 201–208.

[92] F. MacLeod, S. Guiot, J. Costerton, Layered structure of bacterial aggregates produced in an upflow anaerobic sludge bed and filter reactor., Applied and Environmental Microbiology 56 (6) (1990) 1598–1607.

[93] D. Zheng, L. Angenent, L. Raskin, Monitoring granule formation in anaerobic upflow bioreactors using oligonucleotide hybridization probes, Biotechnology and bioengineering 94 (3) (2006) 458–472.

[94] G. Zhang, F. Zhang, G. Ding, J. Li, X. Guo, J. Zhu, L. Zhou, S. Cai, X. Liu, Y. Luo, et al., Acyl homoserine lactone-based quorum sensing in a methanogenic archaeon, The ISME journal 6 (7) (2012) 1336–1344.

[95] J. Li, X. Zheng, X. Guo, L. Qi, X. Dong, Characterization of an archaeal two-component system that regulates methanogenesis in methanosaeta harundinacea, PloS one 9 (4) (2014) e95502.

[96] B. Vanderhaegen, E. Ysebaert, K. Favere, M. Van Wambeke, T. Peeters, V. Panic, V. Vandenlangenbergh, W. Verstraete, Acidogenesis in relation to in-reactor granule yield, Water Science and Technology 25 (7) (1992) 21–30.

[97] Y. Sekiguchi, Y. Kamagata, K. Nakamura, A. Ohashi, H. Harada, Fluorescence in situ hybridization using 16s rrna-targeted oligonucleotides reveals localization of methanogens and selected uncultured bacteria in mesophilic and thermophilic sludge granules, Applied and environmental microbiology 65 (3) (1999) 1280–1288.

[98] G. Collins, T. Mahony, S. McHugh, A. Gieseke, D. De Beer, V. O'Flaherty, Distribution, dynamics and in situ ecophysiology of crenarchaeota in anaerobic wastewater treatment granular biofilms, Water science and technology 52 (7) (2005) 233–239.

[99] A. Doloman, H. Varghese, C. D. Miller, N. S. Flann, Modeling de novo granulation of anaerobic sludge, BMC systems biology 11 (1) (2017) 1–12.

[100] C. Picioreanu, D. J. Batstone, M. Van Loosdrecht, Multidimensional modelling of anaerobic granules, Water Science and Technology 52 (1-2) (2005) 501–507.

[101] J. B. Xavier, M. K. De Kreuk, C. Picioreanu, M. C. Van Loosdrecht, Multi-scale individual-based model of microbial and bioconversion dynamics in aerobic granular sludge, Environmental science & technology 41 (18) (2007) 6410–6417.

[102] I. V. Skiadas, B. K. Ahring, A new model for anaerobic processes of up-flow anaerobic sludge blanket reactors based on cellular automata, Water science and technology 45 (10) (2002) 87–92.

[103] M. Mattei, L. Frunzo, B. D'acunto, Y. Pechaud, F. Pirozzi, G. Esposito, Continuum and discrete approach in modeling biofilm development and structure: a review, Journal of mathematical biology 76 (4) (2018) 945–1003.

[104] J. Seok, S. J. Komisar, Integrated modeling of anaerobic fluidized bed bioreactor for deicing waste treatment. i: Model derivation, Journal of Environmental Engineering 129 (2) (2003) 100–109.

[105] I. Klapper, B. Szomolay, An exclusion principle and the importance of mobility for a class of biofilm models, Bulletin of mathematical biology 73 (9) (2011) 2213–2230.

[106] A. Mašić, H. J. Eberl, Persistence in a single species cstr model with suspended flocs and wall attached biofilms, Bulletin of mathematical biology 74 (4) (2012) 1001–1026.

[107] A. Mašić, H. J. Eberl, A modeling and simulation study of the role of suspended microbial populations in nitrification in a biofilm reactor, Bulletin of mathematical biology 76 (1) (2014) 27–58.

[108] K. A. Rahman, R. Sudarsan, H. J. Eberl, A mixed-culture biofilm model with cross-diffusion, Bulletin of mathematical biology 77 (11) (2015) 2086–2124.

[109] O. Wanner, P. Reichert, Mathematical modeling of mixed-culture biofilms, Biotechnology and bioengineering 49 (2) (1996) 172–184.

[110] F. Abbas, R. Sudarsan, H. J. Eberl, Longtime behavior of one-dimensional biofilm models with shear dependent detachment rates, Mathematical Biosciences & Engineering 9 (2) (2012) 215.

[111] P. S. Stewart, Diffusion in biofilms, Journal of bacteriology 185 (5) (2003) 1485–1491.

[112] S. J. Lim, T.-H. Kim, Applicability and trends of anaerobic granular sludge treatment processes, Biomass and bioenergy 60 (2014) 189–202.

[113] J. De Vrieze, W. Verstraete, Perspectives for microbial community composition in anaerobic digestion: from abundance and activity to connectivity, Environmental microbiology 18 (9) (2016) 2797–2809.

[114] S. Guiot, K. Tawfiki-Hajji, F. Lepine, Immobilization strategies for bioaugmentation of anaerobic reactors treating phenolic compounds, Water science and technology 42 (5-6) (2000) 245–250.

[115] Y. V. Nancharaiah, H. M. Joshi, M. Hausner, V. P. Venugopalan, Bioaugmentation of aerobic microbial granules with pseudomonas putida carrying tol plasmid, Chemosphere 71 (1) (2008) 30–35.

[116] R.-C. Jin, Q.-Q. Zhang, Z.-Z. Zhang, J.-H. Liu, B.-E. Yang, L.-X. Guo, H.-Z. Wang, Bio-augmentation for mitigating the impact of transient oxytetracycline shock on anaerobic ammonium oxidation (anammox) performance, Bioresource technology 163 (2014) 244–253.

[117] S. Bathe, M. K. de Kreuk, B. McSwain, N. Schwarzenbeck, Aerobic granular sludge, IWA Publishing, 2005.

[118] J.-H. Tay, Q.-S. Liu, Y. Liu, The effects of shear force on the formation, structure and metabolism of aerobic granules, Applied microbiology and biotechnology 57 (1-2) (2001) 227–233.

[119] Y. Arcand, S. Guiot, M. Desrochers, C. Chavarie, Impact of the reactor hydrodynamics and organic loading on the size and activity of anaerobic granules, The

Chemical Engineering Journal and the Biochemical Engineering Journal 56 (1) (1994) B23–B35.

[120] S. Mills, A. C. Trego, J. Ward, J. Castilla-Archilla, J. Hertel, I. Thiele, P. N. Lens, U. Z. Ijaz, G. Collins, Methanogenic granule growth and development is a continual process characterized by distinct morphological features, Journal of Environmental Management 286 (2021) 112229.

[121] C. Rollet, L. Gal, J. Guzzo, Biofilm-detached cells, a transition from a sessile to a planktonic phenotype: a comparative study of adhesion and physiological characteristics in pseudomonas aeruginosa, FEMS microbiology letters 290 (2) (2009) 135–142.

[122] M. Berlanga, Ò. Domènech, R. Guerrero, Biofilm formation on polystyrene in detached vs. planktonic cells of polyhydroxyalkanoate-accumulating halomonas venusta, Int Microbiol 17 (2014) 205–212.

[123] K. P. Rumbaugh, K. Sauer, Biofilm dispersion, Nature Reviews Microbiology 18 (10) (2020) 571–586.

[124] H. J. Eberl, D. F. Parker, M. C. Vanloosdrecht, A new deterministic spatio-temporal continuum model for biofilm development, Computational and Mathematical Methods in Medicine 3 (3) (2001) 161–175.

[125] B. O. Emerenini, B. A. Hense, C. Kuttler, H. J. Eberl, A mathematical model of quorum sensing induced biofilm detachment, PloS one 10 (7) (2015) e0132385.

[126] E. Alpkvista, I. Klapper, A multidimensional multispecies continuum model for heterogeneous biofilm development, Bulletin of mathematical biology 69 (2) (2007) 765–789.

[127] B. D'Acunto, L. Frunzo, V. Luongo, M. Mattei, A. Tenore, Free boundary problem for the role of planktonic cells in biofilm formation and development, Bulletin of Mathematical Biology 72 (2021).

[128] A. Tenore, F. Russo, M. Mattei, B. D'Acunto, G. Collins, L. Frunzo, Multiscale modelling of de novo anaerobic granulation, Bulletin of Mathematical Biology 83 (2021).

[129] M.-K. H. Winkler, C. Meunier, O. Henriet, J. Mahillon, M. E. Suárez-Ojeda, G. Del Moro, M. De Sanctis, C. Di Iaconi, D. G. Weissbrodt, An integrative review of granular sludge for the biological removal of nutrients and recalcitrant organic matter from wastewater, Chemical Engineering Journal 336 (2018) 489–502.

[130] C. Nicolella, M. Van Loosdrecht, J. Heijnen, Wastewater treatment with particulate biofilm reactors, Journal of biotechnology 80 (1) (2000) 1–33.

[131] P. Wu, Y. Chen, X. Ji, W. Liu, G. Lv, Y. Shen, Q. Zhou, Fast start-up of the cold-anammox process with different inoculums at low temperature (13° c) in innovative reactor, Bioresource technology 267 (2018) 696–703.

[132] C.-j. Tang, P. Zheng, Q. Mahmood, J.-w. Chen, Start-up and inhibition analysis of the anammox process seeded with anaerobic granular sludge, Journal of Industrial Microbiology and Biotechnology 36 (8) (2009) 1093.

[133] C.-J. Tang, P. Zheng, L.-Y. Chai, X.-B. Min, Characterization and quantification of anammox start-up in uasb reactors seeded with conventional activated sludge, International Biodeterioration & Biodegradation 82 (2013) 141–148.

[134] L. Xiong, Y.-Y. Wang, C.-J. Tang, L.-Y. Chai, K.-Q. Xu, Y.-X. Song, M. Ali, P. Zheng, Start-up characteristics of a granule-based anammox uasb reactor

seeded with anaerobic granular sludge, BioMed research international 2013 (2013).

[135] M. Strous, J. Heijnen, J. G. Kuenen, M. Jetten, The sequencing batch reactor as a powerful tool for the study of slowly growing anaerobic ammonium-oxidizing microorganisms, Applied microbiology and biotechnology 50 (5) (1998) 589–596.

[136] K. Isaka, Y. Date, Y. Kimura, T. Sumino, S. Tsuneda, Nitrogen removal performance using anaerobic ammonium oxidation at low temperatures, FEMS microbiology letters 282 (1) (2008) 32–38.

[137] W. R. Van der Star, W. R. Abma, D. Blommers, J.-W. Mulder, T. Tokutomi, M. Strous, C. Picioreanu, M. C. van Loosdrecht, Startup of reactors for anoxic ammonium oxidation: experiences from the first full-scale anammox reactor in rotterdam, Water research 41 (18) (2007) 4149–4163.

[138] N. Chamchoi, S. Nitisoravut, Anammox enrichment from different conventional sludges, Chemosphere 66 (11) (2007) 2225–2232.

[139] Q. Wang, Y. Wang, J. Lin, R. Tang, W. Wang, X. Zhan, Z.-H. Hu, Selection of seeding strategy for fast start-up of anammox process with low concentration of anammox sludge inoculum, Bioresource technology 268 (2018) 638–647.

[140] H. Park, A. Rosenthal, R. Jezek, K. Ramalingam, J. Fillos, K. Chandran, Impact of inocula and growth mode on the molecular microbial ecology of anaerobic ammonia oxidation (anammox) bioreactor communities, Water Research 44 (17) (2010) 5005–5013.

[141] L. Pokorna-Krayzelova, K. E. Mampaey, T. P. Vannecke, J. Bartacek, P. Jenicek, E. I. Volcke, Model-based optimization of microaeration for biogas desulfurization in uasb reactors, Biochemical Engineering Journal 125 (2017) 171–179.

[142] J. Beun, J. Heijnen, M. Van Loosdrecht, N-removal in a granular sludge sequencing batch airlift reactor, Biotechnology and Bioengineering 75 (1) (2001) 82–92.

[143] F. Fang, B.-J. Ni, X.-Y. Li, G.-P. Sheng, H.-Q. Yu, Kinetic analysis on the two-step processes of aob and nob in aerobic nitrifying granules, Applied microbiology and biotechnology 83 (6) (2009) 1159–1169.

[144] S. Van Hulle, J. Callens, K. Mampaey, M. Van Loosdrecht, E. Volcke, N2o and no emissions during autotrophic nitrogen removal in a granular sludge reactor–a simulation study, Environmental technology 33 (20) (2012) 2281–2290.

[145] N. Hubaux, G. Wells, E. Morgenroth, Impact of coexistence of flocs and biofilm on performance of combined nitritation-anammox granular sludge reactors, Water research 68 (2015) 127–139.

[146] M. Fuentes, N. Scenna, P. Aguirre, M. Mussati, Anaerobic biofilm reactor modeling focused on hydrodynamics, Chemical Engineering Communications 195 (6) (2008) 600–621.

[147] K.-Z. Su, B.-J. Ni, H.-Q. Yu, Modeling and optimization of granulation process of activated sludge in sequencing batch reactors, Biotechnology and Bioengineering 110 (5) (2013) 1312–1322.

[148] M. S. I. Mozumder, C. Picioreanu, M. C. Van Loosdrecht, E. I. Volcke, Effect of heterotrophic growth on autotrophic nitrogen removal in a granular sludge reactor, Environmental technology 35 (8) (2014) 1027–1037.

[149] L. Corbalá-Robles, C. Picioreanu, M. C. van Loosdrecht, J. Pérez, Analysing the effects of the aeration pattern and residual ammonium concentration in a partial nitritation-anammox process, Environmental Technology 37 (6) (2016) 694–702.

[150] C. M. Castro-Barros, L. T. Ho, M. K. Winkler, E. I. Volcke, Integration of methane removal in aerobic anammox-based granular sludge reactors, Environmental technology 39 (13) (2018) 1615–1625.

[151] B. D'ACUNTO, L. Frunzo, V. Luongo, M. R. Mattei, Invasion moving boundary problem for a biofilm reactor model, European Journal of Applied Mathematics 29 (6) (2018) 1079–1109.

[152] A. Tenore, M. Mattei, L. Frunzo, Multiscale modelling of oxygenic photogranules, arXiv preprint arXiv:2104.12273 (2021).

[153] S. Lackner, E. M. Gilbert, S. E. Vlaeminck, A. Joss, H. Horn, M. C. van Loosdrecht, Full-scale partial nitritation/anammox experiences–an application survey, Water research 55 (2014) 292–303.

[154] S. E. Vlaeminck, A. Terada, B. F. Smets, H. De Clippeleir, T. Schaubroeck, S. Bolca, L. Demeestere, J. Mast, N. Boon, M. Carballa, et al., Aggregate size and architecture determine microbial activity balance for one-stage partial nitritation and anammox, Applied and environmental microbiology 76 (3) (2010) 900–909.

[155] B. Kartal, J. v. Kuenen, M. Van Loosdrecht, Sewage treatment with anammox, Science 328 (5979) (2010) 702–703.

[156] J. Luo, H. Chen, X. Han, Y. Sun, Z. Yuan, J. Guo, Microbial community structure and biodiversity of size-fractionated granules in a partial nitritation–anammox process, FEMS microbiology ecology 93 (6) (2017) fix021.

[157] S. S. Ahluwalia, D. Goyal, Microbial and plant derived biomass for removal of heavy metals from wastewater, Bioresource technology 98 (12) (2007) 2243–2257.

[158] K. Chojnacka, Biosorption and bioaccumulation–the prospects for practical applications, Environment international 36 (3) (2010) 299–307.

[159] S. H. Abbas, I. M. Ismail, T. M. Mostafa, A. H. Sulaymon, et al., Biosorption of heavy metals: a review, J Chem Sci Technol 3 (4) (2014) 74–102.

[160] M. Fomina, G. M. Gadd, Biosorption: current perspectives on concept, definition and application, Bioresource technology 160 (2014) 3–14.

[161] K. Anjana, A. Kaushik, B. Kiran, R. Nisha, Biosorption of cr (vi) by immobilized biomass of two indigenous strains of cyanobacteria isolated from metal contaminated soil, Journal of Hazardous Materials 148 (1-2) (2007) 383–386.

[162] B. D'Acunto, L. Frunzo, M. Mattei, On a free boundary problem for biosorption in biofilms, Nonlinear Analysis: Real World Applications 39 (2018) 120–141.

[163] G. M. Gadd, Biosorption: critical review of scientific rationale, environmental importance and significance for pollution treatment, Journal of Chemical Technology & Biotechnology: International Research in Process, Environmental & Clean Technology 84 (1) (2009) 13–28.

[164] S. Papirio, L. Frunzo, M. R. Mattei, A. Ferraro, M. Race, B. D'Acunto, F. Pirozzi, G. Esposito, Heavy metal removal from wastewaters by biosorption: mechanisms and modeling, in: Sustainable heavy metal remediation, Springer, 2017, pp. 25–63.

[165] D. Park, Y.-S. Yun, J. M. Park, The past, present, and future trends of biosorption, Biotechnology and Bioprocess Engineering 15 (1) (2010) 86–102.

[166] H.-C. Flemming, J. Wingender, Relevance of microbial extracellular polymeric substances (epss)-part i: Structural and ecological aspects, Water science and technology 43 (6) (2001) 1–8.

[167] S. Comte, G. Guibaud, M. Baudu, Biosorption properties of extracellular polymeric substances (eps) towards cd, cu and pb for different ph values, Journal of hazardous materials 151 (1) (2008) 185–193.

[168] H. Liu, H. H. Fang, Characterization of electrostatic binding sites of extracellular polymers by linear programming analysis of titration data, Biotechnology and bioengineering 80 (7) (2002) 806–811.

[169] R. Muñoz, M. T. Alvarez, A. Muñoz, E. Terrazas, B. Guieysse, B. Mattiasson, Sequential removal of heavy metals ions and organic pollutants using an algal-bacterial consortium, Chemosphere 63 (6) (2006) 903–911.

[170] X. Yang, Z. Zhao, G. Zhang, S. Hirayama, B. Van Nguyen, Z. Lei, K. Shimizu, Z. Zhang, Insight into cr (vi) biosorption onto algal-bacterial granular sludge: Cr (vi) bioreduction and its intracellular accumulation in addition to the effects of environmental factors, Journal of Hazardous Materials 414 (2021) 125479.

[171] K. Milferstedt, W. C. Kuo-Dahab, C. S. Butler, J. Hamelin, A. S. Abouhend, K. Stauch-White, A. McNair, C. Watt, B. I. Carbajal-González, S. Dolan, et al., The importance of filamentous cyanobacteria in the development of oxygenic photogranules, Scientific reports 7 (1) (2017) 1–15.

[172] A. S. Abouhend, A. McNair, W. C. Kuo-Dahab, C. Watt, C. S. Butler, K. Milferstedt, J. Hamelin, J. Seo, G. J. Gikonyo, K. M. El-Moselhy, et al., The oxygenic photogranule process for aeration-free wastewater treatment, Environmental science & technology 52 (6) (2018) 3503–3511.

[173] R. Ferrentino, A. Ferraro, M. R. Mattei, G. Esposito, G. Andreottola, Process performance optimization and mathematical modelling of a sbr-mbbr treatment at low oxygen concentration, Process Biochemistry 75 (2018) 230–239.

[174] G. Wolf, C. Picioreanu, M. C. van Loosdrecht, Kinetic modeling of phototrophic biofilms: the phobia model, Biotechnology and bioengineering 97 (5) (2007) 1064–1079.

[175] S. Mehta, J. Gaur, Use of algae for removing heavy metal ions from wastewater: progress and prospects, Critical reviews in biotechnology 25 (3) (2005) 113–152.

[176] J. J. Harrison, H. Ceri, R. J. Turner, Multimetal resistance and tolerance in microbial biofilms, Nature Reviews Microbiology 5 (12) (2007) 928–938.

[177] M. J. Rani, B. Hemambika, J. Hemapriya, V. R. Kannan, Comparative assessment of heavy metal removal by immobilized and dead bacterial cells: a biosorption approach, African Journal of Environmental Science and Technology 4 (2) (2010).

[178] A. Tenore, M. Mattei, L. Frunzo, Modelling the ecology of phototrophic-heterotrophic biofilms, Communications in Nonlinear Science and Numerical Simulation 94 (2021) 105577.

[179] S. P. Long, S. Humphries, P. G. Falkowski, Photoinhibition of photosynthesis in nature, Annual review of plant biology 45 (1) (1994) 633–662.

[180] J. H. Steele, Environmental control of photosynthesis in the sea, Limnology and oceanography 7 (2) (1962) 137–150.

[181] J. Muñoz Sierra, C. Picioreanu, M. Van Loosdrecht, Modeling phototrophic biofilms in a plug-flow reactor, Water science and technology 70 (7) (2014) 1261–1270.

[182] M. Henze, W. Gujer, T. Mino, M. C. van Loosdrecht, Activated sludge models ASM1, ASM2, ASM2d and ASM3, IWA publishing, 2000.

[183] T. Li, B. Podola, M. Melkonian, Investigating dynamic processes in a porous substrate biofilm photobioreactor—a modeling approach, Algal research 13 (2016) 30–40.

[184] B. V. Merkey, B. E. Rittmann, D. L. Chopp, Modeling how soluble microbial products (smp) support heterotrophic bacteria in autotroph-based biofilms, Journal of theoretical biology 259 (4) (2009) 670–683.

[185] J. R. Flora, M. T. Suidan, P. Biswas, G. D. Sayles, Modeling algal biofilms: role of carbon, light, cell surface charge, and ionic species, Water Environment Research 67 (1) (1995) 87–94.

[186] B. D'Acunto, G. Esposito, L. Frunzo, M. Mattei, F. Pirozzi, Mathematical modeling of heavy metal biosorption in multispecies biofilms, Journal of Environmental Engineering 142 (9) (2016) C4015020.

[187] D. Brockmann, Y. Gérand, C. Park, K. Milferstedt, A. Hélias, J. Hamelin, Wastewater treatment using oxygenic photogranule-based process has lower environmental impact than conventional activated sludge process, Bioresource Technology 319 (2021) 124204.

[188] N. Ahalya, T. Ramachandra, R. Kanamadi, Biosorption of heavy metals, Res. J. Chem. Environ 7 (4) (2003) 71–79.